Cilt 3 Sayı 2 Aralık 2022
Volume 3 Number 2 December 2022

ISSN: 2717-8811(Online)

JOURNAL

Materials and Mechatronics:A

2022

JMMA

JOURNAL

Materials

and

Mechatronics: A

e-ISSN: 2717-8811

Cilt: 3 Sayı: 2 Aralık 2022

Volume:3 Number:2 December 2022

2022

JOURNAL of
MATERIALS and MECHATRONICS:A

JOURNAL of
MATERIALS and MECHATRONICS:A

JOURNAL of
MATERIALS and MECHATRONICS:A

JOURNAL of
MATERIALS and MECHATRONICS:A

JOURNAL of
MATERIALS and MECHATRONICS:A

JOURNAL of
MATERIALS and MECHATRONICS:A

e-ISSN 2717-8811
JournalMM, 2022, 3(2), 137-150
https://doi.org/10.55546/jmm.1100365

Araştırma Makalesi / Research Article

Burç ve Yatak Uygulamaları için Saf Poli-eter-eter-keton Polimer ve Karbon Elyaf Takviyeli Poli-eter-eter-keton Kompozitin Sürtünme ve Aşınma Performanslarının Karşılaştırılması

Ahmet MASLAVİ[1], Hüseyin ÜNAL[2], Alim KAŞTAN[3]*

[1] Sakarya Uygulamalı Bilimler Üniversitesi, Lisansüstü Eğitim Enstitüsü, Metalurji ve Malzeme Mühendisliği Bölümü, Sakarya, Türkiye,
ORCID ID: https://orcid.org/0000-0002-9571-0640, ahmad.abdulkarim@ogrsakarya.edu.tr
[2] Sakarya Uygulamalı Bilimler Üniversitesi, Lisansüstü Eğitim Enstitüsü, Metalurji ve Malzeme Mühendisliği Bölümü, Sakarya, Türkiye,
ORCID ID: https://orcid.org/0000-0003-0521-6647, unal@sakarya.edu.tr
[3] Düden Mesleki ve Teknik Anadolu Lisesi, Antalya Türkiye,
ORCID ID: https://orcid.org/0000-0002-6514-3796, kastanalim@gmail.com

Geliş/ Received: 08.04.2022; **Kabul / Accepted:** 11.06.2022

ÖZET: Endüstrinin değişik alanlarında, makinelerin bazı aksamlarında plastik malzemeden üretilen burç, makara ve rulman gibi makine elemanları kullanılır. Bu makine elemanlarına bazen kullanım şartlarına bağlı olarak farklı yükler etki etmekte bazen de bu parçalar farklı hızlarda çalışmaktadır. Etki eden şartlara bağlı olarak malzemenin çalışma ömrü belirlenir. Bu çalışmada, saf poli-eter-eter-keton (PEEK) polimeri ile ağırlıkça %30 oranında karbon elyaf (CE) takviyeli poli-eter-eter-keton (PEEK-30KE) kompozitin tribolojik performansları araştırılmıştır. Tribolojik deneyler disk üzerinde pim cihazı kullanılarak oda sıcaklığında ve kuru kayma şartlarında gerçekleştirilmiştir. Deneylerde 30N ve 100N olmak üzere iki farklı yük, 1, 2, 3 ve 4m/s olmak üzere dört farklı hız kullanılmıştır. Deneyler sonucunda saf PEEK polimer ve %30 oranında karbon elyaf takviyeli PEEK kompozitinin sürtünme katsayısı, pim sıcaklığı ve spesifik aşınma oranı belirlenmiştir. Optik mikroskop kullanılarak deney malzemelerinin aşınma yüzeyi incelenmiştir. Deneyler sonucunda kayma hızına bağlı olarak hem saf PEEK hem de karbon elyaf takviyeli PEEK kompozitin sürtünme katsayısı azalırken aşınma oranı artış göstermiştir. Karbon elyaf takviyeli PEEK kompozitin saf PEEK polimerine göre ortalama %50 oranında daha yüksek aşınma direncine sahip olduğu tespit edilmiştir.

Anahtar Kelimeler: PEEK, Karbon Elyaf, Aşınma Oranı, Sürtünme Katsayısı, Kompozit.

*Sorumlu yazar / Corresponding author: kastanalim@gmail.com

Bu makaleye atıf yapmak için /To cite this article

Maslavi, A., Ünal, H., Kaştan A. (2022). Burç ve Yatak Uygulamaları için Saf Poli-eter-eter-keton Polimer ve Karbon Elyaf Takviyeli Poli-eter-eter-keton Kompozitin Sürtünme ve Aşınma Performanslarının Karşılaştırılması. Journal of Materials and Mechatronics: A (JournalMM), 3(2), 137-150.

Comparison of Friction and Wear Performances of Pure Poly-ether-ether-ketone Polymer and Carbon Fiber Reinforced Poly-ether-ether-ketone Polymer Composite for Bushing and Bearing Applications

ABSTRACT: Machine elements such as bushings, rollers and bearings made of plastic materials are used in some parts of the machines in different areas of the industry. Sometimes different loads affect these machine elements depending on the usage conditions and sometimes they work at different speeds. Depending on the affecting conditions, the working life of the material is determined. In this study, the tribological performances of pure poly-ether-ether-ketone (PEEK) polymer and 30% by weight carbon fiber (CE) reinforced poly-ether-ether-ketone (PEEK-30CE) composite were investigated. Tribological experiments were carried out using pin-on-disk device at room temperature and dry sliding conditions. Two different loads, both 30N and 100N, and four different speeds (1, 2, 3 and 4 m/s) were used in the experiments. As a result of the experiments, the friction coefficient, pin temperature and specific wear rate of the pure PEEK polymer and 30% carbon fiber reinforced PEEK composite were determined. In addition, the microstructures of the wear surfaces were examined using an optical microscope. As a result of the experiments, depending on the sliding speed, the friction coefficient of both pure PEEK and carbon fiber reinforced PEEK composite decreased while the wear rate increased. It has been determined that the carbon fiber reinforced PEEK composite has an average of 50% higher wear resistance compared to the pure PEEK polymer.

Keywords: PEEK, Carbon Fiber, Wear Rate, Friction Coefficient, Composite.

1. GİRİŞ

Birçok geleneksel malzeme ile karşılaştırıldığında polimerler, üretim kolaylığı, hafiflik, kendinden yağlama etkisi ve mükemmel korozyon direnci gibi üstün avantajlara sahip olduğundan, endüstrinin neredeyse her alanında yaygın olarak kullanılmaktadır (Yan ve ark., 2020; Yang ve ark. 2020). Rulmanlı ve burçlu yataklar, birbirlerine göre izafi hareket eden iki parça arasındaki doğrusal veya dönme hareketi sırasında sürtünmeyi azaltmak ve kuvvet doğrultusunda hareketlerine engel olmak için kullanılan makine parçalarıdır. Yatağın şekli, yatak için kullanılan malzemenin cinsi, yağlayıcı özellikleri ve yağlama şekli yatakların sürtünme mekanizmalarını belirler (Harris ve Kotzalas, 2007). Kayar sürtünme prensibinden faydalanılarak üretilen yataklara kaymalı, yuvarlanma sürtünme prensibinin kullanıldığı yataklara rulmanlı yataklar denir (Koç, 2006). Şekil 1'de kaymalı ve rulmanlı yataklar şematik olarak görülmektedir.

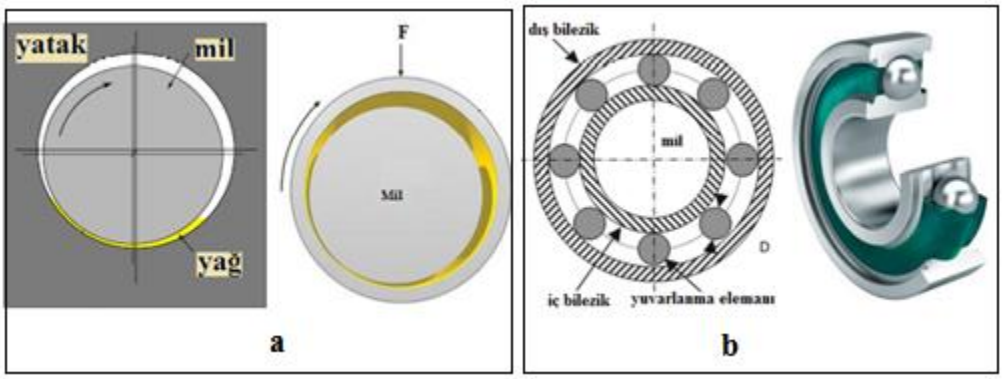

Şekil 1. Kaymalı ve rulmanlı yatakların şematik resimleri a) kaymalı yatak b) rulmanlı yatak (Güngör, 2016)

Çeşitli polimerik malzemelerden ve polimer matrisli kompozitlerden rulmanlar ve burçlar yapılabilmektedir. Polimerik malzemelerin özellikleri metal esaslı malzemelerden bir hayli farklılık göstermektedir. Polimer matrisli malzemelerin en büyük avantajları korozyon ve kimyasallara karşı yüksek direnç, elektrik yalıtkanlığı, iyi sönümleme kabiliyeti, kolay işlenebilirdik, hafif olmaları ve düşük maliyetleridir. Polimerik malzemeler düşük sürtünme katsayısı, kuru ortamda yağlayıcı gerektirmeden çalışabilmeleri, yüksek aşınma ve yorulma dayanımları sayesinde nem ve kimyasallara karşı direncin yüksek olması istenilen ortamlarda rulman ve burç uygulamalarında tercih edilmektedir (Karaçam, 2012). Şekil 2'de polimer malzemelerden üretilmiş rulman ve burç görülmektedir.

Şekil 2. Polimer malzemeden üretilmiş rulman ve yatak

PEEK polimeri ilk defa 1980'lerin başında 'ICI Advanced Materials' firması tarafından üretilerek 'Victrex PEEK' adı altında piyasaya sürülmüştür. PEEK polimeri, yarı kristalin termoplastik yapılı bir malzemedir. PEEK karbon, hidrojen ve oksijen atomları sayesinde tam aromatik, yüksek kararlılıkta ve yarı kristalin yapıya sahiptir. Termal özellikleri mükemmel olan PEEK -60 ºC ile 260 ºC sıcaklıklar arasında özelliklerinde herhangi bir kayıp olmadan kullanılmaktadır. Aynı zamanda PEEK rijit ve tok bir malzemedir. Sürtünme ve aşınma dayanımı yüksek, sürtünme katsayısı düşüktür. Bu özellikleri sayesinde sterilizasyon ve radyasyona karşı oldukça dirençlidir (Şafak, 2001). PEEK uçak sanayinde, elektrik endüstrisinde, takım aletlerinde, giysi parçalarında, ölçme pistonlarında, sürtünmeli yataklarda, yuvarlak valf contalarında, petrol kuyularında, plaka desteklerinde ve kablo endüstrisi gibi birçok alanda kullanılmaktadır. Ayrıca reçine olarak da kullanılabilen PEEK rüzgâr türbin kanatlarında, batarya kılıflarında, tutuşması zor olan tekstil ürünlerinde, robotik ve otonom sistemlerde de tercih edilmektedir (Yılmaz, 2002). PEEK lif olarak da kullanılmaktadır. Polieter eter keton (PEEK) lifleri iyi fiziksel özellikleri ve dayanıklılığı ile günümüzde birçok endüstri dalının vazgeçilmez hammaddesi haline gelmiştir. Monofilament, multifilament ya da stapel lifler olarak çeşitli formlarda ve yapılarda üretilebilen PEEK lifleri; örme, dokuma, dokusuz yüzey gibi temel tekstil formlarında, üç boyutlu kumaşlarda, kompozit ve membran yapılarda da kullanım alanına sahiptir (Hu, 2008; Hanchi ve ark., 1997). PEEK lifleri saf bir yapıya sahip olduğu için üretimi sırasında stabilizasyon için ilave kimyasallar kullanılmamaktadır. Bundan dolayı EEC (European Economic Commission) ve FDA (Food and Drug Administration) tarafından medikal alanda ve yiyecekler ile temas halinde kullanılması uygun görülmüştür (Hearle, 2001; Kalaycı ve ark., 2017). PEEK on yıldan daha uzun süredir yapay kafa plakalarında, parmak ve diz eklemlerinin bileşenlerinde, omurga implantlarında, kemik splintleme vidalarında, kardiyak uygulamalarda ve nörolojik uygulamalarda kullanılmaktadır (Schmidlin ve ark., 2010; May, 1998). Karbon elyafın ilk üretimi 1800'lerin sonunda gerçekleşmiştir. Bambu liflerinin karbonizasyonu sonucunda elde edilen karbon elyaflar akkor lambalarda filament olarak kullanılmıştır. Kompozit

malzemelerdeki kullanımı ise 1950'lerde başlamıştır. Union Carbide Corporation firması gelişmiş malzemeler üretmek amacıyla poliakrilonitrilin karbonizasyonu ile karbon elyaf üreterek Rayon ticari ismi ile satışa sunmuştur. Poliamidler, fenolik reçineler poliesterler ve polivinil alkol gibi polimerlerden de karbon elyaf üretimi yapılmışsa da zift ve PAN'ın karbonizasyonu ile üretilen elyafların mekanik özelliklerinin diğer elyaflardan daha üstün olduğu tespit edilmiştir. Günümüzde karbon elyaflar %90 civarında PAN'dan üretilmektedir (Mazumdar, 2002; Baird, 2001; Çatak, 2016). Karbon elyafların birim fiyatlarının düşmesi sonucunda kullanım alanları giderek artmaktadır. Birçok araştırmacı, polimerlerin, metallerin, seramik matris fazlı malzemelerin özelliklerini geliştirmek için karbon nanotüpü ve karbon elyafı katkı malzemesi olarak kullanmaktadır (Topcu, 2018). Karbon elyafların hafif ve yüksek mukavemetli olması özellikle havacılık sektöründe kullanımını arttırmıştır. Karbon elyaf takviyeli kompozit malzemeler otomobil ve tren kaportalarında, şaftlarında, rulmanlı yataklar ile hidrojen kullanan otomobillerin yakıt depolarında tercih edilmektedir. Karbon elyaflar bisikletler, kanolar, tenis masaları, golf sopaları, sörf tahtaları gibi kullanımlarının yanında, enerji alanında rüzgâr güllerinde, medikal sektöründe tekerlekli sandalye, yapay kol ve bacak protezlerinde ve elektronik alanındaki birçok uygulamalarda tercih edilmektedir (Genç, 2008). Daha önce (Kumar ve Rajmohan, 2019; Gao ve ark., 2022; Koç ve ark., 2019; Yetkin ve ark., 2013, Yi-Lan ve ark., 2019; Zhua ve ark. 2020; Houve ark., 2018; Juanjuan ve ark., 2020; Samyn ve ark., 2007) benzer çalışmalar yapmışlardır. Bu çalışmada burç ve yatak uygulamaları için saf PEEK ve karbon elyaf takviyeli PEEK kompozitlerin sürtünme ve aşınma performansları karşılaştırılmalı olarak incelenmiştir.

2. MATERYAL VE YÖNTEM

Aşınma deneylerinde kullanılan saf PEEK, Ketron PEEK-1000 ticari koduyla 10 mm çapında ve 1000 mm uzunluğunda çubuk formunda temin edilmiştir. Karbon elyaf takviyeli PEEK ise Ketron PEEK-CA30 ticari koduyla yine 8 mm çapında ve 1000 mm uzunluğunda çubuk formunda temin edilmiştir. Deneylerde kullanılan saf PEEK ve %30 karbon elyaf takviyeli PEEK kompozitin fiziksel, mekanik ve termal özellikleri Tablo 1'de verilmiştir. Sürtünme ve aşınma testleri, pim-disk aşınma test cihazında 2000 m kuru kayma şartları altında ve oda sıcaklığında yapılmıştır. Şekil 3'te pim-disk cihazının şematik resmi verilmiştir.

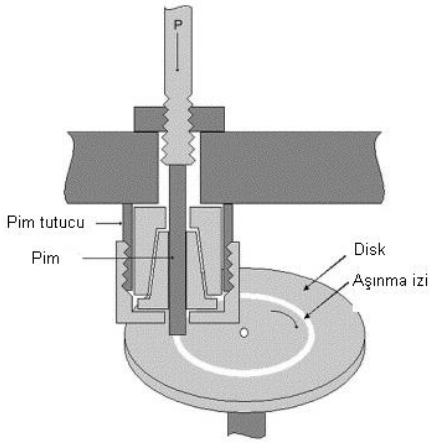

Şekil 3. Pim-disk aşınma test cihazı şematik gösterimi

Aşınma deneylerinde 6 mm çapında ve 50 mm uzunluğunda test numuneleri kullanılmaktadır. Çubuk formundaki numuneleri bu ölçülere getirebilmek için revolver torna tezgâhı kullanılmış ve

numuneler hassas bir şekilde tornada işlenmiştir. AISI 304 paslanmaz çelik ise karşı disk malzeme olarak kullanılmıştır. Çelik disk malzemesi 90 mm çapında ve 5 mm kalınlığında olacak şekilde önce kesilmiş sonra alın ve silindirik yüzey tornalaması yapılmış ve daha sonrasında ise düzlem yüzey taşlama cihazında taşlanmıştır. Taşlama yapılan diskin yüzey pürüzlülüğü ölçülmüş ve yüzey pürüzlülüğü 0,30-0,40 Ra aralığında olduğu tespit edilmiştir. Sürtünme katsayısı yanal kuvvetin, normal uygulanan kuvvete oranı olarak ifade edilir ve eşitlik 1 ile hesaplanır. Burada, μ: Sürtünme katsayısını, F_S: polimerin yanal sürtünme kuvveti (N) ve F_N ise Normal kuvveti (N) ifade eder.

$$\mu = \frac{F_S}{F_N} \tag{1}$$

Her bir aşınma testinden önce ve sonra saf PEEK polimeri ile cam elyaf takviyeli PEEK kompozit pimlerin ağırlıkları ölçülmüş, aradaki fark alınarak ağırlık kaybı (Δm) tespit edilmiştir. Aşağıda verilen formül kullanılarak, aşınma test numunelerinin spesifik aşınma oranları(W) Eşitlik 2 ile hesaplanmıştır. Burada; Δm: ağırlık kaybı (g), L: kayma mesafesi (m), ρ: malzemenin yoğunluğu (g/cm^3), F: uygulanan yük (N).

$$W = \frac{\Delta m}{L * \rho * F} \tag{2}$$

Pim yüzey sıcaklıları kızılötesi termometre ile deney süresince ölçülerek bilgisayara kaydedilmiştir. Çelik disk yüzey pürüzlülüğü için PCE-RT 2300 marka cihaz kullanılmıştır.

Çizelge 1. Saf PEEK ve %30 karbon elyaf takviyeli PEEK kompozitin fiziksel, mekanik ve termal özellikleri

	Saf PEEK	PEEK+%30KE		
Özellik	Değeri		Birimi	Test standardı
Yoğunluk	1.31	1.40	g/cm^3	ASTM D792
Su emme, (24 saat)	0.06	0.05	%	ASTM D570(2)
Çekme mukavemeti	115	144	MPa	ASTM D638
Elastik modülü (çekmede)	4300	9200	MPa	ASTM D638
Kopmadaki % uzama	7	5	%	ASTM D638
Termal iletkenlik	0.25	0.92	W/ m.^{o}K	-
Sertlik	105	102	Rockwell M	ASTM D785
Ergime sıcaklığı	340	340	^{o}C	ASTM D3418
Maksimum sürekli çalışma sıcaklığı	250	250	^{o}C	

3. BULGULAR VE TARTIŞMA

Şekil 4'te saf PEEK polimerinin farklı yükler ve farklı hızlarda yapılan deneylerden elde edilen sürtünme katsayısı kayma hızı grafikleri verilmiştir. Kayma hızının artması ile birlikte hem 30 N ve hem de 100 N yükte yapılan deneylerde sürtünme katsayısı azalmıştır**.** 30 N aşındırma yükü altında yapılan tüm deneylerin sürtünme katsayısı 100 N ile yapılan deneylerden daha yüksek çıkmıştır. En yüksek sürtünme katsayısı 30 N yük ve 1m/s hızda yapılan deneyde μ: 0,54, en düşük sürtünme katsayısının değerinin ise 100 N aşındırma yükü altında 4m/s hızda μ: 0,2 olduğu görülmüştür. Sürtünme katsayısında en fazla azalma 1m/s hızda aşındırma yükünün 30 N'dan 100 N'a çıkarılması ile elde edilmiştir. Bu azalma yaklaşık %52 oranındadır. Daha önce yapılan çalışmada (Kumar ve Rajmohan, 2019) yüksek yükte çelik disk üzerinde aşındırıcı etkinin daha fazla olduğunu, sürtünme kuvvetinin PEEK matris kompozitlerini daha yumuşak hale getirmek için yüksek bir termal etki

sağladığını belirtmişlerdir. Daha yüksek kayma hızlarında, çelik disk yüzeyinin daha kolay modifiye edilebildiğini ve transfer filmin daha hızlı oluşması soncunda yumuşak polimer yüzeyin sert metal yüzeyden koruma sağladığınım ifade etmişlerdir. Ayrıca kayma hızının artması ile sürtünme katsayısındaki azalmayı ise düşük kayma hızında, hem PEEK kompozitlerinin hem de çelik muadili kayma yüzeylerinin pürüzlü olması nedeniyle yüksek sürtünme katsayısı ile sonuçlanan güçlü bir "kilitleme" meydana getirdiğini ancak hızın artması ile bu mekanizmanın zayıflaması sonucunda sürtünme katsayısının azaldığını belirtmişlerdir. Sonuçlar literatür ile uyum göstermektedir.

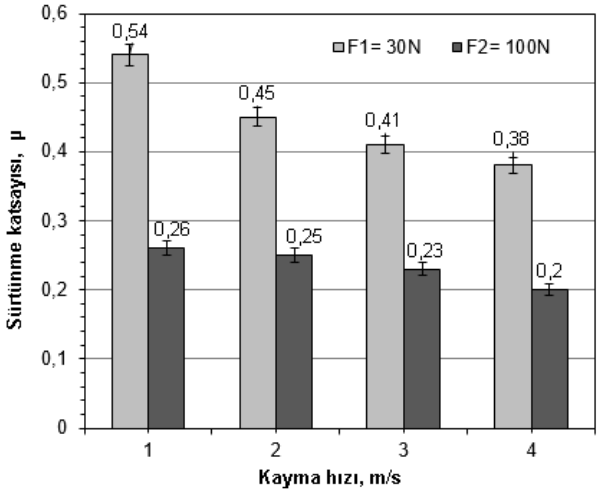

Şekil 4. Saf PEEK polimerinin farklı yükler altındaki sürtünme katsayısı-kayma hızı ilişkisi

Şekil 5'te %30 karbon elyaf takviyeli PEEK polimer kompozitlerin farklı yükler altındaki sürtünme katsayısı-kayma hızı ilişkisi verilmiştir. Katkısız PEEK polimerinde olduğu gibi kayma hızının artması ile sürtünme katsayısında azalma gözlemlenmiştir. Benzer şekilde aşındırma yükünün artması ile de sürtünme katsayısında da azalma olmuştur. Ancak PEEK+%30KE içeren kompozitlerin sürtünme katsayısı değerlerinde katkısız PEEK ile kıyaslandığında çok önemli oranlarda azalma olmuştur. Katkısız PEEK polimerinin 30 N yük ve 1 m/s hızda sürtünme katsayısı değeri 0,54 iken PEEK+%30 KE'in ise sürtünme katsayısında %52 azalma olmuş ve bu değer 0,26'ya gerilemiştir. 30 N aşındırma yükü altında yapılan deneylerde ve 2 m/s hızda sürtünme katsayısında %49, 3 m/s hızda %54, 4 m/s hızda yapılan deneylerde ise %52 azalma olmuştur. 100 N aşındırma yükünde ise 1 m/s hızda %39, 2 m/s hızda %40, 3 m/s hızda %39 ve 4 m/s hızda ise %37 azalma olduğu tespit edilmiştir. PEEK içerisine ilave edilen %30 KE sürtünme katsayısını önemli oranda azaltmıştır. Başka bir çalışmada (Gao ve ark., 2022) PEEK içerisine ilave edilen KE'nin sürtünme katsayısını düşürdüğünü, aşınma yüzeyinde transfer film oluşturmada etkili olduğunu ve oluşan filmin aşınma yüzeyinin topoğrafik yapısıyla ilgili olduğunu belirtmişlerdir. Sürtünme katsayısındaki azalma malzemenin servis sırasındaki performansını olumlu yönde etkileyecektir.

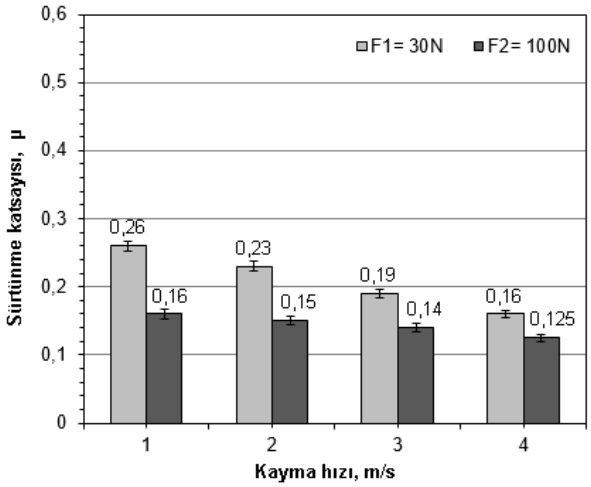

Şekil 5. %30 karbon elyaf takviyeli PEEK polimer kompozitinin farklı yükler altındaki sürtünme katsayısı-kayma hızı ilişkisi

Şekil 6'da saf PEEK polimerinin farklı yükler ve farklı hızlarda yapılan deneylerden elde edilen kayma hızı-pim sıcaklığı ilişkisi verilmiştir. Deneylerden elde edilen veriler incelendiğinde yükün ve hızın artması ile pim sıcaklığının da arttığı söylenebilir. En düşük pim sıcaklığı 1 m/s hızda ve 30 N aşındırma yükünde 39ºC ve en yüksek pim sıcaklığı ise 4 m/s hızda 100 N aşındırma yükü altında 99ºC olarak ölçülmüştür. Kayma hızının benzer olduğu yükün 30 N'dan 100 N'a çıkarılması ile pim sıcaklığındaki değişim en çok 1 m/s hızda 48 ºC, en az değişim ise 2 m/s hızda 35 ºC olmuştur. Aşındırma yükünün 30 N olduğu deneylerde 1 m/s hızda pim sıcaklığı 39 ºC, 2 m/s hızda 54 ºC, 3 m/s hızda 56 ºC ve 4 m/s hızda 59 ºC'ye yükselmiştir. Aynı yükte hızın 1 m/s'den 2 m/s'ye çıkması ile pim sıcaklığında 15 ºC artış olmuştur. Ancak 2 m/s-4 m/s hız aralığında yapılan deneylerde pim sıcaklığında sadece 5 ºC'lik artış gerçekleşmiştir. 30 N alındırma yükünde 1-4 m/s hızlarda yapılan deneylerde pim sıcaklığındaki değişim 20 ºC'dir. 100 N aşındırma yükünde ise 1 m/s hızda pim sıcaklığı 87 ºC, 2 m/s hızda 89 ºC, 3 m/s hızda 93 ºC ve 4 m/s hızda 99 ºC olmuştur. Aynı yükte 1-4 m/s hızlarda yapılan deneylerde pim sıcaklığındaki değişimi 12 ºC olarak ölçülmüştür. Bu veriler doğrultusunda kayma hızına ve aşındırma yüküne bağlı olarak pim sıcaklığında önemli oranda değişimlerin olduğu söylenebilir. Benzer şekilde (Koç ve ark., 2019) artan yük ile deney numunelerinin sıcaklığının da yükseldiğini belirtmişlerdir. Bir başka çalışmada ise (Yetgin ve ark., 2013) benzer sonuçlar bulmuşlardır.

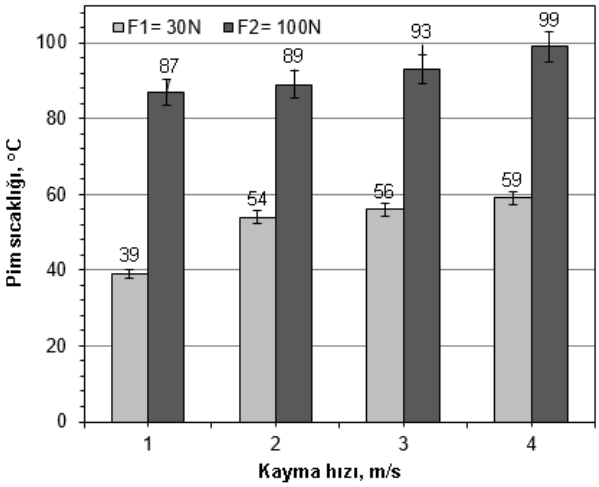

Şekil 6. Saf PEEK polimerinin farklı yükler altındaki kayma hızı-pim sıcaklığı ilişkisi

Şekil 7'de %30 karbon elyaf takviyeli PEEK polimer kompozitlerin farklı yükler altındaki kayma hızı-pim sıcaklığı ilişkisi verilmiştir. Katkısız PEEK polimerinde olduğu gibi kayma hızının ve aşındırma yükünün artması ile pim sıcaklığında artış meydana gelmiştir. Ancak bu artış daha sınırlı olmuştur. PEEK+%30 KE kompozitlerin pim sıcaklığı tüm deneylerde katkısız PEEK polimerinden daha düşüktür. PEEK+%30 KE kompozitlerde en düşük yüzey sıcaklığı 1 m/s kayma hızında ve 30 N aşındırma yükü altında 34 °C olarak ölçülmüştür. Bu sıcaklık değeri katkısız PEEK polimerine göre 5 °C daha düşüktür. En yüksek pim 81 °C sıcaklığına 4 m/s kayma hızında ve 100 N aşındırma yükünde ulaşılmıştır. Benzer şartlarda yapılan deneyde katkısız PEEK polimerine göre 18 °C daha düşük olduğu belirlenmiştir. Yükün 30 N'dan 100 N'a çıkarılması ile pim sıcaklığı 1 m/s kayma hızında 21 °C, 2 m/s kayma hızında 32 °C, 3 m/s kayma hızında 37 °C ve 4 m/s kayma hızında 40 °C artış olmuştur. Katkısız PEEK polimerlerde benzer deneylerde sıcaklık artışının daha fazla olduğu görülmüştür. Pim sıcaklığındaki bu azalma, PEEK içerisine eklenen KE ile ısıl iletkenliğin artması ve kendi kendine yağlama özelliğinin gelişmesinden kaynaklanmaktadır. Benzer çalışmada (Yi-Lan ve ark., 2019) grafitin yüksek termal iletkenliğinden dolayı kayma sırasında temas sıcaklığını düşürdüğünü ve temas alanını azaltarak sürtünmeyi azalttığını belirtmişlerdir. Pim sıcaklığındaki önemli azalmanın gerçek çalışma sırasında çok önemli avantajlar sağlayacağı aşikârdır.

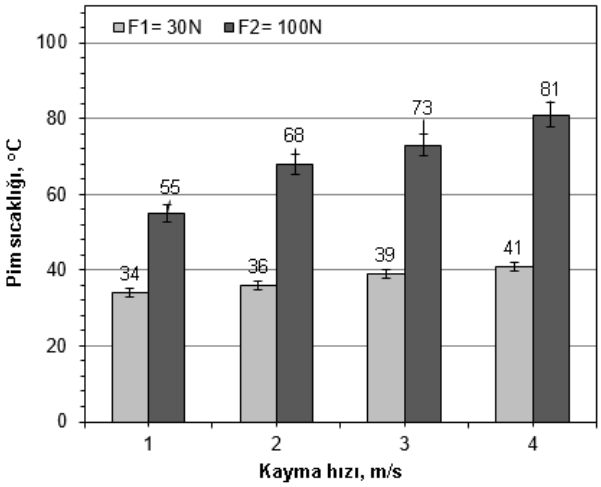

Şekil 7. %30 karbon elyaf takviyeli PEEK polimer kompozitinin farklı yükler altındaki kayma hızı-pim sıcaklığı ilişkisi

Şekil 8'de Saf PEEK polimerinin farklı yükler altındaki spesifik aşınma oranının yüke ve kayma hızına göre değişimi verilmiştir. Polimere uygulanan aşındırma yükünün artması ile aşınma oranında artış görülmüştür. Aşındırma yükünün 30 N'dan 100 N'arttırılması ile 1 m/s hızda $3{,}8\text{x}10^{-6}$ mm^3/Nm'den $8{,}3\text{x}10^{-6}$ mm^3/Nm'ye, 2 m/s hızda $6{,}4\text{x}10^{-6}$ mm^3/Nm'den $11{,}3\text{x}10^{-6}$ mm^3/Nm'ye, 3m/s hızda $12{,}8\text{x}10^{-6}$ mm^3/Nm'den $14{,}2\text{x}10^{-6}$ mm^3/Nm'ye, 4 m/s hızda ise $13{,}7\text{x}10^{-6}$ mm^3/Nm'den $18{,}1\text{x}10^{-6}$ mm^3/Nm'ye yükselmiştir. En fazla değişim 2 m/s hızda $4{,}9\text{x}10^{-6}$ mm^3/Nm ve en az değişim 3m/s hızda $2{,}4\text{x}10^{-6}$ mm^3/Nm olmuştur. Kayma hızının artması ile aşınma oranı da artmıştır. Kayma hızı en düşük 1 m/s hızda $3{,}8\text{x}10^{-6}$ mm^3/Nm ve en yüksek ise 4 m/s hızda $18{,}1\text{x}10^{-6}$ mm^3/Nm değerine ulaşmıştır. 30 N aşındırma yükü altında kayma hızının 1 m/s hızdan 4 m/s hıza yükselmesi ile aşınma oranında %360 artış olmuştur. Bu oran 100 N aşındırma yükünde ise %218 civarında olmuştur. Başka bir çalışmada (Zhua ve ark., 2020) aşındırma yükünün artması ile birlikte spesifik aşınma oranının da arttığını belirtmişlerdir. Şekil 7'de görüldüğü gibi deney sırasında yükün ve hızın artması ile sıcaklıkta ciddi artış olmuştur. Sıcaklık artışının polimer zincirlerinin gevşemesine ve PEEK matrisin mukavemetinin düşmesine neden olduğu sanılmaktadır. Bunun sonucunda aşınma oranında artış gözlemlenmiştir.

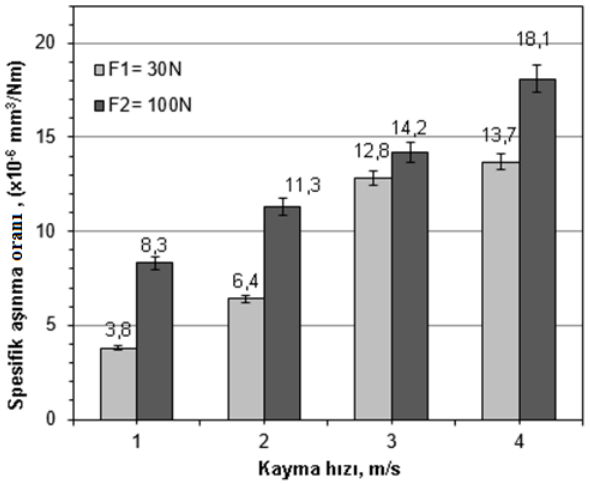

Şekil 8. Saf PEEK polimerinin farklı yükler altındaki aşınma oranı- kayma hızı ilişkisi

Şekil 9'da %30 karbon elyaf takviyeli PEEK polimer kompozitlerin farklı yükler ve hızlardaki aşınma oranında meydana gelen değişim verilmiştir. Kayma hızının artması ile birlikte hem 30 N aşındırma yükünde ve hem de 100 N aşındırma yükünde aşınma oranında artış görülmüştür. Aşınma oranının yük ve hıza göre değişimi bakımından katkısız PEEK ile KE katkılı PEEK polimerlerin benzer davranış gösterdiği söylenebilir. Ancak aşınma oranı değerlerinde çok ciddi farkların olduğu gözden kaçmaması gereken önemli bir parametredir. Tüm deney parametrelerinde KE katkılı PEEK polimerlerin aşınma oranı değerleri katkısız PEEK'e göre çok daha düşüktür. Katkısız PEEK'in 4 m/s hız ve 30 N yükteki aşınma oranı $13{,}7x10^{-6}$ mm^3/Nm iken KE katkılı PEEK'i $7{,}14x10^{-6}$ mm^3/Nm'dir. Bu polimerlerin 100 N'daki aşınma oranları ise katkısız PEEK'in $18{,}1x10^{-6}$ mm^3/Nm iken KE katkılı PEEK'in $8{,}93x10^{-6}$ mm^3/Nm'dir. 100 N yük ve 4 m/s hızda aşınma oranında azalma %52 olmuştur. Başka bir çalışmada (Hou ve ark., 2018) PEEK matrise ilave edilen grafen oksit sayesinde, aşınma yüzeyinde yüksek mukavemet ile mükemmel aşınma davranışına sahip olan yoğun ve düzgün bir transfer filminin oluşması sayesinde, kayma yüzeyine uygulanan yükün büyük bir kısmını taşıyabileceği, bunun sonucunda da aşınma oranında azalma olduğu ifade edilmiştir. PEEK içerisine ilave edilen KE ile spesifik aşınma oranındaki büyük oranda azalma, malzemenin servis ömrünü uzatarak maliyetinde düşüş sağlayacaktır.

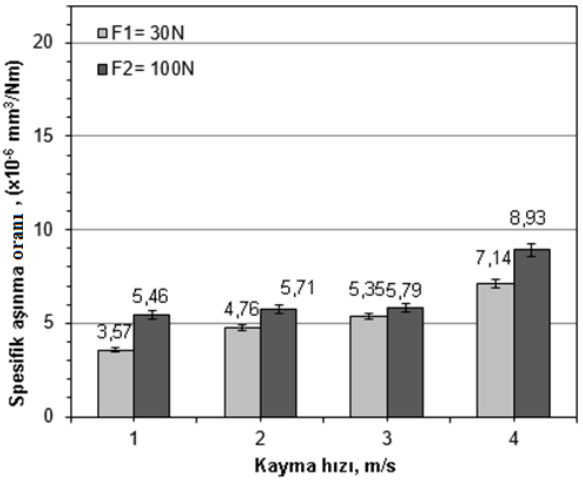

Şekil 9. %30 karbon elyaf takviyeli PEEK polimer kompozitlerin farklı yükler altındaki aşınma oranı- kayma hızı ilişkisi

Şekil 10'da katkısız PEEK polimerinin 1 m/s ve 4 m/s hızda 100 N yükteki pim ve disk yüzeylerinin optik mikroskop görüntüleri yer almaktadır. Katkısız PEEK polimerinin pim ve disk yüzeylerinde aşınma izleri oldukça belirgindir. Şekil 10a'da aşınmaya maruz kalan pim yüzeyinden tabakalar halinde polimerin koparak ayrıldığı, Şekil 10b'de ise disk yüzeyinde herhangi bir koruyucu film tabakasının olmadığı, sadece pim yüzeyinden kopan polimer parçalarının olduğu görülmektedir. Şekil 4 ve 5'te görülen sürtünme katsayısının daha yüksek olmasının sebeplerinden biri de budur. Şekil 10c incelendiğinde hız 4 m/s olduğunda pim yüzeyindeki aşınmanın karakterinin değiştiği çok sayıda küçük parçaların yüzeye yapıştığı, aşınma mekanizmasında adezyonun etkili olduğu söylenebilir. Şekil 10d'de gösterilen disk yüzeyi de bu aşınma mekanizmasını doğrulamaktadır. Artan ısı etkisiyle polimer parçalarının disk yüzeyine yapışmış ve homojen olmayan kalınlıkta film tabakası oluşturmuştur. Genel olarak katkısız polimerlerin birçoğunda benzer aşınma mekanizmasıyla karşılaşıldığı söylenebilir.

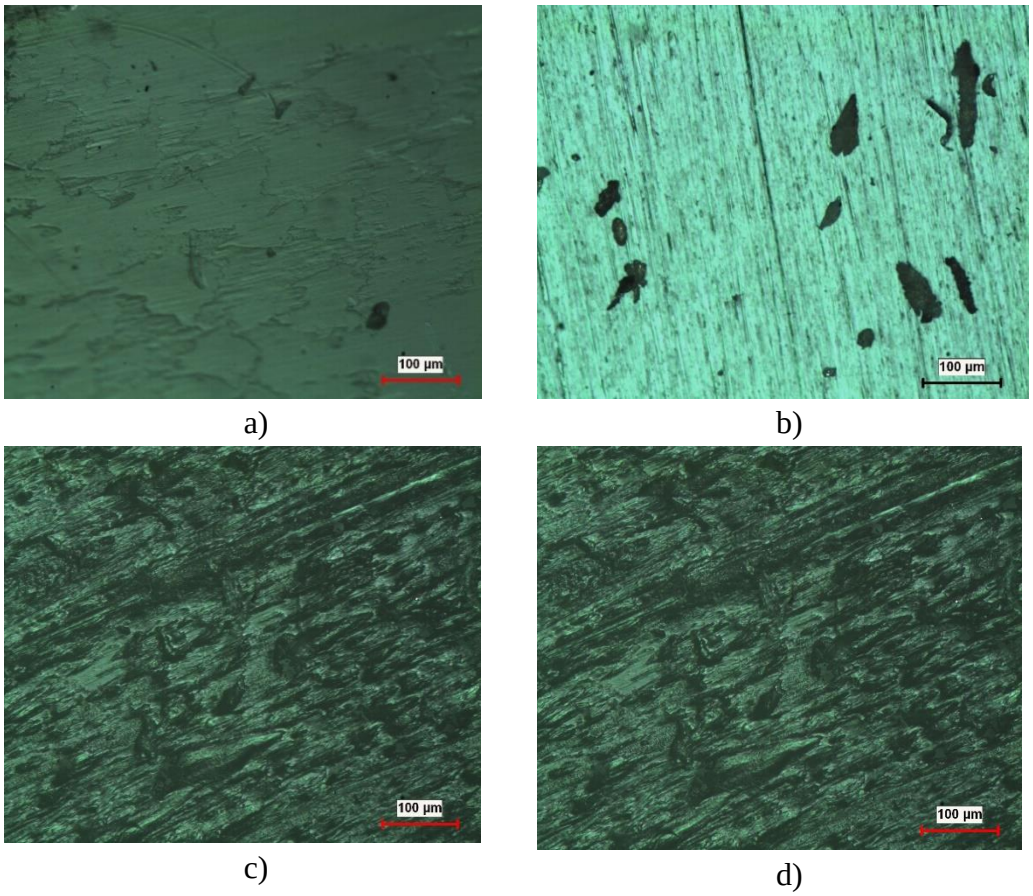

Şekil 10. Katkısız PEEK polimerinin 1 m/s ve 4 m/s kayma hızında aşınan pim ve disk yüzeylerinin optik mikroskop görüntüleri (Yük:100 N), a) saf PEEK pim (100 N, 1 m/s), b) saf PEEK/çelik disk (100 N, 1 m/s), c) saf PEEK pim (100 N, 4 m/s), ve d) saf PEEK/çelik disk (100 N, 4 m/s)

Şekil 11'de %30 karbon elyaf takviyeli PEEK kompozitlerin 1 m/s ve 4 m/s kayma hızında 100 N yükteki aşınan pim ve disk yüzeylerinin optik mikroskop görüntüleri mevcuttur. Şekil 11a'da görülen pim yüzeyi incelendiğinde derin tabaka halinde kopmaların, çiziklerin ve oyukların olmadığı, katkısız PEEK'e göre aşınma yüzeyinin düzgün olduğu söylenebilir. Şekil 11b'de ise pim yüzeyinde aşınma mekanizmasını olumlu yönde etkileyen film tabakasının Şekil 10b'ye kıyasla çok daha fazla oluştuğu görülmektedir. Şekil 11c'de derin olmayan kayma yönünde aşınma çizgileri vardır. Ancak aşınma yüzeyinde tabaka ayrılması ve yapışması gözükmemektedir. Şekil 11c'deki resim

incelendiğinde ise disk yüzeyinin neredeyse tamamen koruyucu film tabakası ile kaplandığı söylenebilir. Karbonun katı yağlayıcı özelliğinin olması aşınma mekanizması üzerindeki etkinliğini göstermiştir. Bunun sonucunda malzemedeki kütle kaybı azalmış ve PEEK+%30KE kompozitlerin aşınma direnci artmıştır. Samyn ve arkadaşları yaptıkları çalışmada (Samyn ve ark., 2007) katı yağlayıcıların, aşınma sırasında daha homojen bir transfer film oluşturması nedeniyle düşük sürtünme ve aşınma için en uygun katkılar olduğunu belirtmişlerdir. Başka bir çalışmada ise Gao ve arkadaşları (Gao ve ark., 2022) karbon fiberlerin kuru sürtünme ortamında transfer film oluşturmada etkin olduklarını ifade etmişlerdir. Şekil 8'de bu olumlu etki açık bir biçimde görülmektedir.

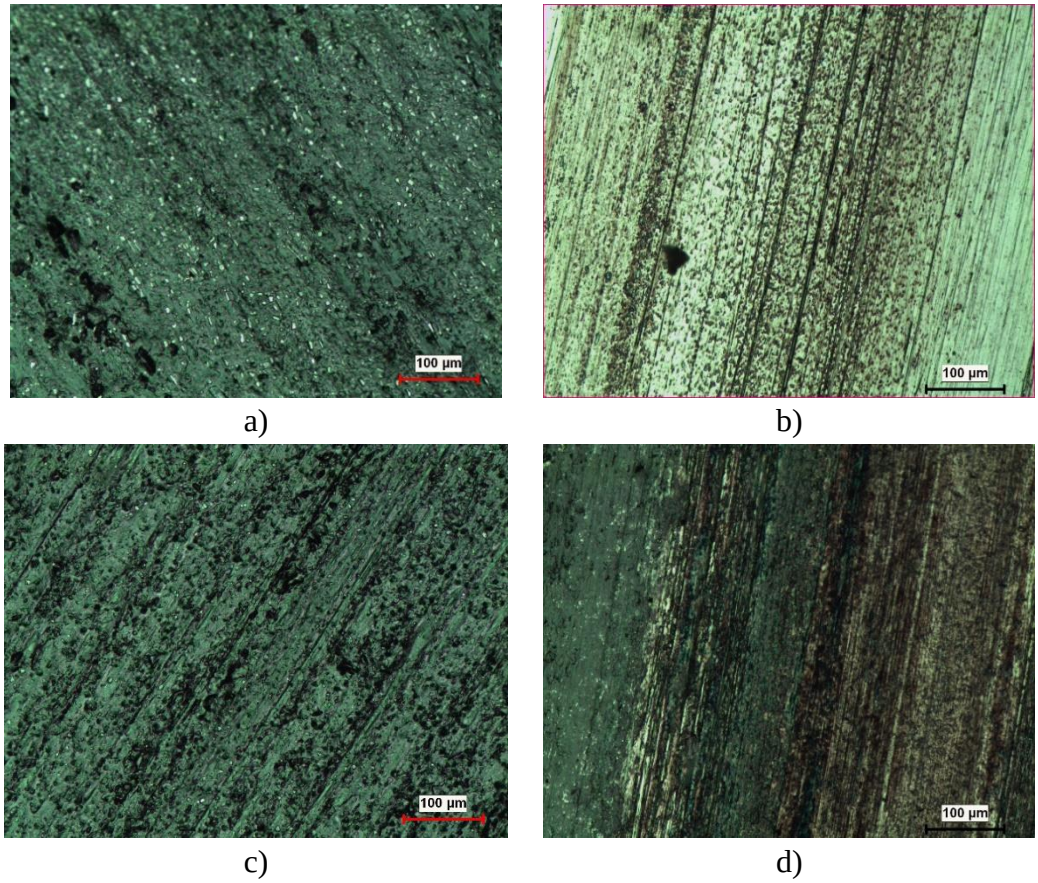

Şekil 11. %30 karbon elyaf takviyeli PEEK kompozitlerin 1 m/s ve 4 m/s kayma hızında aşınan pim ve disk yüzeylerinin optik mikroskop görüntüleri (Yük:100 N), a)30 KE-PEEK pim (100 N, 1 m/s), b) 30 KE-PEEK/çelik disk (100 N, 1 m/s), c) 30 KE-PEEK pim (100 N, 4 m/s), d) 30 KE-PEEK/çelik disk (100 N, 4 m/s)

4. SONUÇ

Bu çalışmada burç ve yatak uygulamaları için saf PEEK ve karbon elyaf takviyeli PEEK kompozitlerin sürtünme ve aşınma performansları karşılaştırılmalı olarak incelenmiş ve aşağıdaki sonuçlara ulaşılmıştır.

- PEEK içerisine %30KE ilave edilmesi sonucunda sürtünme katsayısında %52'ye kadar azalma olduğu tespit edilmiştir. Bu azalma malzemenin aşınma direncini arttıracaktır.
- Katkısız PEEK polimerlerin aşınma sırasında pim sıcaklıkları 39-99 °C arasında iken PEEK+%30KE ilave edilmiş kompozitlerin aşınma sıcaklıkları 34-81 °C aralığında ölçülmüştür. Pim sıcaklığındaki azalma çalışma sırasında avantaj sağlayacaktır.

- KE ilave edilmiş tüm PEEK kompozitlerin aşınma oranında %52'ye kadar azalma olduğu tespit edilmiştir. Aşınma oranındaki bu azalma servis ömrünün uzamasını sağlayacaktır.
- Aşınma yüzeylerinin optik resimleri incelendiğinde katkısız PEEK polimerinin pim yüzeylerinde daha derin aşınma izlerinin olduğu, disk yüzeylerinde ise koruyucu film tabakasının yeterince oluşmadığı görülmüştür. KE katkılı PEEK polimerlerin aşınma yüzeylerinde ise daha az derinlikte çizilmeler ve özellikle disk yüzeyinde transfer film oluştuğu tespit edilmiştir. Oluşan koruyucu film aşınma sırasında avantaj sağlayacaktır.
- Yapılan çalışma sonucunda KE katkılı PEEK polimerlerin rulman ve yatak uygulamalarında kullanımının avantaj sağlayacağı söylenebilir.

5. TEŞEKKÜR

Yazarlar, desteklerinden dolayı Sakarya Uygulamalı Bilimler Üniversitesi, Bilimsel Araştırma Projeleri Koordinatörlüğü'ne (Proje No: 008-2020) teşekkürü bir borç bilir.

6. ÇIKAR ÇATIŞMASI

Yazarlar, bilinen herhangi bir çıkar çatışması veya herhangi bir kurum/kuruluş ya da kişi ile ortak çıkar bulunmadığını onaylamaktadırlar.

7. YAZAR KATKISI

Ahmet MASLAVİ, Hüseyin ÜNAL ve Alim KAŞTAN çalışmanın kavramsal ve tasarım süreçlerinin belirlenmesi ve yönetimi, veri toplama, veri analizi ve yorumlama, makale taslağının oluşturulması, fikirsel içeriğin eleştirel incelenmesine katkı sağlamışlardır ve Alim KAŞTAN son onay ve tam sorumluluk kısmında da katkıda bulunmuştur.

8. KAYNAKLAR

Baird D. G., Encyclopedia of Physical Science and Technology, Third Edition, Elsevier Science Ltd, pp. 621-640, 2001.

Cao H., Dong X., Qu D., Dong C., Zhao C., Sun D., Gu L., Wu B., Transfer film growth of continuous carbon fiber reinforced thermoplastic poly (ether ether ketone) facilitated by surface texture during dry sliding, Journal of Material Science 57, 383-397, 2022.

Çatak K., Fonksiyonlanmış ve silanlanmış karbon elyaf takviyeli poliamid kompozitlerin ısıl ve mekanik özelliklerinin incelenmesi, Yalova Üniversitesi, Fen Bilimleri Enstitüsü, Yüksek Lisans Tezi (Basılmış), 2016.

Genç G., Elyaf sarma yöntemiyle üretilen karbon elyaf kompozitlerde ön gerilme parametrelerinin elyaf ve kompozit mukavemetine etkisi, Marmara Üniversitesi, Fen Bilimleri Enstitüsü, Doktora tezi (Basılmış), 2008.

Güngör K., Sinterlenmiş Bronz Esaslı Kaymalı Yataklarda Polimer Kullanımının Tribolojik Özelliklere Etkisi, Sakarya Üniversitesi, Fen Bilimleri Enstitüsü, Doktora tezi (Basılmış), 2016.

Hanchi J., Eiss Jr. N. S., Dry sliding friction and wear of short carbon-fiber-reinforced polyetheretherketone (PEEK) at elevated temperatures, Wear 203-204, 380-386, 1997.

Harris T., Kotzalas M., Advanced Concepts of Bearing Technology, Fifth Edition, CRC Press, Boca Raton, FL, USA, 2007.

Hearle J.W.S., High-performance Fibres, CRC Press, Cambridge, England, 2001.

Hou X., Hu Y., Hu X., Jiang D., Poly (ether ether ketone) composites reinforced by graphene oxide and silicon dioxide nanoparticles: Mechanical properties and sliding wear behavior. High Performance Polymers 30(4), 406-417, 2018.

Hu J., 3-D Fibrous Assemblies: Properties, Applications and Modelling of Three-Dimensional Textile Structures, Elsevier, Woodhead Publishing, 2008.

Zhu J., Ma L., Dwyer-Joyce R., Friction and wear behaviours of self-lubricating peek composites for articulating pin joints. Tribology International 149, 105741, 2020.

Kalaycı E., Avinç O., Yavaş A., Polieter Eter Keton (Peek) Lifleri. Cumhuriyet Üniversitesi Fen Fakültesi Fen Bilimleri Dergisi 38(2), 168-186, 2017.

Karaçam Dinç S., Yağlayıcıların polimer rulmanlı yatak gürültü karakteristiğine etkisinin deneysel analizi, İstanbul Teknik Üniversitesi, Fen Bilimleri Enstitüsü, Yüksek lisans tezi (Basılmış), 2012.

Koç E., Makina Elemanları, Cilt-II, Nobel Yayınları, Adana, 2006.

Koç V., Demirel M., Epoksi Reçine-MgO Polimer Matrisli Kompozit Malzemelerin Üretilmesi ve Pin On Disk Abrasiv Aşınma Özelliklerinin İncelenmesi. Fırat Üniversitesi Mühendislik Bilimleri Dergisi 31(1), 1-10, 2019.

Kumar D., Rajmohan T., Experimental investigation of wear of multiwalled carbon nanotube particles-filled poly-ether-ether-ketone matrix composites under dry sliding. Journal of Thermoplastic Composite Materials 32(4), 521-543, 2019.

May R., Polyetheretherketones, in: Mark H. F., Bikales N. M., Overberger C. G., Menges G., Kroschiwitz J.I., (Eds.), Encyclopedia of Polymer Science and Engineering, John Wiley and Sons, New York, pp. 313-320,1988.

Mazumdar S. K., Composites Manufacturing: Materials, Product, and Process Engineering, CRC Press, pp. 20-73, 2002.

Samyn P., Baets P. D., Schoukens G., Driessche I. V., Friction, wear and transfer of pure and internally lubricated cast polyamides at various testing scales. Wear 262(11-12), 1433-1449, 2007.

Schmidlin P. R., Stawarczyk B., Wieland M., Attin T., Hämmerle C. H. F., Fischer J., (2010). Effect of different surface pre-treatments and luting materials on shear bond strength to PEEK. Dental Materials 26(6), 553-559, 2010.

Şafak D., Plastik Enjeksiyon Kalıplarının Tasarım Bakımından İncelenmesi ve Uygulamalı Kalıp Örneği, İstanbul Teknik Üniversitesi, Fen Bilimleri Enstitüsü, Yüksek Lisans Tezi (Basılmış), 2001.

Topcu İ., Karbon Nanotüp Takviyeli Alüminyum Matriksli AlMg/KNT Kompozitlerinin Mekanik Davranışlarının İncelenmesi, Çanakkale Onsekiz Mart Üniversitesi Fen Bilimleri Enstitüsü Dergisi 4(1), 99-109, 2018.

Yan Y., Meng Z., Liu H., Wang J., Chen B., Yan F., Nano-M_OS_2 modified PBO fiber hybrid for improving the tribological behavior and thermal stability of TPI/PEEK blends. Tribology International 144, 106117, 2020.

Yang M., Zhang Z., Yuan J., Wu L., Zhao X., Guo F., Men X., Liu W., Fabrication of PTFE/Nomex fabric/phenolic composites using a layer-by-layer self-assembly method for tribology field application. Friction 8, 335-342, 2020.

Yetgin S. H., Ünal H., Mimaroglu A., Fındık F., Influence of Process Parameters on the Mechanical and Foaming Properties of PP Polymer and PP/TALC/EPDM Composites. Polymer-Plastics Technology and Engineering 52(5), 433-439, 2013.

Yılmaz T., PEEK (polyetheretherketone) ve kompozitlerinde kısa fiber takviyesi ve mikro yapının tribolojik özelliklere etkisi, Kocaeli Üniversitesi, Fen Bilimleri Enstitüsü, Yüksek lisans tezi (Basılmış), 2002.

You Y., Liu C., Li D., Liu S., He G., Tribological and flame-retardant modification of polyamide-6 composite. Journal of Central South University 26, 88-97, 2019.

Zhu J., Ma Le., Dwyer-Joyce R., Friction and wear behaviours of self-lubricating peek composites for articulating pin joints. Tribology International 149, 105741, 2020.

JOURNAL of
MATERIALS and MECHATRONICS:A

e-ISSN 2717-8811
JournalMM, 2022, 3(2), 151-162
https://doi.org/10.55546/jmm.1113194

Araştırma Makalesi / Research Article

Investigation of The Effects of Shallow Cryogenic Treatment on The Mechanical and Microstructural Properties of 1.2436 Tool Steel

Nursel ALTAN ÖZBEK[1]*, Onur ÖZBEK[2]

[1] Düzce Üniversitesi, Dr. Engin PAK Cumayeri Meslek Yüksekokulu, Makine ve Metal Teknolojileri Bölümü, Düzce, Türkiye, ORCID ID: https://orcid.org/0000-0003-3241-9423, nurselaltan@duzce.edu.tr
[2] Düzce Üniversitesi, Gümüşova Meslek Yüksekokulu, Makine ve Metal Teknolojileri Bölümü, Düzce, Türkiye, ORCID ID: https://orcid.org/0000-0002-8372-3487, onurozbek@duzce.edu.tr

Geliş/ Received: 06.05.2022; **Kabul / Accepted:** 08.07.2022

ABSTRACT: This study investigates the effects of shallow cryogenic treatment on the microstructure, hardness and wear resistance of 1.2436 steel. For this purpose, quenched (QT) 1.2436 steel samples were subjected to shallow cryogenic treatment at -80 °C for 12 hours (SCT12) and 18 hours (SCT18). Hardness measurement and wear test were carried out on the samples and the samples were examined microstructurally. As a result of the study, it was observed that the cryogenic treatment provided a denser and homogeneous carbide distribution in the microstructure of 1.2436 steel. The amount of carbide in the microstructure increased by 18.80% with shallow cryogenic treatment for 18 hours. As a result of the hardness and wear tests, it was determined that the cryogenic treatment positively affected the hardness and wear resistance of 1.2436 steel. Compared to the quenched sample alone, the sample cryogenically treated for 18 hours exhibited 9.28% higher hardness and 34.37% less wear.

Keywords: 1.2436 Steel, Cryogenic Treatment, Microstructure, Hardness, Wear Resistance.

*Sorumlu yazar / Corresponding author: nurselaltan@duzce.edu.tr

Bu makaleye atıf yapmak için /To cite this article

Altan Özbek, N., Özbek, O. (2022). Investigation of The Effects of Shallow Cryogenic Treatment on The Mechanical and Microstructural Properties of 1.2436 Tool Steel. Journal of Materials and Mechatronics: A (JournalMM), 3(2), 151-162.

1.2436 Takım Çeliğinin Mekanik ve Mikroyapısal Özellikleri Üzerine Sığ Kriyojenik İşlemin Etkilerinin Araştırılması

ÖZET: Bu çalışma, sığ kriyojenik işlemin 1.2436 çeliğin mikroyapısı, sertliği ve aşınma direnci üzerindeki etkilerini araştırmaktadır. Bu amaçla, su verilmiş (QT) 1.2436 çelik numunelere -80 °C'de 12 saat (SCT12) ve 18 saat (SCT18) için sığ kriyojenik işlem uygulanmıştır. Numuneler üzerinde sertlik ölçümü ve aşınma testi gerçekleştirilmiş ve numuneler mikroyapısal olarak incelenmiştir. Çalışma sonucunda kriyojenik işlemin 1.2436 çeliğin mikro yapısında daha yoğun ve homojen bir karbür dağılımı sağladığı gözlemlenmiştir. 18 saat süre sığ kriyojenik işlem ile mikroyapıdaki karbür miktarı yaklaşık %18,80 oranda artmıştır. Sertlik ve aşınma testleri sonucunda kriyojenik işlemin 1.2436 çeliğin sertliğini ve aşınma direncini olumlu yönde etkilediği tespit edilmiştir. Yalnızca su verilmiş numune ile karşılaştırıldığında, 18 saat boyunca kriyojenik işlem görmüş numune %9.64 daha yüksek sertlik ve %34.37 daha az aşınma sergilemiştir.

Anahtar Kelimeler: 1.2436 Çeliği, Kriyojenik İşlem, Mikroyapı, Sertlik, Aşınma Direnci.

1. INTRODUCTION

Heat treatment is the controlled heating and cooling process applied to give the steel the desired properties. Heat treatments applied to steel are related to microstructural transformation. The composition of the steel and the change in its structures directly affect the mechanical properties of the steel. Many thermal methods have been developed for microstructural transformation. These methods depend on the type of steel and the expected properties (such as hardness, strength, toughness, and wear resistance) (Callister and Rethwisch, 2011; Rajan et al., 2011; Altan Özbek and Saraç, 2021; Talaş et al., 2020). The word cryogen, which means cold science, comes from the Greek "kryos" meaning cold. Cold science is a simple materials science that significantly changes the properties of materials at low temperatures (Kalia, 2010). Cryogenic treatments are complementary to conventional heat treatment, which has recently been used to improve metals' mechanical and microstructural properties. In steels, a residual austenite phase is formed in the material after traditional heat treatment. This phase is soft and negatively affects the material's mechanical properties. Cryogenic treatment is an effective method for removing the residual austenite phase. The subzero process includes gradually cooling the material to a specified temperature below zero (between -50 and -196 °C), keeping it at this temperature for a specified time, and then gradually reheating it to room temperature. It is known that the cryogenic process provides high hardness and wear resistance in the material, thanks to secondary carbide precipitation and conversion of residual austenite to martensite (Kara et al, 2020; Özbek, 2020; Kara et al., 2021; Zhirafar, 2007; Nas and Altan Özbek, 2020; Kayalı, 2016; Özbek et al., 2014; Özbek, 2021; Özbek et al., 2016)

Yıldız and Altan Özbek (Yıldız and Altan Özbek, 2022) investigated the effects of cryogenic treatment on the mechanical properties of AISI 431 martensitic stainless steel. Their study reported that the cryogenic treatment increased approximately 3.89% and 62% in the hardness and wear resistance of martensitic stainless-steel samples. In the literature, Altan Özbek et al. (Altan Özbek et al., 2018) applied cryogenic treatment on AISI H11 steel at -80 °C for 6 hours. The cryogenic treatment significantly reduced the residual austenite phase and provided new carbide precipitation. However, it has been determined that the cryogenic process provides a slight increase in the hardness of AISI H11 tool steel but also provides a significant increase in wear resistance. Koneshlou et al. (Koneshlou et al, 2011) reported that the cryogenic treatment applied on AISI H13 tool steel at -72

°C for 8 hours decreased the residual austenite phase and increased its mechanical properties (tensile strength, hardness, impact energy and wear resistance). Bensely et al. (Bensely et al., 2009) found that the cryogenic treatment applied on En353 steel at -80 °C for 5 hours significantly reduced residual austenite and increased the fatigue life of the steel by up to 71%.

In their study, Das et al. (Das et al., 2009) aimed to determine the cryogenic treatment holding time that will provide maximum wear resistance to AISI D2 cold work tool steel. Deep cryogenic treatment was applied on the steel samples at different times as 1, 12, 36, 60, 84, 132 hours. As a result of the wear tests, it was reported that the highest wear resistance was obtained with the cryogenic process applied for 36 hours. Altan Özbek et al. (Özbek et al., 2014) investigated the effects of deep cryogenic treatment on tungsten carbide tool at different holding times on hardness and wear resistance. The study applied deep cryogenic procedures in five different periods, 12, 24, 36, 48 and 60 hours. Maximum hardness and wear resistance were obtained after cryogenic treatment applied for 24 hours. Gu et al. (Gu et al., 2014) investigated the effects of deep cryogenic treatment applied at different holding times on the hardness and wear resistance of Ti-6Al-4V alloy. The study applied deep cryogenic procedures in three periods, 3, 48 and 72 hours. It was determined that the maximum hardness and wear resistance were obtained after the cryogenic treatment applied for 72 hours.

1.2436 tool steel is a cold work tool steel with a ledeburitic structure with 12% chromium. This steel is widely used in the powder metallurgy industry to manufacture powder-forming dies. It is used as a die and punches in cutting, drilling and cold forming processes (Mohamad et al., 2018). In the literature, there are mostly studies on deep cryogenic processing applications. There is very little work done on the shallow cryogenic process. At this point, this study, which was carried out by applying the shallow cryogenic treatment on 1.2436 steel, which has a wide usage area, will have an important place in the literature. This study applied shallow cryogenic treatment on 1.2436 steel samples for 12 and 18 hours. The effects of cryogenic treatment on the hardness and wear resistance of 1.2436 steel were investigated. In addition, all samples were also examined microstructurally.

2. MATERIALS AND METHODS

The chemical composition of 1.2436 steel is shown in Table 1. 1.2436 steel samples were subjected to quenching after kept at 920 °C for 25 minutes. After quenching was applied to the steel samples, cryogenic treatment was applied at -80 °C for 12 and 18 hours. Steel samples were subjected to tempering heat treatment at 300 °C for 2 hours after cryogenic treatment. Heat treatments applied to steel samples are given in Figure 1, and details of heat treatment sequences are given in Table 2.

Table 1. Chemical composition of 1.2436 steel

Element	C	Cr	V	Mo	Mn	Si	W
%	2.28	11.58	0.14	0.24	0.4	0.25	0.59

For microstructural analysis, samples were etched using Murakami solution. Microstructure images were taken using a Quanta FEG 250 model scanning electron microscope. Experimental parameters were determined by examining the studies in the literature for micro hardness measurement (Vickers hardness) and wear test, and the parameters were decided after preliminary measurements/experiments. Microhardness measurements were carried out by applying 500 grams of load in 20 seconds. The hardness values of the samples were determined by taking the average of five different measurements. The wear tests were performed on a computer-controlled TRD Wear pin disk device (Figure 2). AISI M2 steel is used as the abrasive disc. The wear tests were carried out

under a load of 30 N, with a speed of 0.75 m/s and a sliding distance of 900 m. The load was given in one direction, and no lubricant was used. After the wear tests, the amount of wear on the samples was determined with an electronic balance with a precision of ± 0.0001 g. Before the samples were weighed, no action was taken. The wear rates (Ws) were calculated using Equation 1.

$$W_s = \frac{\Delta m}{Lx\rho xF} \quad (1)$$

With Δm: Mass loss (kg), F: Normal load (N), ρ: Density (kg·m-3) and L: Sliding distance (m).

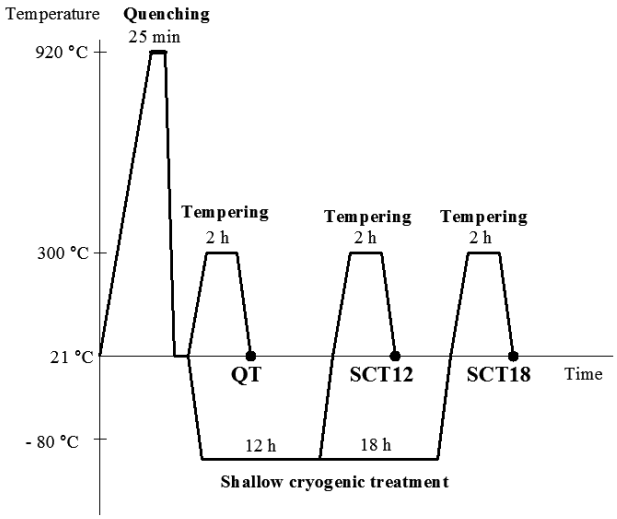

Figure 1. Heat treatments applied on 1.2436 steel.

Table 2. Details of heat treatment sequences.

Sample	Details of heat treatments		
QT	Quenching (at 920 °C for 25 min)	-	Tempering at 300 °C for 120 min
SCT12	Quenching (at 920 °C for 25 min)	Shallow treatment at -80 °C for 12 h	Tempering at 300 °C for 120 min
SCT18	Quenching (at 920 °C for 25 min)	Shallow treatment at -80 °C for 18 h	Tempering at 300 °C for 120 min

Figure 2. TRD wear tester.

3. RESULTS AND DISCUSSION

Figure 3 shows the XRD analysis results of QT and SCT18 steel samples. In Figure 3, it is seen that, in general, phase peaks are at the same 2Θ degrees as a result of both heat treatments. In XRD analysis, it is seen that M_3C, M_7C_3 carbides and Austenite phases can be found in the microstructure of steel samples. Figure 4 shows the carbide distribution of SEM photographs of steel samples using the image processing program. Although there are large and small carbides in all samples, it is seen that large carbides are much more concentrated in certain regions in the microstructure of the QT sample. Compared to the non-cryogenically treated sample, the cryogenically treated samples have a higher carbide content and appear to have a more uniform distribution. As a result of the image processing analysis, the carbide density of the QT, SCT12 and SCT24 samples was found to be 21.64%, 25.46% and 25.71%, respectively. From this, it can be said that the carbide content of SCT12 and SCT18 samples increased by approximately 17.65% and 18.80% compared to the QT sample. In the literature, Kurşuncu et al. (Kursuncu et al., 2018) reported that eta carbide increased by approximately 18% in carbide cutting tools after cryogenic processing using the image processing method. Kurşuncu (Kursuncu, 2020), in another study, determined that the cryogenic process greatly increased the amount of eta carbide in carbide cutting tools.

Figure 5-7 shows the microstructure photographs of 1.2436 steel taken by SEM. The carbide grains (dark colour) in all samples are clearly visible in the microstructure photographs. In the microstructure photographs, the larger carbides are M_7C_3, and the smaller ones are M_3C carbides. EDS analyses confirmed this. M_3C (Point A) is an iron-rich carbide. M_7C_3 (Point B) is a chromium-rich carbide (Vander, 2004). EDS analysis of the smaller carbides in the microstructure photographs confirmed that there are M_3C carbides with more Fe than Cr and some W and Mo. EDS analysis from the larger carbides also confirmed the M_7C_3 carbide with more Cr than Fe.

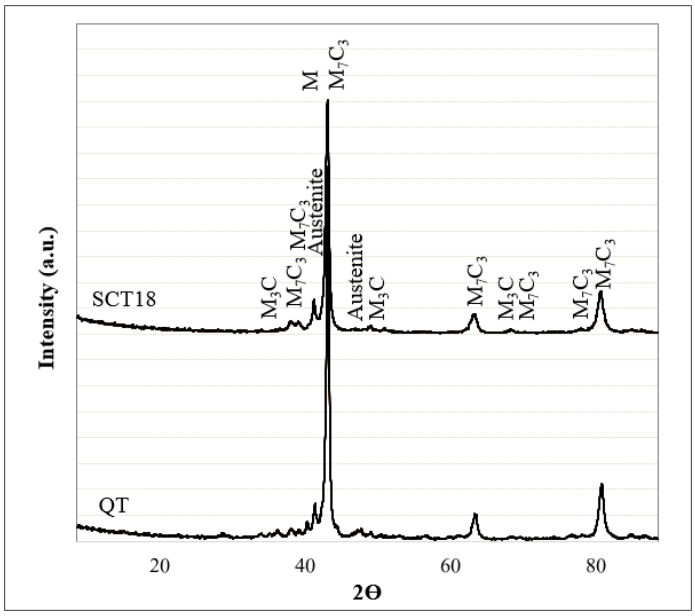

Figure 3. XRD analysis of QT and SCT18 heat-treated 1.2436 steel samples

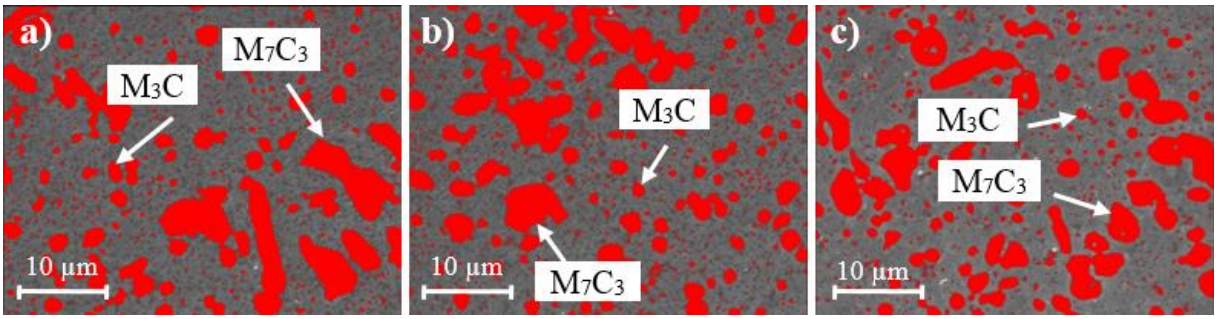

Figure 4. Image processing photographs of different heat-treated 1.2436 steel samples a) QT, b) SCT12, and c) SCT18

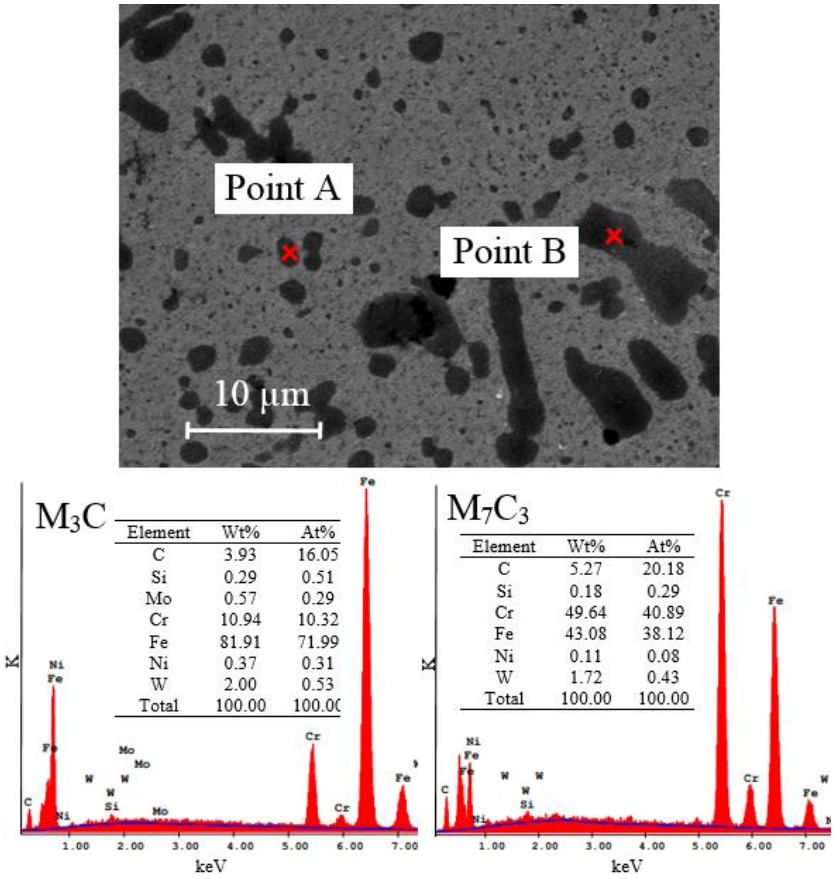

Figure 5. Microstructure photograph of QT heat-treated 1.2436 steel sample taken by SEM and EDS analysis

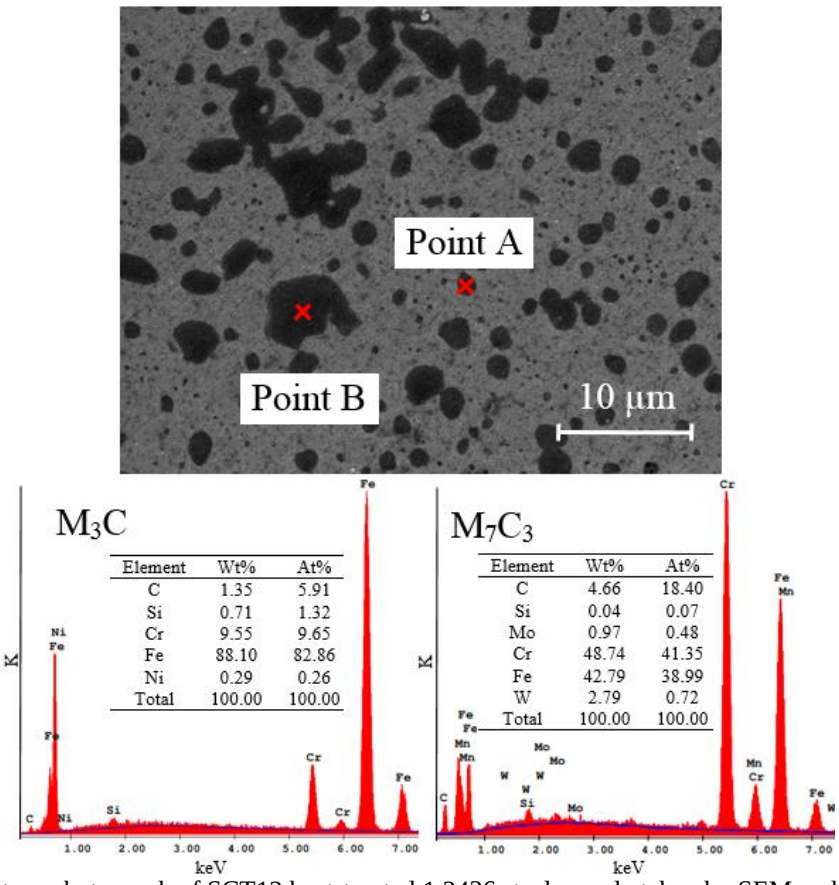

Figure 6. Microstructure photograph of SCT12 heat-treated 1.2436 steel sample taken by SEM and EDS analysis

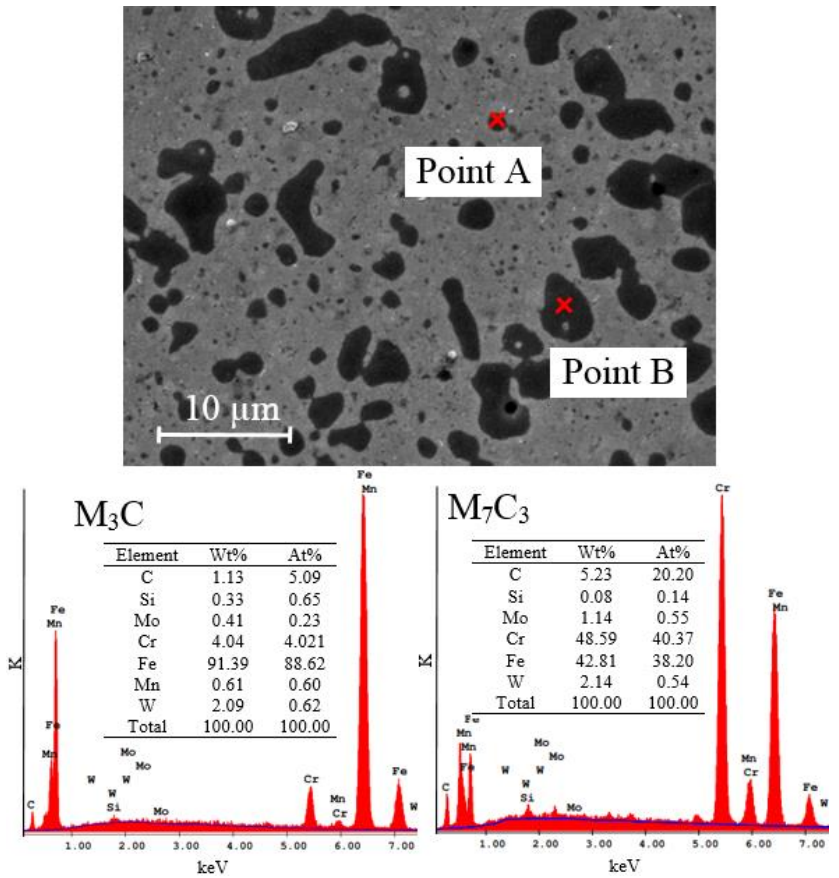

Figure 7. Microstructure photograph of SCT18 heat-treated 1.2436 steel sample taken by SEM and EDS analysis

Figure 8 shows the micro hardness of the steel samples. When the graph is examined, the first thing to notice is that subzero treatment increases the hardness of 1.2436 steel. It was observed that higher hardness occurred at a higher subzero treatment holding time. Compared to the QT sample, the hardness of the SCT12 and SCT18 samples is 6.27% and 9.28% higher. This increase in the hardness of 1.2436 steel is thought to be due to the more homogeneous carbide distribution, new carbide precipitation, and conversion of residual austenite to martensite by subzero treatment. Koneshlou et al. (Koneshlou et al., 2011) reported that the shallow cryogenic treatment applied on AISI H13 steel for 8 hours increased the hardness of the steel by approximately 4.08%. Akhbarizadeh et al. (Akhbarizadeh et al, 2009) found in their study that shallow cryogenic treatment increased the hardness of AIDI D6 steel by up to 3.54%. Altan Özbek (Özbek, 2020) found that after 6 hours of shallow cryogenic treatment, the hardness of the tungsten carbide cutting tool increased by approximately 4.4% compared to the untreated cutting tool.

When Figure 9 is examined, it is seen that the cryogenic treatment greatly increases the wear resistance. In the tests carried out under the same conditions, the cryogenically treated samples were less worn than the QT sample. The highest wear resistance was obtained in the SCT18 sample, which was worn 34.37% rate less than the QT sample. Similarly, the SCT12 sample has 25% rate less worn than the QT sample. Cryogenic treatment increased the hardness and, therefore the wear resistance of the steel samples, thanks to the changes in the microstructure. Akhbarizadeh et al. (Akhbarizadeh et al, 2009) reported that shallow cryogenic treatment provides up to 3.54% increase in wear resistance of AIDI D6 steel. Altan Özbek et al. (Altan Özbek et al., 2018) and Koneshlou et al. (Koneshlou et al., 2011) reported that shallow cryogenic treatment increases wear resistance of AISI H11 and AISI H13 steels.

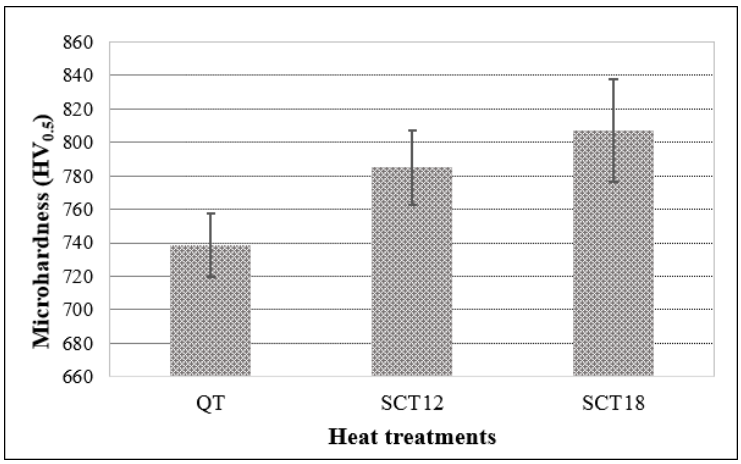

Figure 8. Microhardness graph of different heat-treated 1.2436 steel samples

Figure 10 shows the 1000X magnification SEM images of the worn surfaces as a result of the wear tests. It is observed that plastic deformation occurs with the sliding mechanism due to friction in all three samples. It is observed that oxide layers are formed during wear on the worn surfaces of all samples. It is perceived that the oxide layer acts as a protecting film, which reduces the wear rate of the steel (Prince et al., 2020). Similarly, Kurşuncu (Kurşuncu, 2021) argued in his study that oxidation on the worn surface positively affects wear resistance. Again, it is seen that there are adhesions from the abrasive disc on the worn surfaces of all samples. In addition, micro cavities were formed in the untreated sample, but not in the cryogenically treated samples.

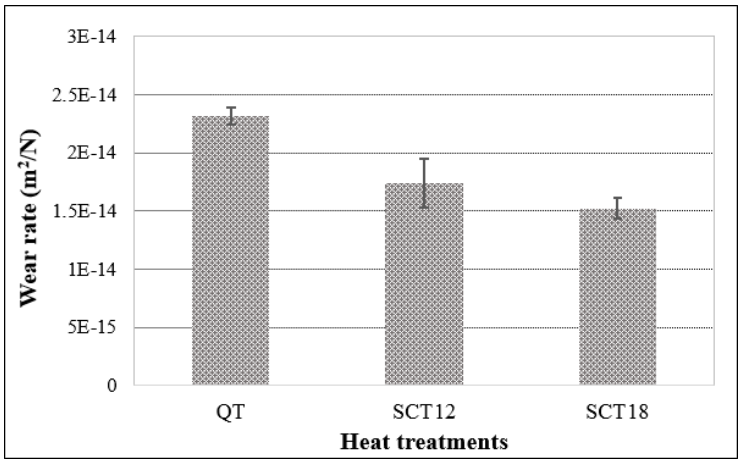

Figure 9. Wear rate graph of different heat-treated 1.2436 steel samples

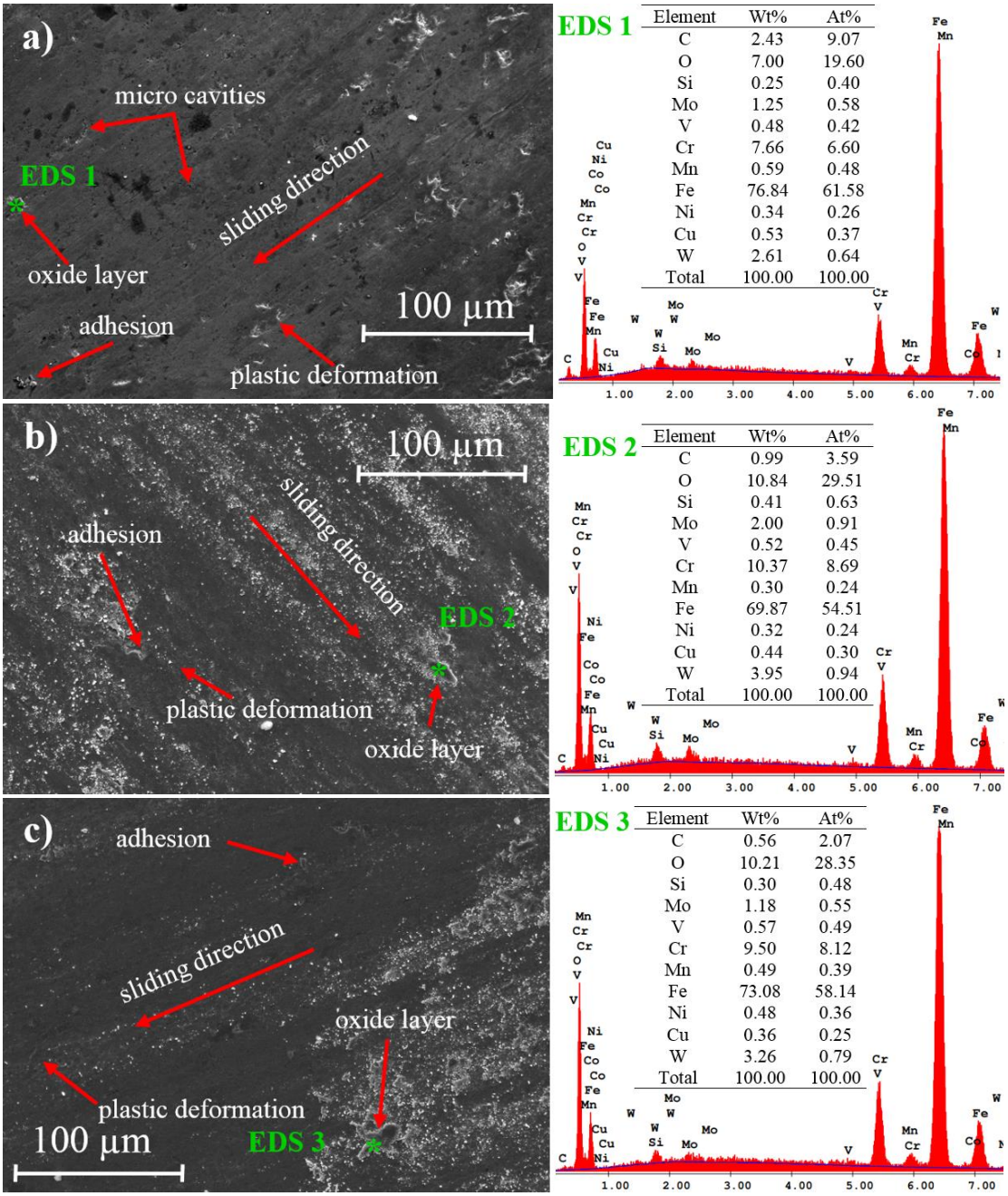

Figure 10. SEM images of different heat-treated 1.2436 steel samples worn surfaces a) QT, b) SCT12, and c) SCT18

4. CONCLUSION

This study investigated the effects of shallow cryogenic treatment on the microstructural and mechanical properties of 1.2436 tool steel. The results obtained from the study are as follows.

- Shallow cryogenic treatment positively affected the microstructure, hardness, and wear resistance of 1.2436 tool steel.
- Shallow cryogenic treatment provided a denser and more homogeneous carbide distribution in 1.2436 steel. After the shallow cryogenic treatment, the carbide content of the steel sample increased by approximately 18.80%.
- Higher hardness was obtained in the cryogenically treated 1.2436 steel samples. Compared to the QT sample, the hardness of the SCT12 and SCT18 samples is 6.27% and 9.28% higher.
- Cryogenic treatment improved the wear resistance of 1.2436 steel. The SCT12 and SCT18 samples were 25% and 34.37% less worn than the QT sample.
- Shallow cryogenic treatment applied for 18 hours gave better microstructural, hardness and wear resistance results.
- Plastic deformation, oxide layers and adhesions were observed on worn surfaces. Micro-cavities were formed on the worn surface of the QT sample.

5. ACKNOWLEDGEMENTS

This work is supported by Düzce University Scientific Project (2021.22.01.1177).

6. CONFLICT OF INTEREST

Authors approve that to the best of their knowledge, there is not any conflict of interest or common interest with an institution/organization or a person that may affect the review process of the paper.

7. AUTHOR CONTRIBUTION

Nursel ALTAN ÖZBEK contributed determining the concept of the research and research management, Nursel ALTAN ÖZBEK and Onur ÖZBEK contributed design process of the research and research management, data analysis and interpretation of the results, critical analysis of the intellectual content, preparation of the manuscript, and final approval and full responsibility.

8. REFERENCES

Akhbarizadeh A., Shafyei A., Golozar M. A., Effects of cryogenic treatment on wear behavior of D6 tool steel. Materials and Design 30(8), 3259-3264, 2009.

Altan Özbek N., Özbek O., Kara F., Investigation of the effects of cryogenic treatment on AISI H11 steel. International Marmara Science and Social Sciences Congress (IMASCON'2018), 23-25 November, 2018, Kocaeli.

Altan Özbek N., Saraç E., Effects of tempering heat treatment temperatures on mechanical properties of carbon steels. Gazi Journal of Engineering Sciences 7(1), 17-25, 2021.

Bensely A., Shyamala L., Harish S., Mohan Lal D., Nagarajan G., Krzysztof Junik, Rajadurai A., Fatigue behaviour and fracture mechanism of cryogenically treated En 353 steel. Materials & Design 30(8), 2955-2962, 2009.

Callister W. D., Rethwisch D. G., Materials science and engineering. Wiley, pp. 1-122, 2011.

Das D., Dutta A. K., Ray K. K., Optimization of the duration of cryogenic processing to maximize wear resistance of AISI D2 steel. Cryogenics 49 (5), 176-184, 2009.

Ebrahimnia M., Baghjari H., Ajdari M., Hajesmaeli A., Hojati M., Application of a low heat input deposition process for refurbishment of worn pm forming dies using Fe-Ni based filler metal. Powder Metallurgy Progress 18(2), 116-120, 2018.

Gu K., Junjie W., Yuan Z., Effect of cryogenic treatment on wear resistance of Ti – 6Al – 4V alloy for biomedical applications. Journal of the Mechanical Behavior of Biomedical Materials 30(29), 131-139, 2014.

Kalia S., Cryogenic processing: A study of materials at low temperatures. Journal of Low Temperature Physics 158(5-6), 934-945, 2010.

Kara F., Özbek O., Altan Özbek N., Uygur, İ., Investigation of the effect of deep cryogenic process on residual stress and residual austenite. Gazi Journal of Engineering Sciences 7(2), 3-11, 2021.

Kayalı, Y., Küresel grafitli dökme demirlere uygulanan farklı ısıl işlemlerin mekanik özelliklerine etkisi. Afyon Kocatepe University Journal of Sciences and Engineering, 16(1), 192-197, 2016.

Koneshlou M., Meshinchi Asl K., Khomamizadeh F., Effect of cryogenic treatment on microstructure, mechanical and wear behaviors of AISI H13 hot work tool steel. Cryogenics 51(1), 55-61, 2011.

Köklü U., The drilling machinability of 5083 aluminum under shallow and deep cryogenic treatment. Emerging Materials Research 9(2), 323-330, 2020.

Kursuncu B., Influence of cryogenic heat-treatment soaking period and temperature on performance of sintered carbide cutting tools in milling of Inconel 718. International Journal of Refractory Metals and Hard Materials 92, 105323, 2020.

Kursuncu B., Çaliskan H., Guven Ş. Y., Panjan P. Improvement of cutting performance of carbide cutting tools in milling of the Inconel 718 super alloy using multilayer nanocomposite hard coating and cryogenic heat treatment. International Journal of Advanced Manufacturing Technology 97 (1-4), 467-479, 2018.

Kurşuncu B., The Effect of cryogenic treatment on dry sliding wear mechanisms in hard coatings. Industrial Lubrication and Tribology 73(1), 97-102, 2021.

Nas E., Altan Özbek N., Optimization of the machining parameters in turning of hardened hot work tool steel using cryogenically treated tools. Surface Review and Letters 27(5), 1950177, 2020.

Altan Özbek N., Çiçek A., Gülesin M., Özbek O., Investigation of the effects of cryogenic treatment applied at different holding times to cemented carbide inserts on tool wear. International Journal of Machine Tools and Manufacture 86, 34-43, 2014.

Altan Özbek N., Investigation of the effects of cryogenic treatment applied on coated tungsten carbide tools on machinability of AISI H11 steel. Duzce University Journal of Science &Technology 8(2), 1650-60, 2020.

Altan Özbek, N., Cicek, A., Gülesin, M., Özbek, O. Application of deep cryogenic treatment to uncoated tungsten carbide inserts in the turning of AISI 304 stainless steel. Metallurgical and Materials Transactions A 47(12), 6270-6280, 2016.

Özbek, O., Investigation of the effects of temper temperature, holding time and cooling environment on the hardness of Al 7050-T7451 alloy after cryogenic processing. International Marmara Sciences Congress (IMASCON 2021 Autumn), 10-11 December 2021, Kocaeli.

Prince R.M.R., Selvakumar N., Arulkirubakaran D., Singh S.C.E., Ramkumar T., Kumar R. M., Surface structural features and wear analysis of a multilayer Ti6Al4V-B4C thin film coated AISI 1040 steel. Materials Research Express, 7(1), 016436, 2020.

Rajan T. V., Sharma C. P., Sharma, A., Heat treatment: Principles and techniques, New Delhi, PHI Learing Private Limited, pp. 1-276, 2011.

Talaş Ş., Seyit Sarı M., Sow A., Aktaş, H., Heat treatment and microstructural analysis of 54SiCr6 and 60SiMn5 spring steels, Journal of Materials and Mechatronics: A (JournalMM) 1(2), 76-84, 2020.

Vander G. F., Metallographic techniques for tool steels, Metallographic techniques for tool steels, pp. 644-669, 2004.

Yıldız E., Altan Özbek N. Effect of cryogenic treatment and tempering temperature on mechanical and microstructural properties of AISI 431 steel. International Journal of 3D Printing Technologies and Digital Industry 6 (1), 74–82, 2022.

Zhirafar S., Rezaeian A., Pugh M., Effect of cryogenic treatment on the mechanical properties of 4340 steel. Journal of Materials Processing Technology 186(1-3), 298-303, 2007.

JOURNAL of
MATERIALS and MECHATRONICS:A

e-ISSN 2717-8811
JournalMM, 2022, 3(2), 163-178
https://doi.org/10.55546/jmm.1117441

Araştırma Makalesi / Research Article

The Effects of Using Brass and Copper Wires on the Cutting Quality of Sleipner Cold Work Steel Cut by WEDM

Ferhat CERİTBİNMEZ[1]*, Erdoğan KANCA[2]

[1] Haier Europe, Candy - Hoover Group, Research and Development Center, Eskişehir, Türkiye,
ORCID ID: https://orcid.org/0000-0002-5615-3124, ferhatceritbinmez@gmail.com
[2] Iskenderun Technical University, Department of Mechanical Engineering, Hatay, Türkiye,
ORCID ID: https://orcid.org/0000-0002-7997-9631, erdogan.kanca@iste.edu.tr

Geliş/ Received: 16.05.2022; **Kabul / Accepted:** 14.07.2022

ABSTRACT: Wire electric discharge machining (WEDM) is widely used in dies, punches, aerospace and automotive sectors, since materials with high hardness, and temperature resistant, which are not possible to be cut with conventional machining methods, can be cut with high precision using the WEDM method. In this study, cutting speed (mm/min), material removal rate (mm^3/min), wire consume (g), machining time (sec), finish measure (mm) and surface roughness (µm) changes as a result of cutting high hardness cold work tool steel using copper and brass wire in WEDM method were investigated. In addition, worn wire and workpiece residues on the machined surfaces were detected by SEM (Scanning Electron Microscope) and EDX (Energy Dispersive X-Ray) analyzes as well as topography and composition were examined. In the case of using copper wire instead of the brass wire, wire consumption and processing time decreased by 23.30 % and 66.29 %, respectively, while MRR increased by 50 % because the copper wire electrode has higher electrical and thermal conductivity than brass wire electrode. In addition, the average dimensional deviation of the parts cut with copper wire decreased from 27 µm to 8 µm compared to the use of brass electrodes, and more precise measurements were obtained.

Keywords: WEDM, Stell, Wear, Surface Roughness, Material Removal Rate.

*Sorumlu yazar / Corresponding author: ferhatceritbinmez@gmail.com

Bu makaleye atıf yapmak için /To cite this article

Ceritbinmez, F., Kanca, E. (2022). The Effects of Using Brass and Copper Wires on the Cutting Quality of Sleipner Cold Work Steel Cut by WEDM. Journal of Materials and Mechatronics: A (JournalMM), 3(2), 163-178.

WEDM ile Kesilen Sleipner Soğuk İş Çeliğinin Kesim Kalitesine Pirinç ve Bakır Tel Kullanımının Etkileri

ÖZET: Geleneksel işleme yöntemleriyle kesilmesi mümkün olmayan yüksek sertlik ve sıcaklığa dayanıklı malzemeler tel elektrik deşarjlı işleme (WEDM) yönteminde yüksek hassasiyetle kesilebildiğinden; bu yöntem kalıp, zımba, havacılık ve otomotiv sektörlerinde yaygın olarak kullanılmaktadır. Bu çalışmada, yüksek sertliğe sahip soğuk iş takım çeliğinin WEDM yönteminde bakır ve pirinç teller ile kesilmesi neticesinde elde edilen kesme hızı (mm/dak), talaş kaldırma oranı (mm^3/dak), tel tüketimi (g), işleme zamanı (sn), bitiş ölçüsü (mm), yüzey pürüzlüğü (µm) değişimi incelenmiştir. Ayrıca SEM (Taramalı Elektron Mikroskobu) ve EDX (Energy Dispersive X-Ray) analizleri ile işlenen yüzeylerde aşınmış tel ve iş parçası kalıntıları tespit edilerek topografya ve kompozisyon incelenmiştir. Pirinç tel yerine bakır tel kullanılması durumunda tel tüketimi ve işlem süresi sırasıyla % 23.30 ve % 66.29 azalırken, bakır tel elektrot pirinç tel elektrota göre daha yüksek elektriksel ve ısıl iletkenliğe sahip olduğundan talaş kaldırma oranı % 50 artmıştır. Ayrıca bakır tel ile kesilen parçaların ortalama ölçüsel sapması pirinç elektrot kullanımına göre 27 µm'den 8 µm'ye düşmüş ve daha yüksek ölçüsel hassasiyet elde edilmiştir.

Anahtar Kelimeler: WEDM, Çelik, Aşınma, Yüzey Pürüzlüğü, Talaş Kaldırma Oranı.

1. INTRODUCTION

Wire Electric Discharge Machining (WEDM) method is a non-conventional processing method in which conductive materials with high hardness are cut by thermoelectric method without mechanical contact, regardless of their hardness and shape (Magabe et al., 2019; Gaitonde et al., 2019). In this method, material erosion occurs as a result of sparking between the workpiece and the electrode material used, and then this debris is usually removed from the environment by spraying deionized water (Mukhopadhyay et al., 2019; Kumar et al., 2011). This method is widely used in dies, punches, aerospace and automotive sectors, since materials with high hardness and temperature resistant, which are not possible to be cut with conventional machining methods, can be cut with high precision using the WEDM method (Chaudhary et al., 2018; Ramaswamy et al., 2020; Lodhi and Agarwal., 2014; Alias et al., 2012). Uddeholm Sleipner material, which is a steel with high hardness, is used in the parts needed in automotive, civil and military aircraft, satellites and spacecraft areas as well as in the cutting, drilling and drawing molds used in these sectors. This steel is a chromium-molybdenum-vanadium alloy, general purpose cold work tool steel with high hardness and wear resistance (Pantazopoulos et al., 2006; Kirkhorn et al., 2012). It is very costly and difficult to cut such hard steels and alloys, which are increasingly used in industrial applications, with high dimensional accuracy and surface quality. For this reason, it has become imperative to determine the most accurate cutting methods and parameters and to obtain successful results by using these parameters. Ceritbinmez examined finish measure, surface roughness and hardness of the cut surfaces by cutting the cold work steel X153CrMoV12 material with different cutting passes and copper electrode in the WEDM method. The author emphasized that as the precision of the wire used in the WEDM method increases, the cutting quality increases, and a smoother surface can be obtained as the amount of rough stock allow left for finishing cutting decreases (Ceritbinmez, 2021). Biswas et al. analyzed the cutting of Al 7075 material with brass wire in the WEDM method. They used multi-objective genetic algorithm to optimize the WEDM process parameters such as pulse-on time, pulse-off time and wire

tension for this alloy. As a result of experiments and analyzes, they recommended the use of pulse-on time (Ton = 0.2 μs), pulse-off time (Toff = 50 μs) and wire tension (Wt = 1.1 kg) parameters, respectively, for the best surface quality and machinability (Biswas et al., 2020). Patnaik et al. cut Ti-6Al-4V material using uncoated brass and zinc coated brass electrode wire with main/rough and finish/trim cutting strategy in WEDM method to analyse kerf width, material removal rate (MRR), phenomena of wire wear, and finally, surface integrity of the end product. They reported that the use of coated electrodes resulted in narrower kerf and higher MRR, respectively, compared to the use of uncoated electrodes. Also, Cu and Zn elements originating from weared wires were found on the machined surfaces. According to the results of the XRD analysis, Oxides of titanium, vanadium, and aluminum were detected on the WEDMed surface. They reported that oxides can form on the machined surfaces and that these oxides can increase the surface hardness (Patnaik et al.,2019). Sudhakara and Prasanthi used the Taguchi Method for the analysis of the surface roughness obtained as a result of cutting the VANADIS 4e (Powder metallurgical cold worked Tool steel) material with the WEDM method using coated brass wire of 0.25 diameter as electrode. As a result of their analysis, they suggested peak current (11-13 Amperes), wire tension (2-8 grams), spark gap set voltage (18-68 volts), water pressure (8-14 kg/cm^2), pulse on time (108-128 μsec), pulse off time (47-63 μsec) intervals for ideal surface roughness (Sudhakara and Prasanthi, 2014). Ramaswamy et al. analyzed the optimization of the process parameters necessary for the successful cutting of D3 die steel in the WEDM method using response surface methodology (RSM). They suggested 180 A current, pulse on time (Ton) 124 μs, pulse off time (Toff) 40 μs, 8 kg/cm^2 wire tension, 6 m/min wire feed and brass wire as optimal parameters to obtain minimum surface roughness (SR), wire consumption rate (WCR) and maximum material removal rate (MRR). They reported that the increase in current increased the MRR but negatively affected the SR. They determined that the wire consumption increased with the increase of wire feed and pulse interval, and that the increase of wire feed could cause wire breaks during machining (Ramaswamy et al., 2020). Ozkul et al. kept the pulse off time, voltage, pressure of fluid circulation, velocity of wire, wire tension and wire diameter parameters at constant values on the other hand used the pulse on time, feed rate, and the current value parameters as variables to drill the Uddeholm Sleipner cold-work tool steel material with WEDM. They reported that increasing the feed rate increases both roughness and deviations, while increasing current increases roughness but decreases deviations. In addition, they reached an average of 2,578 μm surface roughness values, with a minimum of 2,400 μm and a maximum of 3,021 μm in the cuts they made. Aldas et al. conducted a study to estimate the surface roughness with adaptive neuro-fuzzy inference system (ANFIS)-based approach as a result of the processing of Sleipner cold work tool steel in WEDM using feed rate, current, and pulse on time parameters as independent variables. Considering the average error rate, they reported that the Gaussian membership type at 5.53 % was better than the Bell-Shaped membership function at 13.23%.

There are many studies in the literature on the cutting of materials with different properties by WEDM method, but the absence of a similar study on the cutting of Sleipner steel with a hardness of 60-62 HRC using copper and brass electrodes makes this study unique and pioneering. In general, when the literature studies are examined, the processing of different materials with WEDM parameters and the effects of these parameters on the workpiece are reported. But the subjects needed in the industry; processing time, cost, dimensional accuracy and performance of cut quality.

In this study, Sleipner steel, which is increasingly used in the mold industry, is discussed also the material properties and WEDM cutting quality are studied in a way that has never been done before. In the light of this information, cutting speed (mm/min), material removal rate (mm^3/min),

wire consume (g), machining time (sec), finish measure (mm), surface roughness (μm) changes as a result of cutting high hardness cold work tool steel using copper and brass wire in WEDM method were investigated. In addition, worn wire and workpiece residues on the machined surfaces were detected by SEM (Scanning Electron Microscope) and EDX (Energy Dispersive X-Ray) analyzes as well as topography and composition were examined. As a result, process performance and workpiece surface quality were analyzed when copper wire is used instead of brass wire. Although the use of copper wire provides advantages in metal removal rate and machining speed, it has been determined that the machined surfaces are rougher than the use of brass electrodes due to the high electrical and thermal conductivity of copper wire.

2. MATERIALS AND METHODS

2.1 Materials

In this study, cold work tool steel Uddeholm Sleipner, which is increasingly used in industry, was used as workpiece. Thanks to its chrome - molybdenum - vanadium alloy components, this steel has features such as high wear resistance and strength, high hardness and compatibility with heat treatment, and suitability for WEDM (Wire Electric Discharge Machining) and EDM (Electric Discharge Machining) machining. The technical specifications of this steel, which is supplied from Alseko Metal company as hardened billet with dimensions of 250 x 300 x 90 mm, are given in tables 1 and 2, respectively. The test sample sizes used in the experiments were 14.5 x 10 x 90 mm, and these samples were sliced using a WEDM bench from hardened billet material of 250 x 300 x 90 mm.

Table 1. Mechanical and physical properties of Sleipner

Hardness (HRC)	Heat conductivity (W/m•°C)	Specific heat capacity (J/kg•°C)	Modulus of elasticity (kN/mm²)	Thermal expansion coefficient	Density (g/cm³)
60-62	400-500	460	205	$12.7x10^{-6}$	7.73

Table 2. Chemical Composition (% wt.) of Sleipner Stell

Carbon (C)	Silisium (Si)	Manganese (Mn)	Chrome (Cr)	Molybdenum (Mo)	Vanadium (V)	Iron (Fe)
0.9	0.9	0.5	7.8	2.5	0.5	Remnant

The Sleipner used in this study is a high alloy tool steel with a very specific profile. It is also a very good steel for any surface treatment. This combination means that Uddeholm Sleipner is a versatile and classic tool steel for medium duty cold work tools. It is widely used in thin die cutting, die cutting and forming, cold working applications, powder compaction processes due to these properties. It has a special place among modern tool steels, especially with its legendary toughness, very high hardness and very good barrel strength. Sleipner has a very high wear resistance thanks to the mixture of carbon and molybdenum it contains. Originally produced for the mold industry, Sleipner is in the semi-stainless class. Although it is mentioned as stainless steel in some sources due to its high corrosion resistance, it is definitely not stainless. However, thanks to its 7.8 % chromium content and high production technology, it is well above the average in terms of corrosion resistance. In addition, 0.9 % C (Carbon) expressed in table 1 has an effect on wear resistance and hardness, 7.8 % Cr (Chrome) is important for tensile strength and cutting edge durability, 2.5 % Mo (Molybdenum)

increases the machinability and strength of steel, 0.5 % Mn (Manganese) determines hardness and brittleness, 0.9 % Si (Silisium) increases the strength of the material, while 0,5 % V (Vanadium) is very important for wear resistance, it is a major factor in hardening (heat treatment) of steel.

2.2 Machining Methods

In this study, "Charmilles Robofil 290P" brand WEDM machine was used to cut Sleipner cold work tool steel. Since this bench has a cutting precision of 0.003 mm, it is widely used in many industrial areas. It is known in the literature and industry that materials such as Brass, Zinc coated brass, Diffused brass, Molybdenum etc are used as electrodes in the WEDM method (Deshmukh et al., 2019). In this study, "Sodick e35" brand Brass (copper-zinc alloy) and "Bedra topas plus X" brand Copper (zinc rich brass double layer coating) wires with a thickness of 0.25 mm were used as electrodes. As shown in figure 1, the color of the copper wire is brown and the color of the brass wire is shiny gold color. Also, deionized water was used to remove the debris from the workpiece during cutting.

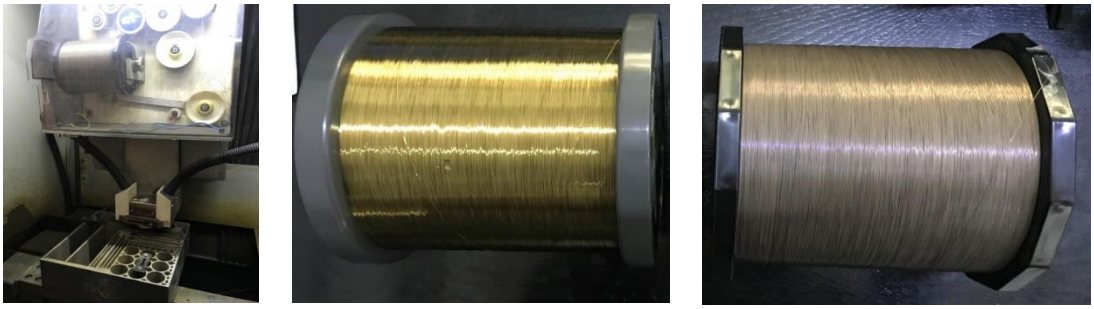

a) b) c)

Figure 1. Work Materials; a) Machining centers, b) Brass Wire (E35), c) Copper Wire (SWX-25)

In this study, the regions to be analyzed according to the cutting direction of the test samples cut with the dimensions of 14.5 x 10 x 90 mm are shown in figure 2. Three different regions of this cut piece were examined as headpiece, middle and underside. Surface roughness and dimensional measurements were made separately from these regions of the test samples cut with copper and brass electrodes. The surface structure and especially the dimensional sensitivity of these areas are very important in terms of their compatibility with the installation site and their service life.

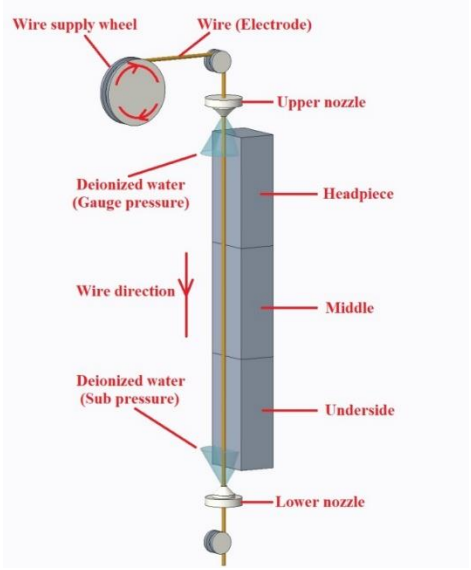

Figure 2. The cut workpiece and the examined areas

2.3 Analysis Methods of Cut Parts

Mitutoyo digital micrometer with 0-25 mm measurement range and 0.001 mm measurement accuracy was used for dimensional checks. In addition, for the surface roughness test, measurements were made from the cut surface of each sample by Mitutoyo SJ-210 and average values were reported as shown figure 3. Measuring force and stylus tip of the roughness measuring device used were 0.75 mN and 2 μmR 60°, respectively. The average values of 3 different measurements for each surface were reported. Average surface roughness value (Ra), which is the most used surface roughness measurement parameter in the literature, were taken into account in surface roughness measurements. This value is the absolute arithmetic average of the profile fluctuations that occur upwards from the center of the material (Nalbant et al., 2007).

Figure 3. Surface roughness measurement device (Mitutoyo SJ-210)

The topography and composition of the sample surface in the machined regions were analyzed using the "Thermo Fisher Scientific Apreo S" Scanning Electron Microscopy (SEM). Çetin et al. used this instrument to also analyze the microstructural, wear and corrosion properties of boronised AISI 904L super austenitic stainless steel (Çetin et al., 2021). Energy Dispersive X-Ray Analysis (EDX) was used for chemical element detection of worn electrode and workpiece residues on machined surfaces. The EDX is an analytical technique used for the elemental analysis or chemical characterization of a sample (Mandaloi et al., 2016). A scanning electron microscope is a type of electron microscope that obtains images by scanning the sample surface with a focused beam of electrons. Electrons interact with atoms in the sample, producing different signals that contain information about the topography and composition on the sample surface. Energy dispersive x-ray spectroscopy, also called EDX, EDS or EDAX, provides a better understanding of the surface material during the SEM analysis process. EDX analysis is used to obtain the elemental composition of a sample and provides a more quantitative result than can be achieved with SEM analysis alone.

3. RESULTS AND DISCUSSION

3.1 Test Parameters and Key Findings

In this work, as a result of industrial applications and machine safe working parameters, the most suitable processing parameters for cutting with copper and brass wire are selected and given in table 3. In addition, these values are the parameters of the WEDM machine that prevent wire breakage and provide the highest performance. After the copper and brass wire selection in the "Robofil 290 P WEDM" machine, the wire tension values were automatically 1.1 and 1.2 kg for copper and brass, respectively. This is related to the strength and electrical conductivity of copper and brass materials. In the literature, there are cutting qualities such as roughing, semi-finishing, finishing in cutting with

WEDM and E2, E3, E7 parameters that can be adjusted according to these cuts (Günen et al., 2022). However, only one cut was made in this study. In addition, 40A current, 80V voltage, 1 µs pulse on time and 21 µs pulse off time machine parameters were used.

Table 3. Experimental set-up and cutting parameters

Wire Type	Wire Tension (kg)	Wire Speed (m/min)	Feed Rate (mm/min)	Gauge Pressure (bar)	Sub pressure (bar)
Copper	1.1	13	70	7.4	7.3
Brass	1.2	13	70	7.4	7.2

After the selected cutting parameters, the cutting speed, MRR values shown in table 4 were read and recorded on the machine control panel. In the wire consumption calculation, the wires consumed in each section were removed from the scrap boiler and weighed on a "Etasis Electronic Scale" (0.001 precision). The processing time was also determined using a stopwatch.

Table 4. Experimental results

Wire Type	Speed (mm/min)	MRR (mm^3/min)	Wire Consume (g)	Processing Time (sec)	Finish (mm) Measure			Surface (µm) Roughness		
					Head	Middle	Under	Head	Middle	Under
Copper	1.20	32.40	1333.00	3170.00	10.012	10.003	10.008	2.707	2.937	2.809
Brass	0.80	21.60	1748.00	4782.00	10.050	10.014	10.017	2.653	2.710	2.573

Since the surface roughness is one of the most important parameters in manufacturing, studies have been carried out on the parameters affecting the surface roughness by cutting materials such as AISI 1040, 2379, 2738 steel materials in the WEDM method (Gökler and Ozanözgü, 2000). Lodhi et al. reported that the current (A) and pulse on time (µm) parameters are the most effective parameters affecting the surface roughness in the WEDM method (Lodhi et al., 2019). In this study, the effects of the wires used in WEDM cutting on the SR of the machined surfaces were examined and it was determined that the average surface roughness was lower in the use of brass wire than in the use of copper wire, due to the lower cutting speed as shown in fig.4 and 5. In addition, the high arc formed in the use of copper wire increased the amount of melted and evaporated material, thus making the surface rougher.

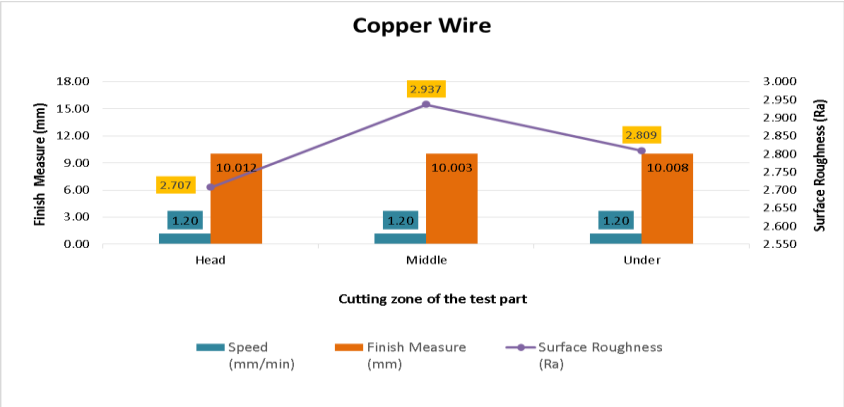

Figure 4. Effects of copper wire usage on cutting Quality

The fact that the cutting speed is lower in the use of brass wire compared to the use of copper wire is due to the fact that the conductivity of the copper wire is higher than that of the brass wire.

Due to the high electrical conductivity of the copper wire, the arc between the workpiece and the electrode has increased, allowing more material to be cut in a shorter time. For these reasons, more MRR and lower machining time were obtained in the use of copper wire compared to the use of brass wire as shown in fig 6. The WEDM method is a thermal material removal method based on the intense sparking, heat and evaporation principle between the workpiece and the electrode. These situations cause sudden heating in the workpiece and cause sudden cooling when the dielectric liquid in the environment comes into contact with the workpiece. This affects the surface morphology of the workpiece, and both the workpiece and the electrode material are worn.

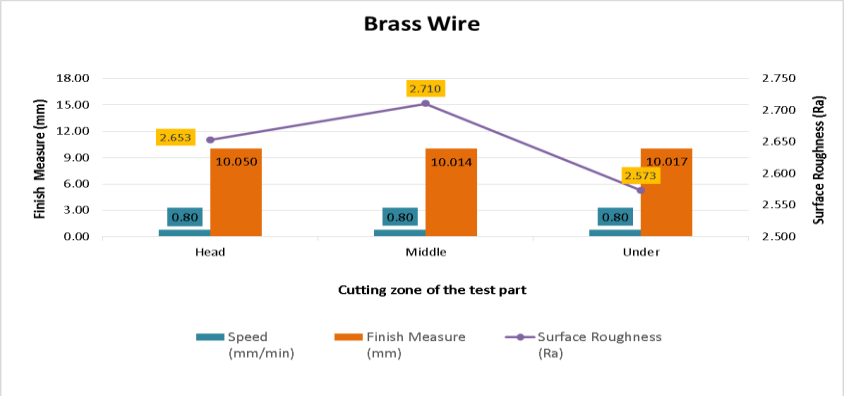

Figure 5. Effects of brass wire usage on cutting quality

The brass wire consumption was higher than copper wire consumption because of same rotation speed of the wire spool in the use of both copper and brass electrodes as well as the copper wire cutting more material in a shorter time as shown figure 6.

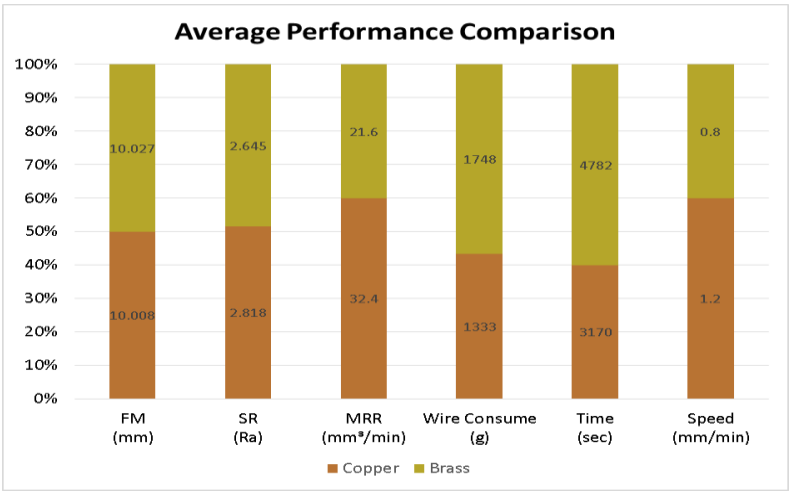

Figure 6. Average performance comparison of using Copper and Brass wire

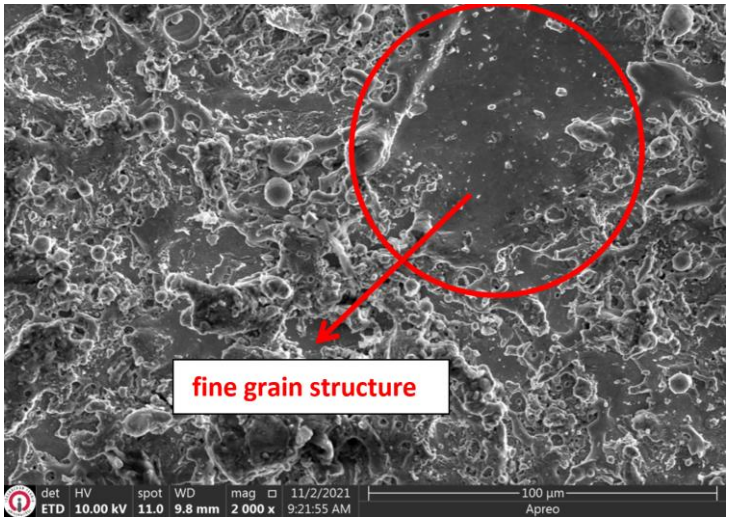

a)

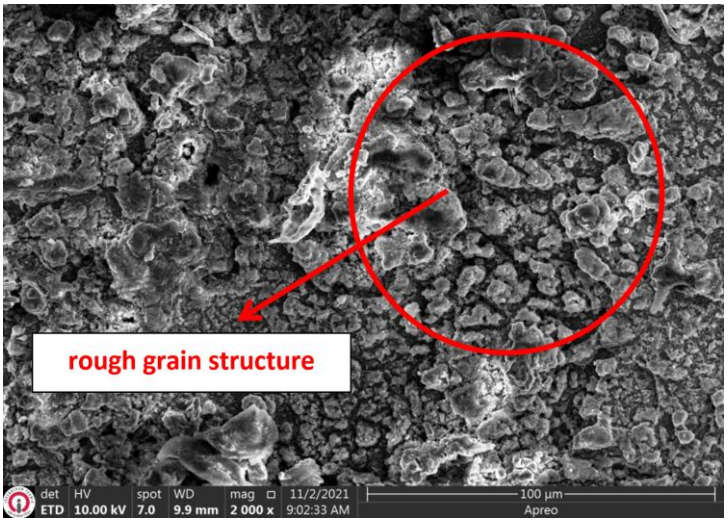

b)

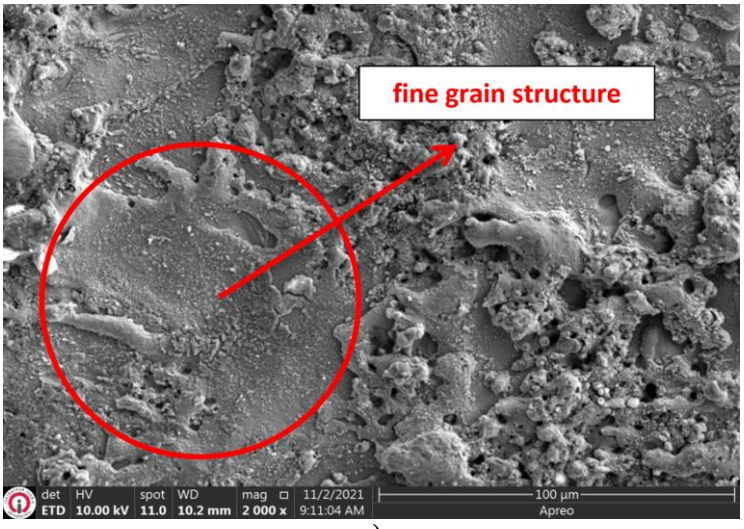

c)

Figure 7. SEM analysis of surfaces cut with Copper Wire; a) Headpiece, b) Middle, c) Underside

Reolon et al. emphasized that in cutting Inconel alloy IN718 material with WEDM, the zinc-coated copper wire has a higher performance in wire feed rate and wire consumption than uncoated brass wire (Reolon et al., 2018). In this study, the use of zinc rich brass-coated copper wire reduced

the processing time and wire consumption by 66.29 % and 23.30 %, respectively, compared to the use of brass wire. Wang et al. analyzed that better machining performance can be achieved by reducing the vibration of the wire electrode used in the WEDM method (Wang et al., 2021).

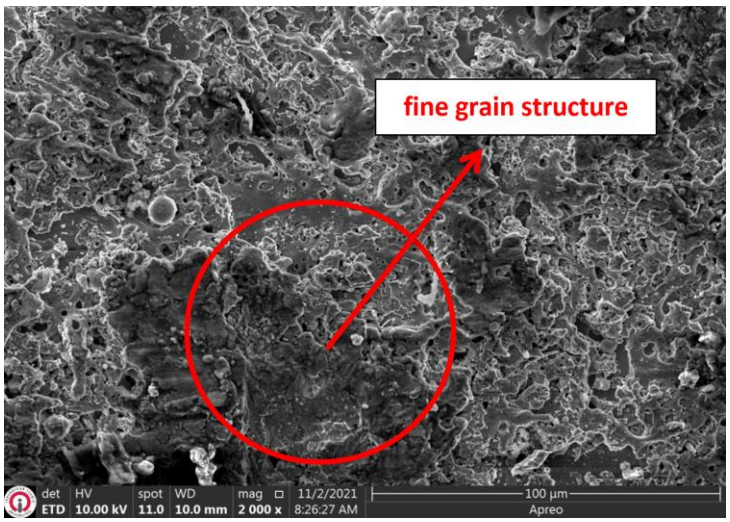

a)

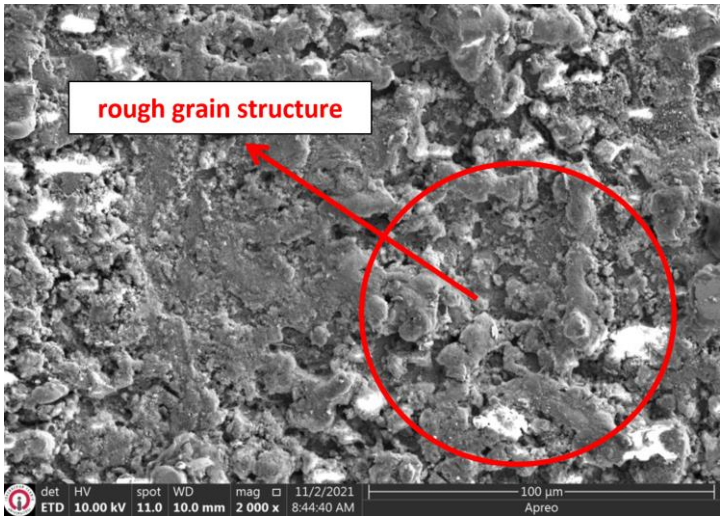

b)

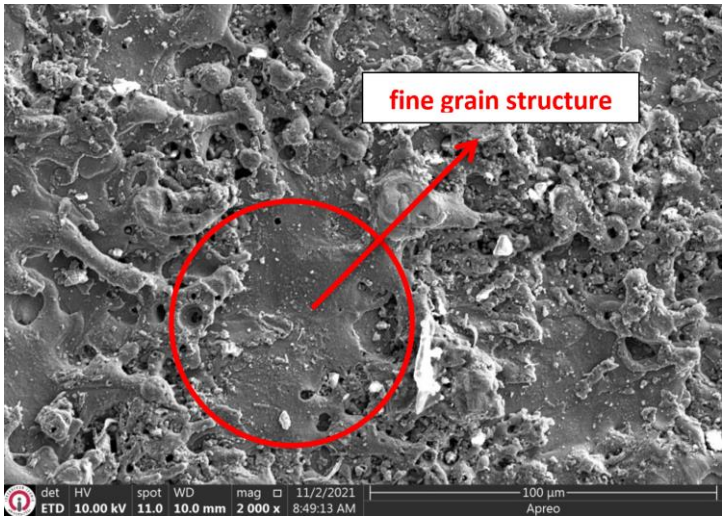

c)

Figure 8. SEM analysis of surfaces cut with Brass Wire; a) Headpiece, b) Middle, c) Underside

Zhang et al. reported that wire vibration affects not only the geometry profile of the components but also the recast layer thickness, material removal rate, surface morphology (Zhang et al., 2018). Rao et al. reported that wire tension has an effect on kerf width and surface roughness, in addition, less surface roughness and smooth surface profiles can be obtained as a result of low current and high wire tension (Rao et al., 2020). Regarding this issue, Straka et al. emphasized that the geometrical accuracy of the eroded surface has deteriorated significantly due to increasing flushing pressure (Straka et al., 2021). The "Charmill Robofil 290P" WEDM machine used in this study sprays water on the upper and lower parts of the cut area of the workpiece during cutting. The sprayed water ensures that the melted material and eroded wire residues are removed from the workpiece as a result of thermal effects. As a result of the measurements made, it has been determined that since the water sprayed on the upper and lower parts of the workpiece first contacted the upper and lower parts of the machined surfaces, it caused the surface roughness of these regions to be lower than the surface roughness of the middle parts. It is clearly seen in the middle regions of figures 7 and 8 that the effect of the washing liquid on the middle parts is low and the washing cannot be done properly, causing the melted materials to stick to the surface again and thus increasing the roughness. Similarly, due to the change of wire stability depending on water pressure, dimensional accuracy increased in the middle parts of the cut workpiece compared to the lower and upper parts. SEM images of regions headpiece, middle and underside cut with copper and brass wire are shown in figure 7 and 8 separately. The element percentages determined according to the EDX analysis results of the middle part of the workpiece cut with copper and brass wire are given in table 5.

Table 5. Average weight % values of the elements contained in the middle regions cut with copper and brass wire

Wire Type	C	O	Si	V	Cr	Mn	Fe	Cu	Zn	Mo
Copper	8.50	22.02	1.22	0.18	2.81	0.38	43.42	3.85	16.45	1.14
Brass	5.36	19.17	0.71	0.21	2.56	0.41	34.43	14.70	21.54	0.88

The average values of EDX results from 3 different regions of machined surfaces as shown in figures 9(a) and 10(a) are listed in table 5. The chemical content of the Sleipner work piece used in this study consists of carbon (C), silisium (Si), manganese (Mn), chrome (Cr), molybdenum (Mo), vanadium (V) and iron (Fe), but elements such as copper (Cu) and zinc (Zn) were found on the machined surfaces as shown in figure 9 c), d), e) and 10 c), d), e). These elements, which are not found in the chemical structure of the workpiece, are eroded electrode residues. Since the outer coating of "Bedra topas plus X" copper wire is zinc rich brass double layer coating, residues of the coating material on the wire surface were found on the processed surfaces as shown in figure 9. It has been determined that the Zn ratio of the worn coating material on the processed surfaces in the use of copper wire is higher than the Cu ratio as shown in table 5. "Sodick e35" contains 63-67 % copper (Cu), 37-33 % zinc (Zn) in its brass wire structure and is called copper/zinc alloy. Cu and Zn elements were found intensively on the surfaces of the cuts made using brass wire as shown in figure 10. In general, according to the EDX analysis results, it was observed that the rate of corroded wire on the machined surfaces was higher in the use of brass wire than in the use of copper wire. In addition, worn elements contained in the structure of the work piece Sleipner material were found on the machined surfaces. In this study, the cutting surfaces of cold work tool steel cut in the WEDM method, which has not been seen before in the literature, were examined by dividing into 3 different areas such as headpiece, middle and underside. As can be seen from the analysis and measurement results, it has been proven that these three different surfaces show different properties from each

other. In addition, two different electrode materials such as copper and brass were used to minimize the differences of these surfaces and to obtain better surface quality.

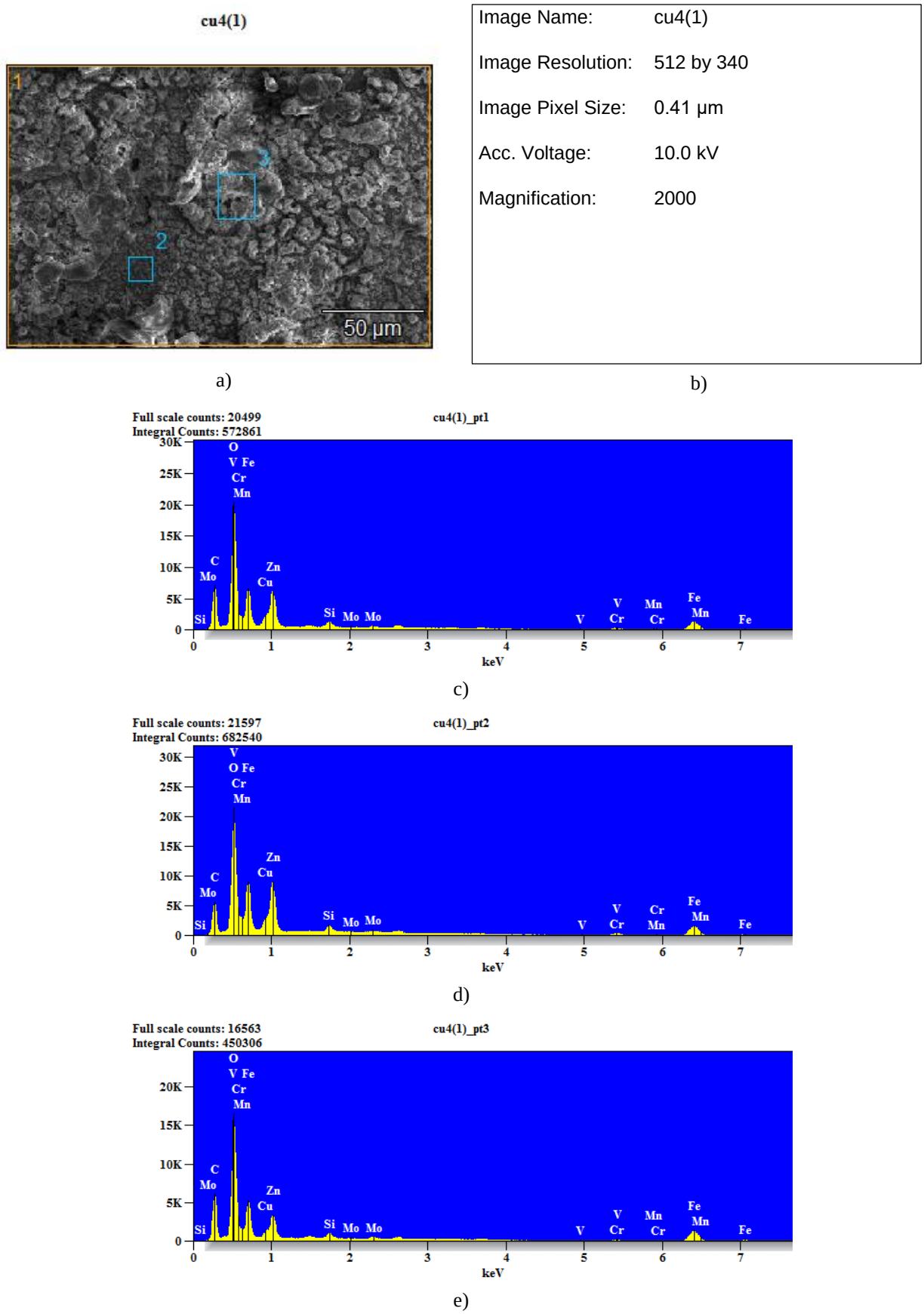

Figure 9. EDS analysis of Copper electrode residues found on machined surfaces

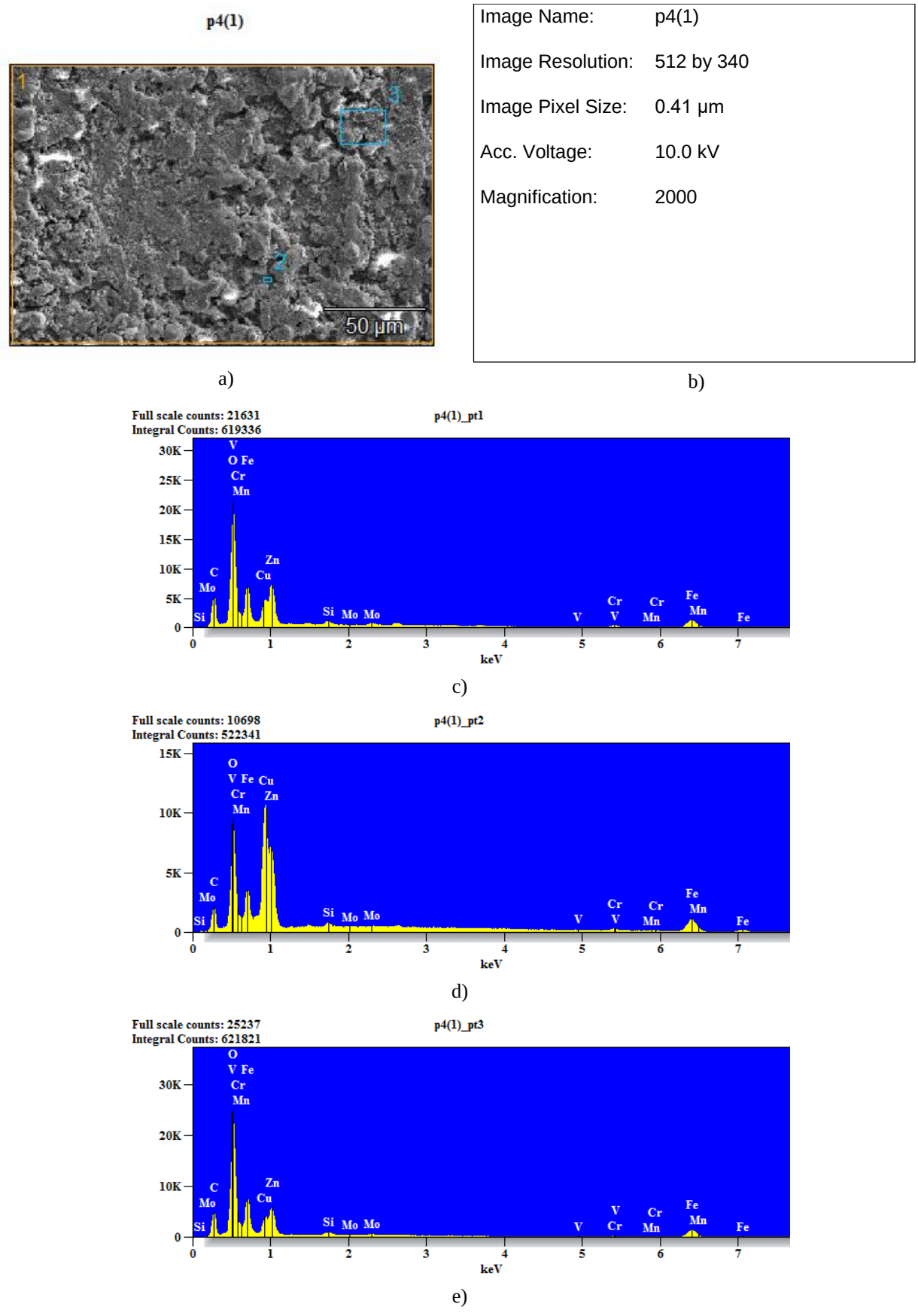

Figure 10. EDS analysis of Brass electrode residues found on machined surfaces

The dimensional accuracy obtained in this study is of great importance in adapting the cut workpiece to the mounting location. Having suitable values for surface roughness, which is another

quality parameter, increases the fatigue strength and corrosion resistance of the material, as well as makes it look aesthetically pleasing (Sangwan et al., 2015). MRR, time and wire consume, which are indispensable for performance and cost evaluation in industrial applications, are the most followed parameters. The analysis of all these values as a result of cutting a high-hardness tool steel with copper and brass electrodes arouses curiosity for users. In addition, as can be seen from the SEM and EDX results obtained in this study, the presence of elements other than the chemical composition of the material on the processed surfaces proved the effect of the processing method on the material. Maybe this situation can be a remarkable issue in the use of mold materials such as Sleipner cold work tool steel in medical applications and food industry.

4. CONCLUSION

The main conclusions are as follows:

- In the case of using copper wire instead of brass wire, wire consumption and processing time decreased by 23.30 % and 66.29 %, respectively, while MRR increased by 50 %. In addition, the average dimensional deviation of the parts cut with copper wire decreased from 27 μm to 8 μm compared to the use of brass electrodes, and more precise measurements were obtained.
- The fact that the cutting speed is lower in the use of brass wire compared to the use of copper wire is due to the fact that the conductivity of the copper wire is higher than that of the brass wire. Due to the high electrical conductivity of the copper wire, the arc between the workpiece and the electrode has increased, allowing more material to be cut in a shorter time. For these reasons, more MRR and lower machining time were obtained in the use of copper wire compared to the use of brass wire.
- It has been determined that since the water sprayed on the upper and lower parts of the workpiece first contacted the upper and lower parts of the machined surfaces, it caused the surface roughness of these regions to be lower than the surface roughness of the middle parts. Similarly, due to the change of wire stability depending on water pressure, dimensional accuracy increased in the middle parts of the cut workpiece compared to the lower and upper parts.

In general, according to the SEM and EDX analysis results, it was observed that the rate of corroded wire on the machined surfaces was higher in the use of brass wire than in the use of copper wire. In addition, worn elements contained in the structure of the work piece Sleipner material were found on the machined surfaces.

5. ACKNOWLEDGEMENTS

We would like to thank the Haier Europe, Candy-Hoover tool shop employees who supported the operation of the Charmilles Robofil 290P WEDM machine used in this study.

6. CONFLICT OF INTEREST

Authors approve that to the best of their knowledge, there is not any conflict of interest or common interest with an institution/organization or a person that may affect the review process of the paper.

7. AUTHOR CONTRIBUTION

Ferhat CERİTBİNMEZ and Erdoğan KANCA designed the structure. Ferhat CERİTBİNMEZ fabricated the device, carried out the experiments work, the theoretical calculations, in collaboration with Erdoğan KANCA, and wrote up the article. Ferhat CERİTBİNMEZ and Erdoğan KANCA contributed to the interpretation and English writing. Both of authors have read and approved the final version of the article.

8. REFERENCES

Aldas K., Özkul İ., Akkurt A., An ANFIS-based approach for predicting the surface roughness of cold work tool steel in WEDM. TEM Journal 2(3), 234-240, 2013.

Alias A., Abdullah B., Abbas N. M., WEDM: Influence of machine feed rate in machining titanium Ti-6Al-4 V using brass wire and constant current (4A). Procedia Engineering 41, 1812-1817, 2012.

Biswas M. S., Mandal K., Sarkar S., MOGA approach in WEDM of advanced aluminium alloy. Materials Today: Proceedings 26(2), 887-890, 2020.

Ceritbinmez F., An investigation on cutting of the cold work steel X153CrMoV12 by WEDM. Aircraft Engineering and Aerospace Technology 93(10), 1674-1680, 2021.

Chaudhary T., Siddiquee A. N., Chanda A. K., Effect of wire tension on different output responses during wire electric discharge machining on AISI 304 stainless steel. Defence Technology 15(4), 541-544, 2019.

Çetin M., Günen A., Kalkandelen M., Karakaş M. S., Microstructural, wear and corrosion characteristics of boronized AISI 904L super austenitic stainless steel. Vacuum 187, 110145, 2021.

Deshmukh S. S., Zubair A. S., Jadhav V. S., Shrivastava R., Optimization of process parameters of wire electric discharge machining on AISI 4140 using Taguchi method and Grey relational analysis. Materials Today: Proceedings 18, 4261-4270, 2019.

Gaitonde V. N., Manjaiah M., Maradi S., Karnik S. R., Petkar P. M., Davim J. P., Multiresponse optimization in wire electric discharge machining (WEDM) of HCHCr steel by integrating response surface methodology (RSM) with differential evolution (DE). In Computational methods and production engineering. Woodhead Publishing, pp. 199-221, 2017.

Gökler M. İ., Ozanözgü A. M., Experimental investigation of effects of cutting parameters on surface roughness in the WEDM process. International Journal of Machine Tools and Manufacture 40(13), 1831-1848, 2000.

Günen A., Ceritbinmez F., Patel K., Akhtar M. A. Mukherjee S., Kanca E., Karakas M. S., WEDM machining of MoNbTaTiZr refractory high entropy alloy. CIRP Journal of Manufacturing Science and Technology 38, 547-559, 2022.

Kirkhorn L., Frogner K., Andersson M., Ståhl J. E., Improved tribotesting for sheet metal forming. Procedia CIRP 3, 507-512, 2012.

Kumar A., Kumar V., Kumar J., A review on the state of the art in wire electric discharge machining (WEDM) process. International Journal of Mechanical Engineering Research and Development (IJMERD) 1(1), 23-29, 2011.

Lodhi B. K., Agarwal S., Optimization of machining parameters in WEDM of AISI D3 Steel using Taguchi Technique. Procedia CIRP 14, 194-199, 2014.

Lodhi B. K., Agarwal S., Ahamad S., Optimization of WEDM parameters on surface roughness of EN41B steel. Materials Today: Proceedings 25, 816-820, 2020.

Magabe R., Sharma N., Gupta K., Davim J. P., Modeling and optimization of Wire-EDM parameters for machining of Ni 55.8 Ti shape memory alloy using hybrid approach of Taguchi and NSGA-II. The International Journal of Advanced Manufacturing Technology 102(5), 1703-1717, 2019.

Mandaloi G., Singh S., Kumar P., Pal K., Effect on crystalline structure of AISI M2 steel using tungsten–thorium electrode through MRR, EWR, and surface finish. Measurement 90, 74-84, 2016.

Mukhopadhyay A., Barman T. K., Sahoo P., Davim J. P., Modeling and optimization of fractal dimension in wire electrical discharge machining of EN 31 steel using the ANN-GA approach. Materials 12(3), 454, 2019.

Nalbant M., Gökkaya H., Sur G., Application of Taguchi method in the optimization of cutting parameters for surface roughness in turning. Materials & Design 28(4), 1379-1385, 2007.

Ozkul I., Buldum B. B., Akkurt A., Machinabilty of Sleipner cold work steel with wire electro discharge machining. International Journal of Electronics, Mechanical and Mechatronics Engineering (IJEMME) 2(3), 252-260, 2013.

Pantazopoulos G., Psyllaki P., Kanakis D., Antoniou S., Papadimitriou K., Sideris J., Tribological properties of a liquid nitrocarburised special purpose cold work tool steel. Surface and Coatings Technology 200(20-21), 5889-5895, 2006.

Patnaik P., Datta S., Mahapatra S. S., WEDM Performance of Ti-6Al-4V: Emphasis on Multi-Cut Strategy, Effects of Electrode Wire. Materials Today: Proceedings 18, 4102-4110, 2019.

Ramaswamy A., Perumal A. V., Jagadeesan J., Nagarajan H. V., Optimization of WEDM process parameters for D3 die steel using RSM. Materials Today: Proceedings 37, 2063-2069, 2021.

Rao K. V., Raju L. R., Kumar C. K., Modeling of kerf width and surface roughness in wire cut electric discharge machining of Ti-6Al-4V. Proceedings of the Institution of Mechanical Engineers, Part E: Journal of Process Mechanical Engineering 234(6), 533-542, 2020.

Reolon L. W., Laurindo C. A. H., Torres R. D., Amorim F. L., WEDM performance and surface integrity of Inconel alloy IN718 with coated and uncoated wires. The International Journal of Advanced Manufacturing Technology 100(5), 1981-1991, 2019.

Sangwan K.S., Saxena S., Kant G., Optimization of machining parameters to minimize surface roughness using integrated ANN-GA approach. Procedia Cirp 29, 305-310, 2015.

Sudhakara D., Prasanthi G., Application of Taguchi method for determining optimum surface roughness in wire electric discharge machining of P/M cold worked tool steel (Vanadis-4E). Procedia Engineering 97, 1565-1576, 2014.

Straka Ľ., Piteľ J., Čorný I., Influence of the main technological parameters and material properties of the workpiece on the geometrical accuracy of the machined surface at wedm. The International Journal of Advanced Manufacturing Technology 115, 3065-3087, 2021.

Wang Y., Wu C. Z., Chai H. Y., Xiong W., Wang R., Yang J., Study on surface characteristics in ultrasonic vibration-assisted WEDM-LS based on spatial vibration of electrode wire. The International Journal of Advanced Manufacturing Technology 114(9), 2677-2695, 2021.

Zhang G., Huang H., Zhang Z., Zhang Y., Study on the effect of three dimensional wire vibration on WEDM based on a novel thermophysical model. The International Journal of Advanced Manufacturing Technology 100(5), 2089-2101, 2019.

JOURNAL of
MATERIALS and MECHATRONICS:A

e-ISSN 2717-8811
JournalMM, 2022, 3(2), 179-193
https://doi.org/10.55546/jmm.1129943

Araştırma Makalesi / Research Article

Characteristics and Corrosion Behavior of Sinter-Aluminized P/M Steels

Selvin TURGUT[1]*

[1] Republic of Turkey Ministry of Trade, General Directorate of Domestic Trade, Ankara, Turkey,
ORCID ID: https://orcid.org/0000-0001-6227-6182, selvinustabas@gmail.com

Geliş/ Received: 13.06.2022; **Kabul / Accepted:** 26.07.2022

ABSTRACT: In this study, the effects of different cold pressing pressures and sintering mediums on microstructure, micro hardness, and corrosion behavior of steels produced by powder metallurgy (PM) method from Distaloy SA powders, were examined. The PM samples were first subjected to two different cold pressing pressures being 150 MPa and 200 MPa, then to the sintering process in two different sintering mediums as aluminum and argon, for 5 hours at 1000°C. The densities and surface roughness of sinter-aluminized and only sintered samples were measured, and it was determined that their densities were increasing by the increase of cold pressing pressure and that their roughness was decreasing by the increase of cold pressing pressure. The determination of microstructural characteristics of PM samples was performed by the use of X-ray diffraction (XRD), scanning electron microscopy (SEM), and energy dispersive spectroscopy (EDS) devices. Corrosion tests were electrochemically conducted in 3.5 wt.% NaCl solution. It was determined that sinter-aluminized samples showed higher corrosion resistance than samples sintered in argon medium depending on the Fe_xAl_y phases forming on the sinter-aluminized samples. Thus, the sinter-aluminizing process is promising for using PM materials in corrosive environments.

Keywords: Powder Metallurgy, X-Ray Diffraction, Sinter-Aluminized, Corrosion.

*Sorumlu yazar / Corresponding author: selvinustabas@gmail.com

Bu makaleye atıf yapmak için /To cite this article

Turgut, S. (2022). Characteristics and Corrosion Behavior of Sinter-Aluminized P/M Steels. Journal of Materials and Mechatronics: A (JournalMM), 3(2), 179-193.

Sinter-Alüminize T/M Çeliklerin Özellikleri ve Korozyon Davranışı

ÖZET: Bu çalışmada, Distaloy SA tozlarından toz metalurjisi (P/M) yöntemiyle üretilen çeliklerin farklı soğuk presleme basıncı ve sinterleme ortamının mikroyapı, mikrosertlik ve korozyon davranışlarına etkisi incelenmiştir. P/M numuneler; 150 MPa ve 200 MPa olmak üzere iki farklı soğuk presleme basıncıyla presleme işlemi sonrası; alüminyum ile argon olmak üzere iki farklı sinterleme ortamında 1000 °C'de 5 saat sinterleme işlemine tabi tutulmuştur. Sinter-alüminyumlanmış ve sadece sinterlenmiş örneklerin yoğunluk ve yüzey pürüzlülükleri ölçülmüş olup yoğunluklarının soğuk presleme basıncının artmasıyla arttığı yüzey pürüzlülüğünün ise azaldığı belirlenmiştir. P/M numunelerin mikroyapısal özelliklerinin belirleme işlemi X- ışını kırınımı difraksiyonu (XRD), taramalı elektron mikroskobu (SEM) ve enerji dağılımlı X-ışını spektroskopisi (EDS) cihazları kullanılarak gerçekleştirilmiştir. Korozyon deneyleri elektrokimyasal olarak %3,5 NaCl çözeltisinde gerçekleştirilmiştir. Sinter-alüminyumlanmış numunelerin yüzeyinde oluşan FexAly fazlarına bağlı olarak argon ortamında sinterlenmiş numunelere göre daha yüksek korozyon direnci gösterdiği tespit edilmiştir. Dolayısıyla sinter-alüminyumlama işlemi P/M malzemelerin korozitif ortamlardaki kullanımları için umut vadetmektedir.

Anahtar Kelimeler: Toz Metalurjisi, X-Işını Difraksiyonu, Sinter-Alüminyumlama, Korozyon.

1. INTRODUCTION

Powder metallurgy (PM), used in producing advanced technology materials, is a technique used for powdering metals and metallic alloys through mechanical and physicochemical methods and producing work pieces utilizing pressure and temperature without melting the powders. It consists of mixing and pressing the powders obtained from metals and metallic alloys and then sintering them to form a bond among the powder particles (German, 1998; Xiao-Su and Shanyi, 2017; Wu et al., 2019). While the pressing process is generally performed at room temperature, the sintering process is performed under the melting temperature of the powder with the highest melting temperature among the powders in the mixture (generally 70°C) and in a protective atmosphere (German, 1998). The pressing process determines the mechanical and physical characteristics of the material, and the density of the piece differs as per the applied pressing pressure and mode of action (Xiao-Su and Shanyi, 2017).

The most critical factors in replacing conventional metal forming methods with powder metallurgy are low energy cost, low material production costs, and availing of the material at the maximum level. In addition, the method’s characteristics such as diversity, production of pieces in complex forms, microstructural and microchemical homogeneity increase its importance in the production of advanced materials (Çavdar and Çavdar, 2015). Nuclear power fuel elements, biomedical prostheses, aircraft brake linings, high-temperature filters, gears, Tungsten filament lamps, electric contacts, orthopedic equipment, rocket fuels, explosives, jet engine pieces may be provided as examples of pieces produced from metal powders by the PM method (Yazıcı and Çavdar, 2017; Alshammari et al., 2019; Sharma et al., 2019; Chávez et al., 2020).

The applications on the material surface are actualized to improve the material's functional characteristics such as physical, chemical, electrical, electronic, magnetic, or mechanical characteristics. In this context, new materials are produced by improving the metallic and non-metallic plating methods. In the industry, surface engineering methods based on plating processes such as painting, dipping, sol-gel processes, cold and thermal spraying, chemical and electrochemical methods (anodization, electroplating, electroless plating, and electrophoretic deposition), plasma-

assisted technologies, physical vapor deposition (PVD), chemical vapor deposition (CVD) are used in order to improve the surface characteristics of steels and alloys. The low setup cost in thermochemical processes, and the obtainment of equivalent surface characteristics enabled the use of this method in powder metallurgy (Erdogan et al., 2020; Turgut and Günen, 2020).

The thermochemical process is the process of diffusion on the surface of the metal and/or non-metal (B, N, Cr, Ti, V, Al etc.) atoms by the use of the thermal diffusion method at high temperatures in order to change the chemical and microstructure of the material's surface (Çavdar and Çavdar, 2015; Günen et al., 2015). Aluminum and its alloys stand out due to their easy accessibility, low density, chemical and physical compatibility, higher wear resistance as well as their superior corrosion resistance in many environments (Erdogan et al., 2020). As a result, depending on the process selected, the borides or intermetalides (aluminates, chromites) diffuse on the surface of the material by temperature activation and cause the change of material's surface and the formation of new phases (Choy, 2003; Mittemeijer and Somers, 2014; Çavdar and Çavdar, 2015; Günen et al., 2015; Erdogan et al., 2020). This change actualizes employing diffusion, unlike the processes such as electrolytic or vapor precipitation, and the layer covers the atoms of original material and foreign elements diffused on it. The construct, thickness, and composition of the new phases formed change depending on parameters such as composition and chemistry of initial materials, characteristics of substrate materials, temperature, exposure time, and gas pressure (Medvedovski, 2016). Depending on the atom diameter of the diffused element, two different surface modifications form. If the atom diameter of the diffused element is small, the substrate material diffuses, and interstitial solid solution or exterior layer forms, and if the atom diameter of the diffused element is large, a compound forms on the surface as in the chromizing and aluminizing. Thermochemical processes are used in many fields of application, such as machinery, automotive, toolmaking, petroleum drilling, mining, and defense (Çavdar and Çavdar, 2015).

Thermochemical processes or plating with diffusion are divided into impregnation with non-metals (carburizing, nitriding, nitrocarburizing, and boronizing) and impregnation with metals (aluminizing, chromizing, siliconizing, vanadiumizing, and berylliumizing) depending on the element diffused. The practice of aluminizing, one of the processes of impregnation with metals from among thermochemical processes, is a preferred method due to its characteristics such as simplicity, reliability, and economy. It was informed by many studies that the corrosion resistance of steels increases as a result of the aluminizing process (Xiang and Datta, 2006; Lu et al., 2019). The materials obtained from the aluminizing process have been interesting for industrial applications thanks to their many properties. Heating element in furnaces or dryers, power units and incinerator pipes, piston valve, exhaust manifolds, petrochemical facilities are some of the areas where these materials are used. The aluminizing process is divided into low activity and high activity aluminizing, depending on the temperature and activity of aluminizing. The low activity aluminizing process is actualized at high temperatures such as 950-1050°C for preserving operation time, and the high activity aluminizing process is actualized at low temperatures such as 700-900°C (Dubiel et al., 2008; Mojaddami et al., 2012).

This plating compound bonds to crystal structures and sublayers by strong and short covalent bonds with high thermodynamic characteristics. High lattice energy ensures more stability in crystal structures and a high covalent bond in solids. It correlates with the materials' chemical stability and integrity in mediums that may damage the material. These platings, along with not covering free Fe and other elements, are not in free from in the elements added. Moreover, this prevents the possibility

of interaction of metals with the anions of the corrosive medium and ensures the increase of corrosion resistance (Grabke and Schutze, 1998; Ladd and Ladd, 1999).

When the studies in the literature were examined, Triani et al., in order to produce iron aluminite platings on stainless-steel substrates, obtained FeAl layers on the surface by performing the aluminizing process through exposing the stainless-steel substrates to thermochemical process in a slurry consisting of polyvinyl butyral, ethyl alcohol, Al, $AlCl_3$, and Al_2O_3 for 2, 4, 6 and 8 hours at 500-650°C. By the result of the study, it was specified that the homogenous FeAl layer of excellent ductility had formed by the increase of temperature and processing time and that this layer had significantly improved the oxidation resistance of the alloy (Triani et al., 2020).

Furthermore, in the study performed by Liu et al. in 2008, they explained the basic technological process of the hot-dip aluminized technique by emphasizing the features such as corrosion resistance, high temperature oxidation resistance. In addition, they summarized the applications of hot-dip aluminized steel in the field of engineering and gave information about its developing aspects (Liu et al., 2008).

Wang et al. (2018) used the single-stage powder pack method to prepare AIN/aluminized plating, having high corrosion resistance, on carbon steel. They examined the phase compositions by X-ray diffraction (XRD), and they examined the cross-sections by scanning electron microscopy (SEM) equipped with energy dispersive spectroscopy (EDS). They measured the corrosion resistance of AIN/aluminized plated sample by electrochemical test and expressed that the plating had improved the material's corrosion resistance (Wang et al., 2019).

Considering the studies performed in recent years, it has resorted to aluminizing process to improve the oxidation and corrosion resistance of the materials. High oxidation and corrosion resistance, provided for the material by the aluminum element, arises from the Al_2O_3 layer that continues to protect the primary metal as remaining on the material's surface. For this reason, superior oxidation and corrosion resistance through the Al_2O_3 layer, obtained through plating materials with aluminum in the medium of high temperature and different corrosive characteristics that the materials cannot resist, has become a more and more meaningful practice. For this purpose, in this study, the microstructure characteristics, hardness, and corrosion resistance -in different mediums- of samples of Distaloy powders that were produced with the PM method under two different pressures and that were sintered in different sintering mediums (Ar and Al), were examined and compared with each other. Considering the usage areas, the hardness and wear resistance properties of the material can be determined in further studies. In this way, the effect of the aluminizing process on hardness and wear is determined and studies for use are carried out.

2. MATERIALS AND METHODS

Initially, commercially available Distaloy SA powders with chemical composition Fe-1.84Ni-1.49Cu-0.8Zn-0.5Mo-0.5C-0.6Zn, and 50-100 μm average grain size were subjected to mechanical alloying for 24 hours to obtain a homogeneous powder mixture. Then, the powder mixture was weighed and cold-pressed by applying different pressures (150 and 200 MPa) to produce samples with a diameter of 40 mm, and thickness of 5 mm. The surfaces of the cold pressed samples were sanded with 320-1200 grit SiC paper before sintering, washed with distilled water and sonicated in methanol to obtain clean and smooth surfaces. The samples to be sintered in an argon environment were placed in crucibles made of stainless steel, their mouths were tightly closed and sintered at 1000°C for 5 hours. In the sintering process in aluminum environment, after the samples were placed

in a stainless-steel crucible, all sides were covered with a powder mixture of 45 wt.% Al + 45 wt.% Al_2O_3 + 10 wt.% NH_4Cl. Then, the mouth of the crucible was tightly closed and sintered for 5 hours by placing it in an electric muffle furnace preheated to the aluminizing temperature (1000 °C). After sintering in argon and aluminum environments, the crucible was removed from the furnace and the samples were left to cool at room temperature. Finally, the aluminized samples were removed from the crucibles and their surfaces were cleaned with a brush to remove any adhesion from the aluminum powder.

Process parameters and exemplary nomenclature for the samples are given in Table 1.

Table 1. Sample nomenclature and process parameters used in the process

Sample	Sintering Temperature (°C)	Sintering Medium	Pressing Pressure (MPa)	Sintering Duration (h)
S1	1000°C	Ar	150	5
S2			200	5
S3		Al	150	5
S4			200	5

The density measurements of the PM materials were determined by including the weights, measured in air and pure water, in the Equation 1. based on Archimedes' principle.

$$\rho = \frac{w_o \rho_w}{w_o - w'_o}$$

The surface roughness (Ra) of the samples was measured using a Wave System Hommelwerke T8000 2D profilometer. Surface roughness was determined as the average of 5 measurements made on each sample surface based on 1mm/s speed and 4mm length.

Metallographic samples were prepared with a precision cutting device for SEM, EDS, and XRD analyses by the end of the sintering and sinter-aluminizing process. Then, the samples were subjected to conventional grinding with 280-2500 SiC paper polished with 6 μm Al_2O_3 and 0.25 μm Al_2O_3 solution and then etched with 3 wt.% Nital solution to reveal microstructural details.

Metallographic studies were carried out on polished and etched cross-sections of the samples using Thermo Scientific Apreo-S SEM equipped with UltraDry EDS Detector and Quasor II EBSD system equipped with EDS. The thicknesses of the aluminite layers were measured by SEM, and the presence of phases (FeAl) formed on the surface of PM samples was identified by X-ray diffraction (XRD) analyses using a computer-controlled Rigaku SmartLab X-ray diffractometer. The diffraction patterns were obtained with Cu Kα radiation at a wavelength of λ = 0.154 nm over a 2θ range from 30° to 90°. Diffraction data were collected with 2.0 deg/min speed and step width of 0.02 degrees.

Corrosion characteristics of the samples were evaluated with the CHI 608E electrochemical workstation, controlled by a computer. A standard setup consisting of three electrodes, one platinum counter electrode, one Ag/AgCl electrode as a reference electrode, and one working electrode (1cm^2 exposed area) was selected for the corrosion assessment studies. All the corrosion tests were carried out using 3.5 wt.% NaCl aqueous solution. Open circuit potential (OCP) measurements of the samples were made over 3600s and plotted as a function of time after stabilization. Potentiodynamic corrosion tests were performed in the potential range of -250mV to +250mV at a scan rate of 0.1 mV/s. The Tafel extrapolation method was applied to reckon the corrosion current densities of the samples over

the linear portion of the anodic and cathodic graphs. The corrosion tests were repeated three times to ensure reproducibility, and the results were averaged.

3. RESULTS AND DISCUSSION

3.1 Density and Surface Roughness

The density and surface roughness values of Distaloy SA powder samples, which were initially pressed under two different pressures and were sintered in two different sintering mediums (Ar and Al), are given in Table 2.

Table 2. The density and roughness of the P/M specimens subjected to sintering and sinter-alumizing heat treatment

Sample	Density (gr/cm^3)	Relative density (%)	Surface roughness (Ra, µm)	Rz (µm)
S1	5.95	76.28	2.60	10.72
S2	6.02	77.17	2.27	9.54
S3	6.13	78.59	1.93	7.86
S4	6.18	79.23	1.75	7.66

When the density and surface roughness values of samples sintered in argon and aluminum mediums were examined as per the pressing pressures applied prior to sintering, it was determined that while the density values increased from 5.95 to 6.02, and from 6.13 to 6.18 by the increase of pressing pressure, the surface roughness values decreased from 2.60 to 2.27, and from 1.93 to 1.75, respectively. The density and surface roughness values of the samples differed as per the sintering medium. It was observed that density values were a bit higher and that the roughness values were lower along with filling of pores with aluminum in sinter-aluminized samples compared to samples sintered in Ar medium (Bagliuk, 2012; Sundaram et al., 2018).

The increase in the density of samples and the increase in pressing pressure may be explained by reducing air gaps among the powder particles. Gökmeşe et al., by their study performed in 2013, expressed that the density values were increasing along with the increase of pressure and that the pores among the particles were closing as the result of the pressing pressure applied from 250 MPa to 625 MPa on alloys prepared by the use powder metallurgy (Gökmeşe and Bostan, 2013).

Moreover, the surface roughness values of sinter-aluminized samples being lower compared to that of samples sintered in Ar medium may be attributed to the filing of porosity and gaps, remaining on the surface following cold pressing, with a secondary powder (sinter-aluminizing powder), and to the plating layer formed on the surface following the thermochemical process.

Considering these factors that affect the density and surface roughness, as the S4 sample is a sample that was sinter-aluminized and pressed under high pressing pressure, it has the highest density and lowest surface roughness among all the samples.

3.2. Characterization of Microstructure

SEM microstructure images, and EDS analyses of Distaloy steel PM samples, sintered for 5 hours in Ar medium are given.

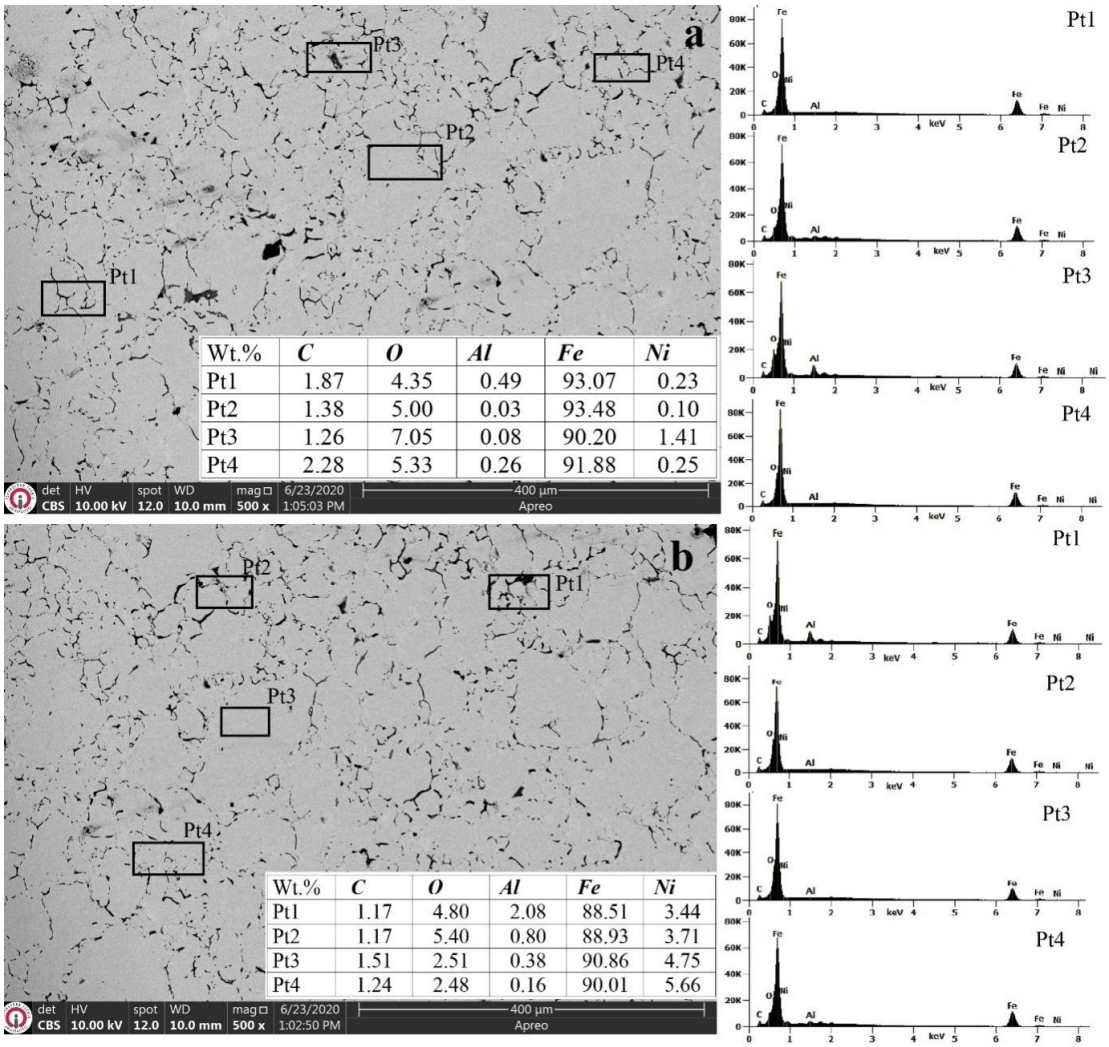

Figure 1. SEM microstructure view and EDS analysis of produced from Distalloy powders by P/M method a)150 MPa, b) 200 MPa pressing pressure after 5 hours at 1000 °C in Ar environment

As seen in Fig. 1, it was observed that the sample generally exhibited a homogenous distribution, but at some parts of the microstructure, oxide areas were being the characteristic of iron-based materials produced by powder metallurgy. Despite a decrease in the oxide contents (Fig. 1b EDS point) by the increase of pressing pressure from 150 MPa to 200 MPa, they were not completely removed. Due to the reduction of air gaps among powders and the increasing pressing pressure, the porosity decreased, and the density increased. Furthermore, the chemical bond formation among powder metal pieces is more substantial (Gökmeşe and Bostan, 2013; Turgut and Günen, 2020).

Moreover, by examining EDS analyses of the samples, it was observed that the construct was substantially comprised of iron and that low rates of carbon, oxygen, aluminum, and nickel were also present in the construct. It was also determined that the oxide content of the samples was 2.48-7.05 wt.%.

In Fig. 2, SEM images and EDS analyses of samples of Distaloy powders, subjected to cold pressing under 150 MPa and 200 MPa, and sinter-aluminizing for 5 hours at 1000°C, are given.

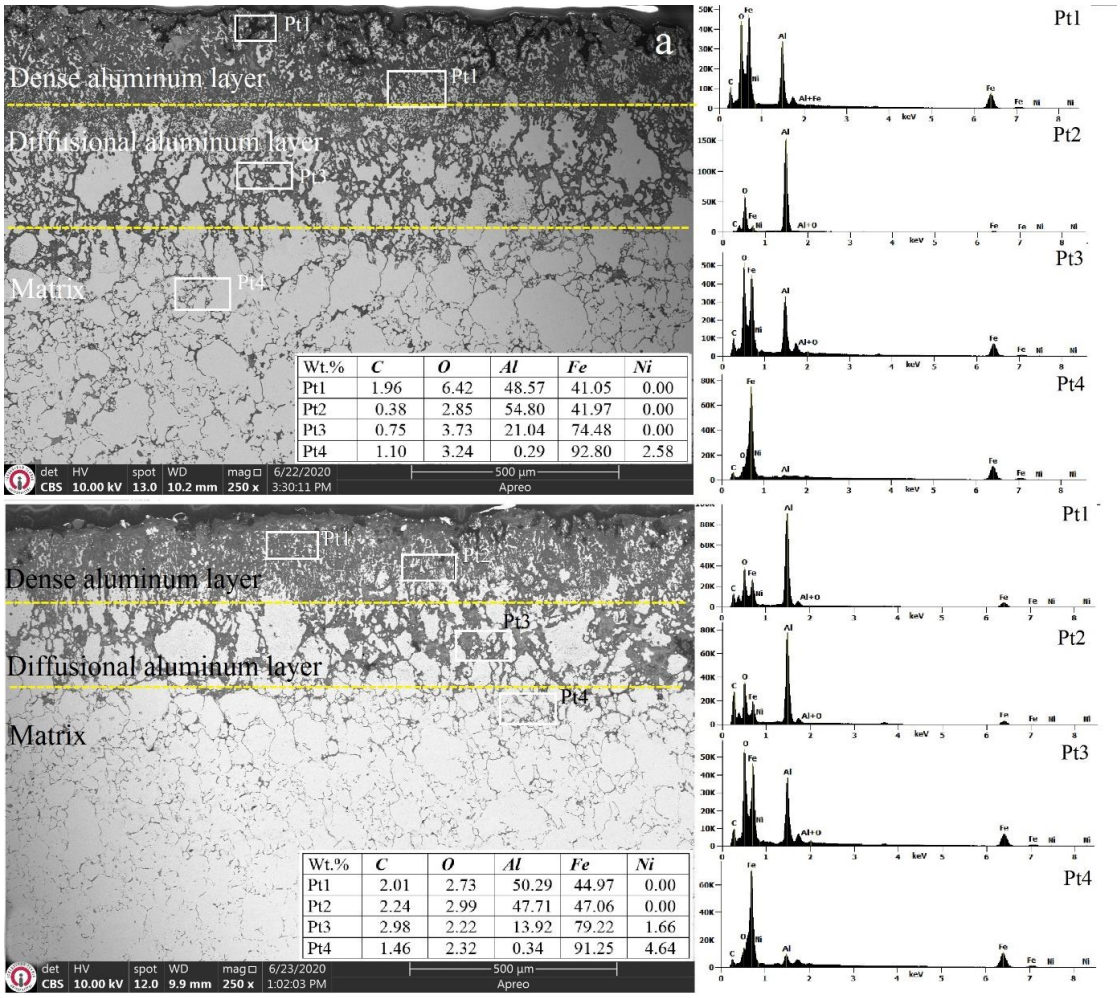

Figure 2. SEM microstructure view and EDS analysis of produced from Distalloy powders by P/M method a) 150 MPa b) 200 MPa pressing pressure after 5 hours at 1000 °C in a sinter-aluminizing medium

When the sectional views of samples, subjected to a sinter-aluminizing process for 5 hours period in Al medium by the use of 10 kV energy in scanning electron microscopy (SEM), were examined, it was observed that 3 different areas formed on the surface of the samples. These areas were i) intense aluminizing area, ii) diffusional aluminizing area, and iii) matrix area not affected by the aluminizing process. Moreover, EDS analyses were obtained from different points of plating layers and the matrix of each sample. It was determined that the contents of layers located at the plating area, being precise in the results of the metallographic examination, were exhibiting differences (Kayali, 2013).

The FeAl layer obtained was examined in terms of content, while about 47.71-54.80 wt.% Al was determined at the dense area, the Al rate at the diffusional area was determined as 13-21 wt.%. It was observed that the concentration of Al element decreased from the plating layer's outmost surface towards the matrix and that the plating layer concentrated in places. These areas, where the Al element concentrated, were the gray areas also observed in the results of EDS analysis, and this status conforms with the FeAl platings obtained in literature (Maki, 2019; Perez et al., 2002).

By the end of the plating process, it was determined that the thickness and contained phases of the plating layer formed on Distaloy SA steel did not differ. It was observed that the thickness of the diffusion layer, formed in samples subjected to the sinter-aluminizing process, was similar to that of samples subjected to different sintering periods. The cause of having no change in the diffusion layer

thickness is the uniformity of sintering temperature. Diffusion speed is directly proportional with temperature, and changes to be made in sintering temperature will change the concentration of diffused aluminum, and accordingly, it causes changes in the layer thickness (Callister, 1991; Li et al., 2008).

When the plating players obtained were examined in terms of morphology, it was determined that aluminum atoms were not intense on the surface as in the aluminizing layers obtained on the alloys produced through casting and forging. This status may be linked to accumulation at a place of aluminum atoms among powders bonded to each other only with mechanical bonds due to powder metallurgy process and their diffusion towards more inner parts instead of making chemical bonding with the elements there. Hence, the obtainment of iron-aluminum layers, which were much thicker than casting and forging alloys, supports this matter.

3.3. XRD Analyses

XRD analyses of samples produced with the PM method and sintered in Ar and Al mediums were performed, and the phase matching of the results obtained was actualized by using the library in PDXL software (Fig. 3).

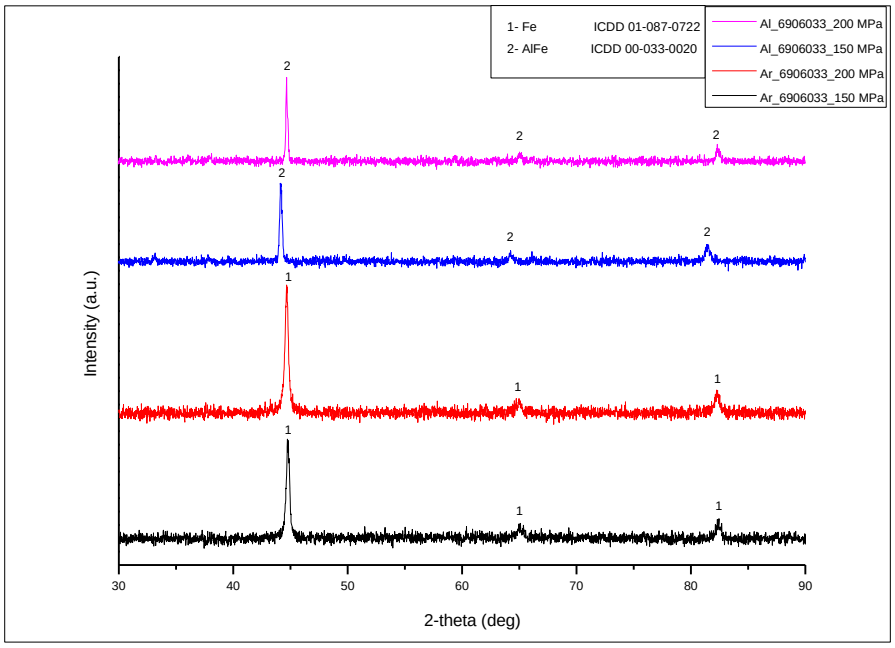

Figure 3. XRD diagram of samples produced from Distalloy SA powders and sintered in aluminum medium

As the result of examining X-ray diffraction (XRD) patterns, it was determined that the dominant phases on Distaloy SA steels produced under different pressing pressures and sintering mediums varied. As the result of XRD analyses, the primary Fe and FeAl compounds were determined. In samples subjected only to the sintering process, Fe phase, in the 229: Im-3m space group with card number ICDD: 01-087-0722, was dominant on the construct. This phase corresponded to peaks at angle values 44, 64, 82 in the XRD diagram.

Moreover, in the samples subjected to a sinter-aluminizing process for 5 hours at 1000°C, characteristic peaks of the construct, at angle values of 44, 64, and 81 of the FeAl phase with card number ICDD: 00-033-0020, were obtained. The phase desired to form in the aluminum plating process by the thermochemical method is the FeAl phase being present at the part rich in iron on the

Fe-Al balance diagram. In the study performed, the presence of this phase was observed. In the aluminizing process, it is avoided from the formation of phases with high Al content as they increase the fragility of the aluminite layer and decrease the oxidation resistance. FeAl phase, forming on the surface of the plating layer, has a high melting point, high resistance, high hardness, high corrosion and oxidation resistance, high elasticity module, and high electric resistance (Martinez et al., 2006).

3.4. Corrosion Analyses

The corrosion resistance of samples produced by sintering of Distaloy SA 6906033 powder in two different mediums (Ar and Al) was evaluated using open circuit potential measurement and potentiodynamic polarization curve measurement. The graphs of samples' corrosion tests, performed in 3.5 wt.% NaCl solution is given in Fig. 4.

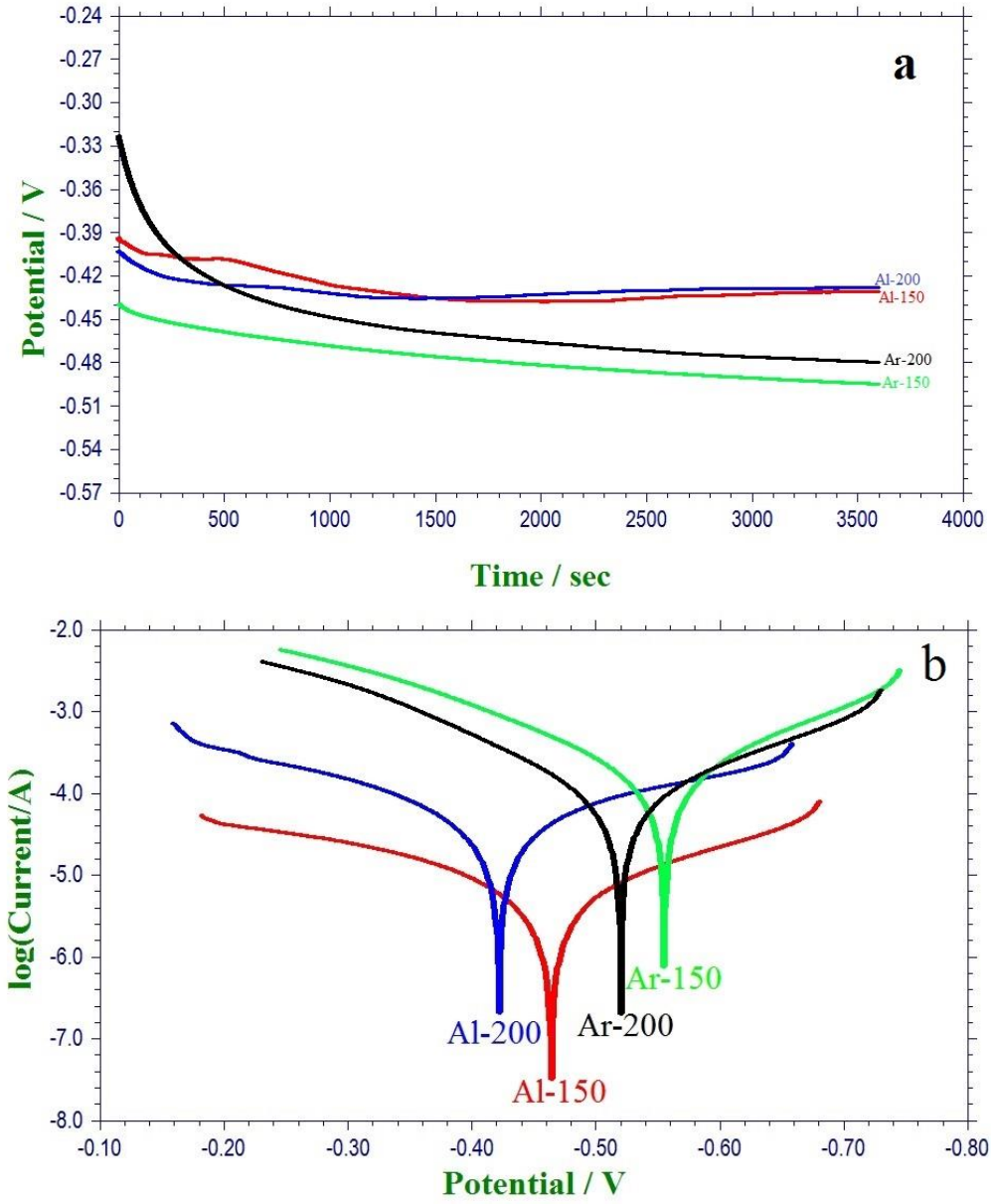

Figure 4. a) OCP curves, b) Tafel curves in NaCI solution of the sintered and sinter-aluminized samples

The potential value is measured in the OCP technique while no current passes from the circuit. The potential value, measured from an ionic solution, is the balance potential of the cathodic and

anodic reactions. Potential difference values, forming due to metal corrosion in a corrosive environment, are recorded as corrosion potential (Figure 4a). It is known that the corrosion resistance of samples of curves, being closer to the positive side on the OCP graphs, is higher (Öztekin, 2014).

When Figure 4a is examined, while samples subjected to sinter-aluminizing were at the narrow range from -0.39 to 0.42 V, it is observed that the samples subjected only to sintering continuously decreased as beginning from -0.33 V towards the potential of -0.48 V, and that they did not reach a stable course by the end of 3600 sec. This status revealed that the samples subjected to sinter-aluminizing were positioned on a more positive side than the samples subjected only to sintering and that they were more stable, and thus their corrosion potential was lower. The corrosion potential exhibited a decrease in Ar-200; Ar-150; Al-150; Al-200, respectively.

Considering the studies in literature, it was expressed that a passive aluminum film was forming on the surfaces of the steel samples through plating with aluminum and that it did not cause a significant change in the anode reaction while slowing down the cathode reaction. Moreover, as a result, they specified that a decrease occurred in the corrosion potential determined by the balance between the two reactions (Chen et al., 2007; Heakal et al., 2011).

The semi-logarithmic current-potential curves, drawn in anodic or cathodic direction as beginning from the corrosion potential, are known as Tafel curves. The current, where the point -on the corrosion potential-, where the Tafel curves intersect -when their linear parts are reversely extrapolated-, is determined, is the corrosion current (Öztekin, 2014). The extrapolation of Tafel curves, Ecorr (corrosion potentials), Icorr (corrosion current), and corrosion speed were calculated, given in Table 3. Ecorr value represents the samples' thermodynamic tendency for corrosion, and Icorr value represents the corrosion rate. The Ecorr values of Ar 150, Ar 200, Al 150, and Al 200 samples were -0.555 V, -0.520V, -0.464V, and -0.422V, respectively; and their Icorr values were $1.56x10^{-4}$ μAcm^{-2}, $8.52x10^{-5}$ μAcm^{-2}, $5.54x10^{-6}$ μAcm^{-2}, and $4.50x10^{-5}$ μAcm^{-2}, respectively. It was observed that the Ecorr values of samples subjected to sintering in argon medium were lower compared to the Ecorr values of samples subjected to sinter-aluminizing. Furthermore, this indicates that the corrosion resistance of PM samples subjected to sintering in Ar medium are lower than samples subjected to sinter-aluminizing.

Table 3. The E_{corr} (corrosion potential), I_{corr} (corrosion current density), and corrosion rate values were determined from the polarization curves

Sample	Solution	Ecorr (V)	Icorr (μAcm^{-2})	Corrosion rate (gr/h)
Ar 150	%3.5 NaCl	-0.555	$1.56x10^{-4}$	$16.30x10^{-5}$
Ar 200		-0.520	$8.52x10^{-5}$	$8.90x10^{-5}$
Al 150		-0.464	$5.54x10^{-6}$	$0.58x10^{-5}$
Al 200		-0.422	$4.50x10^{-5}$	$4.70x10^{-5}$

When Tafel graphs were examined, it was observed that the samples subjected to sinter-aluminizing were positioned more to the right compared to samples subjected only to sintering as in the OCP graphs. This status conforms with the Ecorr values given in Table 4. However, it was observed that the Al-200 sample, which was positioned at the rightmost side in terms of Ecorr values, did not exhibit the lowest corrosion current ($4.50x10^{-5}$) and that the Al-150 sample exhibited the lowest corrosion current as $5.54x10^{-6}$. This status indicates that the samples' log (current/A) values are essential and their Ecorr values in corrosion losses. Because the lowest log (current/A) values were determined in the Al-150 samples among all the samples, and it was the sample in which the

corrosion losses were the lowest. The Icorr values of samples subjected to sinter-aluminizing were lower than the samples subjected only to sintering, and their corrosion resistance was higher. Briefly, in terms of the corrosion resistance of samples produced from Distaloy SA 6906033 powder by the sinter-aluminizing process, an improvement was ensured at the range of 1.90 times (Ar-200/Al200) and 15.34 times (Ar-200/Al-150) compared to samples subjected only to sintering.

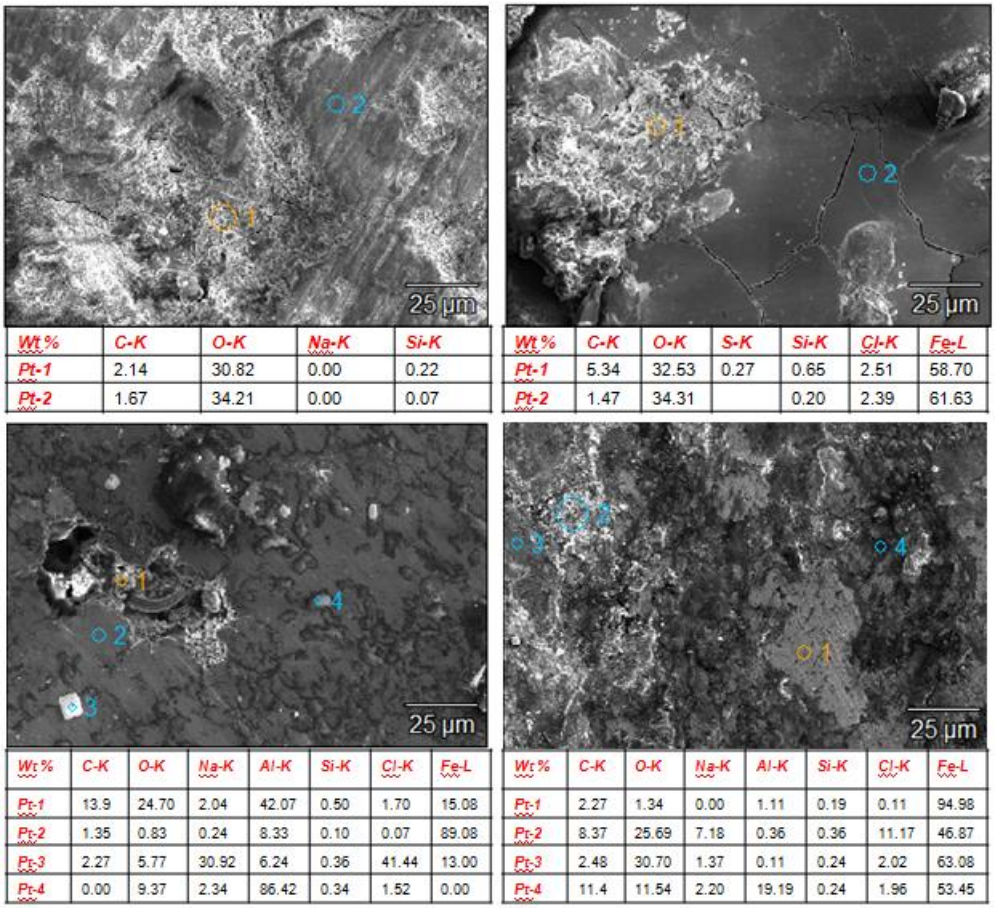

Wt %	C-K	O-K	Na-K	Si-K
Pt-1	2.14	30.82	0.00	0.22
Pt-2	1.67	34.21	0.00	0.07

Wt %	C-K	O-K	S-K	Si-K	Cl-K	Fe-L
Pt-1	5.34	32.53	0.27	0.65	2.51	58.70
Pt-2	1.47	34.31		0.20	2.39	61.63

Wt %	C-K	O-K	Na-K	Al-K	Si-K	Cl-K	Fe-L
Pt-1	13.9	24.70	2.04	42.07	0.50	1.70	15.08
Pt-2	1.35	0.83	0.24	8.33	0.10	0.07	89.08
Pt-3	2.27	5.77	30.92	6.24	0.36	41.44	13.00
Pt-4	0.00	9.37	2.34	86.42	0.34	1.52	0.00

Wt %	C-K	O-K	Na-K	Al-K	Si-K	Cl-K	Fe-L
Pt-1	2.27	1.34	0.00	1.11	0.19	0.11	94.98
Pt-2	8.37	25.69	7.18	0.36	0.36	11.17	46.87
Pt-3	2.48	30.70	1.37	0.11	0.24	2.02	63.08
Pt-4	11.4	11.54	2.20	19.19	0.24	1.96	53.45

Figure 5. a) Ar medium, b) sintered in Al medium SEM and EDS views taken after corrosion treatment in NaCl solution of samples

When the SEM images of samples after corrosion were examined, it was observed that crevice corrosion had formed on the surface of samples subjected to sintering in argon medium and that pitting corrosion formed on the surface of samples subjected to the sinter-aluminizing process. For the development of pitting corrosion, the presence of halogen ions is required in the medium. In the study performed, NaCl was preferred as the corrosion medium, and Cl ions had caused pitting corrosion. This corrosion begins with an anodic reaction formed at any point of the metal surface, and by the effect of environmental conditions, the anodic reaction continues by a series of autocatalytic reactions that give rise to each other and causes the formation of the pit at that point.

The higher Ecorr values of samples subjected to sinter-aluminizing, compared to samples subjected only to sintering, indicate better corrosion resistance. Al-150 sample exhibited the lowest Icorr value ($5.54x10^{-6}$ μAcm^{-2}) attributed to the thick and relatively less porous plating surface. Al-200 sample had a higher Icorr value ($4.50x10^{-5}$ μAcm^{-2}) than the Al-150 sample, and the reason for this was the presence of relatively larger pores and micro-cracks on its surface.

4. CONCLUSION

Distaloy SA 6906033 alloys were pressed with cold pressing method under the pressures of 150 MPa and 200 MPa, and they were subjected to sinter-aluminizing process and only to sintering process for 5 hours at 1000°C. The changes in the microstructural, mechanical, and corrosion behaviors of samples obtained were examined.

While the densities of samples, sintered in argon and aluminum mediums, increased by pressing pressure, their surface roughness decreased. Considering the microstructure characteristics, while the Fe phase was dominant on the construct in samples subjected to sintering in argon medium, a surface structure forming of FeAl phase was subject in samples subjected to sinter-aluminizing. Porosity was present in both the samples subjected to sintering and sinter-aluminizing, and porosity decreased by the increase of cold pressing pressure, but it was not obliterated. Considering the corrosion behaviors, the corrosion potentials of samples subjected to sinter-aluminizing in NaCl medium were lower than those subjected only to sintering. Moreover, when evaluated among themselves, it was determined that the corrosion potential was decreasing along with the increase of cold pressing pressure (Ar-150 > Ar-200; Al-150 > Al-200). The lowness of Ecorr values, obtained as the result of corrosion tests, of samples subjected to sintering compared to samples subjected to only sinter-aluminizing, and the highness of Icorr values, obtained as the result of corrosion tests, of samples subjected to sintering compared to samples subjected to only sinter-aluminizing, indicate that these materials exhibit higher corrosion resistance. Sinter-aluminizing of Distaloy SA 6906033 alloys positively affected the material's corrosion resistance as well as its structural and mechanical characteristics. The actualization in a single step of the sintering process of the alloy along with aluminizing is essential in terms of processing time and energy. The study results indicated that the sinter-aluminizing process is promising in the usage of PM materials in corrosive environments.

5. CONFLICT OF INTEREST

Authors approve that to the best of their knowledge, there is not any conflict of interest or common interest with an institution/organization or a person that may affect the review process of the paper.

6. AUTHOR CONTRIBUTION

Selvin TURGUT has the full responsibility of the paper about determining the concept of the research, data collection, data analysis and interpretation of the results, preparation of the manuscript and critical analysis of the intellectual content with the final approval.

7. REFERENCES

Alshammari Y., Yang F., Bolzoni L., Low-cost powder metallurgy Ti-Cu alloys as a potential antibacterial material. Journal of the Mechanical Behavior of Biomedical Materials 95, 232-239, 2019.

Bagliuk G., Properties and structure of sintered boron containing carbon steels. Sintering–Methods and Products 12, 249-266, 2012.

Callister W. D., Materials science and engineering: an introduction (2nd edition). Materials & Design, 1991, https://doi.org/10.1016/0261-3069(91)90101-9.

Chávez J., Alemán O. J., Martínez M. F., Vergara-Hernández H. J., Olmos L., Garnica-González P., Bouvard D., Characterization of Ti_6Al_4V–Ti_6Al_4V/30Ta bilayer components processed by powder metallurgy for biomedical applications. Metals and Materials International 26(2), 205-220, 2020.

Chen X. H., Dong J. H., Han E. H., Ke W., Effect of Al alloying on corrosion performance of steel. Corrosion Engineering, Science and Technology 42(3), 224-231, 2007.

Choy K. L., Chemical vapor deposition of coatings. Progress in Materials Science 48, 57–170, 2003.

Çavdar P. S., Çavdar U., The evaluation of different environments in ultra-high frequency induction sintered powder metal compacts. Revista de Metalurgia 51(1), e036, 2015.

Dubiel B., Moskalewicz T., Swadzba L., Czyrska-Filemonowicz A., Analytical TEM and SEM characterization of aluminide coatings on nickel based superalloy CMSX-4. Surface Engineering 24(5), 327-333, 2008.

Erdogan A., Kursuncu B., Günen A., Kalkandelen M., Gok M. S., A new approach to sintering and boriding of steels "Boro-sintering": Formation, microstructure and wear behaviors. Surface and Coatings Technology 386, 125482, 2020.

German R. M., Powder metallurgy of iron and steel. New York: John! Wiley & Sons Inc, 1998.

Grabke H. J., Schutze M., Oxidation of Intermetallics. WILEY-VCH Verlag GmbH: Berlin, Germany, 1998.

Gökmeşe H., Bostan B., The Effects of Pressing and Sintering on Pore Morphology and Microstructural Properties in AA 2014 Alloy. Gazi University Journal of Science Part C: Design and Technology 1(1), 1-8, 2013.

Günen A., Kurt B., Somunkıran İ., Kanca E., Orhan N., The effect of process conditions in heat-assisted boronizing treatment on the tensile and bending strength characteristics of the AISI-304 austenitic stainless steel. Physics of Metals and Metallography 116(9), 896-907, 2015.

Heakal F. E. T., Tantawy N. S., Shehta O. S., Influence of chloride ion concentration on the corrosion behavior of Al-bearing TRIP steels. Materials Chemistry and Physics 130(1-2), 743-749, 2011.

Kayali, Y., Investigation of the diffusion kinetics of borided stainless steels. Physics of Metals and Metallography 114, 1061-1068, 2013.

Ladd M., Ladd M. F. C., Crystal Structures: Lattices and Solids in Stereoview. Horwood Series in Chemical Science; Elsevier: Chichester, UK, 1999.

Li G. J., Wang J., Li C., Peng Q., Gao J., Shen B. L., Microstructure and dry-sliding wear properties of DC plasma nitrided 17-4 PH stainless steel. Nuclear Instruments and Methods in Physics Research Section B: Beam Interactions with Materials and Atoms 266(9), 1964-1970, 2008.

Liu X. M., Yi D. W., Liu B., Ma Z. W., Wang G. W., Current status and application of hot-dip aluminizing technique. Materials Protection-Wuhan 41(4), 47, 2008.

Lu C. H., Feng C., Han L. H., Feng J., Zhu L. J., Jiang L., Feng Y. R., Corrosion Behavior Research of Aluminized N80 Tubing in Water Injection Well. Materials Science Forum 944, 1035-1039, 2019.

Maki J., Corrosion Behavior of Aluminized Steel Sheets in 50-Year Outdoor Exposure Test. ISIJ International 59(10), 1870-1877, 2019.

Martinez M., Virguer B., Maugis P., Lacaze J., Relation Between Composition Microstructure and Oxidation in Iron Aluminidies. Intermetallics 14(10-11), 1214-1220, 2006.

Medvedovski E., Formation of corrosion-resistant thermal diffusion boride coatings. Advanced Engineering Materials 18, 11–33, 2016.

Mittemeijer E. J., Somers M. A. J., Thermochemical Surface Engineering of Steels. 1st ed. Elsevier-Woodhead Publishing: Cambridge, UK, 2014.

Mojaddami M., Rastegari S., Arabi H., Rafiee H., Effect of heat treatment on coating microstructure applied by high activity diffusion process on IN738L. Surface Engineering 28(10),772-777, 2012.

Öztekin K., Çinko Kaplanmış Karbon Çeliğinin Na-okzalat ve Na-tartarat Ortamlarında Polianilin ve Poli o-anisidin ile Kaplanarak Korozyon Direncinin Geliştirilmesi, Mustafa Kemal Üniversitesi Fen Bilimleri Enstitüsü,Yüksek Lisans Tezi (Basılmış), 2014.

Pérez F. J., Pedraza F., Hierro M. P., Balmain J., Bonnet G., Comparison of the high-temperature oxidation of uncoated and CVD–FBR aluminized AISI-304 stainless steel. Oxidation of Metals 58(5), 563-588, 2002.

Sharma B. P., Rao G. S., Vates U. K., Powder Metallurgy Processing and Mechanical Characterization of Iron-Based Composite Reinforced. Advances in Industrial and Production Engineering: Select Proceedings of FLAME 2018 303, 2019.

Sundaram M. V., Surreddi K. B., Hryha E., Veiga A., Berg S., Castro F., Nyborg L., Enhanced densification of PM steels by liquid phase sintering with boron-containing master alloy. Metallurgical and Materials Transactions A 49(1), 255-263, 2018.

Triani R. M., Gomes L. F. D. A., Aureliano R. J. T., Neto A. L., Totten G. E., Casteletti L. C., Production of aluminide layers on AISI 304 stainless steel at low temperatures using the slurry process. Journal of Materials Engineering and Performance 29(6), 3568-3574, 2020.

Turgut S., Günen A., Mechanical Properties and Corrosion Resistance of Borosintered Distaloy Steels. Journal of Materials Engineering and Performance 29(11), 6997-7010, 2020.

Wang X. Y., Du J. J., Ma Z. W., A One-Step Pack Cementation Method for Preparing AlN/Aluminizing Coating with Good Corrosion Resistance. Solid State Phenomena, 295, 3-8, 2019.

Wu J., Ma B., Li H., Stanciulescu I., The running-in micro-mechanism and efficient work conditions of Cu-based friction material against 65Mn steel. Experimental Techniques 43(6), 667-676, 2019.

Xiang Z. D., Datta P. K., Relationship between pack chemistry and aluminide coating formation for low-temperature aluminisation of alloy steels. Acta Materialia 54(17), 4453-4463, 2006.

Xiao-Su Y., Shanyi D., Litong Zhang Editors, Composite Materials Engineering. Volume 1, Fundamentals of Composite Materials, 2017.

Yazici A., Çavdar U., A study of soil tillage tools from boronized sintered iron. Metal Science and Heat Treatment 58(11-12), 753-757, 2017.

JOURNAL of
MATERIALS and MECHATRONICS:A

e-ISSN 2717-8811
JournalMM, 2022, 3(2), 194-205
https://doi.org/10.55546/jmm.1131636

Araştırma Makalesi / Research Article

Toz Metalurjisi Yöntemiyle Üretilen Fe Esaslı Fe-Ni-Cu Elmas Kesici Takımında Co'ın Etkisi

İlyas SOMUNKIRAN[1], Ertuğrul ÇELİK[2], Büşra TUNÇ[3]*, Çağdaş GÜNEŞ[4]

[1] Fırat Üniversitesi, Teknoloji Fakültesi, Metalurji ve Malzeme Mühendisliği Bölümü, Elâzığ, Türkiye,
ORCID ID: https://orcid.org/0000-0003-2690-238X, ilyassomunkiran@gmail.com
[2] Munzur Üniversitesi, Mühendislik Fakültesi, Makine Mühendisliği Bölümü, Tunceli, Türkiye,
ORCID ID: https://orcid.org/0000-0001-7104-8288, ecelik@munzur.edu.tr
[3] Fırat Üniversitesi, Teknoloji Fakültesi, Metalurji ve Malzeme Mühendisliği Bölümü, Elâzığ, Türkiye,
ORCID ID: https://orcid.org/0000-0002-0090-5227, busraonce23@gmail.com
[4] Munzur Üniversitesi, Mühendislik Fakültesi, Makine Mühendisliği Bölümü, Tunceli, Türkiye
ORCID ID: https://orcid.org/0000-0001-7405-2063, gunescagdas62@gmail.com

Geliş/ Received: 17.06.2022; **Kabul / Accepted:** 22.08.2022

ÖZET: Bu çalışmada toz metalürjisi (TM) tekniğiyle Fe esaslı Fe-Ni-Cu matrisine ağırlıkça farklı oranlarda (%10-20-30) kobalt (Co) ilave edilerek üretilen numunelerin mikroyapı ve bazı mekanik özellikleri incelendi. Sinterleme; 920 °C' de, 35 MPa basınç altında, 4 dk süreyle argon gazı atmosferinde yapıldı. Numunelerin mikroyapısal karakterizasyonu X-ışınları analizi (XRD), taramalı elektron mikroskobu (SEM), enerji dağılım spektrometresi (EDS) ile incelendi. Yoğunluk ölçümleri yapılan numuneler, sertlik ve üç noktalı eğme deneylerine tabi tutuldu. Sonuç olarak; takviye oranının artması ile porozitede azalma meydana geldi. En yüksek sertlik ve yoğunluk değerinin %20 Co ilaveli numunede olduğu görüldü. Co oranı ilavesiyle başlangıçta eğme gerilmesi ve yüzde uzamanın arttığı ve artan Co oranıyla birlikte eğme gerilmesi ve yüzde uzamanın azaldığı gözlendi.

Anahtar Kelimeler: Elmas Kesici Takımlar, Toz Metalürjisi, Kobalt, Demir Esaslı Alaşım.

*Sorumlu yazar / Corresponding author: busraonce23@gmail.com

Bu makaleye atıf yapmak için /To cite this article

Somunkıran, İ., Çelik, E., Tunç B., Güneş Ç. (2022). Toz Metalurjisi Yöntemiyle Üretilen Fe Esaslı Fe-Ni-Cu Elmas Kesici Takımında Co'ın Etkisi. Journal of Materials and Mechatronics: A (JournalMM), 3(2), 194-205.

The Effect of Co on Fe-Based Fe-Ni-Cu Diamond Cutting Tool Produced by Powder Metallurgy Method

ABSTRACT: In this study, microstructure and some mechanical properties of the samples were investigated produced by adding different weight (10-20-30%) cobalt (Co) to Fe-based Fe-Ni-Cu matrix by powder metallurgy (TM) technique. Sintering; It was carried out at 920 ºC, under 35 MPa pressure, for 4 minutes in an argon gas atmosphere. Microstructural characterization of the samples was examined by X-ray analysis (XRD), scanning electron microscope (SEM), and energy distribution spectrometry (EDS). Density measurements were made and the samples were subjected to hardness and three-point bending tests. As a result; The porosity decreased with the increase in the reinforcement ratio. It was observed that the highest hardness and density value was in the sample with 20% Co added. It was observed that the bending stress and percent elongation increased with the addition of Co ratio and the bending stress and percent elongation decreased with increasing Co ratio.

Keywords: Diamond Cutting Tools, Powder Metallurgy, Cobalt, Iron-Based Alloy.

1. GİRİŞ

Elmas, bilinen en sert malzeme olduğu için kesim ve aşındırma işlemlerinde kullanılmaktadır. Doğal elmas bıçaklarının kullanılmasıyla yüksek sıcaklık ve yüksek basınçlı elmas sentezi ile sentetik elmasların üretimi başlamıştır. Alet yapımcıları polikristal elmas kesme takımlarında, doğal elmas kullanmak yerine sentetik elmas kullanmayı tercih etmiştir. Bunun sebebi; doğal yapılı elmasların farklı kesikleri veya kırılma yüzeyleri sonucunda meydana gelen kristal morfolojileri yerine sentetik elmasta belirli kafes düzlemlerinde kristal büyüme olasılığının daha avantajlı olmasıdır (Kulaksız, 2007). Elmas kesici takımı üretiminde toz metalürjisi (TM) üretim yöntemi yaygın olarak kullanılmaktadır. Ayrıca tozlar basınçsız sinterleme (Burgers, 1978; Thakur, 1978; Dwan, 1998; Haman ve ark., 1999; Gasik ve ark., 1999), sıcak izostatik presleme (Cram, 1995), veya ikisinin kombinasyonu (Ojeda ve ark., 1998, ekstrüzyon (Samvelion ve Manoukion, 1995), lazer ergitme (Grüneis, 1998) sıcak presleme ve lazer kesimin kombinasyonu (Schmid, 1995; Fiechter, 1995) gibi birçok teknikle üretilebilir.

Toz metalürjisi yöntemi (TM), metal tozlarının belli oranlarda karıştırılarak oda sıcaklığında hassas kalıplarda istenilen teknik değerlere uygun basınçlarda sıkıştırılması ve sonrasında kontrollü atmosfer şartlarında fırınlanmasıyla parça üretme yöntemidir. Toz metalürjisini diğer üretim yöntemlerine kıyasla ilgi çekici kılan avantajları karmaşık şekilli ve düşük boyutsal toleransa sahip parçaların üretilebilirliğinin yanı sıra üretimin yüksek kalitede ve ekonomik oluşu, nispeten düşük enerji tüketimi ve malzeme verimliliğinin yüksek olmasıdır (Fayed ve Otten, 1997; German, 1994; German, 2007; Chang ve Zhao, 2013). TM üretim yöntemi ile kontrol edilebilir gözenekli yapıya sahip metaller de seri olarak üretilebilir. Bu üretim yöntemi genel olarak uygun karşım oranlarına sahip metal tozlarının bir karıştırıcı ile karıştırılması ve ardından bir kalıp içerisine preslenmesi esasına dayanır (Froes ve ark., 1980; Qian ve Froes, 2015).

Toz formlardaki kobalt (Co) elmaslı kesici takımların metal matris bileşimlerinde kullanılan esas metal malzemelerindendir. Çünkü kobalt, bu tür elmas tutucu metal matrislerin aşınma dayanımı ve elmas tutma kapasitesi gibi çok önemli iki fonksiyonel özellik parametresinin değerlerini artırmaktadır (Konstanty, 2021; Konstanty ve Tyrala, 2021). Bunların yanı sıra, diğer metallerden ayrı olarak kobalt tozları çok değişik türlerde tane büyüklüklerine, tane şekilleri, tane dağılımları ve

kimyasal saflıklara sahip olabildiğinden eklendikleri matrislerin fonksiyonel parametrelerini geniş skalalarda kontrol etme ve ayarlanabilme imkânı sunmaktadır. Yine teorik yoğunluğa kısmen daha düşük sıcaklık ve basınç koşulları altında yapılan sıcak presleme işlemleriyle ulaşılmasını sağlayarak maliyeti düşürmesi kobalt kullanımının bir diğer avantajıdır (Konstanty, 2021; Konstanty ve Tyrala, 2021). Elmaslı kesici takımlarda kobaltın görevi matrisin tok ve dayanıklı olmasını sağlamaktır. Dünya çapında üretilen kobalt tozunun %75'i kesici ve elmaslı takım endüstrisinde kullanılmaktadır. Bu da her yıl 3500 ton civarlarındadır. Fakat pazar her yıl %2,7– 2,8 büyümektedir (Oishi, 1979).

Çalışmada Fe-Ni-Cu matris malzemesine ağırlıkça farklı oranlarda (%10-20-30) Co takviye edildi. Numuneler 4 dk boyunca argon gazı atmosferinde 35 MPa basınç altında ve 920 °C sıcaklıkta sinterlendi. Daha sonra numunelere sertlik, yoğunluk ve üç nokta eğme deneyleri yapıldı. Mikro yapıdaki analizleri irdelemek amacıyla SEM (taramalı elektron mikroskobu), EDS ve XRD yapıldı. Üç noktalı eğme mukavemeti ve % uzama değerleri, artan Co katkısı ile azaldı. SEM analizinde kobaltın katkı oranı arttıkça porozite çukurlarının azalmış olduğu görüldü ancak üç kat (%30 Co) katkılama olsa da tamamen azalmayıp yer yer derinleşmiş çukur ve oksitleşmelerin olduğu görüldü.

2. MATERYAL VE YÖNTEM

Çalışma kapsamında kullanılan %99.9 saflıktaki Fe, Ni, Cu ve Co elementel tozları piyasadan ticari olarak temin edildi. Deneyde Direkt Dirençli Sıcak Presleme tekniği ile 4 dakika süre boyunca 35 MPa basınç altında 920 °C'de sinterlenerek 40x10x7 mm boyutlarında numuneler üretildi. Şekil 1' de deneyde kullanılan akış şeması ve yapılan ölçüm işlemleri verilmiştir. Deneyde kullanılan numune kodları ve numune içerikleri ise Çizelge 1'de verilmiştir.

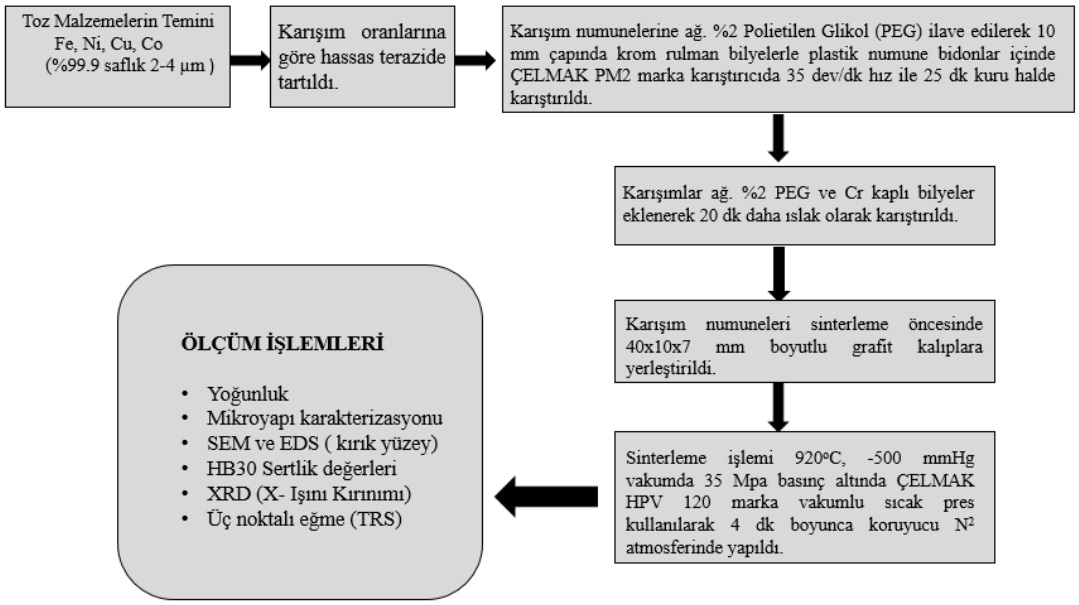

Şekil 1. Deneysel İşlem Akış Şeması ve Ölçüm İşlemleri (Güneş, 2022)

Çizelge 1. Deneyde Kullanılan Numune Kodları ve İçerikleri

NUMUNE KODU	NUMUNE İÇERİĞİ
N0	%85 Fe+%10 Ni+%5 Cu
N1	N0+%10 Co
N2	N0+%20 Co
N3	N0+%30 Co

Matrisi oluşturan %85 Fe-%10 Ni-%5 Cu (% ağ.) oranında olan toz karışımı hazırlanarak ağırlıkça farklı oranlarda (%10-%20-%30) Co tozu matrise eklendi. Deneyde kullanılan tozların Taramalı Elektron Mikroskobu görüntüleri Şekil 2'de gösterilmiştir.

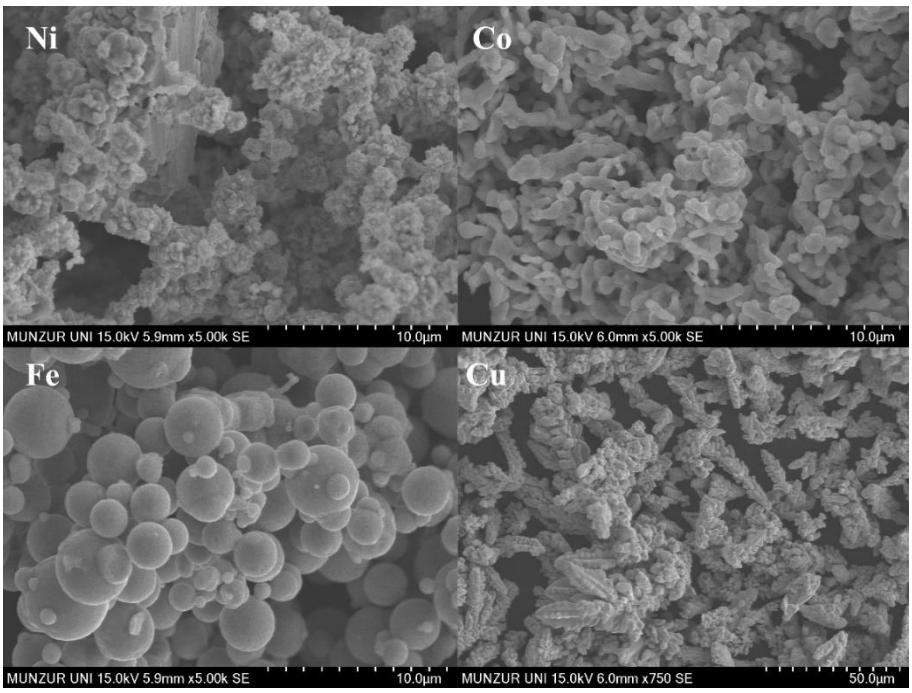

Şekil 2. Deneyde Kullanılan Tozların Taramalı Elektron Mikroskobu Görüntüleri (Güneş, 2022)

Numuneler soğuk presleme işlemi yapılmadan önce direkt grafit kalıp içerisinde üretildi. İlk olarak katkı elementlerinin % bileşimine göre teorik öz kütleleri hesaplandı. Numuneler 0,1 gr hassasiyetinde tartıldı. Ardından toz karışımları preslenmek için grafit kalıplara yerleştirildi. Numunelerin sıcak presleme işleminde; kütle kaybının oluşmaması, grafit kalıba yapışmaması ve kalıptan zarar görmeden çıkartılabilmesi için kalıplara sıvı formda bor nitrür sürüldü. Üretilen numunelerin yüzeyleri 180 mesh su zımparası kullanılarak kir, kalıntı ve çapaklardan arındırıldı. Numuneler epoksi reçine içine alınarak 180, 300, 400, 600, 800, 1200 ve 2000 mesh'lik su zımparasıyla zımparalandı. Zımparalanan numuneler elmas pasta ve etil alkol kullanılarak parlatıldı. Parlatılan yüzeyler $5HNO_3$+5CHCOOH+$1H_3PO_4$+$11H_2O$ dağlayıcısı kullanılarak mikro yapı incelemesine hazır hale getirildi. Sertlik değerlerinin elde edilmesi için numunelerin her iki yüzeyinden HB30 Brinell sertliği cinsinden ölçümler yapıldı. Her bir numuneden 6 adet sertlik değeri alındı ve bu değerlerin aritmetik ortalaması alınıp sertlik değerleri belirlendi. Yoğunluk ölçümü, Arşimet prensibine göre ASTM B-311 standardına uygun olarak yapıldı. Üç noktalı eğme testi ASTM B 528-16 standartları temel alınarak 1 mm/dk hızında 20 mm alt destek boşluğunda gerçekleştirildi. SEM analizi numunelere epoksi reçine kalıptan çıkarmadan elektriği iletmesi için parçaya bir bakır kablo bağlanarak yapıldı.

3. BULGULAR VE TARTIŞMA

Sıcak presleme tekniği ile üretilen numuneler; sertlik, yoğunluk, mikro yapı, 3 noktalı eğme ve XRD açısından yorumlanmıştır.

3.1 Sertlik Ölçüm Sonuçları

Brinell cinsinden yapılan sertlik ölçüm sonuçları Şekil 3'te verilmiştir. Matrisin (%85 Fe+%10 Ni+%5 Cu) ortalama sertlik değeri 162 Brinell olarak ölçüldü. Co elementinin ilave edilmesiyle N1,

N2 ve N3 numunelerinin sertlik değerleri sırasıyla 182, 190 ve 180 Brinell olarak belirlendi. Soketin sertliğinin kullanıldığı yere uygun olması kesici takımlarda oldukça önem teşkil eder. Yapılan bu çalışmada; Co ilavesi ile bu durumun elde edilmesi istendi. Kobaltın (Co) tane boyutu 2 µm, sertliği ise 700 Brinell dir. %30 Co katkılı olan N3 numunesinde sertliğin azaldığı görüldü. Kobalt katkısı ile sertlik sonucunun artarak azalması tane boyutuna bağlı olarak sinterleme sırasında poroziteye neden olmasıdır.

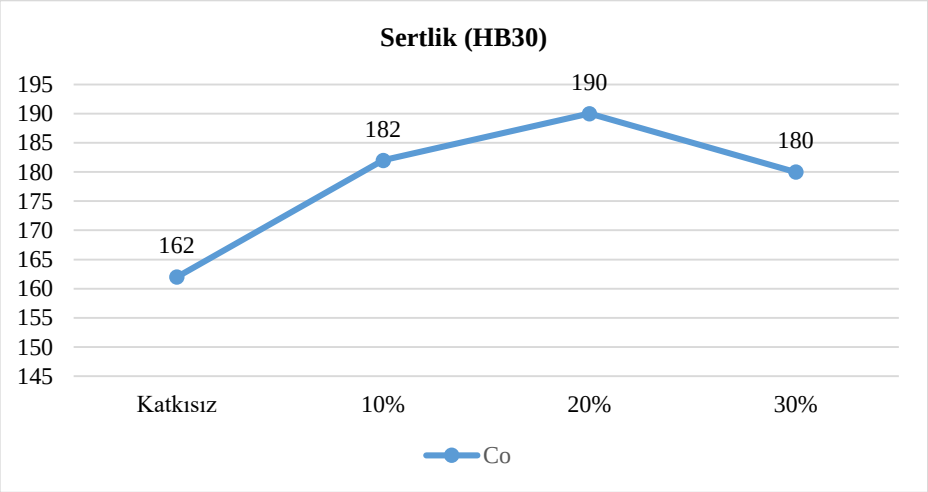

Şekil 3. Numunelerin artan Co oranına karşılık sertlik grafiği

3.2 Yoğunluk Ölçüm Sonuçları

Numunelerin ASTM B 311 standardı ve Arşimet prensibine göre yapılan yoğunluk ölçüm sonuçları Şekil 4'te gösterildiği gibidir. Bu grafiğe göre % Co katkılama oranı arttıkça yoğunluk önce artmış daha sonra eksponansiyel olarak azalmaya başlamıştır. Matris malzemesinin (%85 Fe+%10 Ni+%5 Cu) yoğunluk değeri 7.71 gr/cm^3 iken Co katkılı N1, N2, N3 numunelerinin yoğunluk değerleri sırasıyla 7.93, 7.96 ve 7.81 gr/cm^3 olarak belirlenmiştir. Artan Co oranı ile yoğunluk değerinde artış beklenirken %30 Co katkılı numunede azalmanın meydana geldiği görülmüştür. Bunun nedenini tane boyutuna bağlı olarak Co'ın yapı içerisinde %20 oranından sonra daha fazla poroziteye neden olduğu düşünülmektedir.

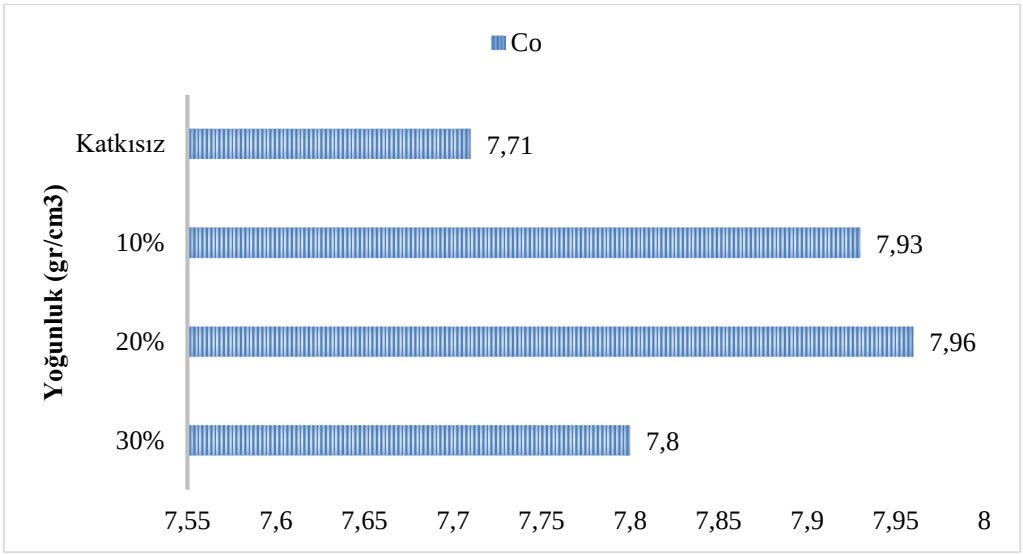

Şekil 4. Numunelerin katkılama oranına bağlı yoğunluk değerleri

3.3 Mikroyapı İncelemeleri

Co elementinin mikroyapı etkisini analiz edebilmek için 250X ve 1000X büyütmelerde SEM görüntüleri alınmıştır. N0 numunesi ile Co katkılı N1, N2 ve N3 numunelerinin 250X büyütmedeki SEM görüntüleri Şekil 5'te verilmiştir. Artan takviye oranına bağlı olarak porozite çukurlarında azalma olduğu görülmüştür. %30 takviyeli olan N3 numunesinde porozitenin tamamen azalmadığı ve yer yer derinleşmiş çukur ve oksitlerin olduğu gözlendi.

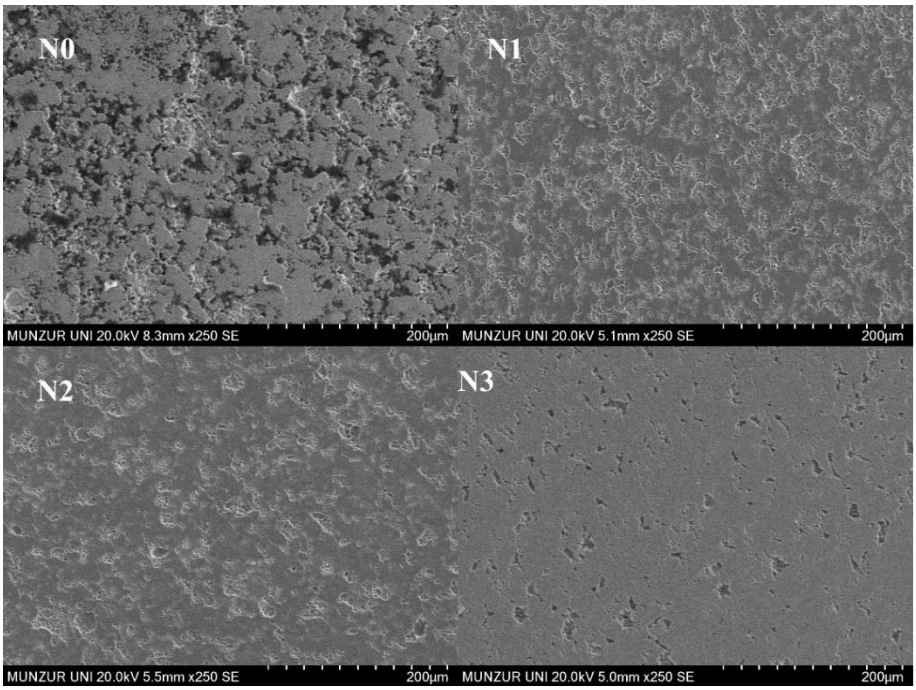

Şekil 5. Matris malzemesi olan N0 ile Co takviyeli N1, N2 ve N3 numunelerinin 250X büyütmedeki SEM görüntüleri

N0 matris numunesi ile kobalt (Co) katkılı N1, N2 ve N3 numunelerinin 1000X büyütmedeki SEM görüntüleri Şekil 6' da verilmiştir. Takviye oranı arttıkça porozite çukurlarında ve oksitlerde azalma görüldü. %30 Co ilaveli olan N3 numunesinde porozitenin azalmış olmasına rağmen derinleşmiş porozite çukurları daha ayrıntılı şekilde gözlendi. Karaduman ve arkadaşlarının 2019 da yapmış oldukları çalışmada porozitenin azaltılması için sinterleme sıcaklığı ve basıncın arttırılmasıyla sağlanabileceğini belirtmişlerdir (Karaduman, 2019).

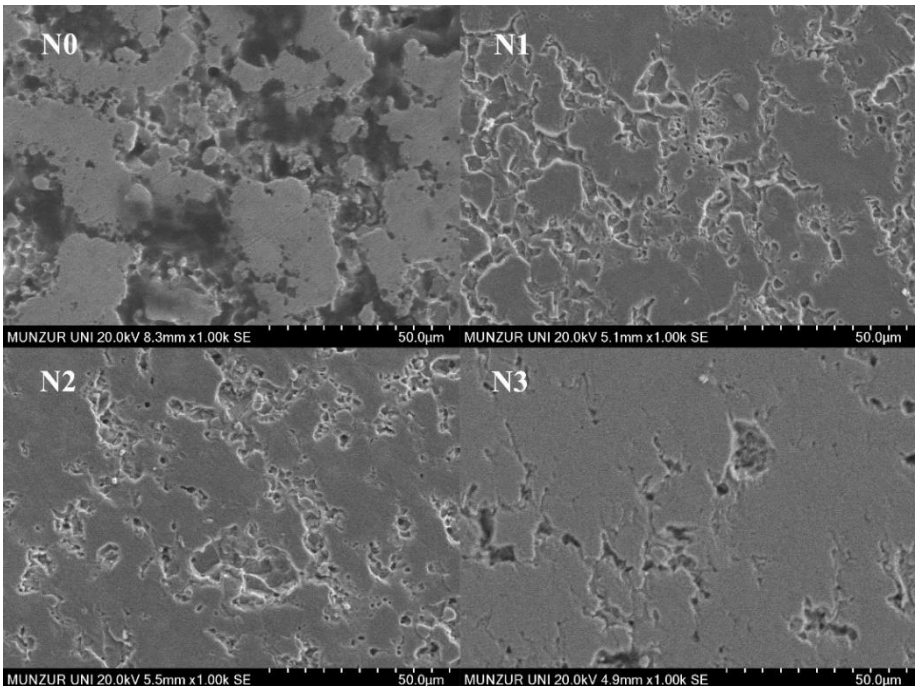

Şekil 6. Matris malzemesi olan N0 ile Co takviyeli N1, N2 ve N3 numunelerinin 1000X büyütmedeki SEM görüntüleri

Numune gruplarının referans N0 matris numunesi ile karşılaştırmalı kırık yüzey EDS görüntüleri Şekil 7'de verilmiştir. N0 referans numunesinin EDS görüntüsünde kırmızı yerler Fe, yeşil renk Ni, açık mavi yerler Cu göstermektedir. N1, N2 ve N3 numunesinde olan Co ise turkuaz rengindedir. Görüntülerdeki koyu siyah bölgeler çatlak veya porozite boşluklarını temsil etmektedir. N0 numunesindeki renklerin dağılımı Fe esaslı FeNiCu malzemesinin kompozisyonuna uygun şekilde meydana gelmiştir. N1-N3 numunelerine ait renkli EDS görüntülerine bakıldığında tek katlı (%10) Co katkılı N1 numunesine Co'ın matris içinde homojen dağıldığını ancak karanlık boşlukların ve oksitlerin fazla miktarda var olduğu görüldü. Takviye oranı iki katına (%20 Co) çıktığında irili ufaklı çok sayıda ve şekilde yerleşmiş Co (yeşil renkli) ile kaplı tanelerin oluştuğu gözlendi. Bu durum yoğunluğu arttırmıştır. Kobalt oranı üç katına (%30 Co) çıkarılan N3 numunesinde, N2 (%20 Co) numunesinde gözlenen bazı küçük tanelerin irileştiği gözlenmiştir. İdeal orandan fazla takviye oranının ilavesi yoğunluğu azaltabilen bir etken olabilmektedir. Fazla katkılamanın tane irileşmesine neden olan yoğunluktaki eksponansiyel azalma; sertlik, eğme gerilmesi ve yüzde uzama değerlerinde de görülmektedir.

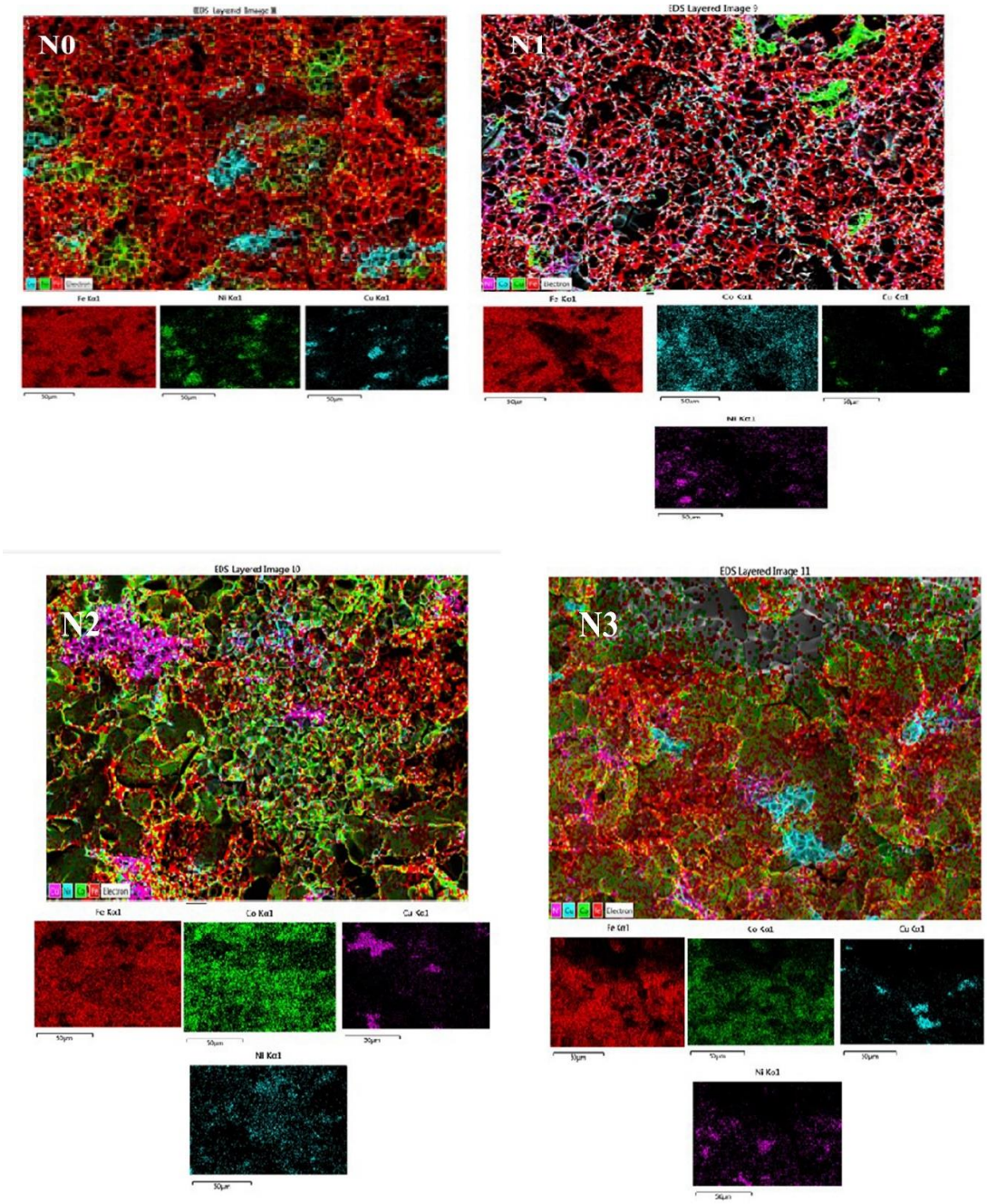

Şekil 7. Referans N0 ile kobalt katkılı N1, N2 ve N3 numunelerinin kırık yüzey EDS görüntüleri

3.4 Noktalı Eğme (TRS) Deneyi Sonuçları

Şekil 8'de üç noktalı eğme sonuçları gösterilmektedir. Deney numunelerinin Gerilme (MPa) ve uzama (%) değerleri ise Çizelge 2'de verilmiştir.

Çizelge 2. Üretilen deney numunelerinin Gerilme (MPa) ve uzama (%) değerleri

Numune Adı	Gerilme (MPa)	Yüzde Uzama (%)
N0	1276	10.72
N1	1612	16.60
N2	1609	14.92
N3	1417	11.23

N1, N2 ve N3 numunelerinin üç noktalı eğme mukavemetleri sırasıyla 1612, 1609 ve 1417 MPa'dır. % uzama değerleri ise 16,6, 14,92 ve 11,23 tür. Üç noktalı eğme mukavemeti ve % uzama değerleri artan Co katkısı ile azalmaktadır. Co toz metalurjisi için önemli matris metallerinden biridir. Özellikle 2 mikron boyutundaki Co, tane boyutu ıslatabilme kabiliyeti ve mekanik özellikleri bakımından matrisin eğme mukavemetinde artışa neden olmuştur (Nguyen, 2020). Fakat artan Co oranı ile üç noktalı eğme mukavemet değerinin artması gerekirken azalmaya neden olmuştur. Bu durum Şekil 6'da 1000X büyütmeli mikro yapı resimlerinden anlaşılmaktadır. Artan Co oranı ile yapıdaki mikro porozite sayısı azalmış ancak %30 aşırı bir Co katkılamasıyla tanelerin büyümesine ve arada kalan poroziteler içlere doğru derinleşerek toplam hacimsel yüzde porozite oranının diğer numunelerden daha yüksek olmasına neden olmuştur. Bu durum artan Co oranı ile matriste tane irileşmesinin meydana geldiğini göstermektedir (Nguyen, 2020). Fe, Ni, Cu ve Co metallerinin yüzey enerjileri arasında Ni>Co>Fe>Cu şeklinde bir büyüklük ilişkisi (Tyson, 1975) vardır ve sinterleme gibi ısıl işlemlerde yüzey enerjisi büyük olan metale doğru difüze (akma) eğilimindedirler (Uhlmann ve ark., 2020).

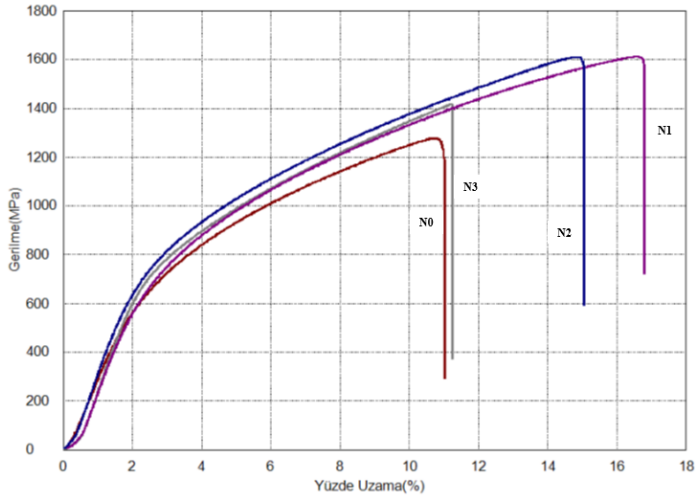

Şekil 8. N0, N1, N2 ve N3 numunesinin 3 noktalı eğme deneyi sonucu grafiği

3.5 XRD Ölçüm Sonuçları

Sinterleme sonrası elde edilen X-ışını kırınım desenlerini gösteren XRD grafikleri Şekil 9 ve Şekil 10'da verilmiştir. Elde edilen tüm numune XRD desenlerinde gözlenen en yüksek pikler (110) atomik kayma düzlemli α-faz (bcc) yapısındaki Fe demir (ferrit) pikleridir (Jamrozek, 2020; Li, 2016; Konstanty, 2021; Konstanty ve Tyrala, 2021). Bunun sebebi demirin tüm numunelerde kütlece oldukça baskın oranda kullanılmasıdır. Bu ana demir piklerinin haricinde başka yönelimli (Miller düzlem indisli) demir ve diğer element esaslı intermetalik ara faz veya bileşik yapılı pikler de gözlenmiştir. Yine bütün numunelerde ikinci en çok miktarda bulunan temel alaşım metali olan nikel (Ni) pikleri de tüm grafiklerde belirmiştir. Tüm numunelerde kullanılan temel alaşım bileşeni olan bakır (Cu) elementi miktarı az oranda olduğundan Cu pikleri yalnızca bazı numunelerde gözlenebilmiştir. Bunlardan ayrı olarak yine tüm numunelerde 20º civarlarında bir veya iki adet küçük sığ karbon (C) pikleri gözlenmiştir ki bu karbon piklerinin XRD ölçümü hazırlığında numunelerin kaplandığı reçine maddesindeki karbon esaslı bileşiğe ait olduğu düşünülmektedir. N1-N3 numunelerinde kobalt (Co) elementleri kullanıldığından bu elementlere ait piklerin oluştuğu da gözlenmiştir. Tüm numuneler arasında ise en az polikristal yapıda (Ghosh, 2018) olan referans N0 numunesidir, diğerlerinde ise dahil olan element sayı ve miktar çeşitliliğinin artışına bağlı olarak ara

faz veya bileşik oluşumlarının sayısı ve çeşidi artmıştır. Bu tane küçülmeleriyle birlikte oluşan küçük fazlı yapılar (polikristal yapılar) elmas tutucu matrislerin elmas tutma kapasitelerini (Çelik, 2009) veya performanslarını artıran bir durumdur.

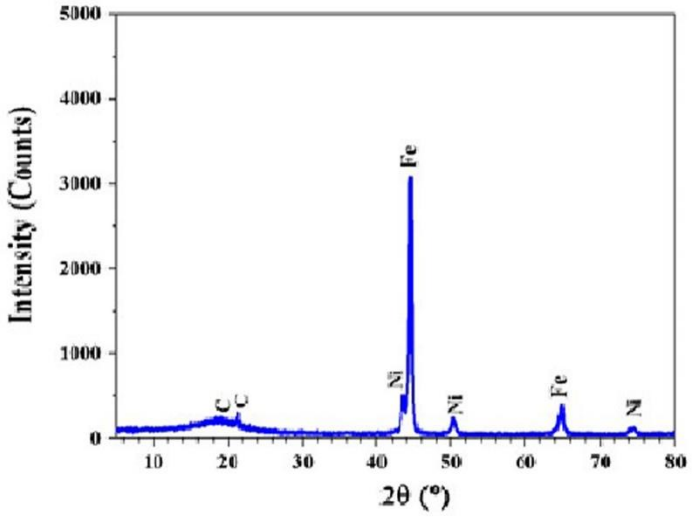

Şekil 9. Üretilen N0 numunesinin XRD grafiği

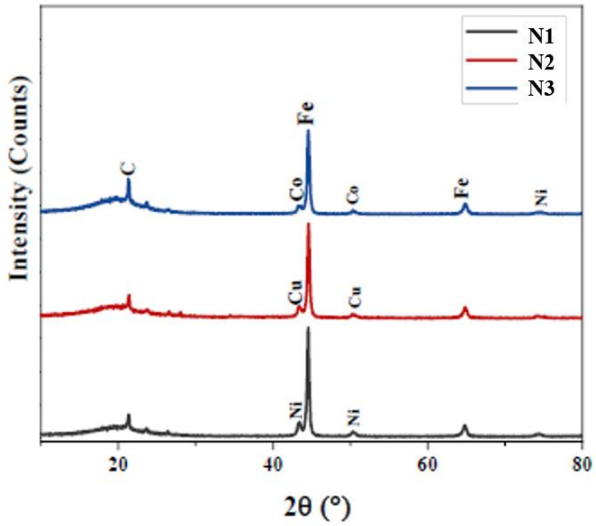

Şekil 10. Üretilen N1, N2 ve N3 numunesinin XRD grafiği

4. SONUÇ

Çalışma kapsamında Fe esaslı Fe-Ni-Cu matris içerisine ağırlıkça %10-%20-%30 oranlarında Co takviye edilerek sıcak presleme tekniğiyle numuneler üretildi. Deneylerde elde edilen sonuçlar aşağıdaki verildiği gibidir.

- Numunelerin HB30 sertlik değerleri kobalt ilavesi ile eksponansiyel olarak artarak azalmıştır. %30 Co ilavesi ile artmadan sonra azalma meydana gelmiştir.
- Yoğunluk verileri irdelendiğinde Fe-Ni-Cu matrise kıyasla %10 Co takviyesi ile artış meydana gelmiş, %20 Co oranında artış devem etmiştir. Ancak takviye oranı %30 olduğunda bir miktar azalma görülmüştür.
- En yüksek porozite %30 Co takviyeli numunede gözlenmiştir.

- SEM ve kırık yüzey renkli EDS görüntülerinde kobalt ilavesi ile tane irileşmesi görülmüştür.
- %10 Co takviyeli numunede eğme dayanımları ve yüzde uzama değerleri katkısız numuneye göre artığı görülmüş ve bu artış artan Co oranıyla azalmıştır.

5. ÇIKAR ÇATIŞMASI

Yazarlar, bilinen herhangi bir çıkar çatışması veya herhangi bir kurum/kuruluş ya da kişi ile ortak çıkar bulunmadığını onaylamaktadırlar.

6. YAZAR KATKISI

İlyas SOMUNKIRAN, Ertuğrul ÇELİK, Büşra TUNÇ ve Çağdaş GÜNEŞ çalışmanın kavramsal ve tasarım süreçlerinin belirlenmesi ve yönetimi, veri toplama, veri analizi ve yorumlama, makale taslağının oluşturulması, fikirsel içeriğin eleştirel incelenmesi ve son onay ve tam sorumluluk kısmında katkıda bulunmuştur.

7. KAYNAKLAR

Aronsson B., On the origins and early growth of stainless steel: A survey with emphasis on the development in Sweden. Outokumpu Stainless research foundation, 2010.

Kulaksız S., Doğaltaş (Mermer) Maden İşletmeciliği ve İşleme Teknolojileri. TMMOB Maden Mühendisleri Odası Yayınları, Ankara, No: 126, 624, 2007.

Burgess R. R., Man-made diamond for stone processing, Proc. 1st Technical Symposium, Bucharest, Romania, October 5-6, 1978.

Thakur U. N., The role of metal powders in manufacturing diamond tools. Proc. Superabrasives'85, Chicago, Illinois, USAS April 22-25, MR85-307, 1985.

Dwan J. D., HP/HT manufacturing of diamond, www.nantech.ie., 1998.

Hamar-Thibault S., Allibert C. H., Tillman W., Phase constitution of Cu77Sn8Ti14Zr1 as a binder for diamond tools, Proc. International Workshop on Diamond Tool Production, Turin, Italy, November 8-10, 1999, pp: 57-64.

Gasik M. M., Kervinen Po., Kaskiala M., Graf P., In situ sintering studies of cobalt powders for diamond tools, Prac, International Workshop on Diamond Tool Production, Turin, Italy, November 8-10, 1999, pp: 107-112.

Cram A. S. D., Hot isostatic pressing, Proc. Seminar on PM Diamond Tools, Lausanne, Switzerland, November 2-3. 1995.

Ojeda R. G., del Villar M., Muro P., Iturriza L., Castro F., Densification of diamond tools with Co, Ni and Fe based metallic binders, Proc. PM World Congress & Exhibition, Granada, Spain, 1998, pp: 481-486.

Samvelion R.V., Manoukion N.V., Extrusion for diamond tool production, Proc. Seminar on PM Diamond Tools, Lausanne, Switzerland, November 2-3, 1995.

Grüneis H. T., Sintering and brazing all in one, Industrial Diamond Review, No. 25, 45-47, 1998.

Schmid H. G., Diamond tool production using the DIAPLATE process. Proc. Seminar on PM Diamond Tools, Lausanne, Switzerland, November 2-3, 1995.

Fiechter A., Schneiden und Schweissen mit gepulsten Nd:YAG Laser, Proc. Seminar on PM Diamond Tools, Lausanne, Switzerland, November 2-3, 1995.

Fayed M. E., Otten L., Handbook of Powder Science and Technology. New York: Chapman & Hall,1997.

German R., Powder Metallurgy Science. New Jersey: Princeton, 1994.

German R., Toz metalurjisi ve Parçacıklı Malzeme İşlemleri. Ankara: TTMD Yayınları, 2007.

Chang I., Zhao Y., Advances in Powder Metallurgy: Properties, Processing and Applications. Woodhead Publishing, 2013.

Froes F. H., Eylon D., Eichelman G. E., Burte H. M., Developments in titanium powder metallurgy. JOM, 32(2), 47-54, 1980.

Qian M., Froes F. H., Titanium powder metallurgy: science, technology and applications. Butterworth-Heinemann, 2015.

Konstanty J., Sintered diamond tools the past, present and future. Archives of Metallurgy and Materials 66(2), 593-599, 2021.

Konstanty J., Tyrala D., Easily sinterable low alloy steel powders for P/M diamond tools. Metals, 11(8), 1204, 2021.

Oishi M., Prospects for cobalt demand. Cobalt News 5 January 11-14, 1979.

Güneş Ç., Ni Esaslı Katkı Malzemelerinin Matris Özelliklerine Etkisinin Araştırılması, Munzur Üniversitesi Lisansüstü Eğitim Enstitüsü, Yüksek Lisans Tezi (Basılmış), 2022.

Karaduman O., Structural and thermodynamical study of Cu-Zn-Al shape memory alloys with new compositions produced by hot isostatic press (HIP). In AIP Conference Proceedings, 2178(1), 30-40, 2019.

Nguyen V. M., Spark plasma sintering of cobalt powders in conjunction with high energy mechanical treatment and nanomodification. Processes, 8(5), 627, 2020.

Tyson W. R., Surface energies of solid metals. Canadian Metallurgical Quarterly 14(4), 307-314. 1975.

Uhlmann E., Polte M., Bolz R., Börnstein J., Fundamental research of applying tungsten carbide-cobalt as tool electrode material for sinking EDM. Procedia CIRP, 95, 466-470. 2020.

Jamrozek J. B., Processing and characterization of Fe-Cu-Ni sinters prepared by ball milling and hot pressing. Arch. Metall Mater, 65(3),1157-1161, 2020.

Li M., Fabrication of Fe-based diamond composites by pressureless infiltration. Materials 9(12), 1006, 2016.

Ghosh B., Defect induced room temperature ferromagnetism in single crystal, polycrystal, and nanorod ZnO: A comparative study. Journal of Applied Physics 123(16), 161507, 2018.

Çelik E., Elmaslı kesici takımlarda alternatif bağlayıcılar, Fırat Üniversitesi Fen Bilimleri Enstitüsü, Doktora Tezi (Basılmış), 2009.

JOURNAL of
MATERIALS and MECHATRONICS:A

e-ISSN 2717-8811
JournalMM, 2022, 3(2), 206-224
https://doi.org/10.55546/jmm.1105012

Araştırma Makalesi / Research Article

Biyoyenilenebilir Enerji Tabanlı Mikro Şebekenin Yük Frekansı Kontrolü İçin Fuzzy PID Kontrolör

Dursun ÖZTÜRK[1]*, Burak YILDIRIM[2], Gizem DOĞAN[3]

[1] Bingöl Üniversitesi, Mühendislik ve Mimarlık Fakültesi, Elektrik-Elektronik Mühendisliği Bölümü, Bingöl, Türkiye,
ORCID ID: https://orcid.org/0000-0002-0335-8118, dozturk@bingol.edu.tr
[2] Bingöl Üniversitesi, Teknik Bilimler Meslek Yüksekokulu, Bingöl, Türkiye,
ORCID ID: https://orcid.org/0000-0002-2118-4297, byildirim@bingol.edu.tr
[3] Çevre ve Şehircilik Bakanlığı İLBANK Genel Müdürlüğü, Ankara, Türkiye,
ORCID ID: https://orcid.org/0000-0001-9286-4479, gyalin23@gmail.com

Geliş/ Received: 19.04.2022; **Kabul / Accepted:** 28.08.2022

ÖZET: Günümüzde enerji tüketiminin giderek arttığı, çevre koruma bilincinin geliştiği ve enerji piyasalarındaki serbestleşmenin istikrarlı şekilde ilerlediği görülmektedir. Bu nedenle, yeni teknolojiler yardımı ile yenilenebilir enerji kaynaklarından (YEK) daha fazla yararlanmaya yönelik politikalar üretilmekte ve dağıtılmış üretim sistemlerine olan ilginin artması sağlanmaktadır. Mikro şebekeler YEK'lerin şebekeye entegrasyonunda önemli avantajlar sağlayan bir çözüm olarak ortaya çıkmıştır. Mikro şebekelerin yapılarında bulunan YEK'lerin değişken üretim yapıları gibi bazı belirsizliklere sahip olması, bu sistemlerde frekans kararlılığını önemli problemlerden biri haline getirir. Bir mikro şebeke modeline etkin bir yük frekansı kontrolünün (YFK) sağlanması, bu sistemlerin kararlılığı ile ilgili iyileştirmelere önemli ölçüde katkıda bulunur. Bu çalışmada, mikro şebekede, YFK'de karşılaşılan zorlukların üstesinden gelmek için bir fuzzy oransal integral türev(PID - Proportional-Integral-Derivative) kontrolör yapısı önerilmiştir. En uygun kontrolör parametrelerinin belirlenmesi için lig şampiyonası algoritması (LŞA), karınca koloni algoritması (KKA) ve parçacık sürü optimizasyon (PSO) algoritmaları kullanılmıştır. Aynı zamanda, fuzzy PID kontrolörünün kazançlarının en uygun değerlerinin elde edilmesi için zaman ağırlıklı mutlak hatanın toplamı (ITAE - Integral Time-weighted Absolute Error) maliyet fonksiyonu kullanılmıştır. Çalışma sonucunda önerilen kontrolörün performansı klasik PID kontrolör ile karşılaştırılmıştır.

Anahtar Kelimeler: Biyoyenilenebilir Enerji, Mikro Şebeke, Yük Frekans Kontrol, Fuzzy PID Kontrolör.

*Sorumlu yazar / Corresponding author: dozturk@bingol.edu.tr

Bu makaleye atıf yapmak için /To cite this article

Öztürk, D., Yıldırım, B., Doğan, G. (2022). Biyoyenilenebilir Enerji Tabanlı Mikro Şebekenin Yük Frekansı Kontrolü İçin Fuzzy PID Kontrolör. Journal of Materials and Mechatronics: A (JournalMM), 3(2), 206-224.

Fuzzy PID Controller for Load Frequency Control of Biorenewable Energy Based Micro Grid

ABSTRACT: Today, it is seen that energy consumption is gradually increasing, environmental protection awareness is developing and liberalization in energy markets is progressing steadily. For this reason, with the help of new technologies, policies are produced to benefit more from renewable energy resources (RES) and the interest in distributed generation systems is increased. Micro grids have emerged as a solution that provides significant advantages in the integration of RES to the grid. The fact that RES in the structures of micro grids have some uncertainties, such as variable generation structures, makes frequency stability one of the important problems in these systems. Providing effective load frequency control (LFC) to a micro grid model contributes significantly to improvements in the stability of these systems. In this study, a fuzzy proportional-integral-derivative (PID) controller structure is proposed to overcome the difficulties encountered in LFC in micro grid. League championship algorithm (LCA), ant colony algorithm (ACA) and particle swarm optimization (PSO) algorithms were used to determine the most suitable controller parameters. At the same time, the integral time-weighted absolute error (ITAE), cost function is used to obtain the optimal values of the gains of the fuzzy PID controller. As a result of the study, the performance of the proposed controller was compared with the classical PID controller.

Keywords: Biorenewable Energy, Micro Grids, Load Frequency Control, Fuzzy PID Controller.

1. GİRİŞ

Artan nüfus, sanayileşme ve modern yaşam tarzındaki değişiklikler nedeniyle dünya çapında meydana gelen aşırı enerji talebi, ekosistemimizi tahrip eden zararlı atıkları çoğaltmaktadır. Bu durum, atıkları kullanan biyoenerji gibi yenilenebilir yeşil enerji üretimine yönelik bazı alternatif çözümlere yönelimi zorunlu kılmaktadır. Mevcut yenilenebilir enerji/biyoenerji kapasitesi, şu anki devasa güç talebine kıyasla çok küçük olmakla beraber atıkları azaltmak ve yeşil enerji üretmek için tüm olası yenilenebilir-biyoenerji kojenerasyon tabanlı hibrit mikro şebekeler ile küresel enerji talebi karşılanabilir (Tucho ve Nonhebel, 2017). Uzak ve küçük yerleşim yerleri, rüzgar/güneş-biyoenerji kojenerasyon tabanlı hibrit mikro şebekeler ile kendi güç gereksinimlerini üretebilirler. Günümüzde başta Hindistan olmak üzere bazı ülkelerde yenilenebilir/biyoelektrik kojenerasyonunu teşvik etmeye yönelik bazı programlar başlatılmıştır (Barik ve Das, 2020).

Dağıtılmış enerji kaynakları, mikro şebeke içerisinde hem dağıtılmış üretim hem de dağıtılmış depolama enerji şeklinde olabilmektedir. Dağıtılmış üretim teknolojileri; içten yanmalı motorlar, gaz türbinleri, kombine çevrim gaz türbinleri, hidrolik türbinler, yakıt hücreleri, rüzgâr türbinleri, PV güneş panelleri, ısı, jeotermal enerjisi, biokütle, gel-git enerjisi ve dalga enerjisi gibi üretim birimleri olarak sıralanmaktadır. Bu üretim birimleri incelendiğinde rüzgâr türbinleri, PV, küçük hidrolik türbinler, jeotermal enerji ve yakıt pillerinin dünyada toplam güç üretiminde piyasa payını arttırması beklenmektedir (Al-Dhaifallah ve ark., 2018). Enerji depolama birimleri ise volanlar/uçan tekerlekler, süper kapasitörler, süper iletken manyetik enerji depolama sistemleri ve elektrokimyasal piller olarak sıralanmaktadır (Parmar ve ark., 2012).

Temel şebekenin bir parçası olan ve endüstriyel/ticari tüketici uygulamalarından oluşan bir mikro şebeke, şebekeden bağımsız veya şebeke bağlantılı mod olarak çalışabilir (Kocaman, 2014). Mikro şebekelerin yapısında rüzgâr türbinleri, hidrolik türbinler, yakıt hücreleri ve PV (Photovoltaic) modüller gibi kaynaklar yer almaktadır. Mikro şebekeler, güç elektroniğine dayalı dönüştürücülerle bir arayüz birimi üzerinden şebekeye bağlanırlar. Güç elektroniği dönüştürücüleri incelendiğinde,

bunların sisteme girmesinin hem bağlı olduğu sistemin güç kalitesini etkilediği hem de yeni kontrol düzenlemeleri gerektirdiği belirlenmiştir (Baykal ve Beyan, 2004; Subramanyam ve ark., 2014).

Elektrik güç sistemlerinde ve mikro şebekelerde üretim ve tüketim arasındaki uyum önemlidir. Bu ikisi arasındaki uyumun bozulması, sistemde frekans sapmalarına neden olur (Mordjaoui ve ark., 2017). Üretim ve tüketim arasındaki dengeyi koruyarak frekans sapmalarını sınırlamak için gereken mekanizma, yük frekansı kontrolü (YFK) olarak adlandırılır (Elkawafi ve ark., 2016; Yıldırım ve ark., 2021). Adalı modda çalışan mikro şebeke ana şebekeden yardım almadığından, YFK bu modda en temel operasyonel gereksinimlerden biri haline gelecektir (Yıldırım, 2021). Adalı biyoyenilebilir enerji tabanlı mikro şebekenin YFK'sı için şimdiye kadar çeşitli kontrol yaklaşımları geliştirilmiştir. Barik ve Das'ın yaptığı çalışmada biyoyenilebilir enerji tabanlı mikro şebeke sistemin YFK'da PID kontrolör kullanılmış ve bu kontrolörün parametre değerlerini belirlemek için QSHO (quasi-oppositional selfish herd optimization) optimizasyon algoritması kullanılmıştır (Barik ve Das, 2020). Barik ve Das'ın yaptıkları başka bir çalışmada ise, biyoyenilebilir enerji tabanlı mikro şebeke sistemin YFK'da PID kontrolör kullanılmış ve bu kontrolörün parametre değerlerini belirlemek için GOA (Grasshopper Optimisation Algorithm) optimizasyon algoritması kullanılmıştır (Barik ve Das, 2018). Barik ve arkadaşlarının yaptıkları diğer bir çalışmada ise, biyoyenilebilir enerji tabanlı mikro şebeke sistemin YFK'da PID kontrolör kullanılmış ve bu kontrolörün parametre değerlerini belirlemek için PSO optimizasyon algoritması kullanılmıştır (Barik ve ark., 2019).

Bu çalışmanın amacı; biyoyenilenebilir enerji tabanlı mikro şebekenin YFK için Fuzzy PID kontrolör kullanmak ve bu kontrolör parametrelerinin en uygun değerlerini LŞA, KKA ve PSO optimizasyon algoritmaları vasıtasıyla belirlemektir. Her ne kadar literatürde farklı güç sistemleri ve mikro şebeke sistemlerde YFK için bu algoritmalar kullanılmışsa da (Bevrani ve ark., 2012; Özdemir ve ark., 2017; Özdemir ve Öztürk, 2017; Yıldırım, 2021) bu çalışma biyoyenilebilir enerji kaynaklarına dayalı mikro şebeke sistemlerin YFK için literatürde bir ilk olma özelliğini taşımaktadır. Ayrıca bu biyoyenilenebilir mikro şebeke sistem için Fuzzy PID kontrolör yapısının kullanımı bu çalışmanın diğer yeniliğidir.

2. MATERYAL VE YÖNTEM

2.1 Mikro Şebeke Modeli

Bu çalışmada kullanılan çok birimli izole yenilenebilir mikro şebeke modeli, yenilenebilir kaynakların optimum kullanımı ile ekolojik yönler ve ekonomik operasyon göz önünde bulundurularak oluşturulmuştur. Bu mikro şebeke sistemi MHTG (Micro-Hydro Turbine Generator) ünitesine, BCHP (Biomass Fired Combined Heat and Power) ünitesine, AE (Aqua electrolizer) ünitesine, FC (Fuel Cell) ünitesine, PV ünitesine ve lineer yüklere sahiptir. Optimal YFK için mikro şebekenin doğrusallaştırılmış modeli Şekil 1'de görülmektedir. Ayrıca bu bölümde her birimin matematiksel modellemesi kısaca sunulmuştur (Barik ve Das, 2018).

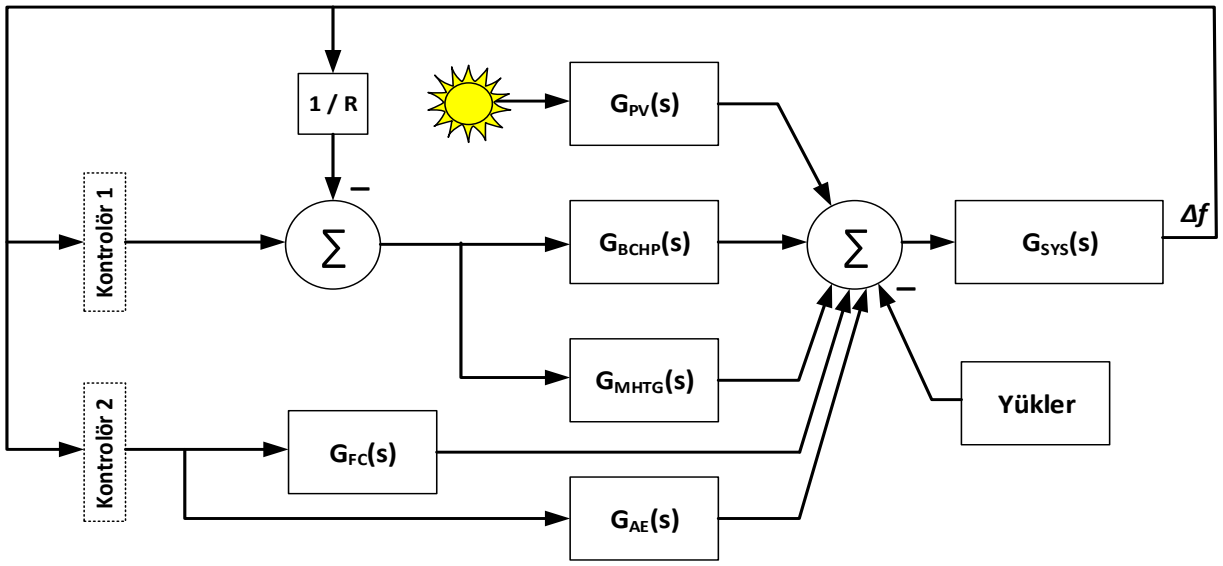

Şekil 1. YFK için önerilen yenilenebilir mikro şebekenin blok diyagramı

2.1.1 PV ünitesi

PV ünitesi, güneş enerjisini elektrik enerjisine dönüştüren PV panel dizilerinden oluşmaktadır. PV ünitesinin düşük frekans alan analizi için doğrusallaştırılmış transfer fonksiyonu Eşitlik 1. de verilmiştir.

$$G_{PV}(s) = \frac{1}{1 + sT_{PV}} \tag{1}$$

2.1.2 MHTG ünitesi

Atık su bazlı MHTG ünitesinin doğrusallaştırılmış transfer fonksiyon modeli, hız regülatörü, cebri boru ve hidro türbin fonksiyonları göz önünde bulundurularak geleneksel düşük düşü hidroelektrik üretim sistemine referansla Eşitlik 2. de verilmiştir.

$$G_{MHTG}(s) = \left(\frac{1}{1 + sT_{HG}}\right)\left(\frac{1 + sT_{RS}}{1 + sT_{RH}}\right)\left(\frac{1 - sT_{HT}}{1 + 0.5sT_{HT}}\right) \tag{2}$$

2.1.3 BCHP ünitesi

Katı atık bazlı BCHP ünitesinin doğrusallaştırılmış transfer fonksiyonu modeli, hız regülatörü, yeniden ısıtıcı ve buhar türbini fonksiyonları göz önünde bulundurularak geleneksel fosil yakıtlı termik üretim sistemine referansla Eşitlik 3. de gösterilmiştir.

$$G_{BCHP}(s) = \left(\frac{1}{1 + sT_{BSG}}\right)\left(\frac{1 + sK_{BR}T_{BR}}{1 + sT_{BR}}\right)\left(\frac{1}{1 + 0.5sT_{BCT}}\right) \tag{3}$$

2.1.4 AE ve FC üniteleri

AE ünitesi, Hidrojen (H_2) gazları üretmek için yoğun olmayan saatlerde mikro şebekenin fazla gücünü çeker. Bu H_2 gazları, yoğun saatlerde güç üretmek için FC ünitesinde yakıt olarak kullanılmak

üzere depolanır. AE ve FC birimlerinin doğrusallaştırılmış transfer fonksiyon modelleri sırasıyla Eşitlik 4. ve Eşitlik 5. de verilmiştir.

$$G_{AE}(s) = \frac{1}{1 + sT_{AE}} \tag{4}$$

$$G_{FC}(s) = \frac{1}{1 + sT_{FC}} \tag{5}$$

2.2 Sistem Dinamiği ve Generatör Modeli

Önerilen sistem için herhangi bir anda güçteki net değişim, Eşitlik 6. daki gibi ifade edilebilir;

$$\Delta P_e = P_{PV} + P_{MHTG} + P_{BCHP} + P_{FC} - P_{AE} - P_L \tag{6}$$

Burada, karşılık gelen alt simge, ilgili birimler için gücü tanımlar ve mikro şebekenin genel sistemi için eşdeğer generatör dinamiği modeli Eşitlik 7. ile formüle edilebilir.

$$\frac{\Delta f}{\Delta P} = \frac{1}{D + sM} = G_{SYS}(s) \tag{7}$$

2.3 Amaç Fonksiyonu

Güç sistemleri incelendiğinde bunların analiz ve tasarımı içerisinde kontrolörün performansını belirleyen indeksler kullanılmaktadır. Burada özellikle sistem değişkenlerinin farklı kombinasyonlarının kullanılmasıyla birçok performans indeksi oluşturulabilmektedir. Bunların içerisinde en yaygın olarak kullanılanları ise ISE, IAE, ITSE ve ITAE indeksleridir (Kılıç ve Özdemir, 2019). ITAE'ye ait hesaplama formülü Eşitlik 8.de verilmiştir.

$$ITAE = \int_0^\infty t|e(t)|dt \tag{8}$$

Önerilen sistem iki kontrolörden oluşmaktadır; Kontrolör1, MHTG ve BCHP birimlerinin güç çıkışını kontrol ederken, Kontrolör2, AE ve FC birimlerinin işlevlerini kontrol etmektedir. Amaç fonksiyonu, önerilen sistem için PID kontrolör parametrelerini ayarlamak için ITAE kriteri dikkate alınarak formüle edilmiştir.

Önerilen mikro şebeke sisteme ait parametre değerleri aşağıdaki Çizelge 1'de verilmiştir.

Çizelge 1. Önerilen biyoyenilenebilir mikro şebeke sisteme ait parametre değerleri

Semboller	Değerleri
T_{PV}	1.8s
T_{HG}, T_{HT}	0.2s, 1.0s
T_{RS}, T_{RH}	5s, 28.75s
T_{BSG}, T_{BCT}	0.08s, 0.3s
K_{BR}, T_{BR}	0.3, 10s
T_{FC}, T_{AE}	4s, 0.5s
M, D, R	0.2, 0.012, 2.4

2.4 Kontrolör Yapısı

Kural tabanlı fuzzy küme teorisi, sistemleri tasarlamada ve takip etmesi kolay dilsel gösterimde gözlemleri ifade etmede daha fazla esneklik sağlar. Ayrıca, girişleri ve çıkışları arasında doğrusal ilişki olmayan sistemler için fuzzy mantık kapalı çevrim kontrol uygulamalarında kontrolör parametrelerinin ayarlanmasında daha iyi performans gösterir. Klasik kontrolörler, orantısal, integral ve türev terimleri için sabit kazanç değerine sahip hataların girdileri temelinde çalışır. Bu nedenle, doğrusal olmayan ve karmaşık sistemler için kontrolör performansı beklenen düzeyde değildir. Sabit kazanç yerine orantısal, integral ve türev terimleri için dinamik kazanç değeri dahil edilmeye çalışılabilir. Bir klasik PID kontrol yapısındaki kazancı dinamik olarak değiştirmek, kontrolör performansını artıracak ve yük değişimi ve harici rahatsızlıklar sırasında sistem çıkışını hızlı bir şekilde kararlı duruma getirecektir. Bu hususlar göz önünde bulundurularak, bu çalışmada, klasik PID kontrol şeması ile birleştirilmiş bir fuzzy mantık yapısı önerilmiştir. FPID (Fuzzy PID) kontrol yapısı, PID kontrolör ile kural tabanlı fuzzy denetimin bir birleşimidir. Bu kontrol stratejisinde FLC (Fuzzy Logic Control), orantısal, integral ve türev terimlerinin ölçekleme faktörünü elde etmek için sistem hatası ve türev hatası girdilerini kullanmak üzere tasarlanmıştır. Bu ölçekleme faktörlerini kullanarak, kontrolör kazanç büyüklüğü her örnekleme periyodunda güncellenecektir. Tipik bir FPID kontrol yapısının çerçevesi Şekil 2'de gösterilmektedir.

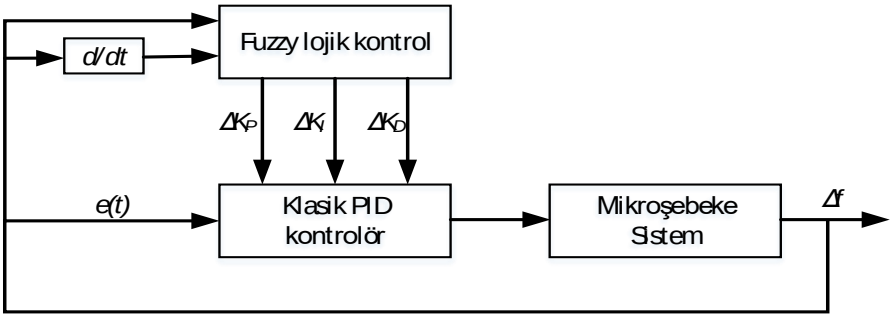

Şekil 2. Fuzzy PID kontrolörünün blok diyagramı

Önerilen kontrol yapısında FLC, hata ve hatanın türevi girdilerini kullanır ve orantısal, integral ve türev terimleri için ölçekleme faktörünü hesaplar ve daha sonra bu değerler klasik PID kontrolörünün kazanç parametrelerini güncellemek için kullanılır. Dolayısıyla, klasik PID denetleyicisi için k_P, $k_I$ve k_D'nin nihai kazanç değerleri aşağıdaki ifadeden hesaplanır:

$$k_P = K_P + \Delta K_P \tag{9}$$

$$k_I = K_I + \Delta K_I \tag{10}$$

$$k_D = K_D + \Delta K_D \tag{11}$$

Burada K_P, K_I ve K_D klasik PID kontrolörün başlangıç değerleridir. ΔK_P , ΔK_I ve ΔK_D ise fuzzy lojik kontrol tarafından hesaplanan ölçeklendirme faktörleridir. Giriş ve çıkış fuzzy kümeleri için üçgen üyelik fonksiyonları kullanılmış ve Mamdani tipi fuzzy çıkarım sistemi uygulanmıştır. Girdiler ve kesin çıktı üretmek için üç üyelik fonksiyonu, çıktılar için ise beş üyelik fonksiyonu seçilmiştir. Her bir çıktı için kullanılan kural tabanı Çizelge 2'de gösterilmektedir. Bu çizelgede N (Negatif), S (Sıfır), P(Pozitif), NK (Negatif küçük), NB (Negatif büyük), PK (Pozitif küçük) ve PB (Pozitif büyük) dil değişkenlerini ifade eder. Her bir durumun girdileri ve çıktıları arasındaki ilişki, Şekil 3'te yüzey

görünümünde gösterilmektedir. Yüzey görünümü, ölçekleme faktörü değerinin giriş hatasına ve hata büyüklüğündeki değişikliğe bağlı olarak nasıl değişebileceğini belirtir (Al-Dhaifallah ve ark., 2018).

Çizelge 2. Fuzzy dilsel kural tabanı ve yüzey görünümü

	Δe		
$\Delta K_P e$	N	S	P
N	NB	NK	S
S	NB	NK	NK
P	PK	PK	PB

a)

	Δe		
$\Delta K_I e$	N	S	P
N	NB	NK	NK
S	NK	S	PK
P	S	PK	PB

b)

	Δe		
$\Delta K_D e$	N	S	P
N	NK	NK	S
S	S	S	PK
P	S	PK	PK

c)

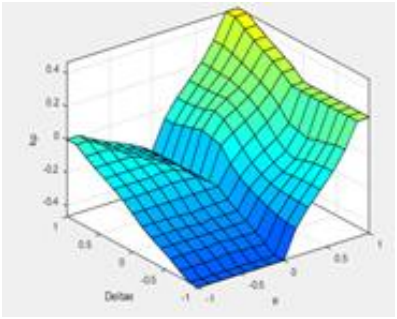

a)

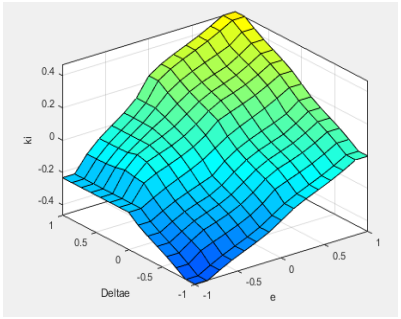

b)

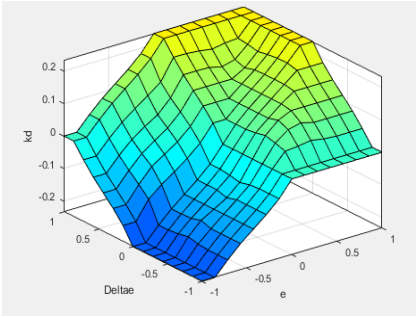

c)

Şekil 3. Girişe karşı çıkış için yüzey görünümleri. a) ΔK_P b) ΔK_I c) ΔK_D

2.5 Sezgisel Optimizasyon Algoritmaları

Dünyada teknolojinin gelişmesiyle birlikte bilgi kullanım miktarının arttığı ve buna bağlı olarak problemlerin çok boyutlu hale geldikleri görülmektedir. Bu nedenle problemleri çözme hızı büyük önem kazanmıştır. Bilim adamları problemlerin en uygun ve hızlı çözümünü bulmak için sürekli

çalışmakta ve yeni yöntemler geliştirmektedir. Optimizasyon kavramı bu çalışmalar sonucu ortaya çıkmış ve kullanılmaya başlanmıştır.

Klasik optimizasyon algoritmalarının çok boyutlu çalışmalarda ve karmaşık problemlerin çözümünde yetersiz kaldığı görülmüştür. Bu nedenlerden dolayı sezgisel algoritmalara yönelim söz konusu olmuş ve çalışmalar yapılmıştır. Sezgisel algoritmalar kullanılan metaforlara göre farklı açılardan sınıflandırılabilir. Bu metaforlara örnekler şu şekilde sıralanabilir;

- Doğadan ilham alan algoritmalar (PSO, KKA)
- Sosyal olaylardan esinlenen algoritmalar (Tabu arama, LŞA)
- Politik olarak esinlenen algoritmalar (Yayılmacı rekabet algoritması)

Doğadan esinlenilmiş olan algoritmalar incelendiğinde bunlarda genel yakınsama, doğadaki fiziksel ve ekolojik işlemler ile algoritmanın kendi optimizasyon mekanizmalarının simülasyonu yoluyla gerçekleştirilmektedir. Bunun sonucunda da etkin sonuçlar elde edilmektedir (Karaboga, 2005; Husseinzadeh, 2009).

2.5.1 Lig Şampiyonası Algoritması (LŞA)

Bir metasezgisel algoritma olan LŞA, spor liglerindeki şampiyonluk sürecinden esinlenerek geliştirilmiştir (Husseinzadeh, 2009). Yapay spor takımları, yapay bir ligde sezon sonuna kadar mücadele ederler (iterasyon). Numaralandırılan takım çiftleri haftalık lig programına bağlı olarak oynarlar ve sonuçlar kazanan, kaybeden ve beraberlik olarak belirlenir. Her takımın geliştirilmeyi hedeflediği oyun gücü, takımın kazanıp kaybetmesini yakından belirleyen bir faktördür. Takımlar, belirli takım formasyonuna/düzenlemesine (çözüme) sahiptirler ve bir sonraki oyunu kazanabilmek için bir önceki oyun tarzında yapılması gereken değişiklikleri (yeni bir çözüm) yaparlar. Böylece şampiyona sezon sonuna (durma koşuluna) kadar devam eder. Popülasyona dayalı bir algoritma olan LŞA'da takımlar PSO'daki parçacıklara benzemekle beraber çok farklı arama yoluna sahiptirler. Bireylerin karşılaştırılmasına odaklanan LŞA, arama fikrini içeriye ve dışarıya doğru etkileyerek kazanacak veya kaybedecek bireyleri belirler. Böylece daha iyi çözüme sahip takımın kazanma oranının daha büyük olması sağlanır. Bu şekilde arama doğrultusunun kazanan takıma yaklaşması ve kaybeden takımdan uzaklaşması beklenir (Husseinzadeh, 2009; Özdemir ve ark., 2017; Bingöl ve Alataş, 2015; Yıldırım, 2021).

2.5.2 Parçacık Sürü Optimizasyonu (PSO)

PSO 1995 yılında James Kennedy ve Russel Eberhart tarafından kuş ve balık sürülerinin besin bulma davranışlarından esinlenerek geliştirilen sürü zekâsına dayalı bir optimizasyon algoritması olarak tanımlanmaktadır (Kennedy ve Eberhard, 1995).

Bu optimizasyonda sürünün her bir bireyinin çözüm uzayında dolaştığı görülmektedir. Burada görülen her bir parçacığın optimizasyon probleminin birer aday çözümünü gösterdiği belirlenmiştir. Optimizasyonun, arama uzayında tüm parçacıkların rasgele bir konum alması sonucunda başladığı görülmektedir. Burada devam eden adımlar incelendiğinde parçacıkların, komşularının en iyi koordinatları ile kendi en iyi koordinatlarına göre pozisyonlarını güncellendikleri görülmektedir. Burada en iyi sonucun bulunması için arama işleminin bu şekilde devam edeceği belirlenmiştir.

2.5.3 Karınca Koloni Algoritması

KKA; meta sezgisel bir algoritma olup popülasyon temelli bir yaklaşım olarak görülmektedir. Karınca kolonisi algoritmasının temel ilkeleri ilk olarak Marco Dorigo ve arkadaşları tarafından özellikle ayrık optimizasyon problemlerini çözmek için ortaya konulmuştur. Bu algoritma, karınca kolonilerinin salgıladıkları feromon hormonu yardımıyla yiyecek kaynakları ile yuvaları arasındaki en kısa yolu bulmalarından esinlenerek oluşturulmuş olan bir tekniktir (Dorigo ve ark., 1999).

Dorigo; karınca kolonilerinin davranışlarının matematiksel modelleri üzerine dayandırdığı algoritmasını ilk kez gezgin satıcı problemi üzerinde uygulayarak olumlu sonuçlar elde ettiğini göstermiştir. Bunun sonucunda karınca kolonisi algoritmaları diğer araştırmacılar tarafından kullanılmaya başlanılmış ve günümüzde yaygın olarak kullanılan bir yapay zekâ tekniği haline gelmiştir (Dorigo ve Gambardella, 1997).

Bu makalede mikro şebeke sistemin YFK işlemini gerçekleştiren kontrol yapısına ait genel akış şeması şekil 4'te verilmiştir.

3. BULGULAR VE TARTIŞMA

3.1 PSO ile Optimize Edilen Klasik PID ve Fuzzy PID Kontrolör

Bu bölümde PSO kullanılarak mikro şebeke sistemde YFK için kullanılan Klasik PID ve Fuzzy PID kontrolörlerin en iyi frekans yanıtını veren parametre değerlerinin hesaplanması gerçekleştirilmiştir. Elde edilen sonuçlar yardımı ile mikro şebeke sistemde YFK'de klasik PID kontrolör ve fuzzy PID kontrolörün sonuçları karşılaştırılmıştır. Analiz çalışmalarında sisteme t=30 sn.'de ΔP=0.1 p.u.'luk bir yük değişikliği uygulanmıştır. Mikro şebeke sistem için klasik PID ve fuzzy PID kontrolörlere ait elde edilen sonuçlar aşağıda verilmiştir.

Şekil 4.'de PSO ile optimizasyon işlemi gerçekleştirilen Klasik PID kontrolör için mikro şebeke sisteme ait frekansın zamana göre değişimi gösterilmiştir. Burada optimizasyon işlemi sonucunda elde edilen en iyi ITAE performans kriteri için elde edilen PID kontrolör parametrelerine ait değerler Çizelge 3.'de verilmiştir. Benzer biçimde Şekil 5'te ise PSO ile optimizasyon işlemi gerçekleştirilen hem klasik PID hem de Fuzzy PID kontrolör için mikro şebeke sisteme ait frekansın zaman göre değişimleri gösterilmiştir.

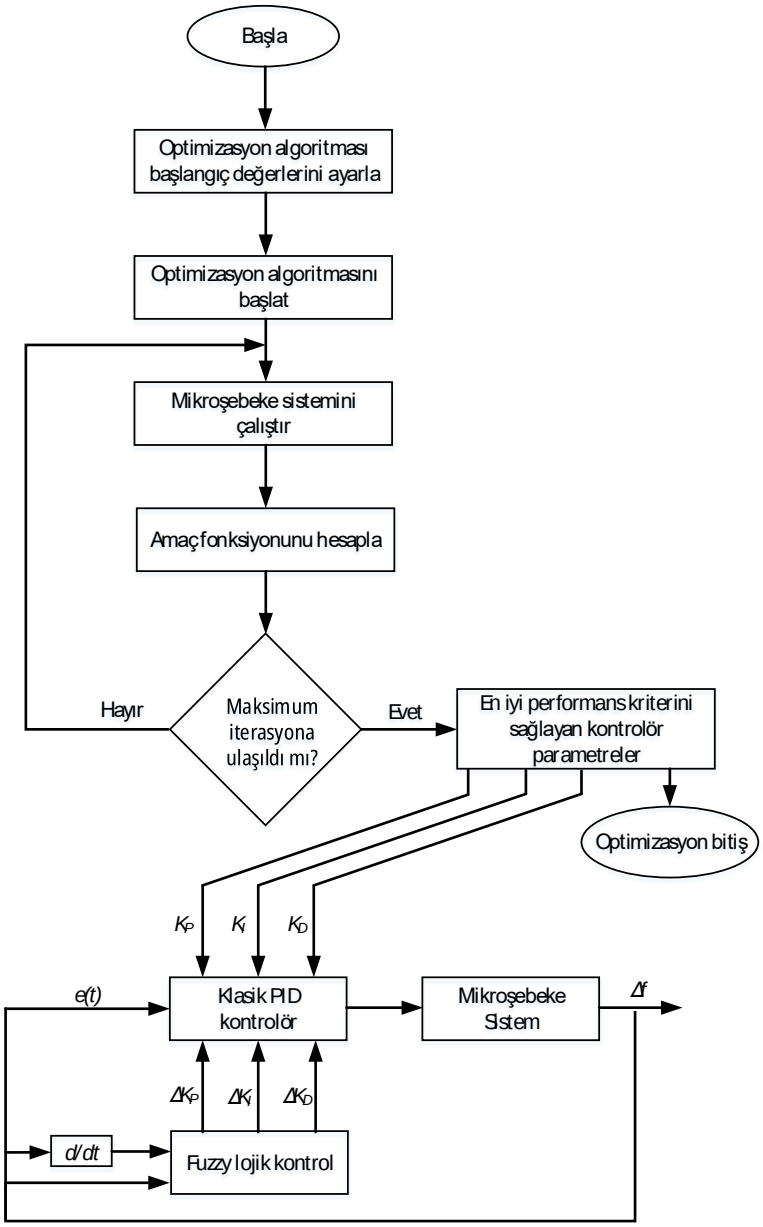

Şekil 4. Mikro şebeke sistem YFK şeması

Çizelge 3. PSO için Kontrolör 1 ve Kontrolör 2 ye ait parametre değerleri

Kp1	1.38668534	1. kontrolör Kp değeri
Ki1	3.00947908	1. kontrolör Ki değeri
Kd1	0.85619338	1. kontrolör Kd değeri
Kp2	8.28458295	2. kontrolör Kp değeri
Ki2	-35.11750388	2. kontrolör Ki değeri
Kd2	-24.19755357	2. kontrolör Kd değeri

Şekil 5. ve Şekil 6.'da verilen frekansın zamana göre değişimleri karşılaştırıldığı zaman genel olarak Fuzzy PID kontrolör bulunan sistemin frekans yanıtı dinamik olarak daha iyi sonuç verdiği görülmektedir. Şekiller incelendiğinde Fuzzy PID kontrolörlü sistemin hem maksimum aşma yönünden hem de sürekli duruma erişme zamanı açısından daha iyi bir performans sergilediği görülmektedir.

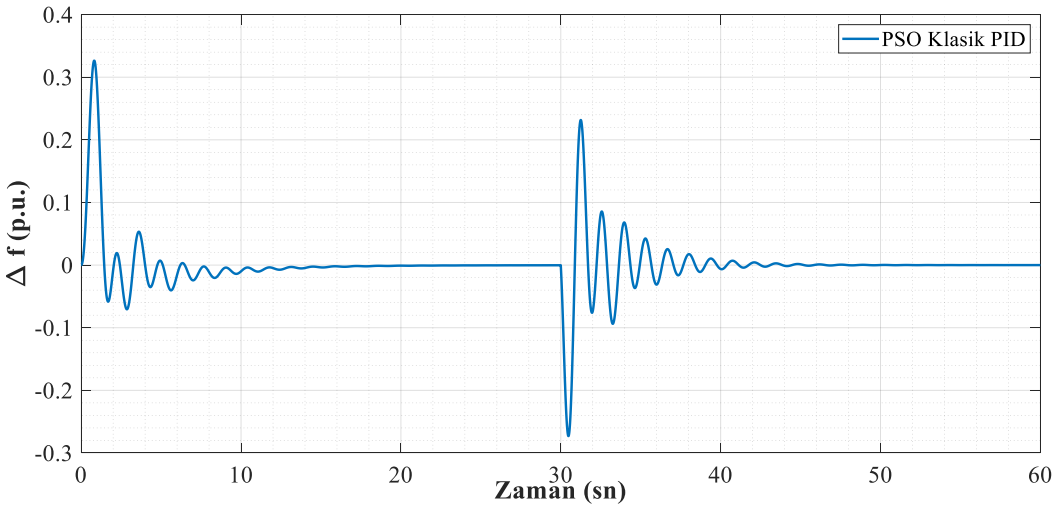

Şekil 5. PSO klasik PID için frekansın zamana göre değişimi

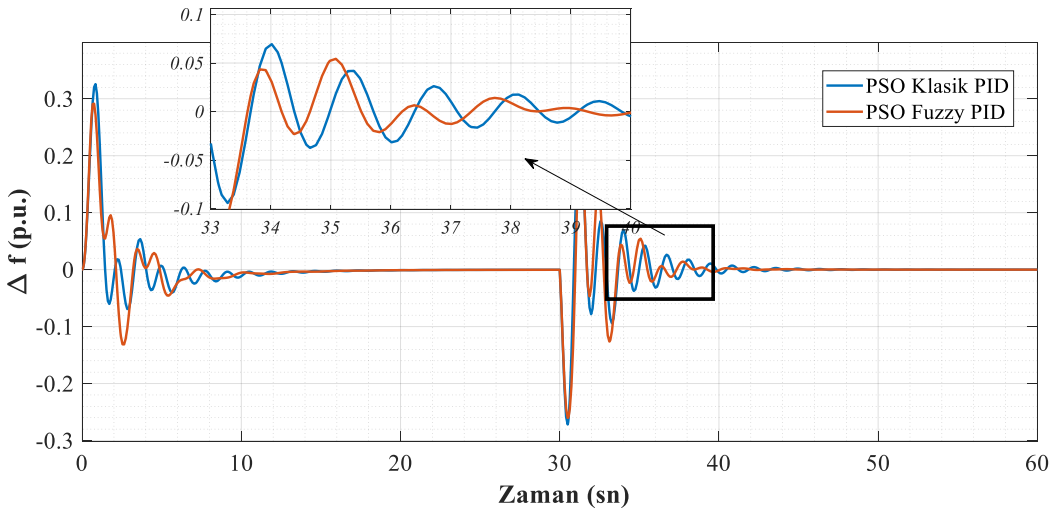

Şekil 6. PSO klasik PID ve fuzzy PID için frekansın zamana göre değişimi

Çizelge 4. PSO için Klasik PID ve Fuzzy PID kontrolörler ile elde edilen performans verilerinin karşılaştırılması

Kontrolör	***Tepe değeri***	***Yerleşme zamanı***	***ITAE***	***Sürekli durum hatası***
Klasik PID	0.2731	40.92	17.8984	0.0073
Fuzzy PID	0.2637	38.05	17.4987	0.002

Çizelge 4.'de Klasik PID kontrolöre sahip mikro şebeke sistem ile Fuzzy PID kontrolöre sahip mikro şebeke sistemlerde frekans değişimi için hesaplanan performans verilerine ait değerler verilmiştir. Burada tepe değeri, yerleşme zamanı ve sürekli durum hata değeri 30. sn'de gerçekleştirilen yük değişimi sonrasına ait değerlerdir. ITAE değeri ise t=0'dan simülasyon sonuna kadar süredeki hataya aittir. Yerleşme zamanı, frekans yanıtının sürekli durum değerinin belirli bir yüzdesine ulaşması için geçen süreyi ifade eder ve bu değerin küçük olması sistemin dinamik yanıtının daha iyi olduğunu göstermektedir. Tepe değeri, yanıtın sürekli durum değeri ile ulaştığı maksimum değer arasındaki farkı gösterir ve bu değerin de küçük olması istenmektedir. Sürekli durum hatası ise analiz sonunda yanıtın sürekli durum değerinde hata değerini gösterir ve yine bu değerin küçük olması sistemin yanıtının iyi olduğunu göstermektedir. ITAE performans kriter değerleri karşılaştırıldığı zaman Fuzzy PID kontrolöre sahip sistemin ITAE performans kriter

değerinin daha küçük olduğu görülmüştür. Performans kriter değerinin küçük olması bu kontrolöre sahip mikro şebeke sistemin performansının daha iyi olduğunu göstermektedir. Burada elde edilen değerler ayrıca yukarıda açıklanan maksimum aşma ve yerleşme zamanı gibi diğer dinamik analiz sonuçları ile uygundur. Ayrıca sürekli durumdaki hata değerleri karşılaştırıldığı zaman Fuzzy PID kontrolör kullanılması durumunda daha düşük bir sürekli durum hatası elde edildiği görülmektedir. Yukarıda gösterilen veriler sonucunda mikro şebeke sistemde PSO ile parametre değerleri belirlenen Klasik PID ve Fuzzy PID kontrolörlerin kullanımı açısından Fuzzy PID kontrolör kullanımının sistemde daha iyi bir dinamik yanıt sağlayacağı sonucuna varılmıştır. Bulanık mantık kullanan Fuzzy PID kontrol şemasındaki çevrimiçi kazanç modifikasyonu nedeniyle, oransal, integral ve türev terimlerinin kazanç faktörü, kontrolörün daha iyi performans göstermesini sağlayacak şekilde her örnekleme zamanında güncellenir. Buradaki analiz sonuçlarından, Fuzzy PID kontrolörünün bu çalışmada verilen mikro şebeke sistemin YFK için daha uygun olduğu rahatlıkla söylenebilir.

3.2 LŞA ile Optimize Edilen Klasik PID ve Fuzzy PID Kontrolör

Bu bölümde biyoyenilebilir mikro şebeke sistemin YFK için kullanılan kontrolörlerin parametre değerlerinin belirlenmesinde LŞA kullanılmıştır. Yapılan analizlere ait elde edilen sonuçlar yukarıda verilen bölüme uygun şekilde LŞA için de gerçekleştirilmiştir. Çizelge 5 de kontrolörlere ait parametre değerleri verilirken Çizelge 6'da ITAE performans kriteri için elde edilen sonuçlar verilmiştir.

Çizelge 5. LŞA için Kontrolör 1 ve 2 ye ait parametre değerleri

Kp1	0.65980542	1. kontrolör Kp değeri
Ki1	1.54979079	1. kontrolör Ki değeri
Kd1	0.90730012	1. kontrolör Kd değeri
Kp2	1.54664092	2. kontrolör Kp değeri
Ki2	5.78725279	2. kontrolör Ki değeri
Kd2	-6.99802265	2. kontrolör Kd değeri

Şekil 7 ve 8'de verilen frekansın zamana göre değişimleri karşılaştırıldığı zaman genel olarak Fuzzy PID kontrolör bulunan sistemin frekans yanıtı dinamik olarak daha iyi sonuç verdiği görülmektedir. Şekiller incelendiğinde Fuzzy PID kontrolörlü sistemin hem maksimum aşma yönünden hem de sürekli duruma erişme zamanı açısından daha iyi bir performans sergilediği görülmektedir.

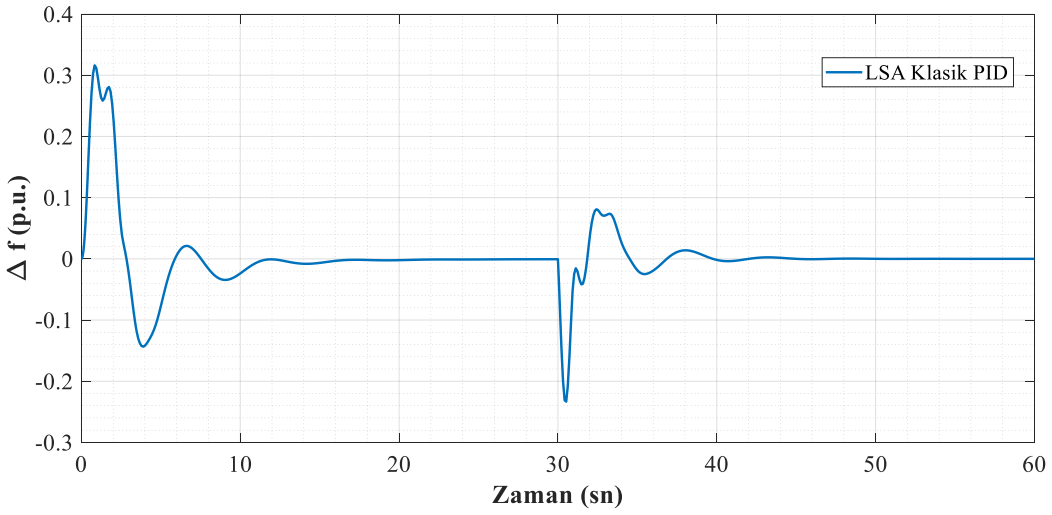

Şekil 7. LŞA Klasik PID için frekansın zamana göre değişimi

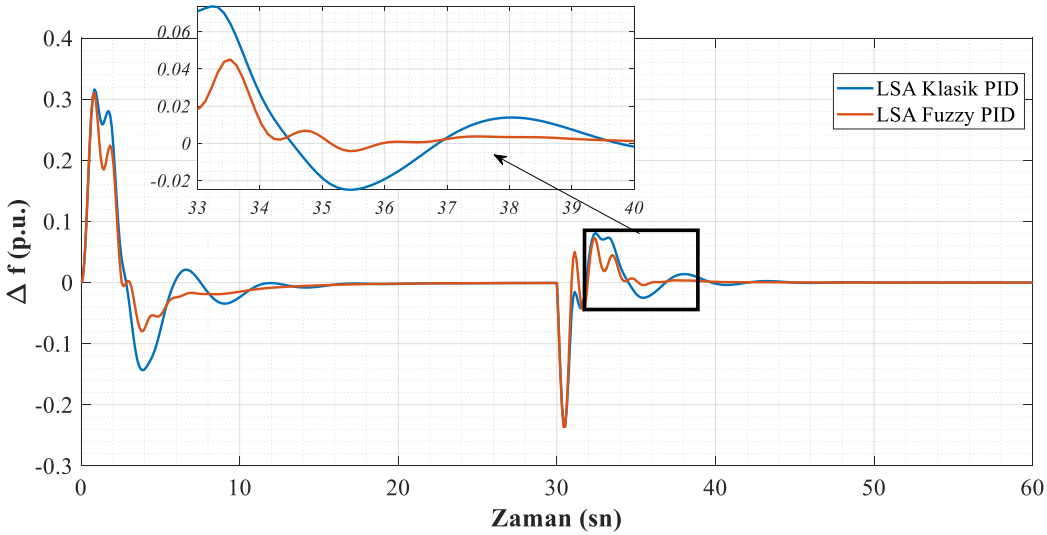

Şekil 8. LŞA Klasik PID ve fuzzy PID için frekansın zamana göre değişimi

Çizelge 6. LŞA için Klasik PID ve Fuzzy PID kontrolörler ile elde edilen performans verilerinin karşılaştırılması

Kontrolör	*Tepe değeri*	*Yerleşme zamanı*	*ITAE*	*Sürekli durum hatası*
Klasik PID	0.2333	39.2628	15.9513	0.0004
Fuzzy PID	0.2362	34.92	11.3876	0.00006

Çizelge 6.'da Klasik PID kontrolöre sahip mikro şebeke sistem ve Fuzzy PID kontrolöre sahip mikro şebeke sistemlerde frekans değişimi için hesaplanan performans verilerine ait değerler verilmiştir. Klasik PID ve Fuzzy PID kontrolöre sahip sistemlere ait ITAE performans kriter değerleri karşılaştırıldığı zaman Fuzzy PID kontrolöre sahip sistemin ITAE performans kriter değerinin daha küçük olduğu görülmüştür. Burada Fuzzy PID kontrolör yapısı kullanılması maksimum aşma yönünden klasik PID kontrolöre göre daha kötü bir performansa sahip iken yerleşme zamanı açısından sisteme önemli bir iyileştirme gerçekleştirmiştir. Ayrıca sürekli durum hatası değerleri incelendiği zaman sistemde bu açıdan da Fuzzy PID kontrolör yapısının kullanılması önemli bir iyileştirme sağlamıştır. Yukarıda elde edilen veriler sonucunda mikro şebeke sistemde LŞA ile parametre değerleri belirlenen Klasik PID ve Fuzzy PID kontrolörlerin kullanımı açısından Fuzzy PID kontrolör kullanımının sistemde daha iyi bir dinamik yanıt sağlayacağı sonucuna varılmıştır.

3.3 KKA ile Optimize Edilen Klasik PID ve Fuzzy PID Kontrolör

Bu bölümde biyoyenilebilir mikro şebeke sistemin YFK için kullanılan kontrolörlerin parametre değerlerinin belirlenmesinde KKA kullanılmıştır. Yapılan analizlere ait elde edilen sonuçlar yukarıda verilen bölüme uygun şekilde KKA için de gerçekleştirilmiştir. Çizelge 7'de kontrolörlere ait parametre değerleri verilirken Çizelge 8'de ITAE performans kriteri için elde edilen sonuçlar verilmiştir.

Çizelge 7. KKA için Kontrolör 1 ve 2 ye ait parametre değerleri

Kp1	1.24242424	1. kontrolör Kp değeri
Ki1	2	1. kontrolör Ki değeri
Kd1	0.75757575	1. kontrolör Kd değeri
Kp2	2	2. kontrolör Kp değeri
Ki2	2	2. kontrolör Ki değeri
Kd2	-1	2. kontrolör Kd değeri

Şekil 9 ve 10'da verilen frekansın zamana göre değişimleri karşılaştırıldığı zaman genel olarak Fuzzy PID kontrolör bulunan sistemin frekans yanıtı dinamik olarak daha iyi sonuç verdiği görülmektedir. Şekiller incelendiğinde Fuzzy PID kontrolörlü sistemin hem maksimum aşma yönünden hem de sürekli duruma erişme zamanı açısından daha iyi bir performans sergilediği görülmektedir.

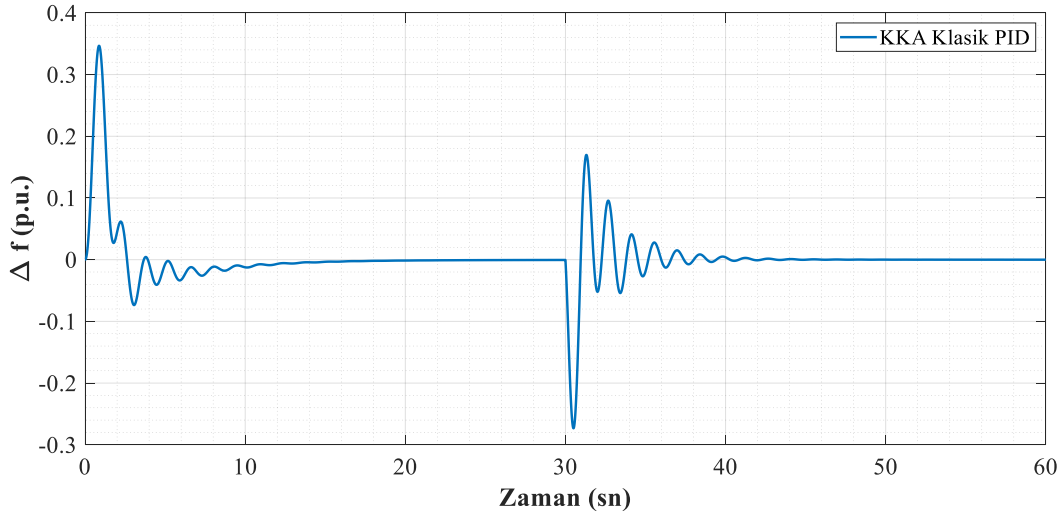

Şekil 9. KKA Klasik PID için frekansın zamana göre değişimi

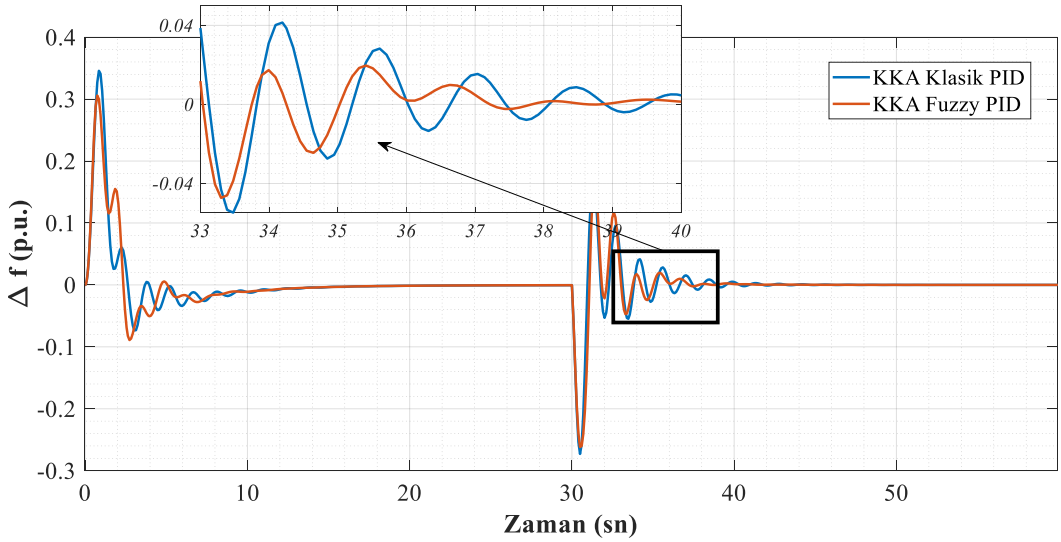

Şekil 10. KKA Klasik PID ve fuzzy PID için frekansın zamana göre değişimi

Çizelge 8. KKA için Klasik PID ve Fuzzy PID kontrolörler ile elde edilen performans verilerinin karşılaştırılması

Kontrolör	*Tepe değeri*	*Yerleşme zamanı*	*ITAE*	*Sürekli durum hatası*
Klasik PID	0.2733	38.64	15.1015	0.0021
Fuzzy PID	0.2604	36.95	14.6865	0.00026

Çizelge 8.'de Klasik PID kontrolöre sahip mikro şebeke sistem ve Fuzzy PID kontrolöre sahip mikro şebeke sistemlerde frekans değişimi için hesaplanan performans verilerine ait değerler verilmiştir. Klasik PID ve Fuzzy PID kontrolöre sahip sistemlere ait ITAE performans kriter değerleri karşılaştırıldığı zaman Fuzzy PID kontrolöre sahip sistemin ITAE performans kriter değerinin daha küçük olduğu görülmüştür. Burada elde edilen değerler ayrıca yukarıda açıklanan maksimum aşma

ve yerleşme zamanı gibi diğer dinamik analiz sonuçları ile uygundur. Sürekli durum hatası performans değerine göre karşılaştırma yapıldığı zaman Fuzzy PID kontrolör kullanımı sistemi önemli ölçüde iyileştirmektedir. Yukarıda elde edilen veriler sonucunda mikro şebeke sistemde KKA ile parametre değerleri belirlenen Klasik PID ve Fuzzy PID kontrolörlerin kullanımı açısından Fuzzy PID kontrolör kullanımının sistemde daha iyi bir dinamik yanıt sağlayacağı sonucuna varılmıştır.

3.4 PSO, LŞA ve KKA için Klasik ve Fuzzy PID Kontrolör Yanıtlarının Karşılaştırılması

Biyoyenilebilir mikro şebeke sistemi, ITAE maliyet fonksiyonu kullanılarak hem Klasik PID kontrolör hem de Fuzzy PID kontrolör durumları için 3 farklı optimizasyon algoritması ile ayrı ayrı optimize edilmiştir. Bu bölümde bu işlemlere ait elde edilen şekiller ve değerler verilmiştir. Burada çizelge 9 ve 10'daki tepe değeri, yerleşme zamanı ve sürekli durum hata değerleri 30. sn'de gerçekleştirilen yük değişimi sonrasına ait değerlerdir. ITAE değeri ise t=0'dan simülasyon sonuna kadar süredeki hataya aittir.

Çizelge 9. Klasik PID için LŞA, KKA ve PSO ile elde edilen performans verilerinin karşılaştırılması

Optimizasyon yöntemi	*Tepe değeri*	*Yerleşme zamanı*	*ITAE*	*Sürekli durum hatası*
LŞA	0.2333	39.2628	15.9513	0.0004
KKA	0.2733	38.64	15.1015	0.0021
PSO	0.2731	40.92	17.8984	0.0073

Çizelge 9'da mikro şebeke sistemde YFK işleminin bir klasik PID kontrolör tarafından gerçekleştirildiği duruma ait performans veri değerleri verilmiştir. Çizelge 9'un verileri incelendiği zaman en iyi maliyet değeri KKA için elde edilirken en kötü sonuç PSO algoritmasında elde edilmiştir. En iyi tepe ve sürekli durum hata değeri LŞA ile elde edilirken en iyi yerleşme zamanı değeri ise KKA ile elde edilmiştir.

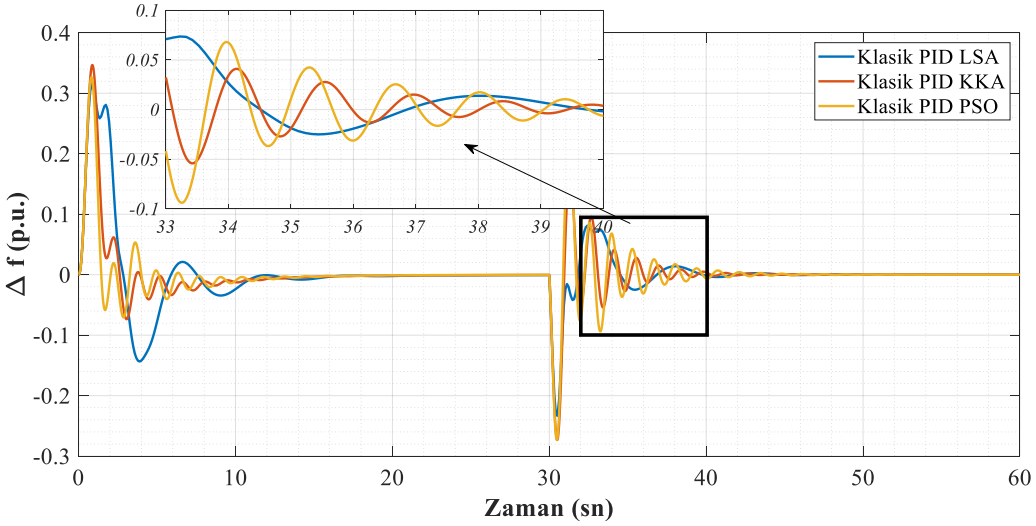

Şekil 11. Klasik PID LŞA, KKA ve PSO için frekansın zamana göre değişimi

Şekil 11'de 3 farklı optimizasyon yöntemleri ile parametre değerleri optimize edilen klasik PID kontrolör için mikro şebekenin frekansının zamana göre değişimi gösterilmiştir. Şekil incelendiğinde ilk 10 sn. lik frekans değişimi esnasında her ne kadar LŞA ile optimize edilmiş sistemin frekans

değişimi negatif yönde büyük bir aşma gerçekleştirmişse de genel olarak sistemin daha az salınıma sahip olması ve özellikle 30. sn'de meydana gelen yük değişimi sonrası göstermiş olduğu daha iyi bir dinamik cevap nedeniyle PSO'ya göre daha düşük bir ITAE performans değerine sahiptir. Şekilde ayrıca KKA ve PSO ile optimize edilen sistemler için frekans değişimleri incelendiği zaman elde edilen sonuçların Çizelge 9 değerleri ile uygun olduğu görülmektedir. Şekil 11'de görüleceği üzere klasik PID kontrolörler KKA algoritması ile elde edilen değerlere sahip iken en iyi dinamik zaman yanıtına sahiptir.

Çizelge 10. Fuzzy PID için LŞA, KKA ve PSO ile elde edilen performans verilerinin karşılaştırılması

Optimizasyon yöntemi	***Tepe değeri***	***Yerleşme zamanı***	***ITAE***	***Sürekli durum hatası***
LŞA	0.2362	34.92	11.3876	0.00006
KKA	0.2604	36.95	14.6865	0.00026
PSO	0.2637	38.05	17.4987	0.002

Çizelge 10'da mikro şebeke sistemde YFK işleminin bir Fuzzy PID kontrolör tarafından gerçekleştirildiği duruma ait ITAE performans kriter değerleri verilmiştir. Çizelge 10'un verileri incelendiği zaman en iyi maliyet değeri LŞA için elde edilirken en kötü sonuç PSO için elde edilmiştir. En iyi tepe, sürekli durum hata değeri ve yerleşme zamanı değeri LŞA ile elde edilmiştir.

Şekil 12'de 3 farklı optimizasyon yöntemleri ile parametre değerleri optimize edilen Fuzzy PID kontrolör için mikro şebekenin frekansının zamana göre değişimi gösterilmiştir. Şekil incelendiği zaman hem ilk 10 sn. lik frekans değişimi esnasında hem de 30. sn'de meydana gelen yük değişimi sonrasında en iyi dinamik cevap LŞA ile optimize edilen sisteme aittir. Şekilde ayrıca KKA ve PSO ile optimize edilen sistemler için frekans değişimleri incelendiği zaman elde edilen sonuçların Çizelge 10 değerleri ile uygun olduğu görülmektedir. Şekil 12'de görüleceği üzere Fuzzy PID kontrolör LŞA ile elde edilen değerlere sahip iken en iyi dinamik zaman yanıtına sahiptir.

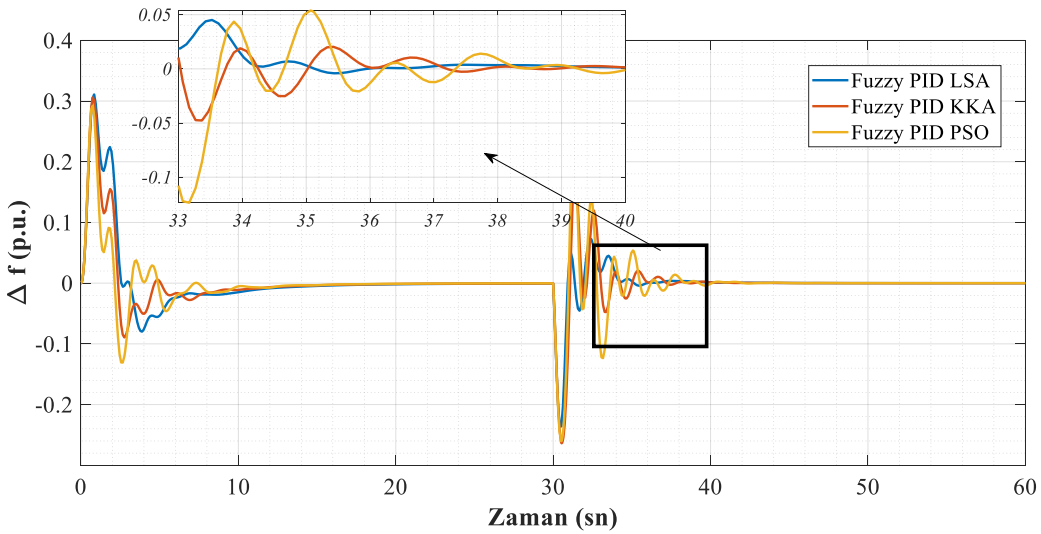

Şekil 12. Fuzzy PID LŞA, KKA ve PSO için frekansın zamana göre değişimi

4. SONUÇ

Yapmış olduğumuz bu çalışmada biyoyenilenebilir enerji tabanlı mikro şebekelerde YFK için klasik PID kontrolör ile fuzzy PID kontrolör sonuçları karşılaştırılarak incelenmiştir. Bu çalışmada, klasik PID kontrolör ve fuzzy PID kontrolörün en uygun parametre değerlerinin belirlenmesi için

LŞA, KKA ve PSO algoritmaları kullanılmıştır. Farklı optimizasyon algoritmaları ile en uygun parametre değerlerinin belirlenmesi için ITAE maliyet fonksiyonundan yararlanılmıştır. Çalışmada elde edilen sonuçlara göre, klasik PID ve fuzzy PID kontrolöre sahip sistemlerin frekans yanıtları karşılaştırıldığında 3 farklı optimizasyon algoritması için fuzzy PID kontrolör daha iyi sonuçlar vermiştir. Bu sonuçlar hem frekansın zamana göre değişimleri hem de performans veri değerleriyle gösterilmiştir. Fuzzy PID kontrol yapısı klasik PID kontrol yapısına göre LŞA ile elde edilen kontrolör parametre değerleri durumunda ITAE performans kriterinde %28,61, PSO optimizasyon değerleri için %2.23 ve KKA optimizasyon değerleri için %2.74 oranında daha iyi sonuçlar elde edilmesini sağlamıştır. Fuzzy PID kontrol yapısının bulanık mantık sistemi, çevrimiçi kazanç ayarlama mekanizması aracılığıyla kontrolör performansını artırmaktadır. Ayrıca çalışma sonuçlarında fuzzy PID kontrolörün parametre değerlerini ayarlamak için en uygun optimizasyon algoritmasının LŞA olduğu belirlenmiştir.

5. ÇIKAR ÇATIŞMASI

Yazarlar, bilinen herhangi bir çıkar çatışması veya herhangi bir kurum/kuruluş ya da kişi ile ortak çıkar bulunmadığını onaylamaktadırlar.

6. YAZAR KATKISI

Dursun ÖZÜRK, çalışmanın kavramsal ve tasarım süreçlerinin belirlenmesi ve yönetimi, veri toplama, veri analizi ve yorumlama, makale taslağının oluşturulması, fikirsel içeriğin eleştirel incelenmesi ve son onay ve tam sorumluluk, Burak YILDIRIM, çalışmanın kavramsal ve tasarım süreçlerinin belirlenmesi ve yönetimi, makale taslağının oluşturulması, fikirsel içeriğin eleştirel incelenmesi ve son onay ve tam sorumluluk, Gizem DOĞAN, çalışmanın kavramsal ve tasarım süreçlerinin yönetimi, veri toplama, veri analizi ve yorumlama, fikirsel içeriğin eleştirel incelenmesi ve son onay ve tam sorumluluk kısmında katkıda bulunmuştur.

7. KAYNAKLAR

Al-Dhaifallah M., Kanagaraj N., Nisar K. S., Fuzzy Fractional-Order PID Controller for Fractional Model of Pneumatic Pressure System. Mathematical Problems in Engineering 2018, 5478781, 2018.

Barik A. K., Das D. C., Active power management of isolated renewable microgrid generating power from Rooftop solar arrays, sewage waters and solid urban wastes of a smart city using Salp swarm algorithm, Technologies for Smart-City Energy Security and Power (ICSESP), Bhubaneswar, India, March 28-30, 2018, pp: 1-6.

Barik A. K., Das D. C., Muduli R., Demand Response Supported Optimal Load-Frequency Regulation of Sustainable Energy based Four-Interconnected Unequal Hybrid Microgrids, 2019 IEEE International Conference on Sustainable Energy Technologies and Systems (ICSETS), Bhubaneswar, India, March 26-01, 2019, pp: 273-278.

Barik A. K., Das, D.C., Expeditious frequency control of solar photovoltaic/biogas/biodiesel generator based isolated renewable microgrid using grasshopper optimisation algorithm, IET Renewable Power Generation 12(14), 1659-1667, 2018.

Barik A. K., Das D.C., Coordinated regulation of voltage and load frequency in demand response supported biorenewable cogeneration-based isolated hybrid microgrid with quasi-oppositional

selfish herd optimization, International Transactions on Electrical Energy Systems 30(1), 12176, 2020.

Baykal N., Beyan T., Bulanık Mantık İlke ve Temelleri, Bıçaklar Kitabevi, Ankara, 2004.

Bevrani H., Habibi F., Babahajyani P., Watanabe M., Mitani Y., Intelligent frequency control in an AC microgrid: Online PSO-based fuzzy tuning approach, IEEE Transactions Smart Grid 3(4), 1935-1944, 2012

Bingöl H., Alataş B., Metasezgisel Optimizasyon Tekniklerine Spor Tabanlı Yeni Bir Yaklaşım: Lig Şampiyonası Algoritması, Fırat Üniversitesi Fen Bilimleri Dergisi 27(1): 1-11, 2015.

Dorigo M., Gambardella L. M., Ant Colonies for the Travelling Salesman Problem, Biosystems, 43 (2), 73-81, 1997.

Dorigo M., Dicaro G., Gambardella L. M., Ant Algorithms for Discrete Optimization, in Artificial Life 5(2), 137-172, 1999.

Elkawafi S., Khalil A., Elgaiyar AI., Wang J., Delay-dependent stability of LFC in Microgrid with varying time delays, 22nd International Conference on Automation and Computing (ICAC), Colchester, UK, September 07-08, 2016, pp: 354-359.

Husseinzadeh K. A., League Championship Algorithm: A New Algorithm for Numerical Function Optimization, International Conference of Soft Computing and Pattern Recognition, Malacca, Malaysia, December 04-07, 2009, pp: 43-48.

Karaboga D., An idea based on honeybee swarm for numerical optimization, Technical ReportTR06, Erciyes University, Engineering Faculty, Computer Engineering Department, 2005.

Kennedy J., Eberhard R. C., Particle swarm optimization, Proceedings of ICNN'95 - International Conference on Neural Networks, Perth, WA, Australia, November 27-01, 1995, pp: 1942-1948.

Kılıç E., Özdemir M. T., Güç Sistemlerindeki Optimum Otomatik Gerilim Regülasyonu için Çoklu Amaç Fonksiyonunun Belirlenmesi, Dicle Üniversitesi Mühendislik Fakültesi Mühendislik Dergisi 10(1), 1-12, 2019.

Kocaman B., Mikro Şebekeler İçin Örnek Bir Enerji Yönetimi Uygulaması, BEÜ Fen Bilimleri Dergisi, 3(1), 35-52, 2014.

Mordjaoui M., Haddad S., Medoued A., Laouafi A., Electric load forecasting by using dynamic neural network. International Journal of Hydrogen Energy 42(28), 17655-17663, 2017.

Özdemir M. T., Öztürk D., Comparative performance analysis of optimal PID parameters tuning based on the optics inspired optimization methods for automatic generation control. Energies 10(12), 2134, 2017.

Özdemir M. T., Yıldırım B., Gülan H., Gençoğlu M. T., Automatic generation control in an AC isolated microgrid using the league championship, Fırat Üniversitesi Mühendislik Bilimleri Dergisi 29(1), 109-120, 2017.

Parmar K. P. S., Majhi S., Kothari D. P., Load Frequency Control of a realistic power system with multi-source power generation. International Journal of Electirical Power &Energy Systems 42(1), 426-433, 2012.

Subramanyam M. V., Satyaprasad K., Gopi Krishna Rao P. V., Study on PID Controller Design and Performance Based on Tuning Techniques, International Conference on Control, Instrumentation, Communication and Computational Technologies (ICCICCT), Kanyakumari, India, July 10-11, 2014, pp:1411-1417.

Tucho G.T., Nonhebel S., Alternative energy supply system to a rural village in Ethiopia, Energy Sustainability and Society 7:33, 2017.

Yıldırım B., Bir Mikro Şebekenin Yük Frekans Kontrolü İçin Tamsayı Derece Yaklaşımlı Kesir Dereceli PID Kontrolörün Optimizasyonu. DÜMF Mühendislik Dergisi 12(1), 79-87, 2021.

Yıldırım B., Advanced controller design based on gain and phase margin for microgrid containing PV/WTG/Fuel cell/Electrolyzer/BESS, International Journal of Hydrogen Energy 46(30), 16481-16493, 2021.

Yıldırım B., Gheisarnejad M., Khooban M. H., Delay-Dependent Stability Analysis of Modern Shipboard Microgrids, IEEE Transactions on Circuits and Systems-I: Regular Papers 68(4), 1693-1705, 2021.

JOURNAL of
MATERIALS and MECHATRONICS:A

e-ISSN 2717-8811
JournalMM, 2022, 3(2), 225-239
https://doi.org/10.55546/jmm.1094815

Araştırma Makalesi / Research Article

FPGA Tabanlı LogSig ve TanSig Transfer Fonksiyonlarının IQ-Math Sayı Standardında Tasarımı ve Gerçeklenmesi

Mehmet Şamil AKÇAY[1]*, İsmail KOYUNCU[2], Murat ALÇIN[3], Murat TUNA[4]

[1] Afyon Kocatepe Üniversitesi, Teknoloji Fakültesi, Elektrik Elektronik Mühendisliği Bölümü, Afyonkarahisar, Türkiye, ORCID ID: https://orcid.org/0000-0003-1603-8903, msakcay@usr.aku.edu.tr
[2] Afyon Kocatepe Üniversitesi, Teknoloji Fakültesi, Elektrik Elektronik Mühendisliği Bölümü, Afyonkarahisar, Türkiye, ORCID ID: https://orcid.org/0000-0003-4725-4879, ismailkoyuncu@aku.edu.tr
[3] Afyon Kocatepe Üniversitesi, Teknoloji Fakültesi, Mekatronik Mühendisliği Bölümü, Afyonkarahisar, Türkiye, ORCID ID: https://orcid.org/0000-0002-2874-7048, muratalcin@aku.edu.tr
[4] Kırklareli Üniversitesi, Teknik Bilimler Meslek Yüksekokulu, Elektrik Bölümü, Kırklareli, Türkiye, ORCID ID: https://orcid.org/0000-0003-3511-1336, murat.tuna@klu.edu.tr

Geliş/ Received: 28.03.2022; **Kabul / Accepted:** 09.09.2022

ÖZET: Yapay Sinir Ağları (YSA), günümüzde sinyal işleme, optimizasyon, tahmin, karar verme ve kontrol gibi bir çok mühendislik alanında yoğun şekilde kullanılmaktadır. YSA yapılarının çalışmasını doğrudan etkileyen önemli bölümlerinden birisi de Transfer Fonksiyonlarıdır (TF). Doğrusal olmayan TF tasarımlarının gerçek zamanlı tasarımı üstel fonksiyon içerdiğinden oldukça zor bir şekilde gerçekleştirilmektedir. Bu çalışmanın ilk aşamasında, literatürdeki çalışmalardan farklı olarak doğrusal olmayan Logaritmik Sigmoid (LogSig) ve Tanjant Sigmoid (TanSig) TF, 32-bit (16I-16Q) IQ-Math formatında VHDL dilinde tasarlanmıştır. İkinci aşamada, VHDL dilinde FPGA çiplerinde çalışmak üzere örnek bir üç giriş-üç çıkışlı bir YSA (ileri beslemeli) yapısı 32-bit IQ-Math formatında modellenmiştir. Tasarımın gizli katmanında 8 adet nöron, gizli katmanda LogSig ile TanSig TF ve çıkış katmanında ise PureLin TF kullanılmıştır. Örnek YSA tasarımı iki farklı TF tasarımı için ayrı bir testbench dosyası oluşturulmuş ve bu tasarımlar VHDL ile Xilinx ISE DS programı ile test edilmiştir. Elde edilen simülasyon sonuçlarına göre nümerik tabanlı LogSig ve TanSig TF içeren YSA tasarımları için MSE ve RMSE hata analizleri yapılarak sonuçlar sunulmuştur. Ardından her bir tasarım XC7K70T-3FBG676 FPGA (Kintex-7) için sentezlenerek Place-Route prosesi gerçekleştirilmiştir. Place-Route prosesinden elde edilen FPGA çip kaynak kullanımı istatistikleri sunulmuştur. Tasarımlara ait hata analizi sonuçlarına göre YSA-LS (LogSig-tabanlı YSA) tasarımı 8.86E-06 MSE ve YSA-TS (TanSig-tabanlı YSA) tasarımı 7.92E-02 MSE sonuçları elde edilmiştir. Bu çalışmadan elde edilen sonuçlar ile IQ-Math tabanlı LogSig ve TanSig aktivasyon fonksiyonu tasarımlarının gerçek zamanlı YSA uygulamalarında güvenli bir şekilde kullanılabileceği gösterilmiştir.

Anahtar Kelimeler: Transfer Fonksiyonları, IQ-Math Sayı Standardı, YSA, FPGA, VHDL, LogSig, TanSig.

*Sorumlu yazar / Corresponding author: muratalcin@aku.edu.tr

Bu makaleye atıf yapmak için /To cite this article

Akçay, M. Ş., Koyuncu, İ., Alçın, M., Tuna, M. (2022). FPGA Tabanlı LogSig ve TanSig Transfer Fonksiyonlarının IQ-Math Sayı Standardında Tasarımı ve Gerçeklenmesi. Journal of Materials and Mechatronics: A (JournalMM), 3(2), 225-239.

Design and Implementation of FPGA Based LogSig and TanSig Transfer Functions in IQ-Math Number Standard

ABSTRACT: Artificial Neural Networks (ANNs) have been used extensively in engineering fields where many processes such as optimization, prediction, signal processing, decision making and control today. Transfer Functions (TF) used in these operations affect directly the output of the result by affecting the ANN structure. In the first stage of this study, apart from the studies in the literature, non-linear LogSig and TanSig TF have been coded using VHDL in accordance with the 32-bit (16I-16Q) IQ-Math standard. The exponential function e^n, which is common to these two TF structures, has been designed using the CORDIC-LUT approach. In the second stage, an FPGA-based sample three-input-three-output ANN has been performed. 8 neurons have been used in the hidden layer of this design. LogSig and TanSig TF have been used in the hidden layer and PureLin TF has been used in the output layer. The sample ANN has been coded using VHDL with 32-bit IQ-Math standard for two different TF. A separate testbench file has been created for each design, and all these designs have been tested using VHDL with the Xilinx ISE DS. For the simulation results obtained, MSE and RMSE error analyzes were performed using numerical-based LogSig-TanSig TF and ANN designs, and the results were presented. Then, each design has been synthesized for the XC7K70T-3FBG676 FPGA (Kintex-7), and the chip statistics have been presented by performing the Place-Route process. As a result, ANN-LS (Artificial Neural Networks-LogSig) design produced more successful results with 8.86E-06 MSE and 2.98E-03 RMSE error analysis results. In future studies, real-time ANN applications can be realized on FPGA chips by using these ANN and TF designs.

Keywords: Activation Functions, IQ-Math Number Standard, ANN, FPGA, VHDL, LogSig, TanSig.

1. GİRİŞ

Yapay zekânın alt çalışma alanlarından olan Yapay Sinir Ağları (YSA-(Artificial Neural Networks)) günümüzde görüntü işleme, kaotik osilatör tasarımı, optimizasyon, rasgele sayı üreteci, kontrol, haberleşme ve otomotiv gibi geniş bir alanda yaygın bir şekilde kullanılmaktadır. Bu nedenle mühendislik uygulamalarında bu ağlara yaygın olarak rastlamak mümkündür. Bu ağların kullanıldığı bazı mühendislik uygulamalarına, otomotiv sanayi (Ahmed ve ark., 2015), optik (Mello ve Ventura, 2020), rasgele sayı üreteçleri (Alçın ve ark., 2021), haberleşme (Kaur ve Sivia, 2020), uzay sanayi (Wang ve ark., 2020) ve robotik (Du, 2011) örnek verilebilir.

YSA-tabanlı çalışmalar genellikle yazılımsal ve donanımsal olmak üzere iki ana başlığa ayrılmaktadır (Koyuncu ve ark., 2019). Yazılımsal YSA çalışmaları hız, paralellik ve yoğun matematiksel hesaplamanın çok önemli olduğu gerçek zamanlı YSA uygulamalarında performans açısından yetersiz kalmaktadır. Bu yüzden donanımsal YSA çalışmalarında, FPGA (Field Programmable Gate Array-Alan Programlanabilir Kapı Dizileri), ASIC (Application Specific Integrated Circuit-Uygulamaya Özel Tümleşik Devre) ve GPU (Graphic Processor Unit-Grafik İşlemci Birimi) gibi birçok platform kullanılmaktadır. Bu platformlar içerisinde FPGA çipleri düşük güç tüketimi, yüksek çalışma frekansları, tekrar tekrar programlanabilme, hızlı ilk prototipleme, paralel çalışma ve esneklik gibi önemli avantajları bir araya getirmektedir. FPGA platformları bu avantajları sayesinde YSA uygulamalarında gerekli olan yüksek hız ve yüksek performansı sağlamaktadır (Akçay ve ark., 2020).

Literatürde FPGA platformlarında yapılan YSA çalışmalarında, Şahin ve Koyuncu tarafından LogSig (**Log**arithmic **Sig**moid), TanSig (**Tan**gent **Sig**moid) ve RadBas (**Rad**ial **Bas**is) Transfer Fonksiyonları (TF) kullanılarak FPGA-tabanlı 32-bitlik IEEE 754-1985 kayan noktalı standardında

YSA tasarımı gerçekleştirmişlerdir. Sunulan çalışmada, FPGA çipinde 10 ya da daha fazla nörona sahip bir YSA tasarımının kolaylıkla uygulanabileceği gösterilmiştir (Sahin ve Koyuncu, 2012).

Adetiba ve arkadaşları, FPGA tabanlı olarak Çok Katmanlı Perseptron YSA (Multi-Layer Perceptron-Artificial Neural Networks-MLP-ANN) yapısını gerçekleştirmişlerdir. TanSig ve LogSig TF kullanılarak nöron test edilmiştir. Sonuçta, TanSig TF ile daha verimli sonuçların alındığı ifade edilmiştir (Adetiba ve ark., 2014).

Gupta ve diğerleri, FPGA yongalarında çalışabilecek ve gömülü uygulamalarda sıklıkla tercih edilen SNN (Spiking Neural Networks) modelini geliştirmişlerdir. Tasarım Xilinx firması Virtex-6 FPGA çipi için gerçeklenmiştir. Sunulan çalışmaya göre 800 nöronlu bir ağ analiz edilebilmektedir (Gupta ve ark., 2020).

Çavuşlu, parçacık sürü optimizasyonu algoritması ile FPGA tabanlı YSA eğitimi uygulaması tasarlamışlardır. Tasarım Altera firmasına ait EP2C35F672C6 FPGA çipi için gerçeklenmiştir. Gerçeklenen yapıda, giriş katmanında 2, gizli katmanda 2 nöron ve çıkış katmanında ise 1 adet nöron bulunmaktadır (Çavuşlu ve ark., 2010).

Jiang ve Kong, FPGA tabanlı ektopik ventriküler atımların sınıflandırılmasına yönelik bir çalışma yapmışlardır. Çalışmada geliştirilebilir blok-tabanlı (Block-based Neural Networks) yapı ile FPGA platformlarında kullanılmak üzere bir sınıflandırıcı tasarımı yapılmıştır. Sonuçta, YSA yapısından % 98.1 oranında bir ağ hassasiyeti elde edilmiştir (Jiang ve Kong, 2007).

Alçın tarafından yapılan çalışmada, Pehlivan-Uyaroglu kaotik sistemi YSA üzerinde çalışmak üzere modellenmiştir. Yapılan YSA-tabanlı tasarım, Xilinx FPGA çipleri üzerinde çalışmak üzere gerçeklenmiştir. Çalışmada son olarak FPGA çipleri üzerinde YSA tabanlı kaotik sistemlerin başarılı bir şekilde modellenebileceği belirtilmiştir (Alçın ve ark., 2016).

Yılmaz tarafından jeotermal enerji destekli hidrojen üretimi sistemine ait ekonomik analiz çalışması gerçekleştirilmiştir. Çalışmada sunulan Çok Katmanlı İleri Beslemeli (Multi-Layer Feed Forward) YSA modelinde 3 giriş ve 3 adet çıkış bulunmaktadır. Tasarımın gizli (hidden) katmanında 8 adet nöron vardır. YSA gizli katmanında TanSig TF kullanılarak tasarıma ait MSE hata analizleri yapılmıştır (Yılmaz ve ark., 2019).

Bu çalışmada, literatürdeki çalışmalardan farklı olarak 32-bit IQ-Math sayı formatında VHDL (**V**ery High Speed Integrated Circuit **H**ardware **D**escription **L**anguage-Çok Yüksek Hızlı Tümleşik Devre Donanımı Tanımlama Dili) ile doğrusal olmayan LogSig ve TanSig TF kodlanmıştır. Daha sonra FPGA tabanlı örnek bir üç giriş-üç çıkışlı bir YSA (ileri beslemeli) yapısı tasarlanmıştır. Tasarlanan YSA yapısında bir adet gizli katman ve bu katmanda 8 adet nöron kullanılmıştır. Yapının gizli katmanına LogSig ve TanSig TF, çıkış katmanına ise doğrusal PureLin TF yerleştirilmiştir. Örnek YSA tasarımı iki farklı TF için 32 bit IQ-Math standardı ile VHDL dilinde kodlanmıştır. İki TF ve örnek YSA tasarımları Xilinx ISE Design Suite 14.7 (X-ISE-DS) ortamında simüle edilerek test edilmiştir. Bu işlemden elde edilen simülasyon sonuçları kullanılarak MSE (Ortalama Karesel Hata-Mean Square Error) ve RMSE (Root Mean Square Error-Kök Ortalama Karesel Hata) hata analizleri yapılmış ve analizlerden elde edilen sonuçlar sunulmuştur. Bu aşamadan sonra tasarlanan YSA yapıları Xilinx firması tarafından geliştirilen Kintex-7 geliştirme kartı üzerinde bulunan XC7K70T FPGA için sentezlenmiştir. Bu işlemden sonra gerçekleştirilen Place-Route prosesinden elde edilen FPGA kaynak kullanımı istatistikleri verilmiştir. Çalışmanın İkinci Bölümünde YSA ve FPGA çiplerinden özet bilgiler ifade edilmiştir. Üçüncü Bölümde FPGA tabanlı LogSig ve TanSig TF tasarımları ile örnek YSA tasarımı sunulmuştur. Dördüncü Bölümde tasarımlardan elde edilen sonuçlar yorumlanarak değerlendirilmiştir.

2. MATERYAL VE YÖNTEM

2.1 Yapay Sinir Ağları

İnsan beyni en kompleks yapıya sahip sistemlerden birisidir. İnsan beyninin muhteşem yapı ve işleyişinin incelenmesi ve matematiksel modellenmesi ile YSA çalışma alanı meydana gelmiştir. YSA'da her giriş verisine kendi ağırlığı ile çarpma işlemi uygulanmakta ve daha sonra toplama fonksiyonunda sonuçlar eşik değeri ile toplanmaktadır. Buradan çıkan sonucun aktivasyon fonksiyonunda işlenmesi ile çıkış bilgisi üretilmektedir. Aktivasyon fonksiyonu sonucu doğrudan etkilemekte ve çıkış bilgisini gerekli sonlu aralıklarda sınırlandırmaktadır. Bu fonksiyonlar YSA uygulamalarında doğrusal veya doğrusal olmayan biçimlerde yaygın olarak tercih edilmektedir. Bu çalışmada kullanılan LogSig TF'ye ait matematiksel eşitlik Eşitlik 1'de ve LogSig TF'ye ait grafik Şekil 1'de verilmiştir.

$$LogSig\ (x) = \frac{1}{1 + e^{-x}} \tag{1}$$

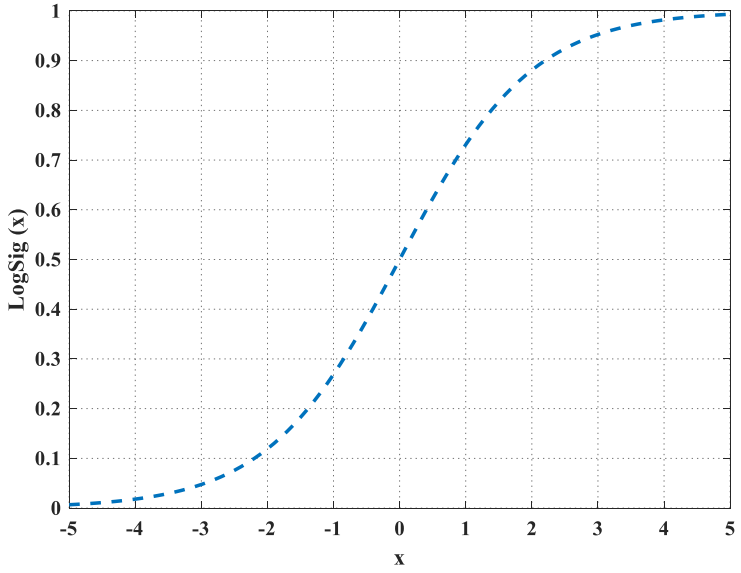

Şekil 1. LogSig TF değişim grafiği

Bu çalışmada kullanılan TanSig TF'ye ait matematiksel eşitlik Eşitlik 2'de ve TanSig TF'ye ait grafik Şekil 2'de verilmiştir.

$$TanSig\ (x) = \frac{2}{1 + e^{-2x}} - 1 \tag{2}$$

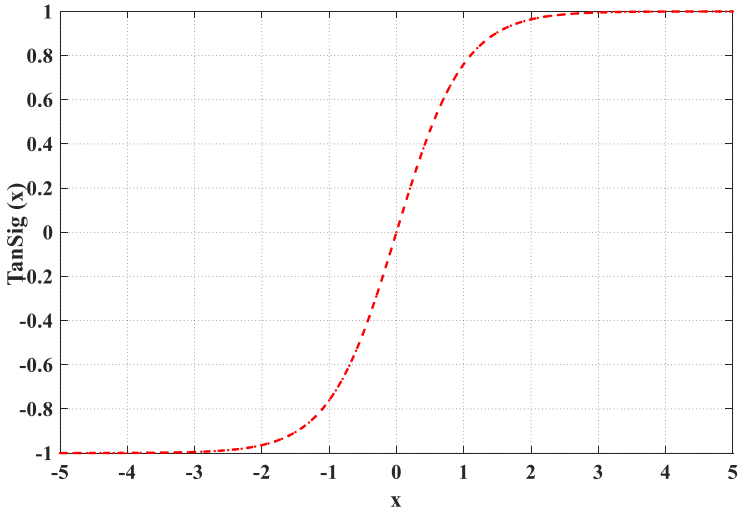

Şekil 2. TanSig TF değişim grafiği

YSA giriş katmanı, gizli katman ya da katmanlar ve çıkış katmanından meydana gelmektedir. Üzerinde çalışılan probleme göre gizli katman ve bu katmandaki nöron sayısı, tercih edilen TF farklılık göstermektedir. Bu çalışmada giriş ve çıkış katmanlarında üçer nöron gizli katmanda ise 8 nöron bulunan ileri beslemeli bir YSA tasarlanmıştır.

2.2 FPGA Çipleri

Günümüzde oldukça popüler sayısal sinyal işleme platformlarından birisi olan FPGA (Alan(da)/Saha(da) Programlanabilir Kapı Dizileri-Field Programmable Gate Array) çiplerinin diğer sayısal platformlara göre düşük güç tüketimi, yüksek çalışma frekansları, tekrar tekrar programlanabilme, hızlı ilk prototipleme, paralel çalışma ve esneklik gibi önemli avantajları bulunmaktadır. Bu nedenle sinyal-görüntü işleme (Paukštaitis ve Dosinas, 2009), modelleme (Tuntas, 2015), kaos (Koyuncu ve ark., 2018), rasgele sayı üretimi (Alçın ve ark., 2019), algoritma hızlandırma (Sahin, 2010), tıp (Abdullah ve Younis, 2019), YSA (Koyuncu ve ark., 2017), robotik (Bargsten ve Fernandez, 2020), modülasyon (Mohammed ve Abdullah, 2020), güvenli haberleşme (Savran, 2017) ve hidrojen üretimi (Yılmaz ve ark., 2019) gibi birçok çalışma alanında bu yongalar sıklıkla kullanılmaktadır. Ayrıca FPGA çipleri System C, VHDL, Handel-C ve Verilog gibi farklı dillerde kodlanabilmektedir. Şekil 3'te Xilinx Kintex-7 FPGA kartı gösterilmiştir.

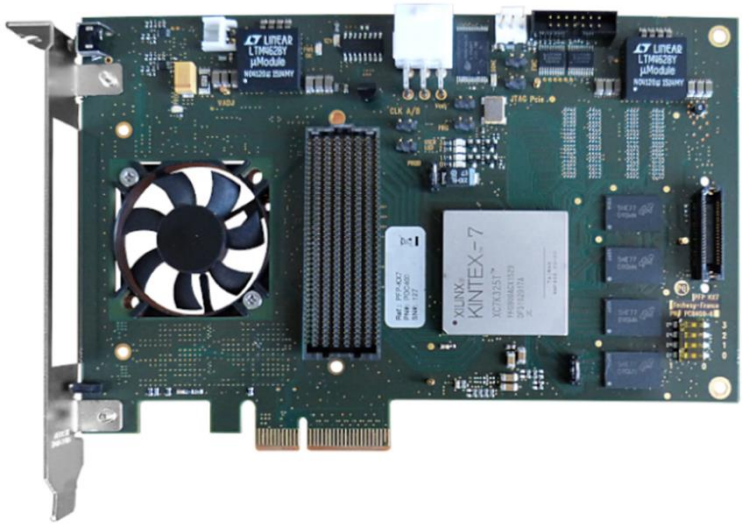

Şekil 3. Xilinx Kintex-7 FPGA kartı

2.3 IQ-Math Sayı Standardı

IQ-Math sabit noktalı sayı standardını işaret biti (S), tam sayı kısmı (integer-I) ve kesirli kısım (fractional-Q) oluşturmaktadır. Kayan noktalı sayılardan farklı olarak bu sayı standardında tam sayı ve kesirli sayı kısımları tasarımcının ihtiyacı doğrultusunda ayarlanabilmektedir. Sabit noktalı sayı standardı Şekil 4'te gösterilmiştir. Bu şekildeki S işaret bitini temsil etmekte ve 0 değerini aldığında ilgili sayı pozitif, 1 değerinde ise negatif olmaktadır. İlgili sayının tam sayı kısmındaki bitleri hesaplamak için sayının tam kısmı ikilik sayı tabanına çevrilmektedir (Erick, 2007, Özkan ve ark., 2011).

İşaret Biti (S)	Tam Sayı Kısmı (I)	Kesirli Kısım (Q)
0 / 1	I_n ..... $I_3I_2I_1I_0$	Q_n ..... $Q_3Q_2Q_1Q_0$

Şekil 4. IQ-Math sabit noktalı sayı formatı gösterimi

3. BULGULAR VE TARTIŞMA

3.1 FPGA Tabanlı TF ve YSA Tasarımları

Sunulan bu çalışmada doğrusal olmayan LogSig ve TanSig TF 32-bit IQ-Math formatında VHDL dilinde FPGA tabanlı olarak tasarlanmıştır. Bu iki TF yapısındaki e^x üstel fonksiyonun FPGA tabanlı olarak gerçekleştirilmesinde CORDIC-LUT (**CO**ordinate **R**otation **DI**gital **C**omputer-**L**ook-**U**p **T**able) ikili yaklaşımları birlikte kullanılmıştır. TF tasarımların X-ISE-DS ortamında her bir tasarıma farklı bir testbench dosyası oluşturularak simülasyonu yapılmıştır. Simülasyon sonuçları kullanılarak MSE ve RMSE hata analizleri yapılmıştır. Bunun ardından tasarımlar Xilinx firmasına ait Kintex-7 FPGA çipi için sentezleme işlemi gerçekleştirilmiştir.

Sentez işleminin ardından Place-Route prosesi gerçekleştirilmiştir. Bu süreç yerleştirme ve yönlendirme işlemlerini kapsamaktadır. Yerleştirme işleminde tasarımın hangi konumdaki kaynaklara yerleştirilmesi ve bu kaynaklar arasındaki bağlantıların nasıl yapılması gerektiği belirlenmektedir. Bu işlemi takiben yönlendirme işleminde FPGA yonga yapısındaki hücrelerin kendi arasındaki ve Giriş/Çıkış blokları arasındaki bağlantılar tanımlanmaktadır. Bu proseste kaynak kullanımı optimize edilmektedir. Diğer bir ifade ile tasarımın FPGA yapısında en dar alana yerleştirilmesi ve bu yerleşimin oluşturacağı toplam bağlantı yolunun en kısa seviyede olması hedeflenmektedir (Lortoğlu 2019). Place-Route prosesinin tamamlanması ile elde edilen FPGA kaynak kullanım oranları sunulmuştur. 32-bit IQ-Math-tabanlı LogSig ve TanSig TF blok şemaları sırası ile Şekil 5 ve 6'da verilmiştir. Bu şekillerde gözlemlenen IEEE-754-1985 kayan noktalı sayı (floating point number standard) ve IQ-Math sayı standardındaki tüm toplayıcı, çıkarıcı, çarpıcı, bölücü ve dönüştürücü gibi üniteler Xilinx Design Tools tasarım araçları tarafından geliştirilen IP CORE Generator kullanılarak otomatik olarak oluşturulmuştur. Şekil 5'te x giriş sinyali negatifleyici ünitesinde negatifleme işlemine tabi tutulup çarpıcı ünitesinde ilgili sayı ile çarpılmaktadır. Ardından dönüştürücü ünitesinde 32 bit değerindeki sinyal 23 bit değerine dönüştürülmektedir. Elde edilen bu sinyal, sayının tam ve kesirli sayı kısmını ifade eden sırasıyla t ve k kısımlarına ayrılmaktadır. Daha sonra t değerine gecikme ünitesinde 25 saat darbesi gecikme işlemi uygulanarak ROM (Read Only Memory) hafızaya iletilmektedir. Bu ünitede ROM hafıza LUT işlevinde kullanılmıştır. ROM hafızaya $e^{t.0.75}$ değerleri t=(-64...+63) tam sayı aralığında olarak önceden hesaplanmış ve kaydedilmiştir. Bu üniteden çıkan sinyal kayan noktalı sayı standardına sahip olduğundan dolayı dönüştürücü ünitesinde IQ-Math sabit noktalı sayı standardına dönüştürülmektedir. Diğer taraftan

girdi sinyalinin kesirli kısmını ifade eden k değeri 2 bit değeri genişletilerek 18 bit olarak çarpıcı ünitesine iletilmektedir. Çarpıcı ünitesinde 0.75 ve k değerleri çarpılarak elde edilen sonuç çıkışa w sinyali olarak aktarılmaktadır. Bu sinyal CORDIC ünitesinde işlenerek çıkıştan IQ-Math sabit noktalı sayı standardına sahip sinh(w) ve cosh(w) değerleri eş zamanlı olarak elde edilmektedir. Ardından toplayıcı ünitesinde sinh(w) ve cosh(w) değerlerine toplama işlemi yapılarak w değerine göre e^{w} değeri hesaplanmaktadır. Hesaplanan bu değer dönüştürücü ünitesinde 20 bit değerinden 32 bit değerine dönüştürülerek gecikme ünitesinde 6 saat darbesi geciktirilmektedir. Bu sayede e^{w} değeri ile $e^{t.0.75}$ değeri senkron olarak çarpıcı ünitesinde işlenmektedir. Çarpım sonucunda çarpma ünitesinden e^{-x} değeri elde edilmektedir. Bu değer toplayıcı ünitesinde 1 sayısı ile toplanarak dönüştürücü ünitesine iletilmektedir. Bu sinyal, dönüştürücü ünitesinde IQ-Math sabit noktalı sayı standardından kayan noktalı sayı standardına dönüştürülmektedir. Daha sonra bölücü ünitesinde 1 sayısı bu değere bölünmektedir. Elde edilen bu sinyal kayan noktalı sayı standardına sahiptir ve dönüştürücü ünitesine iletilerek IQ-Math sabit noktalı sayı standardına dönüştürüldükten sonra LogSig TF çıkışına 32-bit IQ-Math-tabanlı olarak aktarılmaktadır.

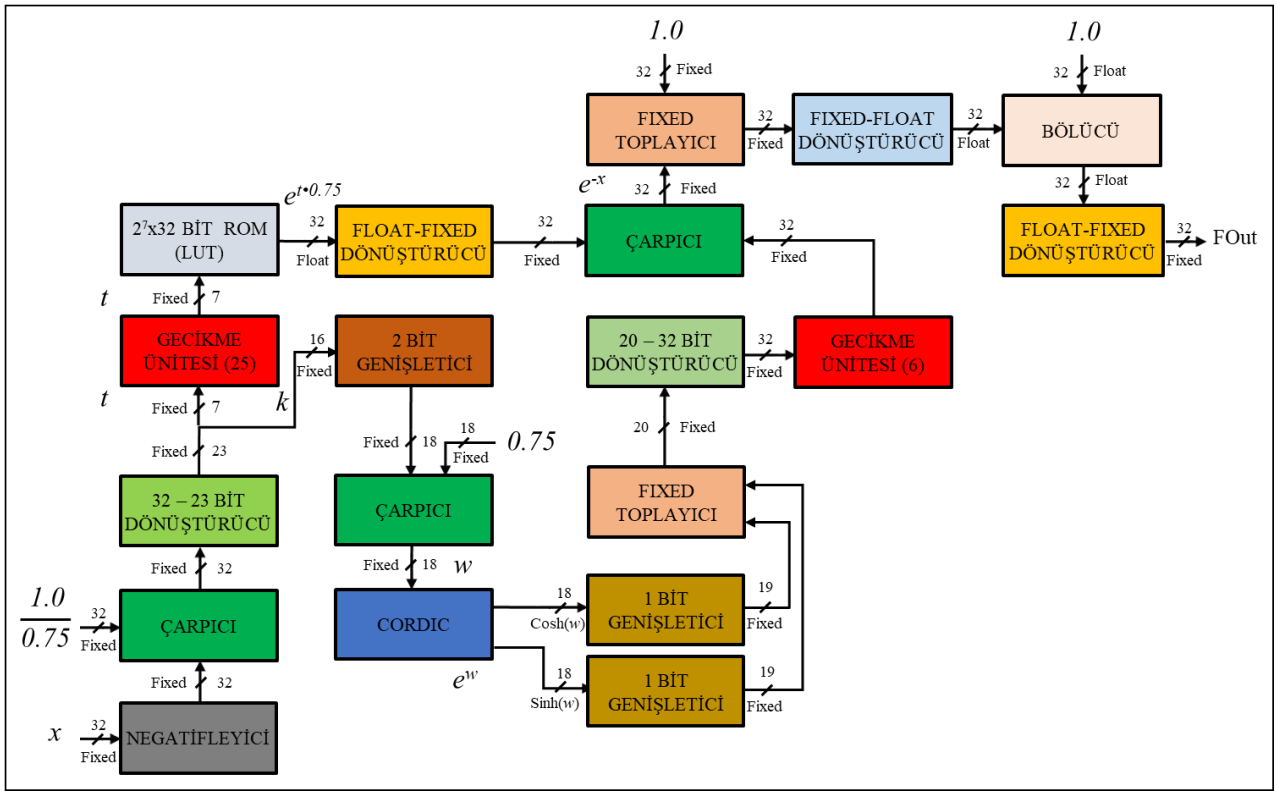

Şekil 5. LogSig fonksiyonun IQ-Math sabit noktalı sayı tabanlı blok şeması

Şekil 6'da 32-bit IQ-Math-tabanlı TanSig TF'nin blok şeması verilmiştir. Şemada çarpıcı ünitesinde x giriş sinyali 2 sayısı ile çarpılmaktadır. Ardından elde edilen sonuç negatifleyici ünitesinde negatifleme işlemine tabi tutulmaktadır. Daha sonra şemada görüldüğü üzere e^{-2x} değerinin elde edildiği çarpıcı ünitesine kadar yapılan işlemler LogSig TF tasarımı ile benzer niteliktedir. Ardından çarpıcı ünitesinden çıkan e^{-2x} değeri toplayıcı ünitesinde 1 sayısı ile toplanmaktadır. Elde edilen sonuç sinyali dönüştürücü ünitesinde IQ-Math sabit noktalı sayı standardından kayan noktalı sayı standardına dönüştürülmektedir. Bu sinyal bölücü ünitesine iletilerek 2 sayısı bu değere bölünmektedir. Elde edilen bu sinyal kayan noktalı sayı standardına sahiptir ve dönüştürücü ünitesine iletilerek IQ-Math sabit noktalı sayı standardına dönüştürülmektedir. Ardından bu sinyal çıkarıcı

ünitesine iletilmektedir. Çıkarıcı ünitesinde bu değerden 1 sayısı çıkarılmakta ve bu elde edilen sonuç TanSig TF yapısının çıkışına 32-bit IQ-Math-tabanlı olarak gönderilmektedir.

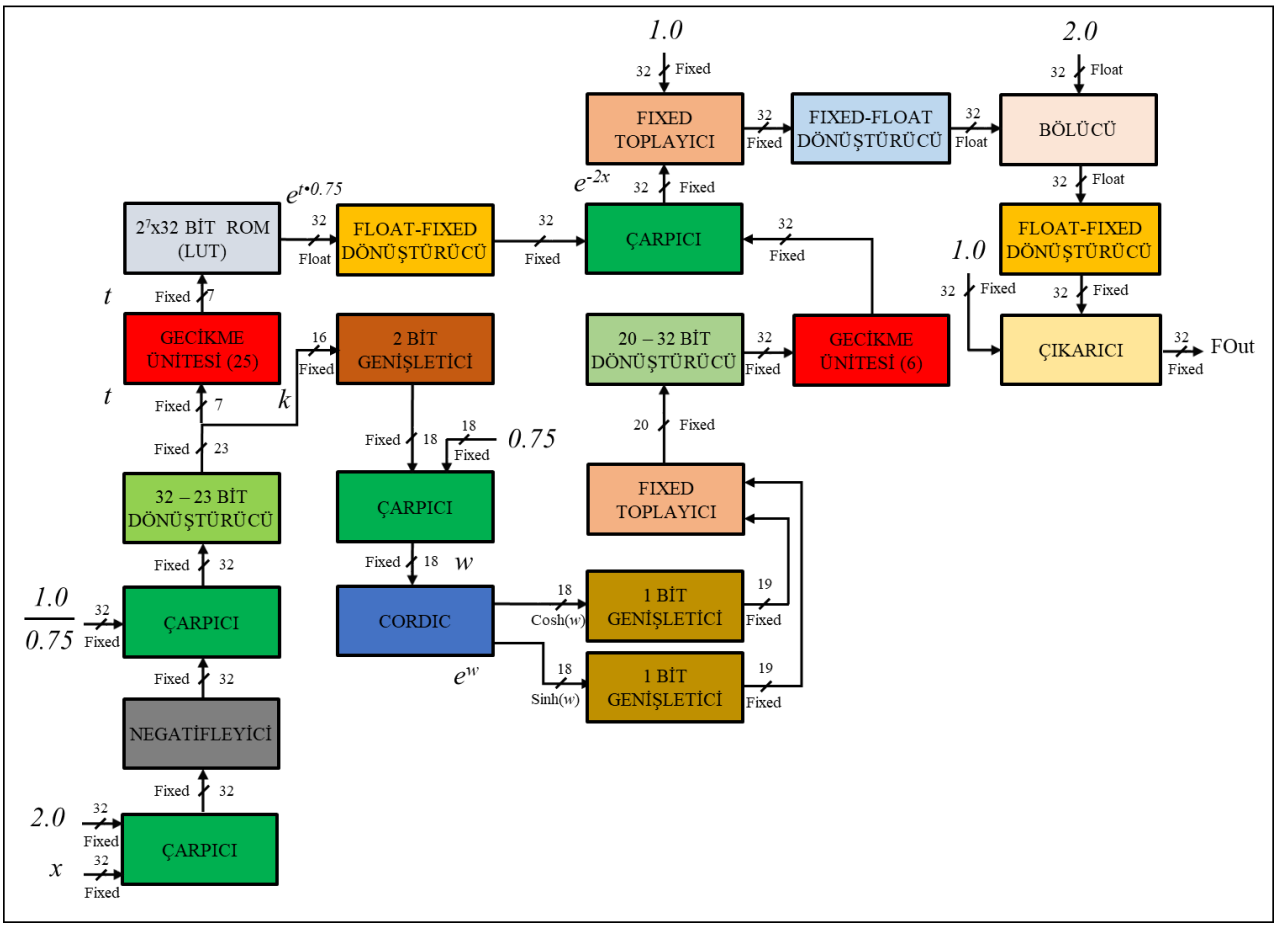

Şekil 6. TanSig fonksiyonun IQ-Math sabit noktalı sayı tabanlı blok şeması

LogSig ve TanSig TF tasarımlarının ardından örnek ileri beslemeli bir YSA tasarımı gerçekleştirilmiştir. Şekil 7'de gizli katmanında LogSig TF'nin kullanıldığı YSA-LS tasarımının, Şekil 8'de ise gizli katmanında TanSig TF'nin kullanıldığı YSA-TS tasarımının ikinci seviye FPGA blok şemaları verilmiştir. Tasarlanan YSA-LS ve YSA-TS yapıları içerisinde bulunan ağırlık ve bias değerleri doğrudan VHDL dilinde 32-bit std_logic_vector türünde signal sınıfı ile tanımlanarak saklanmıştır. 32-bit IQ-Math-tabanlı LogSig ve TanSig TF blok şemalarında iki adet Gecikme Ünitesi kullanılmıştır. İlgili üniteler tasarımlardaki pipeline hattın korunarak sistemin senkron bir şekilde çalışabilmesi amacı ile 6 saat darbesi ve 25 saat darbesi gecikme sağlamak için tasarlanmışlardır.

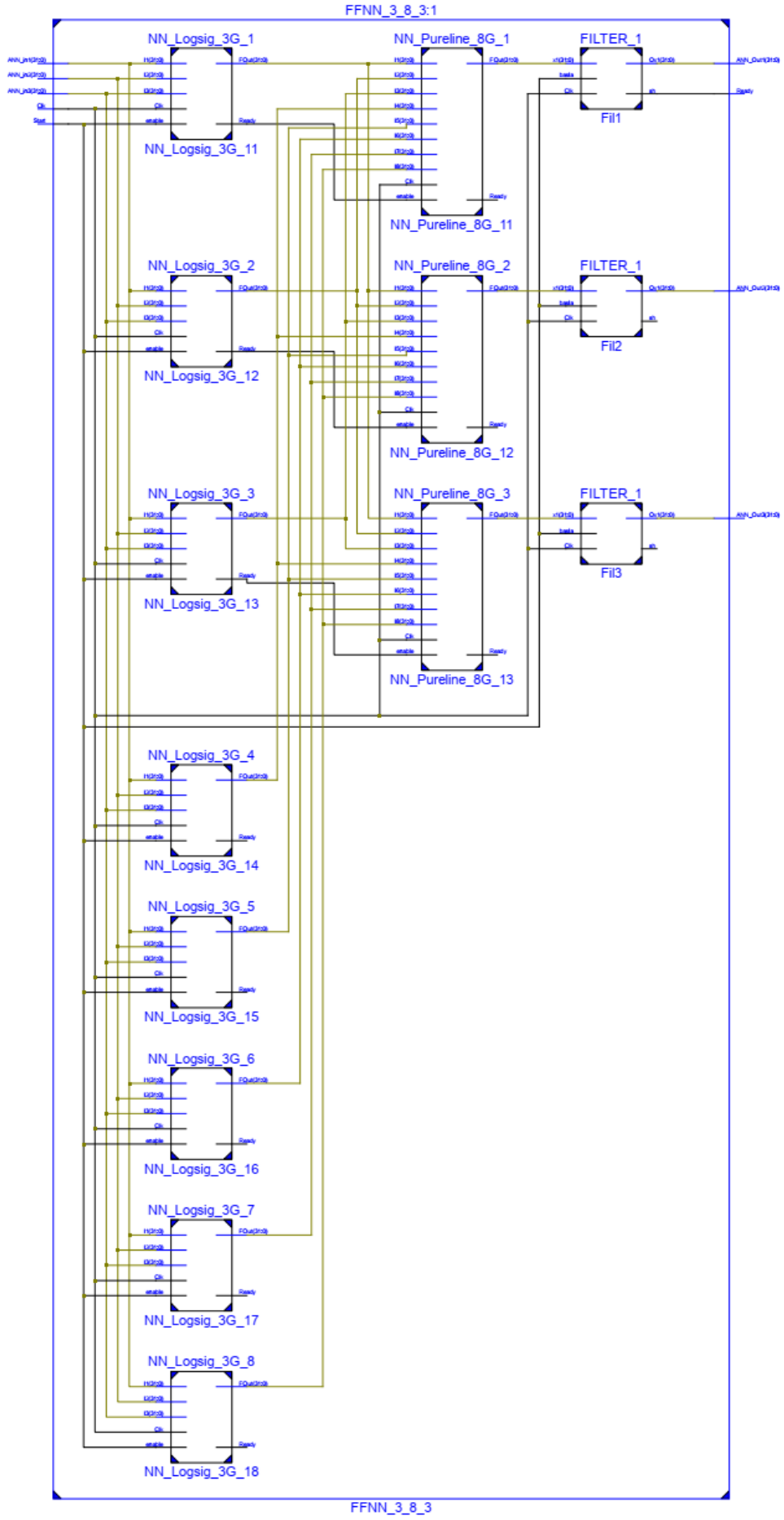

Şekil 7. FPGA-tabanlı YSA-LS tasarımının ikinci seviye blok şeması

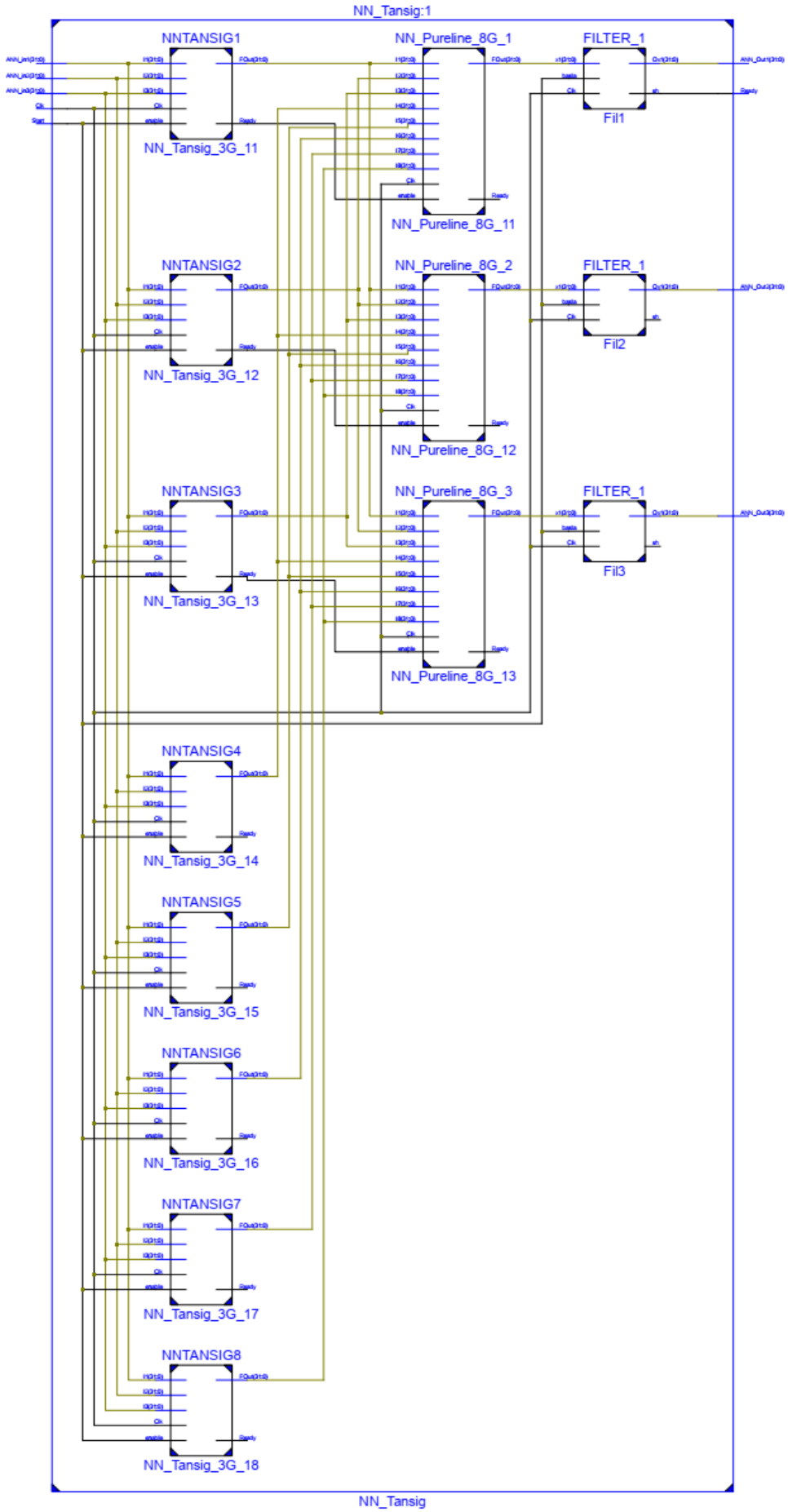

Şekil 8. FPGA-tabanlı YSA-TS tasarımının ikinci seviye blok şeması

Tüm tasarımlar X-ISE-DS ortamında bir testbench dosyası oluşturulmuştur. Bu işlemin ardından tasarımlar test edilmiş ve simülasyon sonuçları gösterilmiştir (Şekil 9-12).

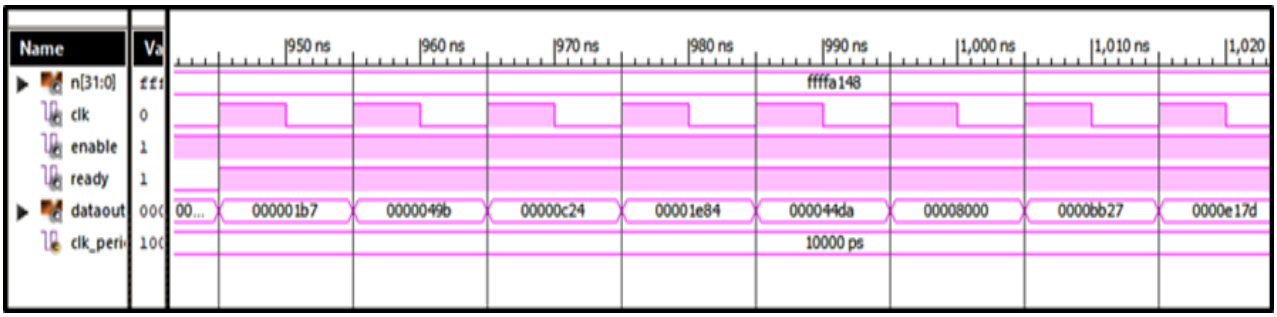

Şekil 9. FPGA-tabanlı LogSig fonksiyonun X-ISE simülasyon sonuçları

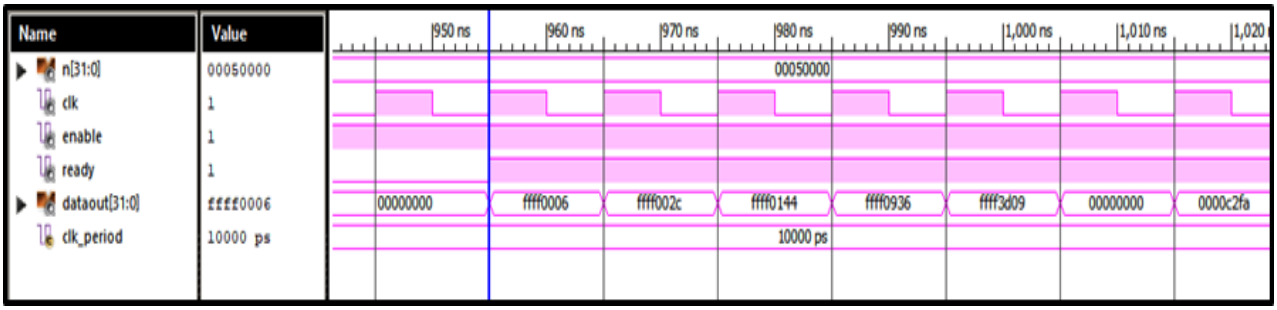

Şekil 10. FPGA-tabanlı TanSig fonksiyonun X-ISE simülasyon sonuçları

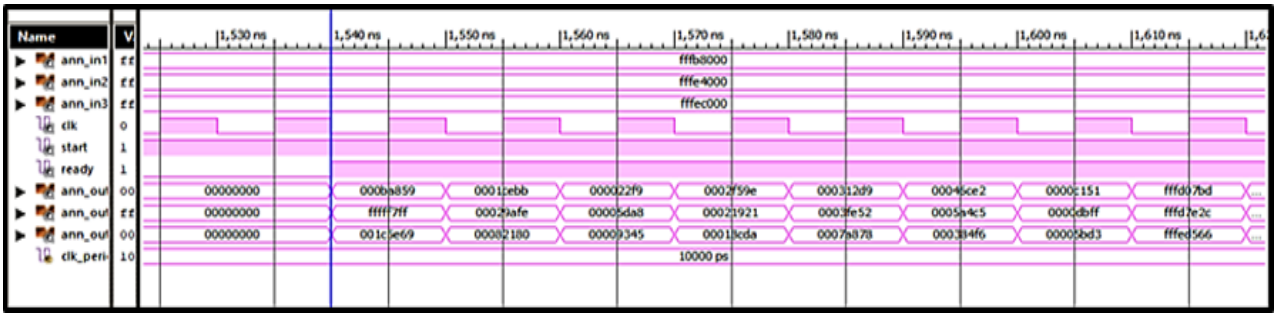

Şekil 11. FPGA-tabanlı YSA-LS tasarımının X-ISE simülasyon sonuçları

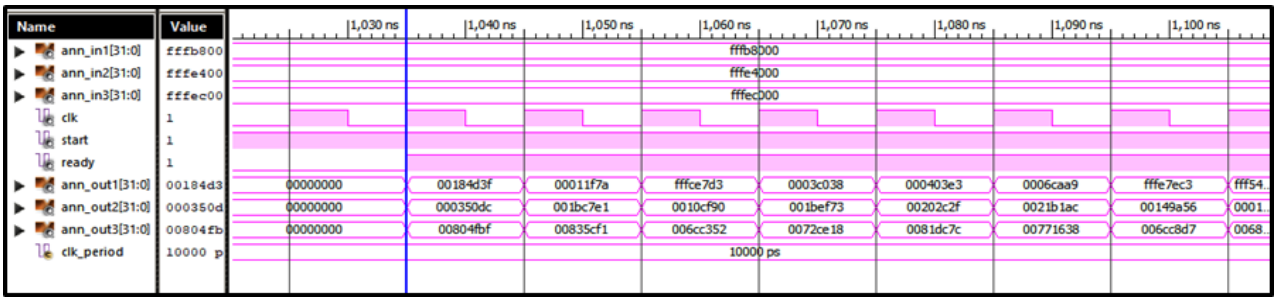

Şekil 12. FPGA-tabanlı YSA-TS tasarımının X-ISE simülasyon sonuçları

Ardından tüm tasarımların simülasyon sonuçları ile nümerik tabanlı sonuçlar karşılaştırılmıştır. Karşılaştırma işleminden elde edilen MSE ve RMSE hata analiz sonuçları aşağıda sunulmuştur (Çizelge 1). Tasarımların test edilebilmesi için negatif değerleri de kapsayacak biçimde 27 farklı değer kullanılarak MSE ve RMSE hata değerleri hesaplanmıştır.

Çizelge 1. TF ve YSA tasarımlarının hata analizleri

Transfer Fonksiyonları-Yapay Sinir Ağları	MSE	RMSE
LogSig TF	8.64E-11	9.30E-06
TanSig TF	2.31E-10	1.52E-05
YSA-LS	8.86E-06	2.98E-03
YSA-TS	7.92E-02	2.81E-01

Yapılan tüm TF ve YSA tasarımları test aşamasından sonra Xilinx firmasının tarafından geliştirilen XC7K70T FPGA (Kintex-7 kiti) için sentezleme işlemi gerçekleştirilmiştir. Bu işlemin ardından Place-Route prosesi gerçekleştirilmiştir. Bu işlemden elde edilen FPGA çip istatistikleri aşağıda sunulmuştur (Çizelge 2). Sunulan çalışmada öncelikle LogSig ve TanSig AF ve ardından bu iki AF kullanılarak LogSig-tabanlı YSA (YSA-LS) ile TanSig-tabanlı YSA (YSA-TS) olmak üzere 4 farklı tasarım gerçekleştirilmiştir. Aşağıda verilen Çizelge 2'de bulunan ilk 2 sütun LogSig ve TanSig AF tasarımlarına ve diğer sütunlar ise LogSig ve TanSig tabanlı YSA tasarımlarına ait IOB değerlerini ifade etmektedir.

Çizelge 2. TF ve YSA tasarımlarının FPGA çip istatistikleri

FPGA Çip İstatistikleri	LogSig	TanSig	YSA-LS	YSA-TS
Mak. Çalışma Frekans (MHz)	168.990	168.990	168.990	168.990
Slice Registers Sayısı	3696/ 82000 (% 4)	3729 / 82.000 (% 4)	31926/ 82000 (% 38)	31646 / 82000 (% 38)
Slice LUTs Sayısı	3073 / 41000 (% 7)	3100 / 41000 (% 7)	26878 / 41000 (% 65)	26658 / 41000 (% 65)
IOBs Sayısı	67 / 300 (% 22)	67 / 300 (% 22)	195 / 300 (% 65)	195 / 300 (% 65)
BUFG/BUFGCTRLs Sayısı	1 / 32 (% 3)	1 / 32 (% 3)	1 / 32 (% 3)	1 / 32 (% 3)
DSP48E1s Sayısı	7 / 240 (% 2)	7 / 240 (% 2)	188 / 240 (% 78)	195/ 240 (% 78)

Çizelge 3'te literatürdeki bir çalışmada yapılan 4 girişli YSA nöron tasarımları ile sunulan çalışma kapsamında tasarımları yapılan LogSig ve TanSig AF ile oluşturulan 4 girişli YSA nöronlarının FPGA çip kullanımları, kullanılan platform ile platformun nöron kapasitesi ve çalışma frekansı bakımından karşılaştırılması verilmiştir. Elde edilen sonuçlara göre sunulan çalışmada tasarlanan AF tasarımlarının FPGA kaynak tüketimi açısından daha düşük kaynak kullanmıştır. Ancak literatürde sunulan kayan noktalı sayı standardı tabanlı AF tasarımları ise maksimum çalışma frekansı bakımından daha avantajlı olduğu görülmektedir.

Çizelge 3. FPGA-tabanlı dört girişli LogSig ve TanSig AF-tabanlı YSA tasarımlarının çip istatistikleri

Çalışma	Kullanılan AF	Sayı standardı	Kullanılan FPGA	Slice Regs. Sayısı (%)	Slice LUTs sayısı (%)	Slices Utilization (%)	Çalışma Frekansı (MHz)
Koyuncu vd. (2017)	LogSig	32 Bit IEEE-754 Floating-point	Xilinx Virtex-6 XC6VLX75T	10	18	22	304.53
Sunulan Çalışma	LogSig	32 bit (16I-16Q) IQ-Math	Xilinx Kintex-7 XC7K70T	5	9	17	168.99
Koyuncu vd. (2017)	TanSig	32 Bit IEEE-754 Floating-point	Xilinx Virtex-6 XC6VLX75T	10	18	23	304.53
Sunulan Çalışma	TanSig	32 bit (16I-16Q) IQ-Math	Xilinx Kintex-7 XC7K70T	11	12	22	168.99

4. SONUÇ

Sunulan bu çalışmada, YSA yapılarının FPGA çipleri üzerinde gerçeklenmesi için ihtiyaç duyulan kaynak tüketimini azaltmak amacı ile 32-bit IQ-Math sayı standardında doğrusal olmayan LogSig ve TanSig TF VHDL dili kullanılarak kodlanmıştır. Ardından FPGA çiplerinde çalışmak üzere IQ-Math sayı tabanlı örnek bir üç girişli-üç çıkışlı bir YSA (ileri beslemeli) yapısı tasarlanmıştır. Tasarımın gizli katmanında 8 adet nöron, gizli katmanda LogSig ile TanSig TF ve çıkış katmanında ise PureLin TF bulunmaktadır. Sunulan iki farklı YSA yapısının test edilebilmesi için testbench dosyası oluşturulmuş ve bu tasarımlar VHDL ile X-ISE-DS programı ile test edilmiştir. Test simülasyon sonuçlarına göre LogSig-tabanlı YSA tasarımından 8.86E-06 MSE ve TanSig-tabanlı YSA tasarımdan 7.92E-02 MSE sonuçları elde edilmiştir. Tasarımlar test için simüle edilerek MSE ve RMSE hata analizleri bakımından incelendiğinde LogSig TF ve YSA-LS tasarımlarının daha başarılı sonuçlar ürettiği gözlemlenmiştir. Son aşamada ise her bir tasarım (XC7K70T-3FBG676 çipini içeren Kintex-7 kiti) FPGA için sentezlenerek Place-Route prosesi gerçekleştirilmiştir. Bu işlemden elde edilen FPGA kaynak kullanımı oranları sunulmuştur. Sonuçlara göre her iki YSA tasarımının maksimum çalışma frekansı 168.990 MHz olarak elde edilmiştir. Gelecekteki çalışmalarda, derin öğrenme ve YSA uygulamalarında kullanılan diğer aktivasyon fonksiyonları FPGA çiplerinde çalışmak üzere IQ-Math tabanlı olarak gerçekleştirilebilir.

5. TEŞEKKÜR

Bu çalışma 19.FEN. BİL.14 proje numarası ile Afyon Kocatepe Üniversitesi Bilimsel Araştırma Projeleri Koordinasyon Birimi tarafından desteklenmiştir.

6. ÇIKAR ÇATIŞMASI

Yazarlar, bilinen herhangi bir çıkar çatışması veya herhangi bir kurum/kuruluş ya da kişi ile ortak çıkar bulunmadığını onaylamaktadırlar.

7. YAZAR KATKISI

Yazarlar Mehmet Şamil AKÇAY, İsmail KOYUNCU, Murat TUNA ve Murat ALÇIN sunulan çalışmanın tasarım süreçlerinin belirlenmesi ve yönetimi, modellenmesi ve yorumlanması, makale taslağının oluşturulması, fikirsel içeriğin eleştirel incelenmesi, son onay ve tam sorumluluk süreçlerine katkı sağlamışlardır.

8. KAYNAKLAR

Abdullah H. T., Younis B. M., FPGA Based Bone Fracture Detector. IOP Conference Series: Materials Science and Engineering 745, 012052, 2019.

Adetiba E., Ibikunle F., Daramola S., Olajide A., Implementation of Efficient Multilayer Perceptron ANN Neurons on Field Programmable Gate Array Chip. International Journal of Engineering and Technology IJET-IJENS 14, 151-159, 2014.

Ahmed R., Sayed M. E., Gadsden S. A., Tjong J., Habibi S., Automotive Internal-Combustion-Engine Fault Detection and Classification Using Artificial Neural Network Techniques. IEEE Transactions on Vehicular Technology 64, 21-33, 2015.

Akçay M. Ş., Koyuncu I., Alçın, M., Tuna M., IQ-Math Tabanlı RadBas Aktivasyon Fonksiyonunun FPGA Üzerinde Gerçeklenmesi, International Asian Congress on Contemporary Sciences-IV, Baku, Azerbaijan, June 26-28, 2020, pp: 599-607.

Alçın M., Koyuncu I., Tuna M., Varan M., Pehlivan I., A novel high speed Artificial Neural Network-based chaotic True Random Number Generator on Field Programmable Gate Array. International Journal of Circuit Theory and Applications 47, 365-378, 2019.

Alçın M., Pehlivan I., Koyuncu I., Hardware design and implementation of a novel ANN-based chaotic generator in FPGA. Optik 127(13), 5500-5505, 2016.

Alçın M., Tuna M., Erdoğmuş P., Koyuncu İ., FPGA-based Dual Core TRNG Design Using Ring and Runge-Kutta-Butcher based on Chaotic Oscillator. Chaos Theory and Applications 3, 20-28, 2021.

Bargsten V., de Gea Fernández J., Distributed computation and control of robot motion dynamics on FPGAs. International Journal of SN Applied Sciences, 2, 1239, 2020.

Çavuşlu M. A., Karakuzu C., Şahin S., Parçacık Sürü Optimizasyonu Algoritması ile Yapay Sinir Ağı Eğitiminin FPGA Üzerinde Donanımsal Gerçeklenmesi. Politeknik Dergisi 13, 83-92, 2010.

Du X. K., The New Elman ANN Application in Accuracy Improvement of Robot Navigation and Obstacle Avoidance Technology. Advanced Materials Research 383-390, 1447-1451, 2011.

Erick L. O., Fixed-point representation & fractional math. Oberstar Consulting, revision, Madison, United States, 2007.

Gupta S., Vyas A., Trivedi G., FPGA Implementation of Simplified Spiking Neural Networks, 27th IEEE International Conference on Electronics, Circuits and Systems, Glasgow, UK, November 23-25, 2020, pp: 1-4.

Jiang W., Kong S. G., Block-Based Neural Networks for Personalized ECG Signal Classification, IEEE Transactions on Neural Networks 18, 1750-1761, 2007.

Kaur M., Sivia J. S., ANN and FA Based Design of Hybrid Fractal Antenna for ISM Band Applications. Progress in Electromagnetics Research C 98, 127-140, 2020.

Koyuncu I., Akçay M. Ş., Tuna M., Alçın M., Implementation of IQ-Math-based Linear Activation Functions on FPGA. 1st International Congress of Multidisciplinary Studies and Research, Turkey, June 19, 2019, pp: 114-124.

Koyuncu I., Sahin I., Gloster C., Saritekin N K., A neuron library for rapid realization of artificial neural networks on FPGA: A case study of rössler chaotic system, Journal of Circuits, Systems, and Computers 26, 1750015, 2017.

Koyuncu İ., Şeker H., Tuna M., Alçın M., Dormand-Prince tabanlı kaotik osilatör tasarımının FPGA üzerinde gerçeklenmesi. International Eurasian Conference on Science, Engineering and Technology, Ankara, Turkey, November 22-23, 2018, pp: 1059-1065.

Lortoğlu M., FPGA tabanlı yapay sinir ağı kullanılarak buğday türlerinin sınıflandırılması, KTO Karatay Üniversitesi, Fen Bilimleri Enstitüsü, Yüksek Lisans Tezi (Basılmış), 2019.

Mello M. M., Ventura L., Method for estimating luminous transmittance using an RGB sensor and ANN. Optical Engineering 59, 124109, 2020.

Mohammed R. K., Abdullah H. A., Implementation of digital and analog modulation systems using FPGA. Analog Modul Indonesian Journal of Electrical Engineering and Computer Science 18, 485-493, 2020.

Özkan İ. A., Sarıtaş İ., Herdem S., Manyetik Filtreler için FPGA Tabanlı Bulanık Kontrolör Tasarımı. Selçuk Teknik Dergisi 10, 271-284, 2011.

Paukštaitis V., Dosinas A., Pulsed Neural Networks for Image Processing. Elektronika Ir Elektrotechnika 95, 15-20, 2009.

Sahin I., A 32-bit floating-point module design for 3D graphic transformations. Scientific Research and Essays 5, 3070-3081, 2010.

Sahin I., Koyuncu I., Design and Implementation of Neural Networks Neurons with RadBas, LogSig, and TanSig Activation Functions on FPGA. Elektronika Ir Elektrotechnika 120, 51-54, 2012.

Savran İ., Donanım Tanımlama Dili VHDL ve FPGA Uygulamaları. Papatya Yayıncılık Eğitim, İstanbul, 2017.

Tuntas R., The Modeling and Hardware Implementation of Semiconductor Circuit Elements by Using ANN and FPGA. Acta Physica Polonica A, 128(2B), 78-81, 2015.

Wang G., Liu K., Sun Z., Li Y., Attitude-Orbit Cooperative Control for Small-Scale Spacecraft with Chemical Propulsion: Adaptive Sliding Mode Control Based on Neural Network. Journal of Aerospace Engineering 33, 04020080, 2020.

Yılmaz C., Koyuncu I., Alçın M., Tuna M., Artificial Neural Networks based thermodynamic and economic analysis of a hydrogen production system assisted by geothermal energy on Field Programmable Gate Array. International Journal of Hydrogen Energy 44, 17443-17459, 2019.

JOURNAL of
MATERIALS and MECHATRONICS:A

e-ISSN 2717-8811
JournalMM, 2022, 3(2), 240-256
https://doi.org/10.55546/jmm.1161542

Araştırma Makalesi / Research Article

A Method to Classify Steel Plate Faults Based on Ensemble Learning

Erkan Caner OZKAT[1]*

[1] Recep Tayyip Erdogan University, Faculty of Engineering and Architecture, Department of Mechanical Engineering, Rize, Turkey, ORCID ID: https://orcid.org/0000-0003-0530-5439, erkancaner.ozkat@erdogan.edu.tr

Geliş/ Received: 13.08.2022; **Kabul / Accepted:** 01.10.2022

ABSTRACT: With the industrial revolution 4.0, machine learning methods are widely used in all aspects of manufacturing to perform quality prediction, fault diagnosis, or maintenance. In the steel industry, it is important to precisely detect faults/defects in order to produce high-quality steel plates. However, determining the exact first-principal model between process parameters and mechanical properties is a challenging process. In addition, steel plate defects are detected through manual, costly, and less productive offline inspection in the traditional manufacturing process of steel. Therefore, it is a great necessity to enable the automatic detection of steel plate faults. To this end, this study explores the capabilities of the following three machine learning models Adaboost, Bagging, and Random Forest in detecting steel plate faults. The well-known steel plate failure dataset provided by Communication Sciences Research Centre Semeion was used in this study. The aim of many studies using this dataset is to correctly classify defects in steel plates using traditional machine learning models, ignoring the applicability of the developed models to real-world problems. Manufacturing is a dynamic process with constant adjustments and improvements. For this reason, it is necessary to establish a learning process that determines the best model based on the arrival of new information. Contrary to previous studies on the steel plate failure dataset, this article presents a systematic modelling approach that includes the normalization step in the data preparation stage to reduce the effects of outliers, the feature selection step in the dimension reduction stage to develop a machine learning model with fewer inputs, and hyperparameter optimization step in the model development stage to increase the accuracy of the machine learning model. The performances of the developed machine learning models were compared according to statistical metrics in terms of precision, recall, sensitivity, and accuracy. The results revealed that AdaBoost performed well on this dataset, achieving accuracy scores of 93.15% and 91.90% for the training and test datasets, respectively.

Keywords: Machine Learning, Classification, Ensemble Methods, Fault Detection, Artificial Learning.

*Sorumlu yazar / Corresponding author: erkancaner.ozkat@erdogan.edu.tr

Bu makaleye atıf yapmak için /To cite this article

Ozkat, E. C. (2022). A Method to Classify Steel Plate Faults Based on Ensemble Learning. Journal of Materials and Mechatronics: A (JournalMM), 3(2), 240-256.

1. INTRODUCTION

A product must be manufactured to meet the defined permissible upper and lower limits of each attribute and any deviation from these specified limits is considered a defect (Ozkat et al., 2017a; Liu et al., 2019; Kahveci et al., 2022). Without an effective monitoring and control strategy, today's complex manufacturing systems tend to produce faulty parts more frequently. These defects, defined by undesirable system dynamics, can lead to serious consequences such as a reduction in production, great economic losses, and unwanted downtimes (Ozkat et al., 2017b; Bektas et al., 2019; Gao et al., 2020). Early detection of defects and fault diagnosis is an important task in manufacturing to enhance the quality of the product and optimize the cost. With the integration of computer technology into production systems with Industry 4.0, the human factor has been minimized at every stage of production and it has enabled production to take place faster, with low cost and with a low margin of error (Xu et al., 2018; Kurt, 2019; Alkan & Bullock, 2021).

Steel is one of the most widely used materials in most engineering applications due to its strength, ductility, and recyclability (Lennox et al., 2000; Backman et al., 2019). One of the major challenges for the entire steel industry is the quality assurance of steel during manufacturing since steel goes through many different manufacturing processes from casting to drawing, pressing, to rolling (Widodo & Yang, 2007; Nkonyana et al., 2019). As a result, there are usually several kinds of defects on the steel plate that need to be localized and classified.

Traditionally, statistical processing control (SPC) methods have been deployed for monitoring quality during production, but they cannot predict the actual values relevant to product quality or estimate when the failure will occur. Because of this situation, machine learning (ML) models have been applied in a wide range in the field of manufacturing during recent years to solve real-world classification problems (Bektas et al., 2018; Ceryan et al., 2021; Özkat et al., 2021). The classification aims to accurately assign the sample to one of the predefined classes.

One issue regarding the steel quality control problem is the lack of large-scale, high-quality, industry-level, open-source datasets (Zhang et al., 2020). Due to the limited datasets, the well-known steel plate failure dataset has been used in many studies. The dataset is provided by the Semeion, Research Centre of Sciences of Communication, via Sersale 117, 00128, Rome, Italy (Buscema et al., 2010, Kaggle, 2017). The aim of many research works using this dataset is to correctly classify faults in steel plates employing the traditional ML models, neglecting the applicability of the developed ML models to real-world problems. With the integration of good and accurate models into manufacturing, defective steel plates can be identified as plates as early in the manufacturing process as possible, saving time and cost. However, manufacturing is a dynamic process, and constant adjustments and improvements are made. If the ML models cannot be updated with new data, they will quickly become obsolete and suffer a decline in accuracy. Therefore, it is necessary to establish artificial learning processes that determine the best model based on the arrival of new information.

The learning process often includes four main stages: data preparation, dimension reduction, model development, and model selection. Dimension reduction deals with the elimination of non-critical features without significant loss of information from the original dataset. This stage helps reduce computation time and develop a simpler structure in the machine learning model. Moreover, hyperparameter optimisation, which is one of the steps of the model development stage, is an important part of achieving a more accurate and updatable model. Regarding the studies using the steel plate fault dataset, the following ML models, namely: logistic regression (LR) (Fakhr and

Elsayad, 2012; Simić et al., 2014; Kharal, 2020; Gamal et al., 2021), support vector machine (SVM) (Simić et al., 2014; Tian et al., 2015; Nkonyana et al., 2019; Srivastava, 2019; Gamal et al., 2021; Tasar, 2022), k-nearest neighbour (kNN) (Srivastava, 2019; Gamal et al., 2021; Tasar, 2022), naive Bayes (NB) (Kazemi et al., 2018; Gamal et al., 2021), decision tree (DT) (Fakhr and Elsayad, 2012; Chen, 2018; Kazemi et al., 2018; Srivastava, 2019; Gamal et al., 2021; Tasar, 2022), random forest (RF) (Chen, 2018; Nkonyana et al., 2019; Srivastava, 2019; Kharal, 2020; Gamal et al., 2021; Tasar, 2022), neural network (NN) (Fakhr and Elsayad, 2012; Simić et al., 2014; Zhao et al., 2015; Kazemi et al., 2018; Nkonyana et al., 2019; Gamal et al., 2021; Tasar, 2022) have developed to address the fault classification problem. However, among all these ML models, studies involving hyperparameter optimization are rarely addressed (Tian et al., 2015; Zhao et al., 2015; Nkonyana et al., 2019; Kharal, 2020), while studies involving dimension reduction using feature selection step are not available. Instead, some studies have reduced the number of target classes (Zhao et al., 2015; Chen, 2018; Kazemi et al., 2018; Kharal, 2020; Gamal et al., 2021; Tasar, 2022). As a matter of fact, the description of the currently used dataset already states that the seventh target class is not unique. In addition, it is clearly stated in some studies that the data set is not divided into training and test data sets, and the success of the developed ML model is calculated over the entire data set (Srivastava, 2019; Tasar, 2022).

In contrast to the previous studies, this article provides a systematic modelling approach that includes the normalization step in the data preparation stage to reduce the effects of outliers, the feature selection step in the dimension reduction stage to develop an ML model with short computation time, and hyperparameter optimization step in the model development stage to increase the accuracy of the ML model. Furthermore, the ensemble machine learning model, which is a recent trend in the classification problems to overcome the individual drawbacks of each ML model (Yang et al., 2021; Pham et al., 2022; Xiong et al., 2022), was utilized to provide intelligent multi-class diagnostics for steel plates. The basic purpose of implementing ML models is to help operational decision-makers to organise effective and efficient manufacturing. The classification performances of the proposed models were computed using the following four statistical metrics: precision, recall, sensitivity, and accuracy score.

The rest of the paper is organized as follows: Section 2 presents a brief overview of some of the studies conducted using the provided dataset. Section 3 introduces the methodology used in the presented study in detail. Section 4 provides the results and is followed by concluding remarks in Section 5.

2. RELATED STUDIES ON THE STEEL PLATE FAULT DATASET

Classification is the process of finding which classes that new data belong to in a given dataset. The steel plate fault diagnosis dataset has been widely studied in machine learning for automatic pattern recognition. In this regard, relevant literature is summarized below.

Fakhr and Elsayad, (2012) employed a decision tree with boosting, a multi-perception neural network with pruning and logistic regression with step forward models, and tested their effectiveness using accuracy, specificity, and sensitivity. According to their results, the decision tree with boosting algorithm has achieved a remarkable performance with 97.25 and 98.09% accuracy on training and test sets. Similarly, Kazemi et al., (2018) studied decision tree, multi perception neural network, Bayesian network and ensemble random forest models. The data set is partitioned into 70% training

and 30% testing. It was indicated that the decision tree was superior to other models with reaching an accuracy score of 95.66 in both training and test.

Simić et al., (2014) utilized a remarkable approach by hybridizing random forest and bagging algorithms, called as Treebagger, and compare this novel algorithm against support vector machine, logistic regression, and multi perception neural network classification algorithms. The dataset was divided into training and test by the ratio of 70:30 in percentage, respectively. It was demonstrated that the Treebagger outperformed the other models in both training and test. However, the time required to create the tree bagger model reached up to four minutes, which is the most time-consuming task among others. A recent study conducted by Chen, (2018) reported that Adaboosting, another hybrid approach, could achieve 100% and 88.57% accuracy in the training and test set, respectively. In this study, ten-fold cross-validation was applied to each machine learning model, and other fault class was eliminated from the dataset in which the number of classes became 6.

Another important aspect of machine learning methodology is hyperparameter optimization. It is possible to further improve the performance of the model by choosing an optimal combination of hyperparameters that minimizes a predefined loss function. For example, Tian et al., (2015) utilized genetic algorithm (GA), grid search (GS) and particle swarm optimization (PSO) optimization methods to obtain the optimum hyperparameters for the support vector machine classification model. In addition, the classification accuracy was improved by normalizing all features. The implementation of GS, GA, and PSO in SVM yielded accuracy scores of 94.6%, 95.2%, and 88% for training, and 77.7%, 77.2%, and 78% for testing, respectively. Similarly, Zhao et al., (2015) integrated the local outlier factor (LOF) anomaly detection method with a back-propagation neural network to classify steel plate faults. Levenberg–Marquardt was employed to obtain optimal hyperparameters. As a result, the average training and test accuracy scores were 94.68% and 88.05%, respectively.

Kharal, (2020) performed the classification of faults on steel surfaces by applying optimization. It was found that the features in this dataset were imbalanced and to handle this problem undersampling, oversampling and synthetic minority oversampling technique methods were employed to balance the dataset. The best classification performance was obtained from an optimized random forest with 10-fold cross validation. Gamal et al., (2021) utilized the most common classification machine learning algorithms namely, decision trees, k-nearest neighbour, random forest, support vector machine, naive Bayes, logistic regression, and multi-layer perceptron neural network. The dataset was divided in half (50:50%) as training and test sets, and 10-fold cross validation was applied to each machine learning model. It was demonstrated that the accuracy scores of the listed machine learning methods were 91.14%, 82.86%, 93.29%, 86%, 59%, 88.29% and 73.86%, respectively. The lowest score was achieved using the naïve Bayes model, whereas the highest score was obtained using the random forest model. More interestingly, it was reported that the faults such as stains were easily classified, but other faults class could not be easily classified using any of these machine learning models. In addition, some faults such as Z scratch, and K scratch could be classified with less error depending on the performance of the machine learning.

Srivastava, (2019) showed that the random forest algorithm using a 20-fold cross validation achieved 79.23 % accuracy with 0.203 root mean square error on contrary to the k-nearest neighbour, decision tree, support vector machine, and deep neural network. In a tremendously similar and the most recent study conducted by Tasar, (2022) investigated the performance of linear discriminant, k-nearest neighbour, decision tree, support vector machine, random forest, and deep neural network machine learning model without applying data partitioning and feature selection. The accuracy score of each model was found as 90.136%, 91.7880%, 93.013%, 93.287%, 95.479%, and 96.986%,

respectively. The essential idea in machine learning is to test the performance of the developed model on a dataset completely independent of the data used during model development. In the presented, the data set was not divided into two as training and testing, and any feature selection method was not employed, but the cross-validation technique was applied for the developed models. In such a modelling method, it was thought that the models memorized the data set rather than learning. Therefore, the reliability of the obtained results is open to discussion.

To sum up, Table 1 groups the listed publications in terms of the feature selection step in the dimension reduction stage and the hyperparameter optimization step in the model development stage to increase the accuracy of the ML model.

Table 1. Comparison table for related studies on ML models for steel plate fault diagnosis

Feature Selection \ Hyperparameters Optimization	No	Yes
No	Fakhr and Elsayad, 2012 Simić et al., 2014 Chen, 2018 Kazemi et al., 2018 Srivastava, 2019 Gamal et al., 2021 Tasar, 2022	Tian et al., 2015 Zhao et al., 2015 Nkonyana et al., 2019 Kharal, 2020
Yes	N/A	Proposed in this study

3. METHODOLOGY FOR MULTICLASS FAULT DIAGNOSIS IN STEEL PLATES

The methodology flow used in the presented work is illustrated in Figure 1. The fishbone diagram consists of four main stages which are (i) data preparation, (ii) dimension reduction, (iii) model development (iv) model selection. The detailed information required for each stage is given in the following sections.

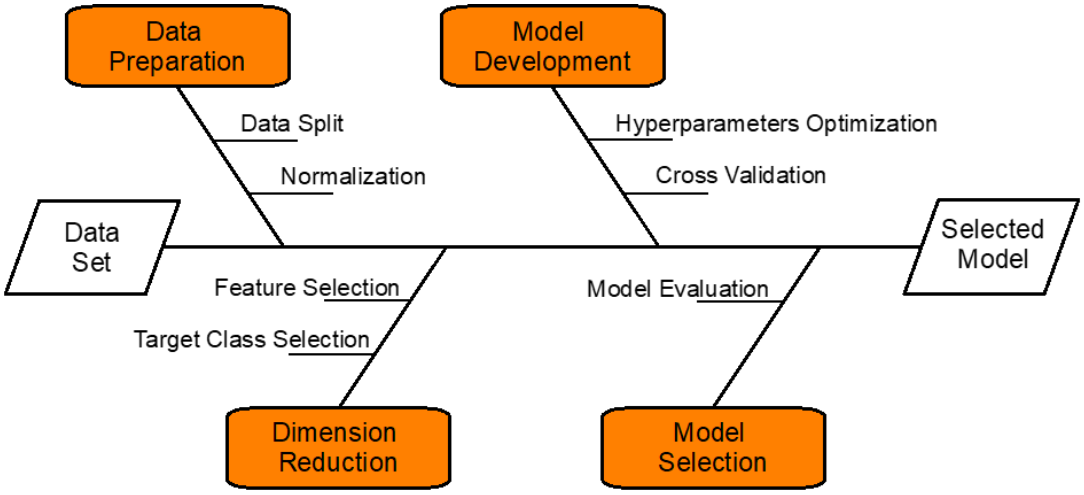

Figure 1. The methodology flow used in this study

3.1 Dataset Description

The dataset used in this study is a public dataset and it can be accessed through the online data science platform Kaggle (Kaggle, 2017). The dataset contains 1941 experiments. Each experiment has 27 independent features and one of 7 different types of classified steel surface defects, which are Dirtiness, Stains, Pastry, Z-Scratch, K-Scratch, Bumps, and Other Faults. The failure types and corresponding sample numbers are listed in Table 2, and detailed information on the 27 independent features is given in Table 3.

Table 2. Types of faults and sample sizes

Fault class	Failure types	Sample numbers
1	Dirtiness	55
2	Stains	72
3	Pastry	158
4	Z-Scratch	190
5	K-Scratch	391
6	Bumps	402
7	Other Faults	673

Table 3. Independent features of the faulty steel plates data set

Number	Feature	Type	Number	Feature	Type
1	X Minimum	Numerical	15	Edges Index	Numerical
2	X Maximum	Numerical	16	Empty Index	Numerical
3	Y Minimum	Numerical	17	Square Index	Numerical
4	Y Maximum	Numerical	18	Outside X Index	Numerical
5	Pixels Areas	Numerical	19	Edges X Index	Numerical
6	X Perimeter	Numerical	20	Edges Y Index	Numerical
7	Y Perimeter	Numerical	21	Outside Global Index	Numerical
8	Sum of Luminosity	Numerical	22	Log of Areas	Numerical
9	Minimum of Luminosity	Numerical	23	Log X Index	Numerical
10	Maximum of Luminosity	Numerical	24	Log Y Index	Numerical
11	Length of Conveyer	Numerical	25	Orientation Index	Numerical
12	Type of Steel A300	Categorical	26	Luminosity Index	Numerical
13	Type of Steel A400	Categorical	27	Sigmoid of Areas	Numerical
14	Steel Plate Thickness	Numerical	-	-	-

3.2 Data Preparation

3.2.1 Data split

The most crucial item of data preparation in machine learning methodology, which should not be neglected, is the separation of data into training and test sets. Training data is utilized to learn the patterns in the data and develop the machine learning model. Testing data is employed to test the model on unseen data to validate the results across different models. The factor to be considered here is the separation rate. The training set should not only contain a large amount of data to enable learning, but also a small amount of data so that the pattern in the data is not memorized. For this purpose, the dataset has been randomly split into 80% training data and 20% test data.

3.2.2 Normalization

Another step that should be applied in the data preparation stage in order to improve the machine learning performance is normalization. The purpose of this step is to move the values of only the numerical data into a common scale, without distorting the differences in the value ranges of the numerical data. The Z-score normalization technique was applied in this study, each numerical feature

was centred and scaled by the corresponding weighted mean and standard deviation. The method of Z-score normalization is given in Equation 1.

$$x_{i,j}^{*} = \frac{x_{i,j} - \mu_{x,i,j}}{\sigma_{x,i,j}} \tag{1}$$

where i is the index of the feature, j is the index of the sample, $x_{i,j}$ is the ith feature of the jth sample, $x_{i,j}^{*}$ is the ith normalized feature of the jth sample, $\mu_{x,i,j}$ is mean and $\sigma_{x,i,j}$ is standard deviation of the ith feature of the jth sample. It is very important to emphasize that normalization was first applied to the training dataset. The mean and standard deviation of each feature obtained in the training dataset was utilized to normalize the test dataset. The reason behind this approach is that test data should be independent of the training data in terms of information content.

3.3 Dimension Reduction

3.3.1 Target class selection

Traditionally, dimension reduction has been applied to features in machine learning, but in this study, it has been applied to both target classes and features. The reason for this is that target class 7 (i.e., Other Faults), as stated in the dataset definition, is not a specific kind of fault but a combination of several faults that are different fault from 1 to 6. It is quite difficult to determine samples of the 7th failure class as samples belonging to this class do not share certain features, also it is difficult to find dominant features to train. In addition, some features in class 7 may have similar properties to features in other classes. There are 673 samples of Other Failures that are not clearly classified. For this reason, as in some studies in the literature (Tian et al., 2015; Kazemi et al., 2018; Gamal et al., 2021), class 7 was excluded from the data set, as it would significantly affect the modelling.

3.3.2 Feature selection

It is not correct to use all the features in the model development stage. Since some features will cause errors and the developed model can diverge; hence, it is of great importance to detect and remove these features that are not relevant to the target class. Many methods are utilized to determine the features used in model development, among which the widely accepted method is Principal Component Analysis (PCA). Since it transforms high-dimensional data into low-dimensional data using the computationally simple linear algebra method, as it enables machine learning methods to converge faster when trained on the principal components rather than the original dataset. The main steps to be followed in PCA are standardization of the data, calculation of the covariance matrix and finding the eigenvalues and eigenvectors for the covariance matrix, respectively. While the eigenvector determines the principal component, the eigenvalue determines the magnitude corresponding to this principal component. Dimension reduction is performed by determining the eigenvectors corresponding to the eigenvalues with a magnitude above the pre-defined threshold value.

3.4 Model Development

Classification in machine learning is the problem of determining which class set a new observation belongs to, based on a training set containing examples of the known classes. Ensemble machine learning methods combine multiple ML models to obtain better predictive performance than could be obtained from any of the ML model alone. The final classification depends on the combined outputs of the individual models. The common ensemble classification techniques include boosting,

bagging and random forest. This section explains about different machine learning algorithms used in this study. All the proposed models were developed in the MATLAB R2022a environment. During model development, random seeds were used at training in hyperparameters optimization that performs reproducibility of models.

3.4.1 Hyperparameters optimization

Adaptive Boosting (Adaboost) is an ensemble model in which different weak classifiers are trained on the same training set and then these weak classifiers are combined to create a stronger classifier with a certain weight. This weak classifier can be any algorithm such as decision tree, and k near neighbour. In addition, the weight of a classifier is calculated according to the accuracy error that the model will make during the training phase. The boosting algorithm adopts an iterative approach which will tend to give more weight to misclassified samples in the hope that the next model will be more accurate. In this study, the weak classifier is selected as decision tree and three hyperparameters, maximum number of splits, number of learners and learning rate. These hyperparameters were varied in the range of 1-1014, 10-500, and 0-1, respectively.

Bootstrap Aggregation (Bagging) is another ensemble model which aims to create a set of classifiers having the same importance unlike boosting. The bagging and boosting algorithms appear the same, but the way to train the base classifier is completely different. For instance, given a data set containing “n” samples, select randomly one point from the training dataset and repeat this selection “N” times without replacement, eventually resulting in a new dataset in which some samples may appear several times while others may never appear. With this process, different training datasets and therefore different classifiers are created. Since the training method of each base classifier is independent and identical, an equal weighted strategy is used to vote by the classifier. Each model will vote on the outcome of the prediction and the overall output will be the class that has received the most votes. In this study, the weak classifier is selected as decision tree and three hyperparameters, maximum number of splits, number of learners and number of predictors to sample. These hyperparameters were varied in the range of 1-1014, 10-500, and 1-15, respectively.

The random forest model is an ensemble method that operates by building several decision trees trained on randomly sampled training data using the bootstrap sampling method. For each decision tree, a dataset is created by the bootstrap procedure. Constructing a large number of trees and aggregating them reduces the overfitting problem of a single tree and thus improves the generalization ability of the random forest. Two hyperparameters, minimum number of leaf sizes, and number of trees need to be optimized to obtain a good model. These hyperparameters were varied in the range of 1–500 and the minimum number of leaf sizes was chosen using the Bayesian method.

3.4.2 Cross validation

Cross validation is a method that ensures that the developed machine learning model is independent of the separation of the data set into training and test sets. Typically, the training dataset is divided into k parts. The machine learning model is trained on k−1 parts of the data, and the rest of the data is used for validating the model. This process is repeated k times to reduce the variance. The k-fold cross-validation method gets its name from this process. The results of each k-fold can then be averaged to produce a single result of the machine learning model. In the presented work, 10-fold cross-validation was applied to each developed model.

3.5 Model Selection

The developed machine learning models aim to determine the failure types that a steel plate may have using the selected features as inputs. Since it is a classification problem, the models

developed are evaluated using the following statistical metrics: precision, recall, sensitivity and accuracy. These metrics explain how well a target class is predicted or how bad if a prediction has missed the class. In addition, these metrics are defined using the confusion matrix. It has two dimensions matrix; the rows of the matrix represent samples of the actual classes and the columns represent the samples of the class predicted by the machine learning model. Generally, the confusion matrix is a result of the binary classification problem, which has only two classes to be classified, preferably one positive class and one negative class. However, the presented work is a multi-class classification problem that classifies samples into one of six classes, and no generalized formulae are provided for calculating the precision, recall, specificity, and overall accuracy of the model, having many classes to consider. Let us suppose that N, i and j represent the number of samples, the actual and predicted classes, respectively. An example of the multi-class confusion matrix is given in Table 4.

Table 4. An example of the multi-class confusion matrix

Predicted Classes / **Actual Classes**	**Class 1**	***Class 2***		**Class j**
Class 1	N_{11}	N_{12}	⋯	N_{1j}
Class 2	N_{21}	N_{22}	⋯	N_{2j}
⋮	⋮	⋮	⋱	⋮
Class i	N_{i1}	N_{i2}	⋯	N_{ij}

The numbers of true positive (TP), true negative (TN), false positive (FP), and false negative (FP) for each class i are computed in Equations 2-5., respectively (Markoulidakis et al., 2021). In addition, the formulation of the following metrics used in this study, precision (P), recall (R), and specificity (S) for each class i and the accuracy score (A) are given in Equation 6-9., respectively (Markoulidakis et al., 2021).

$$TP_i = N_{i,i} \tag{2}$$

$$TN_i = \sum_{\substack{j=1 \\ j \neq i}}^{n} \sum_{\substack{k=1 \\ k \neq i}}^{n} N_{jk} \tag{3}$$

$$FP_i = \sum_{\substack{j=1 \\ j \neq i}}^{n} N_{ji} \tag{4}$$

$$FN_i = \sum_{\substack{i=1 \\ i \neq j}}^{n} N_{ij} \tag{5}$$

$$P_i = \frac{TP_i}{TP_i + FP_i} \tag{6}$$

$$R_i = \frac{TP_i}{TP_i + FN_i} \tag{7}$$

$$S_i = \frac{TN_i}{TN_i + FP_i} \tag{8}$$

$$A = \frac{\sum_{i=1}^{n} TP_i}{\sum_{i=1}^{n} \sum_{j=1}^{n} N_{ij}} \tag{9}$$

4. RESULTS AND DISCUSSION

The quality and quantity of the dataset have a huge impact on the performance of machine learning models. In this regard, the features and target classes of the dataset were initially thoroughly examined. As stated in Table 2, the type of steel is a categorial feature so it is important to examine the errors that occur according to the steel type before data splitting. Figure 2 illustrates the radar plot of fault classes by steel type. Upon closer inspection, only one sample of K Scratch and Stains was found for type A300 steel. Additionally, Dirtiness is also infrequent for this type of steel. On the other hand, Z Scratch is a relatively rare class of failure for steel type A400. Therefore, these samples along with samples that contain other faults class were excluded from the data set in order to improve the performance of the machine learning methods before data splitting.

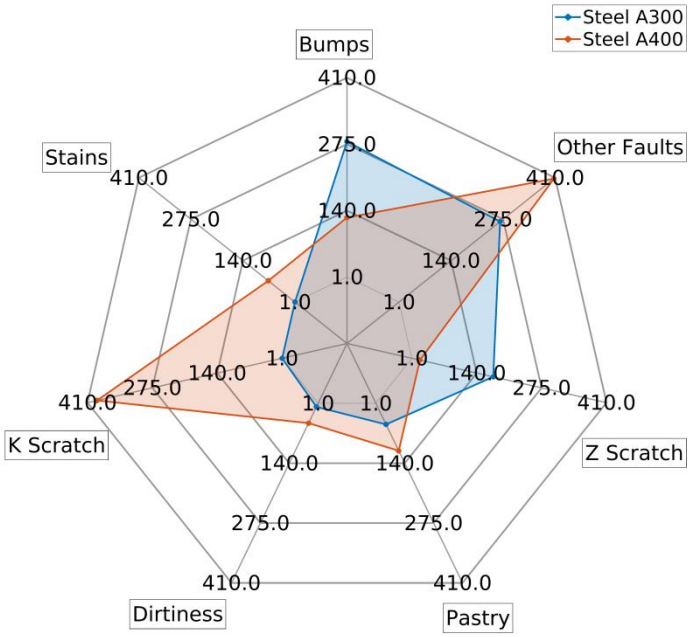

Figure 2. Fault classes according to the steel type

The dataset initially contains 1941 samples, after excluding samples with other faults class, along with samples with lesser fault classes when fault classes are classified according to the steel type, 1239 samples remained in the dataset. The dataset was randomly split into 80% training data (992 samples) and 20% test data (247 samples) before normalization. In the presented work, 'Type of Steel' and 'Outside Global Index' were considered as categorial features. The dimension reduction was conducted to the remaining features by ranking the metric and eliminating features that did not reach a certain score. In order to determine the most important feature influencing the target classes, PCA was conducted, and the importance score is presented in Figure. 3. It is evident that the elbow point is observed at 'X Maximum' feature which implies that the number of important features is 13,

and adding the two categorical features, the most important features obtained for modelling are 'Sum of Luminosity', 'X Minimum', 'Orientation Index', 'Minimum of Luminosity', 'Empty Index', 'Outside X Index', 'Y Minimum', 'Edges Y Index', 'Y Perimeter', 'Length of Conveyer', 'X Perimeter', 'X Maximum', 'Type of Steel' and 'Outside Global Index'.

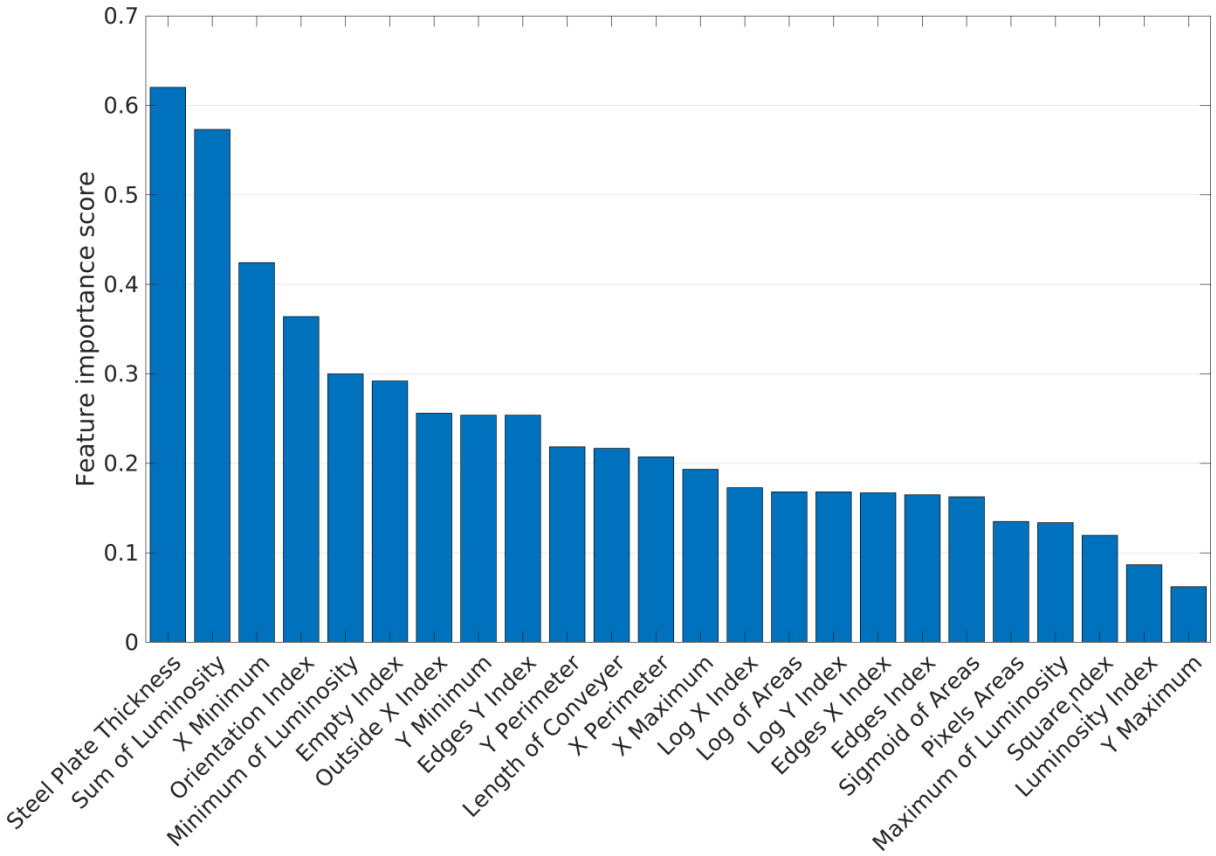

Figure 3. Feature importance ranking for dimension reduction

The optimum model was observed in the Adaboost model (i.e., ML1) with a learning rate of 0.9851, number of learners was 311, and maximum number of splits was 59. Similarly, the values of optimal hyperparameters for the Bagging model (i.e., ML2) were 174 for the number of learners, 345 for the maximum number of splits, and 15 for the number of predictors to sample. Moreover, the Random Forest model (i.e., ML3) performed best when the number of trees was 300, and the minimum number of leaf size was 1. The hyperparameters of each machine learning model were obtained during the training phase with 10-fold cross validation and, then, the trained models were utilized to predict the test set. Since the purpose of this study is to classify steel plate faults utilizing a machine learning model, it is important to determine the best models among the models developed.

Three statistical metrics namely, precision, recall and specificity are introduced to access the performance of the models developed. The results of these metrics for the training and test datasets are given in Tables 4 and 5, respectively. Moreover, the results are given in percentages, which means that a value close to 100 represents a good correlation between actual and predicted classes.

In brief, precision indicates the classifier's certainty of correctly predicting a particular class. In other words, it is the ratio of the number of TP to the total positive prediction including TP and FP. Therefore, FP, which is the cost of the model, are represented as part of precision. Once the models are accessed based on the precision value, the model with the highest precision would be chosen as the final model. On the other hand, recall and specificity represent the number of correct positive (TP) and negative (TN) predictions out of the total true positive and negatives, respectively. They assess the usefulness of the model in a single class. In this regard, the results clearly confirm that Adaboost (i.e., ML1) is the most effective model in fault detection with respect to all the

performance measures. The second-best effective model for detecting the faults in steel plates is the Bagging (i.e., ML2) model.

In Table 5, it can be observed that the highest precision is obtained using the Adaboost (i.e., ML1) model. With the ML1 model, a score of 100% was obtained in Dirtiness, K-Scratch and Z-Scratch, fault classes, and all the classes predicted as positive were found to be positive. For Recall, the highest scores were obtained with the ML1 model in the Bumps and Dirtiness fault classes, with the Bagging (i.e., ML2) model in the K-Scratch and Pastry fault classes, and with the Random Forest (i.e., ML3) model in the Stains and Z-Scratch fault classes. Accordingly, it was determined that the values estimated as TP in the fault classes related to each model were estimated correctly at the highest level. For specificity, the highest value in the Pastry fault class was obtained with the ML3 model, but the highest value in other fault classes was obtained with the ML1 model. Thus, it was determined that the values estimated as TN by the ML1 method were estimated correctly at the highest level.

Table 5. Precision, Recall and Specificity results for each fault class obtained from the training dataset

Fault Class	Training dataset								
	Precision (%)			Recall (%)			Specificity (%)		
	ML1	ML2	ML3	ML1	ML2	ML3	ML1	ML2	ML3
Bumps	87.826	87.021	91.447	94.099	91.615	86.335	93.731	93.433	96.119
Dirtiness	100	93.939	82.927	89.189	83.784	91.892	100	99.791	99.267
K-Scratch	100	98.722	95.652	98.397	99.038	98.718	100	99.412	97.941
Pastry	79.487	78.992	74.194	73.228	74.016	72.441	97.225	97.11	96.301
Stains	96.364	94.444	91.525	94.643	91.071	96.429	99.786	99.679	99.466
Z-Scratch	100	97.761	95.775	97.826	94.928	98.551	100	99.649	99.297

ML1: Adaboost, **ML2**: Bagging, **ML3**: Random Forest Ensemble models

The values of the statistical metrics, precision, recall, and specificity of each model were computed using the test dataset and presented in Table 6. According to the presented results, in particular, the ML1 model has come to the fore, similar to the results obtained with the training set for the recall and specificity values, while the ML2 and ML3 models have been put forward for the precision value, and this situation is evident for the stain fault class. However, the average precision is the highest for the ML1 model. Dirtiness has the highest precision, recall and the specificity values for the ML1 model. To sum up, the Adaboost (i.e., ML1) model is the most suited for detecting these fault classes.

Table 6. Precision, Recall and Specificity results for each fault class obtained from the test dataset

Fault Class	Test dataset								
	Precision (%)			Recall (%)			Specificity (%)		
	ML1	ML2	ML3	ML1	ML2	ML3	ML1	ML2	ML3
Bumps	88.608	89.474	95.522	87.5	85	80	94.611	95.21	98.204
Dirtiness	100	88.889	72.727	88.889	88.889	88.889	100	99.58	98.739
K-Scratch	97.468	98.701	93.902	98.718	97.436	98.718	98.817	99.408	97.041
Pastry	79.310	77.143	73.529	74.194	87.097	80.645	97.222	96.296	95.833
Stains	93.750	100	100	100	100	100	99.569	100	100
Z-Scratch	94.444	94.286	89.474	100	97.059	100	99.061	99.061	98.122

ML1: Adaboost, **ML2**: Bagging, **ML3**: Random Forest Ensemble models

In the current problem precision and accuracy are the key metrics to compare the models. Generally, the accuracy score is a measure of how often the model predicts correctly. The Adaboost model provides accuracy scores of 93.15% and 91.90% for training and testing, respectively. Similarly, the Bagging model provides accuracy scores of 91.83% and 91.90% for training and testing, respectively. In the same way, the Random Forest model provides accuracy scores of 90.93% and 90.28% for training and testing, respectively. According to the test set, which is the unseen data set, the accuracy scores of Adaboost and Bagging are the same. Since the precision of Adaboost is better than other models for both training and test sets, it is found to be better to utilize the Adaboost model in the classification of faults.

The multiclass confusion matrix for the steel plate failure classification derived using the Adaboost model for both the training and test datasets is illustrated in Figure 4. The results of the statistical metrics presented for the ML1 model given in Tables 5 and 6 were calculated using the values given in Figure 4. The results in Figure 4 are parallel to the results in Tables 5 and 6.

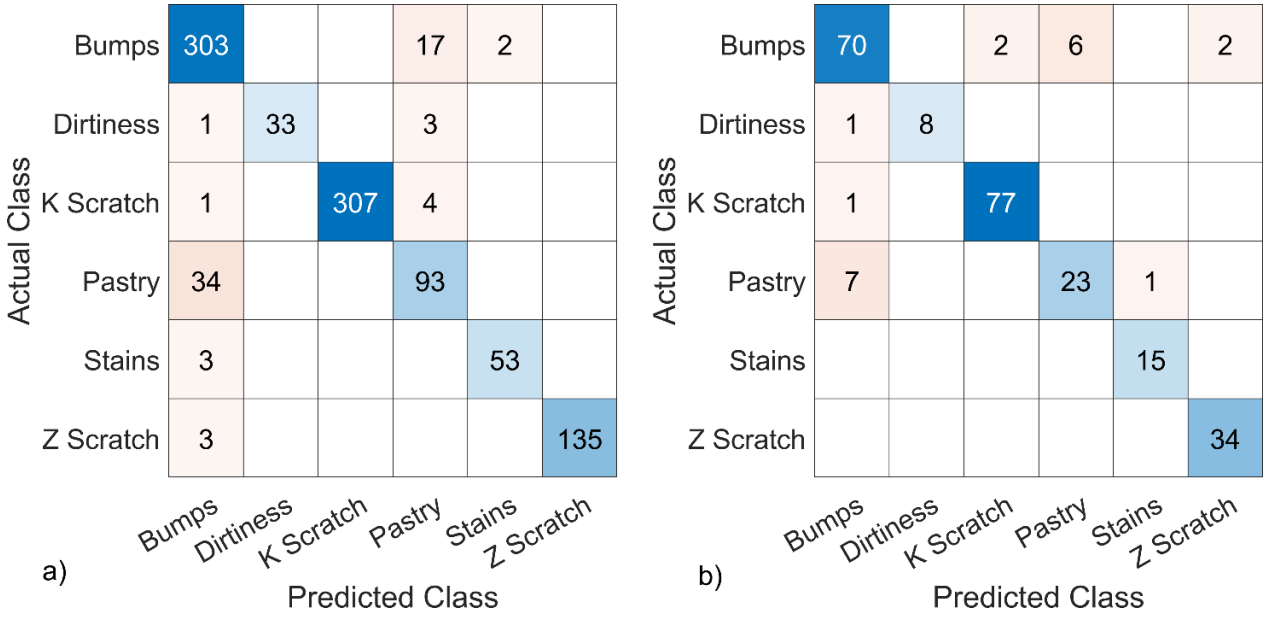

Figure 4. Multiclass confusion matrix for steel plate fault classification obtained from a) training dataset, b) test dataset

The performances of the developed models are compared with the related studies in the literature using the steel plate fault dataset in Table 7. The performances of the developed machine learning models were compared according to statistical metrics in terms of precision, recall, sensitivity and accuracy. However, in most of the studies, the majority of the aforesaid metrics are not given, instead only the accuracy score can be easily obtained. In some studies, the data set is also not divided into two as training and testing. Therefore, the values that cannot be found are marked as Not Given (NG).

Table 7. Comparison of the performance of the ML models with respect to related studies

References	ML Model	Training Dataset Metrics				Training Dataset Metrics			
		A (%)	P (%)	R (%)	S (%)	A (%)	P (%)	R (%)	S (%)
Fakhr and Elsayad, (2012)	DT	98.09	NG	NG	NG	97.25	NG	NG	NG
	NN	79.14	NG	NG	NG	74.79	NG	NG	NG
Tian et al., (2015)	GS-SVM	94.6	NG	NG	NG	77.7	NG	NG	NG
	GA-SVM	95.2	NG	NG	NG	77.2	NG	NG	NG
	PSO-SVM	88	NG	NG	NG	78.0	NG	NG	NG
Zhao et al., (2015)	NN	94.67	NG	NG	NG	88.05	NG	NG	NG
Chen, (2018)	DT	93.57	NG	NG	NG	85.43	NG	NG	NG
	RF	100	NG	NG	NG	90.29	NG	NG	NG
	Adaboost	100	NG	NG	NG	88.57	NG	NG	NG
	Bagging	96.30	NG	NG	NG	90.00	NG	NG	NG
Srivastava, (2019)	DT	NG	NG	NG	NG	76.04	NG	NG	NG
	RF	NG	NG	NG	NG	79.9	NG	NG	NG
	kNN	NG	NG	NG	NG	71.35	NG	NG	NG
	Adaboost	NG	NG	NG	NG	78.41	NG	NG	NG
	SVM	NG	NG	NG	NG	74.90	NG	NG	NG
Nkonyana et al., (2019)	SVM	NG	NG	NG	NG	73.6	NG	NG	NG
	NN	NG	NG	NG	NG	69.6	NG	NG	NG
	RF	NG	NG	NG	NG	77.8	NG	NG	NG
Kharal, (2020)	LR	89.13	NG	NG	NG	70.56	NG	NG	NG
	RF	94.18	NG	NG	NG	91.25	NG	NG	NG
Gamal et al., (2021)	DT	NG	NG	NG	NG	91.14	91.29	NG	91.14
	RF	NG	NG	NG	NG	91.29	91.86	NG	91.29
	SVM	NG	NG	NG	NG	86.00	74.57	NG	86.00
	LR	NG	NG	NG	NG	88.29	86.71	NG	88.29
Tasar (2022)	kNN	91.78	86.00	87.15	87.05	NG	NG	NG	NG
	SVM	93.28	88.02	89.28	88.44	NG	NG	NG	NG
	DT	93.01	88.47	89.30	88.82	NG	NG	NG	NG
	RF	95.47	92.09	93.17	92.37	NG	NG	NG	NG
	NN	96.98	94.75	95.54	94.87	NG	NG	NG	NG
This study	Adaboost	93.15	93.95	91.23	98.46	91.90	92.26	91.55	98.21
	Bagging	91.83	91.81	89.08	98.18	91.90	91.42	92.58	98.26
	RF	90.93	88.59	90.73	98.07	90.28	87.53	91.38	97.99

5. CONCLUSION

This article presents a comparative study of ensemble machine learning models such as Adaboost, Bagging, and Random Forest for multiclass fault classification of steel plates. The classification performance of the proposed models is presented using statistical metrics precision, recall, sensitivity and accuracy. The dataset provided in this study contains 27 independent features and 7 different failure classes. The dimension reduction method PCA was applied before training machine learning models. It is found that removing 12 insignificant features improves the performance of models. In addition, the other failure class, which was one of the failure classes, was excluded from the dataset since it was not a specific kind of failure class, but it was a combination of several classes. In conclusion, it can be said that the innovations and main contributions of this article are two-folds. First, this work discusses existing ML models using a steel plate failure dataset, and then, this work provides a comprehensive modelling approach to construct a computationally cheaper and more accurate ML model by applying the feature selection and hyperparameter optimization steps. Thus, it is thought that the developed model can more accurately adapt to sudden changes during production by determining the best model based on new information. Furthermore, in contrast to the previous studies, this article provides a systematic modelling approach that includes the normalization step in the data preparation stage to reduce the effects of outliers, the feature selection step in the dimension reduction stage to develop an ML model with a short computation time, and hyperparameter optimization step in the model development stage to increase the accuracy of the ML model. As the basic conclusion, this work determines that the Adaboost model is the most suitable model for fault detection problems. It can achieve high accuracy compared with the Bagging and Random Forest models. The Adaboost model achieves accuracy scores of 93.15% and 91.90% for training and test datasets, respectively. The second-best model is the Bagging model, which shows accuracy scores of 91.83% and 91.90% for training and test datasets, respectively. In conclusion, this study shows that ensemble machine learning models have the ability to accurately classify faults that occur during manufacturing, and they can replace manual inspection in decision support systems despite potential problems in practice.

7. CONFLICT OF INTEREST

Authors approve that to the best of their knowledge, there is not any conflict of interest or common interest with an institution/organization or a person that may affect the review process of the paper.

8. AUTHOR CONTRIBUTION

Erkan Caner OZKAT has the full responsibility of the paper about determining the concept of the research, data collection, data analysis and interpretation of the results, preparation of the manuscript and critical analysis of the intellectual content with the final approval.

9. NOMENCLATURE

A	accuracy score	NB	naive Bayes
DT	decision tree	NN	neural network
FN	false negative	P	precision
FP	false positive	PCA	principal component analysis
GA	genetic algorithm	PSO	particle swarm optimization
GS	grid search	R	recall
i	the index of actual class	RF	random forest
j	the index of predicted class	RMSE	root mean square error
kNN	k-nearest neighbour	S	specificity
LOF	local outlier factor	SPC	statistical processing control
LR	logistic regression	SVM	support vector machine
ML	machine learning	TN	true negative
N	number of sample	TP	true positive

10. REFERENCES

Alkan B., Bullock, S., Assessing operational complexity of manufacturing systems based on algorithmic complexity of key performance indicator time-series. Journal of the Operational Research Society 72(10), 2241-2255, 2021.

Backman J., Kyllönen V., Helaakoski H., Methods and tools of improving steel manufacturing processes: Current state and future methods. IFAC-PapersOnLine 52(13), 1174-1179, 2019.

Bektas O., Jones J. A., Sankararaman S., Roychoudhury I., Goebel K., Reconstructing secondary test database from PHM08 challenge data set. Data in Brief 21, 2464-2469, 2018.

Bektas O., Jones J. A., Sankararaman S., Roychoudhury I., Goebel K., A neural network framework for similarity-based prognostics. MethodsX 6, 383-390, 2019.

Buscema M., Terzi S., Tastle W., A new meta-classifier. Annual Meeting of the North American Fuzzy Information Processing Society (NAFIPS), Toronto, ON, Canada, July 12-14, 2010, pp: 1-7.

Ceryan N., Ozkat E. C., Korkmaz Can N., Ceryan S., Machine learning models to estimate the elastic modulus of weathered magmatic rocks. Environmental Earth Sciences 80(12), 1-24, 2021.

Chen J., The Application of tree-based ML algorithm in steel plates faults identification. Journal of Applied and Physical Sciences 4(2), 47-54, 2018.

Fakhr M., Elsayad A. M., Steel plates faults diagnosis with data mining models. Journal of Computer Science 8(4), 506-514, 2012.

Gamal M., Donkol A., Shaban A., Costantino F., Di G., Patriarca R., Anomalies detection in smart manufacturing using machine learning and deep learning algorithms. In Proceedings of the International Conference on Industrial Engineering and Operations Management, Rome, Italy, August 2-5, 2021, pp: 1611-1622.

Gao Y., Gao L., Li X., Yan X., A semi-supervised convolutional neural network-based method for steel surface defect recognition. Robotics and Computer-Integrated Manufacturing 61, 101825, 2020.

Kaggle, A., Faulty Steel Plates, Research Center of Sciences of Communication, https://www.kaggle.com/datasets/uciml/faulty-steel-plates, (Retrieved August 8, 2022), 2017.

Kahveci S., Alkan B., Musab H, A., Ahmad B., Harrison R., An end-to-end big data analytics platform for IoT-enabled smart factories: A case study of battery module assembly system for electric vehicles. Journal of Manufacturing Systems 63, 214-223, 2022.

Kazemi M. A. A., Hajian S., Kiani N., Quality Control and Classification of Steel Plates Faults Using Data Mining. Applied Mathematics Information Sciences Letters 6(2), 59-67, 2018.

Kharal A., Explainable artificial intelligence based fault diagnosis and insight harvesting for steel plates manufacturing. arXiv preprint arXiv:2008.04448, 2020.

Kurt R., Industry 4.0 in terms of industrial relations and its impacts on labour life. Procedia computer science 158, 590-601, 2019.

Lennox B., Montague G., Marjanovic O., Detection of faults in Batch Processes: Application to an industrial fermentation and a steel making process. Water Science and Technology, 2000.

Liu Y., Gao H., Guo L., Qin A., Cai C., You Z., A data-flow oriented deep ensemble learning method for real-time surface defect inspection. IEEE Transactions on Instrumentation and Measurement 69(7), 4681-4691, 2019.

Markoulidakis I., Rallis I., Georgoulas I., Kopsiaftis G., Doulamis A., Doulamis N., Multiclass Confusion Matrix Reduction Method and Its Application on Net Promoter Score Classification Problem. Technologies 9(4), 81, 2021.

Nkonyana T., Sun Y., Twala B., Dogo E., Performance evaluation of data mining techniques in steel manufacturing industry. Procedia Manufacturing 35, 623-628, 2019.

Ozkat E. C., Franciosa P., Ceglarek D., Laser dimpling process parameters selection and optimization using surrogate-driven process capability space. Optics & Laser Technology 93, 149-164, 2017a.

Ozkat E. C., Franciosa P., Ceglarek D., Development of decoupled multi-physics simulation for laser lap welding considering part-to-part gap. Journal of Laser Applications 29(2), 022423, 2017b.

Özkat E. C., Makine Öğrenmesi Metodolojisi Kullanılarak Yüksek Hızlı Rulmanlarda Sağlık Göstergesinin Belirlenmesi. Avrupa Bilim ve Teknoloji Dergisi (22), 176-183, 2021.

Pham T. A., Tran V. Q., Developing random forest hybridization models for estimating the axial bearing capacity of pile. Plos one, 17(3), e0265747, 2022.

Simić D., Svirčević V., Simić S., An approach of steel plates fault diagnosis in multiple classes decision making. In International Conference on Hybrid Artificial Intelligence Systems, Salamanca, Spain, June 11-13, 2014, pp: 86-97.

Srivastava A. K., Comparison analysis of machine learning algorithms for steel plate fault detection. International Research Journal of Engineering and Technology 6(4), 1231-1234, 2019.

Tasar B., Comparison Analysis of Machine Learning Algorithms for Steel Plate Fault Detection. Düzce Üniversitesi Bilim ve Teknoloji Dergisi 10(3), 1578-1588, 2022.

Tian Y., Fu M., Wu F. Steel plates fault diagnosis on the basis of support vector machines. Neurocomputing 151, 296-303, 2015.

Widodo A., Yang B. S., Support vector machine in machine condition monitoring and fault diagnosis. Mechanical systems and signal processing 21(6), 2560-2574, 2007.

Xiong J., Pang Q., Cheng W., Wang N., Yong Z., Reservoir risk modelling using a hybrid approach based on the feature selection technique and ensemble methods. Geocarto International 37(11), 3312-3336, 2022.

Xu L. D., Xu E. L., Li L. Industry 4.0: state of the art and future trends. International journal of production research 56(8), 2941-2962, 2018.

Yang K., Yu Z., Chen C. P., Cao W., Wong H. S., You J., Han G., Progressive hybrid classifier ensemble for imbalanced data. IEEE Transactions on Systems, Man, and Cybernetics: Systems 52(4), 2464-2478, 2021.

Zhang X., Kano M., Tani M., Mori J., Ise J., Harada K., Prediction and causal analysis of defects in steel products: Handling nonnegative and highly overdispersed count data. Control Engineering Practice 95, 104258, 2020.

Zhao Z., Yang J., Lu W., Wang X., Application of local outlier factor method and back-propagation neural network for steel plates fault diagnosis. In The 27th Chinese Control and Decision Conference (2015 CCDC), Qingdao, China, 23-25 May, 2015, pp: 2416-2421.

JOURNAL of
MATERIALS and MECHATRONICS:A

e-ISSN 2717-8811
JournalMM, 2022, 3(2), 257-274
https://doi.org/10.55546/jmm.1188617

Araştırma Makalesi / Research Article

Numerical Investigations on Operation Modes and Transients of IPM Machines with Dual Windings

Tayfun GUNDOGDU[1, 2]*

[1] Hakkâri Üniversitesi, Mühendislik Fakültesi, Elektrik-Elektronik Mühendisliği Bölümü, Hakkâri, Türkiye
[2] GAMAK Makina Sanayi A.Ş., Dudullu OSB, Baraj Yolu Cad. No:2 34776 Ümraniye/İstanbul, Türkiye
ORCID ID: https://orcid.org/0000-0002-7150-1860, tgundogdu@gamak.com

Geliş/ Received: 13.10.2022; **Kabul / Accepted:** 07.11.2022

ABSTRACT: This paper investigates the flux-weakening characteristics and transient response of a dual winding interior permanent magnet (DWIPM) machine designed using the 2010 Toyota Prius IPM Machine specifications. In order to thoroughly adjust the main flux, dual windings are fed by separate identical inverters. Thus, significantly high-torque for high-speed requirements can be simply achieved by making one of the inverters open-circuited. Transient response of the DWIPM machine, including torque and current pulsations, occurring during normal drive or deactivation of one of the inverters has also been investigated for different operation modes. The flux-weakening performance characteristics of the proposed DWIPM machine have been compared with those of its single-fed counterpart in order to highlight the benefits and drawbacks of the dual-winding topology. The steady-state performance characteristics, torque/speed and power/speed curves, efficiency maps, machine transient response, different machine design options with various numbers of turns per phase and current amplitudes, and the importance of the electromagnetic coupling between dual windings have all been addressed. For transient and steady-state analyses, 2D, nonlinear, time-stepping finite element method (FEM) has been employed. It has been revealed that the proposed DWIPM machine exhibit significantly improved flux-weakening characteristics, particularly high-power at constant power region and high efficiency at constant torque region, and quite low current and torque pulsations occurring during operation mode change.

Keywords: Flux-Weakening, Interior Permanent Magnet Machine, Dual Winding Topology, Traction Application, Transient Response.

*Sorumlu yazar / Corresponding author: tgundogdu@gamak.com

Bu makaleye atıf yapmak için /To cite this article

Gundogdu T. (2022). Numerical Investigations on Operation Modes and Transients of IPM Machines with Dual Windings. Journal of Materials and Mechatronics: A (JournalMM), 3(2), 257-274.

1. INTRODUCTION

In recent years, the flux-weakening capability of an electric machine has grown increasingly crucial in specific applications such more electric vehicles, aircraft, rail traction, and ship propulsion. It is frequently necessary to increase an electric machine's speed control range. The highest possible inverter voltage, and consequently the voltage that is available for a particular back-electromotive force (EMF) amplitude, set a limit on the speed. In the case that the motor is fed by an inverter using voltage to frequency (V/f) regulation, the speed range is roughly two to three times the base speed (Dubey, 1989). The flux-weakening concept, machine parameter changes, and inverter rating can all be used to some extent to extend the speed range.

Many different methods have been proposed to improve the flux-weakening capability of electric machines. Among these methods, winding reconfiguration/changeover and number of turn change techniques (Swamy et al., 2005; Maemura et al., 2005; Kume et al., 1991; Gündoğdu, 2022) and double fed or dual inverter method (Tang et al., 2017; Takatsuka et al., 2014; Fuchs et al., 2008; Schraud et al., 2008; Hijikata et al., 2012; Lin et al., 2020) are the most popular ones. The electrical winding changeover technique is an effective way to extend the speed control range (Kume et al., 2004; Swamy et al., 2005; Maemura et al., 2005; Kume et al., 1991; Gündoğdu, 2022). Making the power losses in the converter as modest as feasible is another crucial factor to take into account for motor drive systems (Gündoğdu, 2022; Tang et al., 2017; Takatsuka et al., 2014). In (Gündoğdu, 2022), the windings number of turn change method has been successfully implemented into an IPM machine and a significantly improved torque at constant power region and increased efficiency at constant torque region has been achieved. It has been reported in (Tang et al., 2017) that the reconfigurable windings enable a reduction in motor size for a given power rating as well as an increase in motor output power for a given size, while also enhancing system drive cycle efficiency. In order to achieve high efficiency motor driving, (Takatsuka et al., 2014) describes an electronic winding changeover technique that effectively controls the low- and high-speed winding modes. Using electronic switches, it has been suggested in (Fuchs et al., 2008) and (Schraud et al., 2008) to increase the speed range by reconfiguring the windings in real-time. The windings can be switched from one containing a variable number of poles to another, or from one connecting in series to another, depending on how many turns are in each phase. In a similar study (Hijikata et al., 2012), an online winding reconfiguration method is proposed to change the winding layout from conventional to concentrated or vice versa in order to change the motor's whole characteristics. Moreover, the winding reconfiguration method is utilized for a line-start permanent magnet machine to improve the starting and steady-state performance characteristics (Lin et al., 2020).

A comprehensive study on double-fed IPM machines has been presented in (Gundogdu, 2022). It is reported that the proposed double winding with double inverter topology provides a good field-regulation capability without magnet demagnetization. In (Fukuda et al., 2019) and (Barcaro et al., 2010), a multi-phase double-winding permanent magnet machine with an integrated inverter is proposed to reduce the current per output power, extend speed range and also to increase the fault tolerance. Moreover, improved drive characteristics, fault-tolerant features, and redundancy of a double-winding permanent magnet machine have been experimentally shown (Noguchi et al., 2018).

By switching the coil arrangement from series to parallel or altering the number of turns per coil, windings can be reconfigured in order to alter the flux-weakening properties. This could result in losses directly correlated to rotor speed due to an undesired voltage unbalance between winding

groups and circulating currents, or even failures. Therefore, transient response and circulating currents for machines with reconfigurable or dual windings have been studied by many researchers (Copt et al., 2015; Daniels et al., 2019; Im et al., 2019; Sin et al., 2020; Sadeghi et al., 2012).

In this study, the flux-weakening capability and also the efficiency map of an IPM machine having dual windings have been investigated together with transient response during operation mode change. Activation of windings according to different operation modes has been determined for different maximum current levels. In addition, how to design a cost-effective drive with inverters having low current levels is presented. The main idea behind dual winding and inverter topology is to change the number of turns of windings and hence change the inductance in order to reduce the level of induced voltage and consequently increase the torque level at constant power region by keeping the current level at high. Firstly, the steady-state and the flux-weakening performance characteristics, including torque/speed curves, power/speed curves and efficiency maps of the DWIPM machine have been calculated and compared to its single-fed counterpart. Then, transient responses, including phase current and torque pulsations, occurring during operation mode change have been investigated. It has been found that significantly improved flux-weakening characteristics can be achieved thanks to the proposed topology. In addition, the significant level of torque and current pulsations occurring during operation mode change can be minimized by gradually changing the current level of inverters.

2. OPERATION MODES AND STEADY-STATE PERFORMANCE

2.1 Design Specifications and Steady-State Performance

Dual windings, each accommodated in the same stator slots and fed by separate inverters, are proposed in order to alter the main flux and so enhance the flux-weakening capability of an IPM machine. The proposed IPM machine is designed using the primary geometric and operational requirements of the Toyota Prius 2010 IPM machine which has 48-stator slot, 8-pole and conventional (integer slot distributed winding) single-layer windings. Note that the dual winding counterpart (proposed) IPM machine of the Toyota Prius 2010 IPM machine has the identical winding layout. The design specifications, material properties and also the some key steady-state performance characteristics of the proposed IPM machine is listed in Table 1. The 2D view of the proposed IPM machine's model, mesh structure and also the steady-state flux distributions are shown in Figure 1(a), (b), (c) and (d), respectively. In addition, the BH curve and core loss characteristics for various frequencies are illustrated in Figure 2. For the numeric calculations, the ANSYS Electronics program, which is based on the 2D, non-linear, time-stepping finite element method (FEM), is employed to calculate the transients and steady-state characteristics. Note that once both windings (main and aux) are excited simultaneously, the proposed IPM machine works as a conventional single three phase machine. More details about the operation modes of the proposed IPM machine is given in Section 2.2.

Table 1. Design, operating, and material specifications of the IPM machine together with the steady-state (rated) performance characteristics

Parameter	Unit	Value
Phase Current	A	236
Max. Inverter Voltage	V	650
Rated Speed	rpm	950
Rated Torque	Nm	222
Torque Ripple @ 950 rpm	%	8.43
Back-EMF Amplitude @ 950 rpm	V	65

Table 1. (Continued) Design, operating, and material specifications of the IPM machine together with the steady-state (rated) performance characteristics

Parameter		Unit	Value
Back-EMF THD @ 950 rpm		%	14.3
Efficiency @ 950 rpm		%	~81
Max. Speed		rpm	20000
Stator Outer Diameter		mm	264
Stator Inner Diameter		mm	161.9
Stator axial length		mm	50.8
Rotor Inner Diameter		mm	51
Air-gap		mm	0.73
Number of Slot			48
Turns per coil			11
Parallel brunches			2
Coils in series per phase			8
Number of turns per phase			88×2
PM dimensions (W× T)		mm^2	35.76×7.16
Slot fill factor			0.45
Core Material			M270-35A
	Hysteresis loss coefficient (K_h)		179.04
	Classical loss coefficient (K_c)		0.375
	Excess loss coefficient (K_e)		0.262
	Mass density (ρ)	kg/m^3	7650
	Stacking factor (K_{fe})		0.93
PM material			NdFeB35
	Permeability		1.05
	Conductivity (σ)	s/m	625000
	Coercivity (H_c)	A/m	-805399.8
	Mass density ρ	kg/m^3	7607

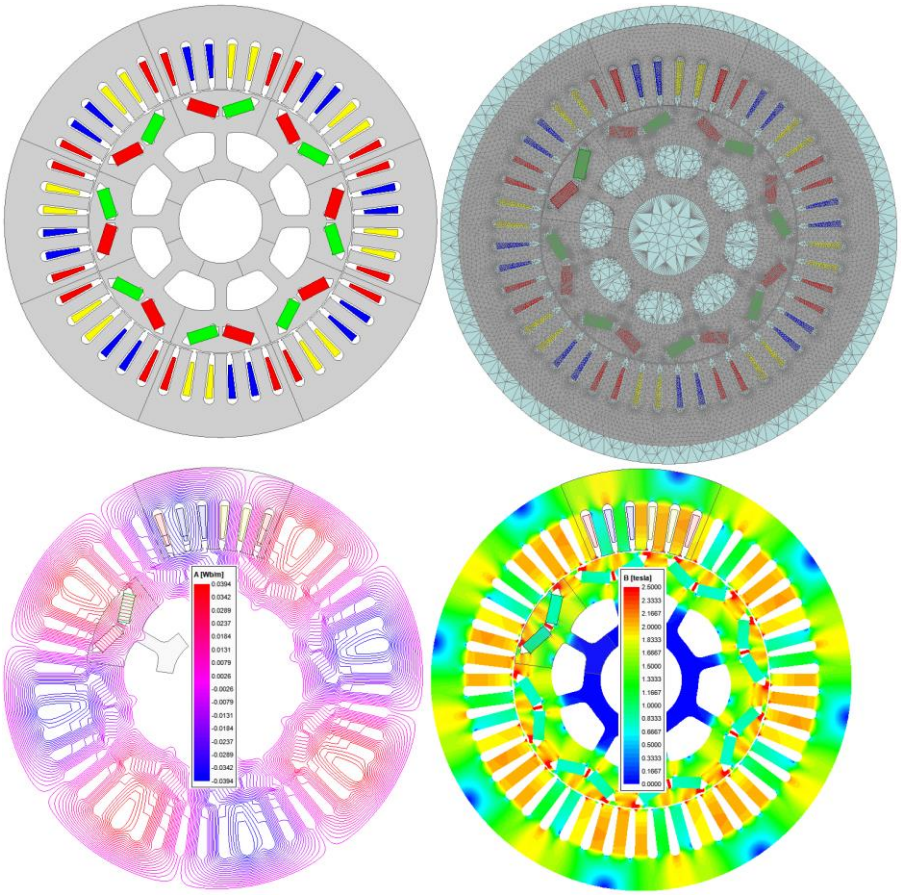

Figure 1. Machine model and magnetic field distributions: (a) IPM Machine model; (b) mesh stracture; (c) magnetic flux distribution; (d) flux density distributions

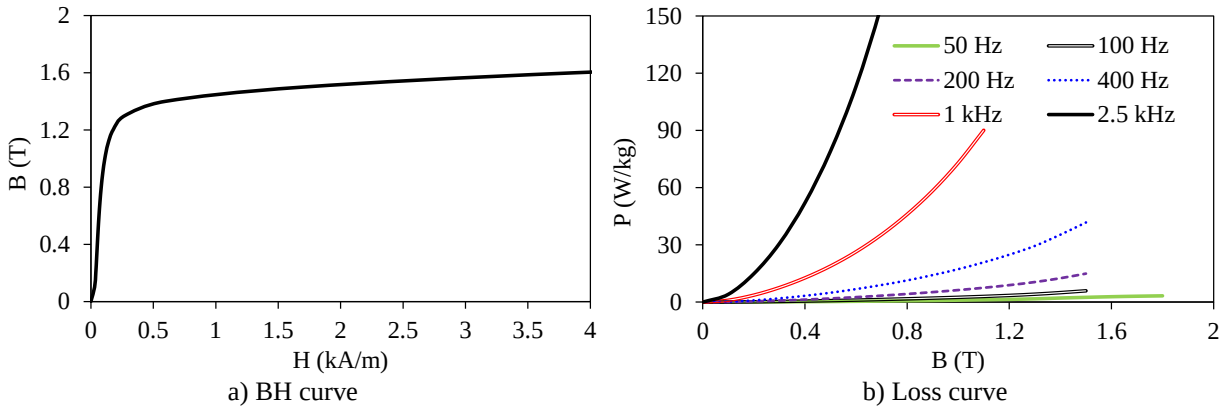

a) BH curve b) Loss curve

Figure 2. Magnetic properties of M270-35A core material

2.2 Operation Modes

In order to drive the DWIPM machine in accordance with traction applications, the IGBT inverters, consisting of IGBT power modules to assure high frequency and voltage/power switching operations, can be utilized. Depending on the inverters' maximum current, it is feasible to determine the number of turns for the windings. The same torque amplitude can be obtained by utilizing a parallel branched winding arrangement because the output torque is a function of MMF, or indeed the number of turns multiplied by current amplitude. Thus, cheaper excitation system (batteries and inverters) with low current levels can be utilized to operate the machine without sacrificing the torque amplitude. The both topologies have been shown in Figure 3. As can be seen, it is possible to operate the proposed dual winding IPM machine by connecting the identical inverters in parallel and changing the excitation current level. Thus, high efficiency at low-speed (cruise mode) operation and high-power at high-speed operation mode can be achieved.

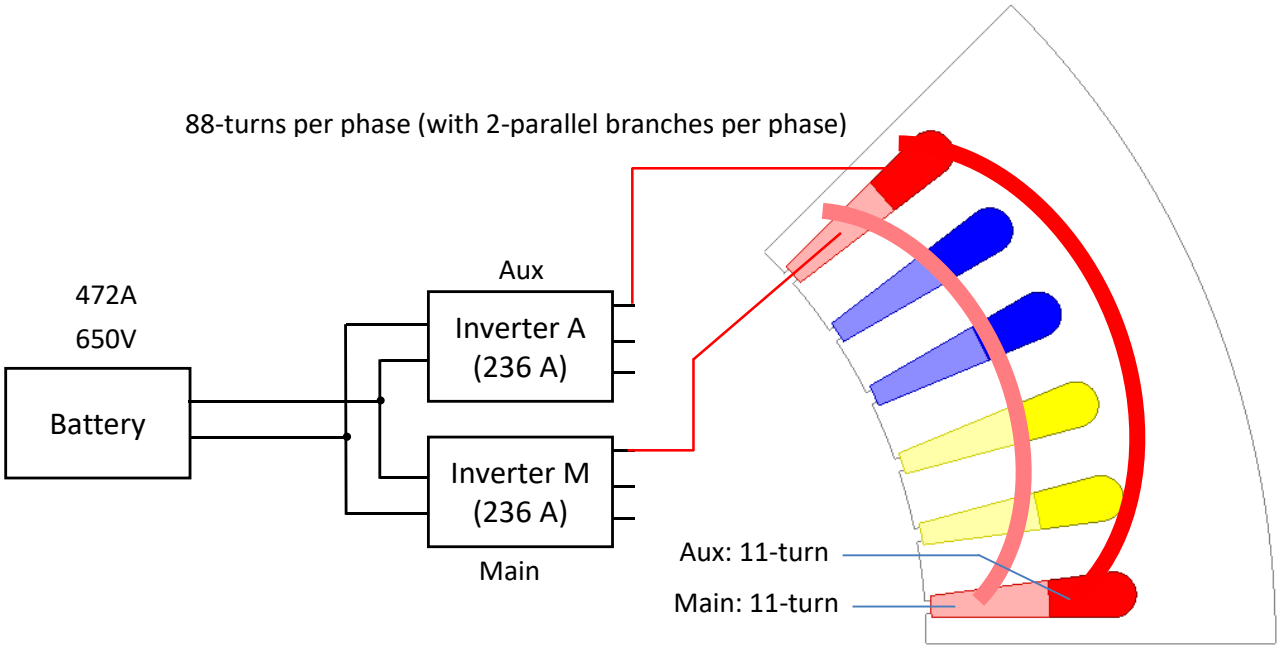

a) 236A Inverter (DWIPM-1)

Figure 3. Parallel connected identical inverters for improved flux-weakening capability and redundancy

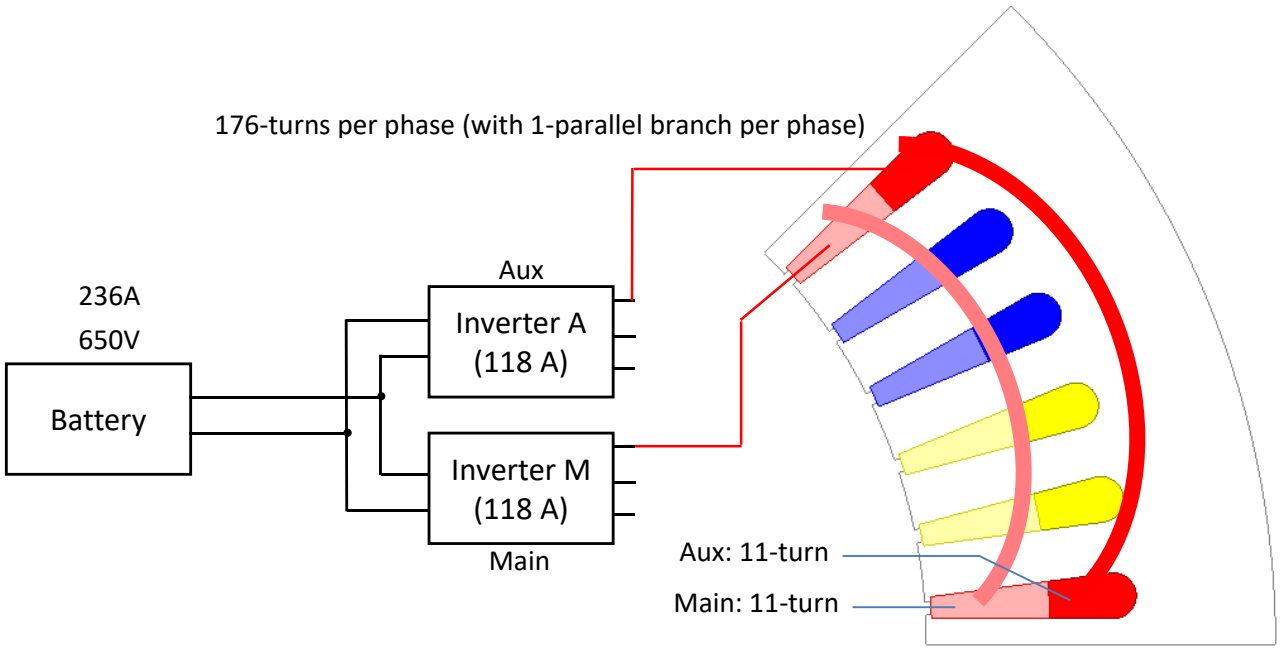

b) 118A Inverter (DWIPM-2)

Figure 3. (Continued) Parallel connected identical inverters for improved flux-weakening capability and redundancy

Different operation modes and corresponding inverter current (I_{max}) rates and also the phase resistance (R_{phase}) and the maxsimum torque (T_{max}) amplitudes are given in Table 2. Note that 'M//A' indicates that the main 'M' and auxiliary 'A' windings are connected parallel through the inverters and excited simultaneously. As can be seen, thanks to the dual windings, it is possible to obtain cruise, hill climbing, and high-speed modes. Depending on the road conditions, the possible highest efficiency can be achieved thanks to the orientation of the active winding and hence the inverter. Each winding group has 11-turn per phase with 2-parallel branches. Therefore, the total number of serial turns per phase is 11. As seen in Figure 3, two identical inverter whose maximum current rates are 236A is used for each winding group. Note that, if the battery current is limited to 236A (see Figure 3(a)), then the maximum inverter current rate can be reduced to half. However, in order to maintain the torque, the number of turns should be doubled. It can be done easily by reducing the parallel branch number from two to one. Thus, all the electromagnetic performance characteristics will remain the same for the constant torque region. However, since the voltage requirement is doubled, theoretically, the power at high speed will be halved. If the inverter voltage doubled (2×650V), then the similar performance with the 236A excitation can be obtained. Moreover, it is advantageous to use more stranded windings in terms of avoiding extra eddy current losses at high-speed operations.

Table 2. Operation modes and corresponding inverter currents at constant torque region

		Mode	Active Winding	I_{max} per inverter (A)	R_{phase} @ 100°C (Ω)	T_{max} @ 1krpm (Nm)
472A DWIPM-1	1	Cruise 1	M//A	59	0.0248177	64.61
	2	Cruise 2	M//A	118	0.0248177	136.33
	3	Hill	M//A	236	0.0248177	239.3
	4	High-Speed 1	M	236	0.04737	139.3
	5	High-Speed 2	M	118	0.04737	65.03
236A (k_{fill} = 0.448) DWIPM-2 (650V)	1	Cruise 1	M//A	29.5	0.10087	64.61
	2	Cruise 2	M//A	59	0.10087	136.33
	3	Hill	M//A	118	0.10087	239.3
	4	High-Speed 1	M	118	0.19248	139.3
	5	High-Speed 2	M	59	0.19248	65.03

As a conclusion, if very high-power is not required for the high-speed operations, then in order to reduce inverter cost and size; 118A design can be more reasonable candidate. The investigation of design with 118A (with doubled number of turns as shown in Figure 3(b) corresponding to DWPIM-1 in Table 2) has been considered in this study.

3. FLUX-WEAKENING CHARACTERISTICS ACCORDING TO OPERATION MODES

The torque/speed and power/speed characteristics, calculated based on Table 2 for various operation modes, are illustrated in Figure 4 and Figure 5, respectively. 'MA' indicates that both the main and auxiliary windings are excited simultaneously and 'M' indicates that only the main winding is excited. Note that the flux-weakening characteristics of 'MA (236A)' mode is identical to Toyota Prius 2010 IPM machine's performance. Because, as mentioned previous, once both windings are excited simultaneously with the maximum inverter current, it acts as a conventional single-fed machine. As seen in the figure, by reducing the current of the auxiliary winding to zero, it is possible to change to the number of turns from 88 to 44 per phase. Consequently, it is possible to achieve quite high power at high-speed operations. In the same manner, it is possible to achieve high torque at the constant torque region by simultaneously exciting the both the main and auxiliary windings with the maximum current (236A). Corresponding efficiency maps for each operation mode are illustrated between Figure 6 and Figure 8.

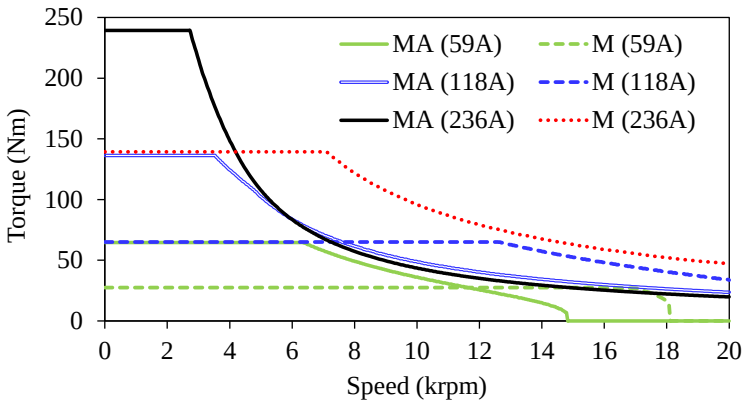

Figure 4. Torque/speed characteristics for different operation modes

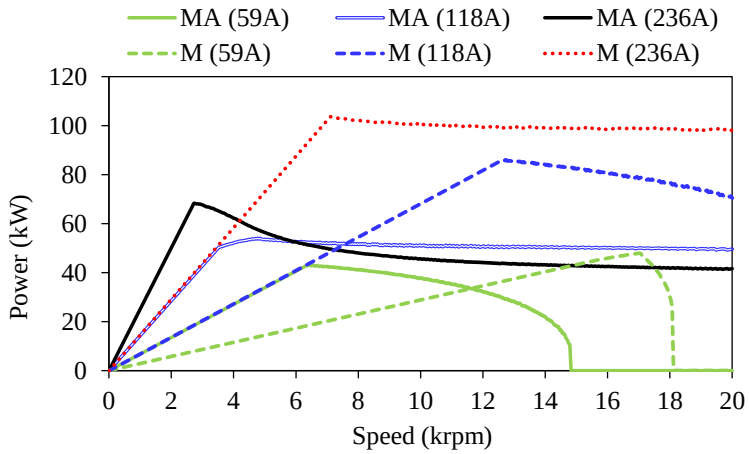

Figure 5. Power/speed characteristics for different operation modes

In order to determine which winding group excitation at low-speed operation mode has the advantage in terms of torque and efficiency, the torque/power-speed and efficiency maps can be compared. Considering efficiency map graphs, it can be deduced that at low-speed operations the 'MA' ensures higher torque and higher efficiency at the same current excitation level as the 'M'. In the same manner, at high-speed operations, excitation of the 'M' ensures higher torque and efficiency than that of the 'MA'.

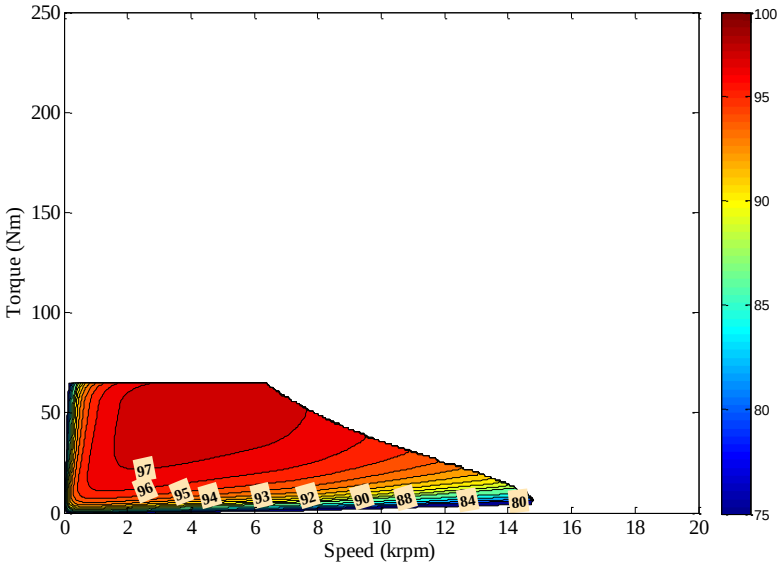

a) 'MA' (59A)

Figure 6. Efficiency map of 59A operation modes with (a) MA

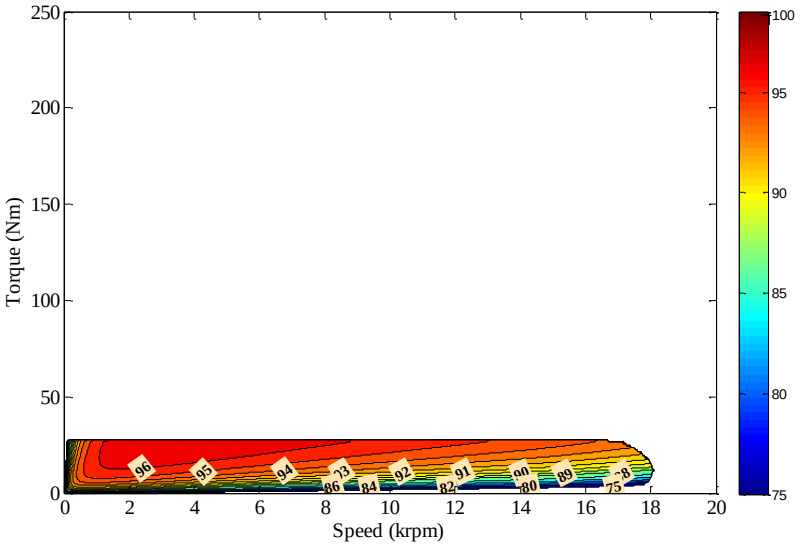

b) 'M' (118A)

Figure 6. (Continued) Efficiency map of 59A operation modes with (b) M

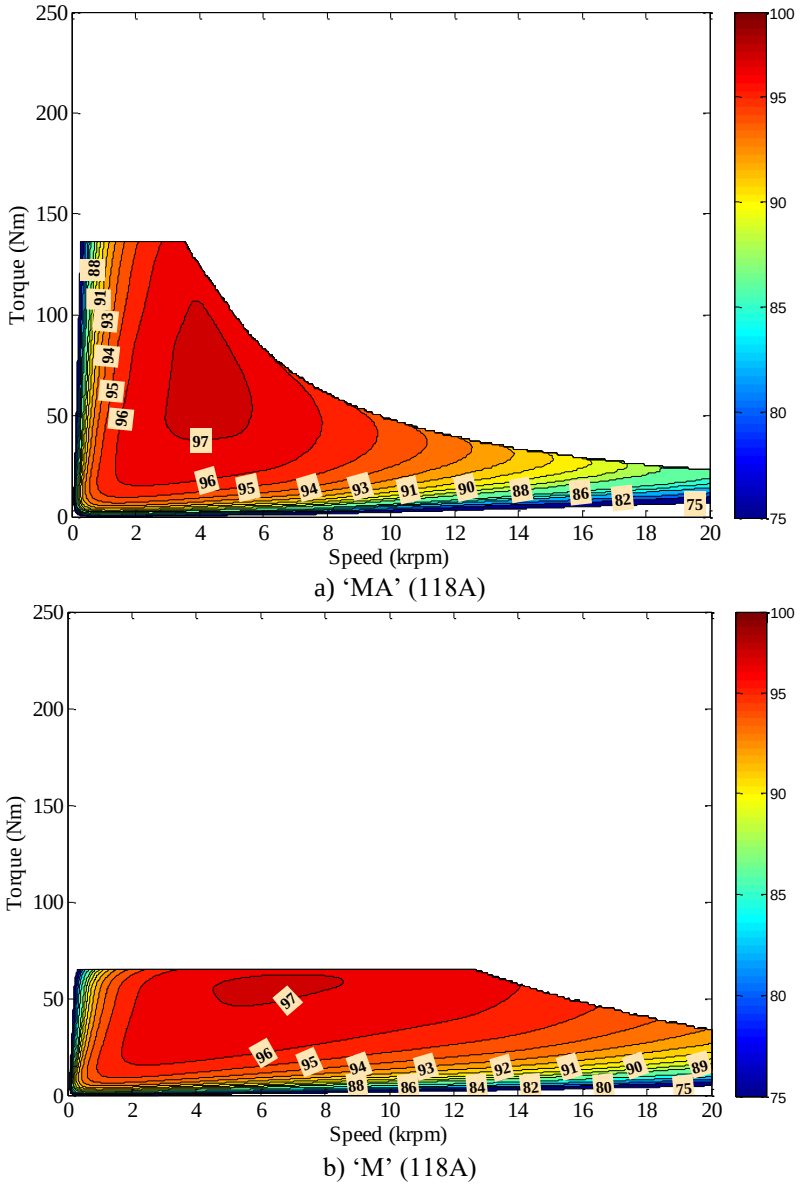

a) 'MA' (118A)

b) 'M' (118A)

Figure 7. Efficiency map of 118A operation modes with 'MA' (a) and 'M' (b)

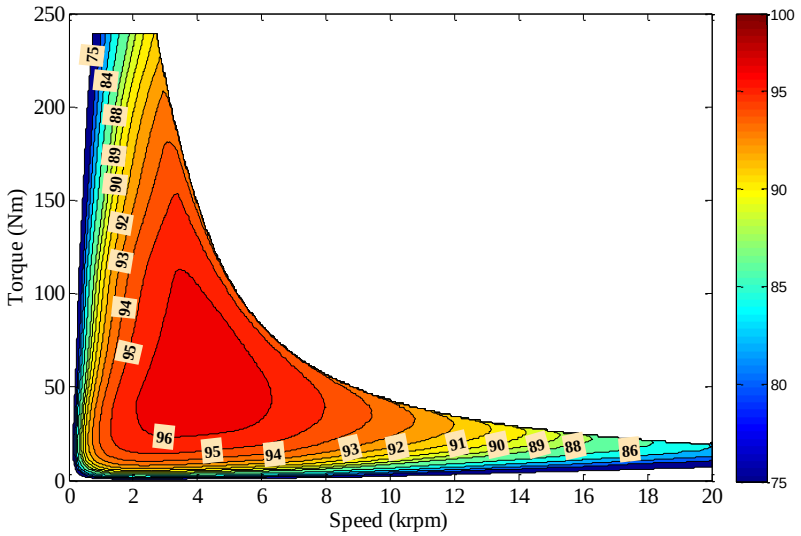

a) 'MA' (236A) and also original Toyota Prius IPM machine (ORG)

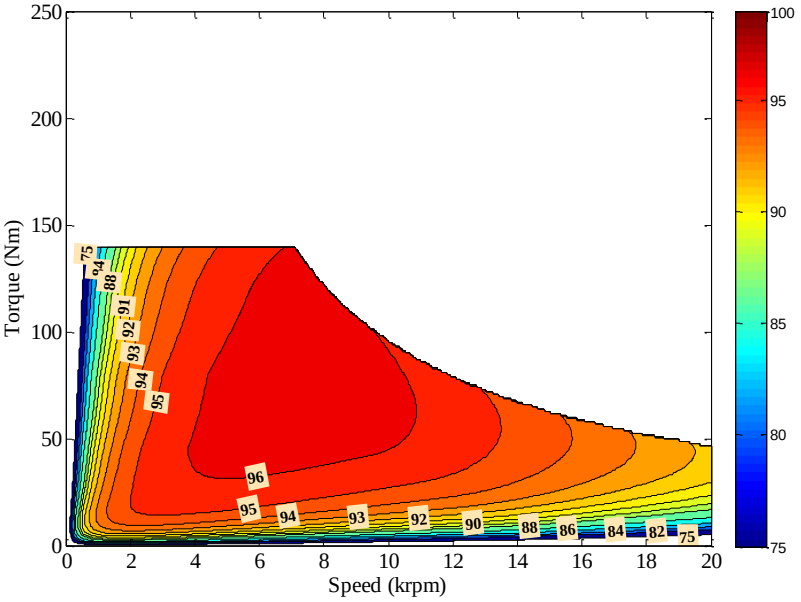

b) 'M' (236A)

Figure 8. Efficiency map of 236A operation modes with 'MA' (a) and 'M' (b)

In order to reveal the merits of the proposed method, the torque/power-speed characteristics of the DWIPM machine is compared with the original (ORG) IPM machine having conventional single 3-phase, single-layer windings and single inverter. It is obvious that thanks to the dual inverter drive, the maximum power at deep-flux weakening region is increased from ~40kW to ~100kW without sacrificing the maximum torque at the constant torque region as seen in Figure 9.

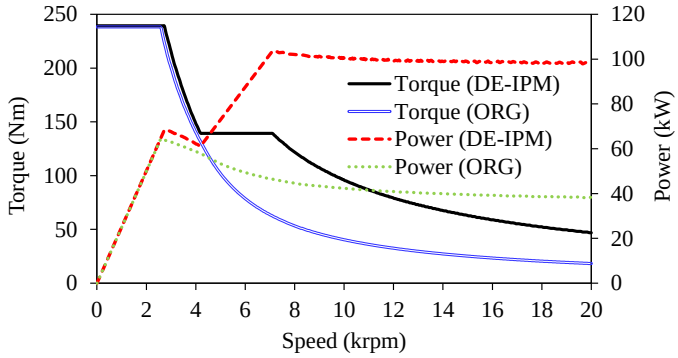

Figure 9. Integrated torque/power-speed characteristics

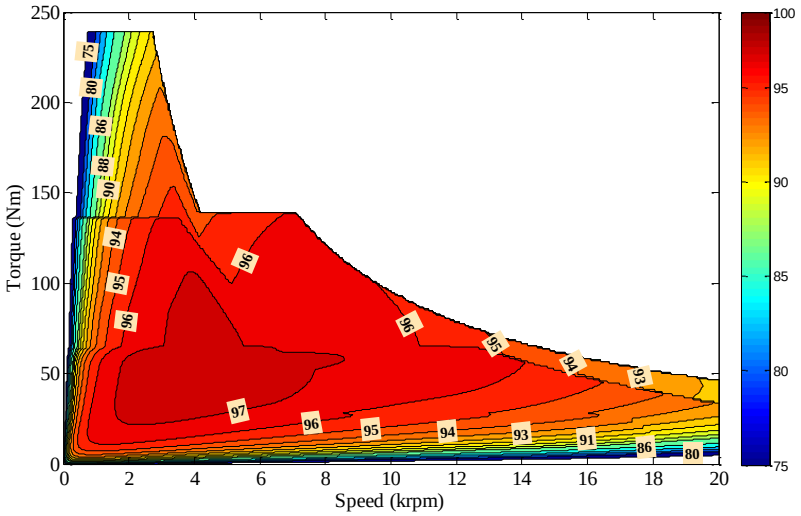

Figure 10. Integrated efficiency map showing all the available operation modes

The efficiency map, integrated from all the available operation modes, is shown in Figure 10. As clearly seen, 96% covers the larges area and the maximum efficiency is 97% achieved between ~1.8krpm and ~9krpm. Considering the original IPM machine's efficiency map (see Figure 8(a)), the efficiency at the cruise mode operation is increased significantly.

In conclusion, thanks to the proposed DWIPM topology, much higher efficiency in cruise mode and much higher power at the high-speed operation mode have been achieved when compared to single-excitation operation.

4. TRANSIENTS OCCURING DURING OPERATION MODE CHANGE

In this section, transient-state of the DWIPM machine during the operation mode change has been examined. Normally, the voltage and hence current level can be adjusted smoothly for operating mode changes by changing the voltage amplitude slowly. However, in some road conditions, fast voltage chance or winding changeover can be required. Therefore, it is necessary to investigate the transient response during operation mode changes. The electromagnetic torque and phase current transient responses during changing winding or voltage have been investigated by FEM. In order to observe the transients during the mode changes, different voltage injections have been assigned to the phase windings. Operating modes and corresponding phase current excitations are illustrated in Figure 11. Operating modes of the DWIPM is summarized as follows.

$\boxed{A}$ → Both inverters are active and the control is identical $I_A = I_M$
$\boxed{B}$ → Both inverters are active, the control is not identical $I_A = I_{max}$ and $I_M \to 0$
$\boxed{C}$ → Only one inverter feeding the main windings is active, $I_A = I_{max}$
$\boxed{D}$ → Only one inverter feeding the main windings is active, $I_A \to 0$

Note that I_A and I_M indicate the auxiliary and main winding inverter current amplitudes, respectively. Considering the operation modes and Figure 11, it can be deduced that transients occur only 'A' and 'B' regions since both inverters are activated.

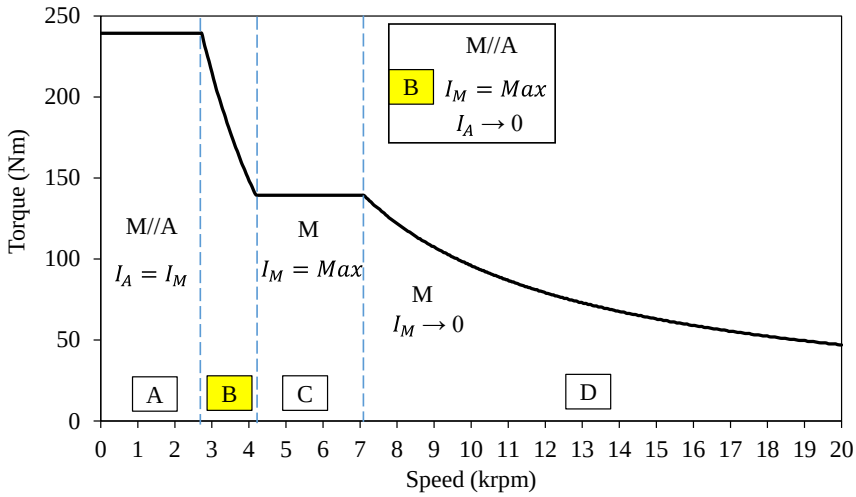

Figure 11. Operating modes and corresponding winding currents

4.1 Operation Region A

In this section, the transient response during region 'A' operation, illustrated in Figure 11, is investigated. The imposed speed is 1krpm and the maximum inverter current is taken as 118A. In order to observe the transient responses, the simulations have been set up to be run at (a) 29.5A and then (a') 63A peak current. The torque and phase current pulsations occurring during voltage change from (a) to (a') are illustrated in Figure 12 and Figure 13, respectively and summarized in Table 3. It can be observed that if the current is increased to its two times higher amplitude directly, very high pulsations occur. Therefore, it would be very safe to perform the operation mode changes should be done gradually with several steps. For instance, in order to avoid the high pulsations, ripples, faults, and any other devastating effects, instead of increasing the current from 29.5A to 59A directly, it can be increased by 5A by 6-steps. As seen in Figure 13, a very smooth transition can be obtained by gradually increasing the current amplitude. It has been shown that it is possible to reduce the torque pulsations ~5 times by increasing the current gradually rather than increasing the current according to direct current increment. Investigation of the pulsation for the 118A maximum inverter current is also investigated and the obtained results have been shown in Figure 14 and Figure 15. It has been revealed that once the current amplitude is increased, the fault time is shortened. The peak-to-peak (T_{p2p}) and average torque (T_{avg}) amounts are shown in Figure 14. Considering the findings presented for the operation region 'A', it can be deduced that in order to reduce the transient response and its effects, current regulation should be done by relatively small steps.

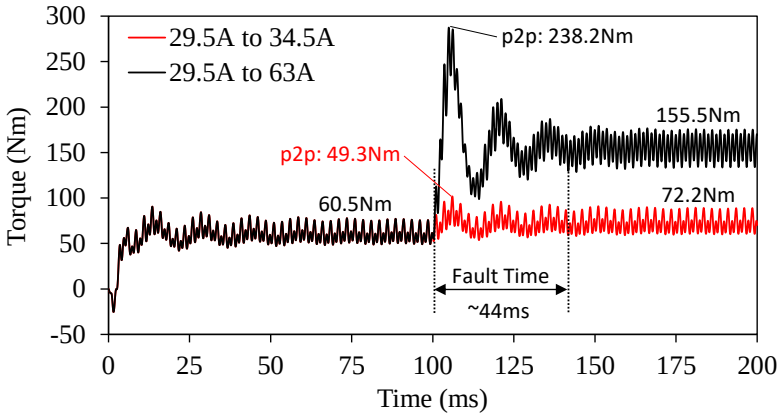

Figure 12. DWIPM machine electromagnetic torque and its transient response during the mode changing operation in region 'A'

Table 3. Torque and current pulsation percentages

State	I_{phase} Resultant	T_{ripple} (%) Before Fault	T_{p2p} (%) During Fault	T_{ripple} (%) After Fault	I_{p2p} (%) During Fault
(a)	29.5A → 34.5A	52.6	81.5/65.28	44.16	46.77/40
(a')	29.5A → 63A	52.6	393.72/153.2	30.6	423.7/198.4

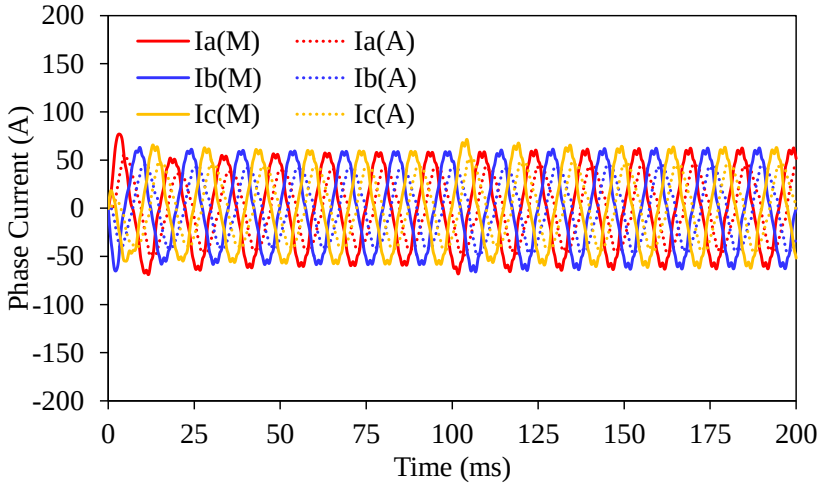

a) Phase current pulsation for the 29.5A→34.5A

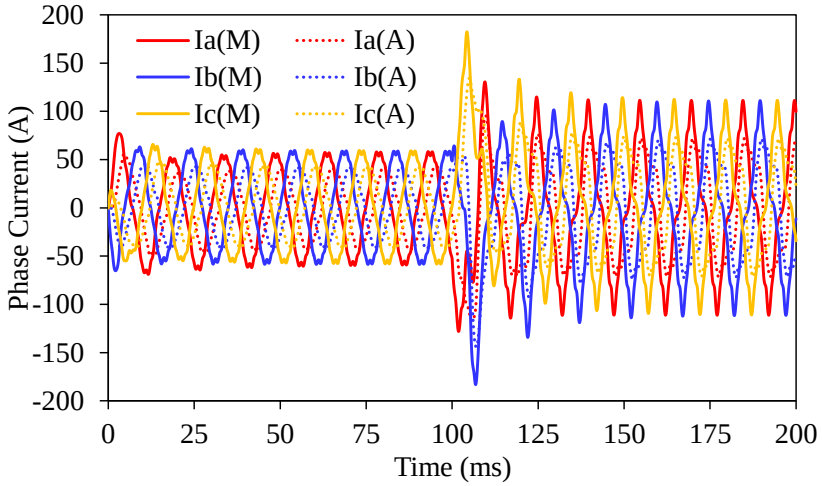

b) Phase current pulsation for the 29.5A→63A

Figure 13. Current pulsations during the mode change operation in region 'A'

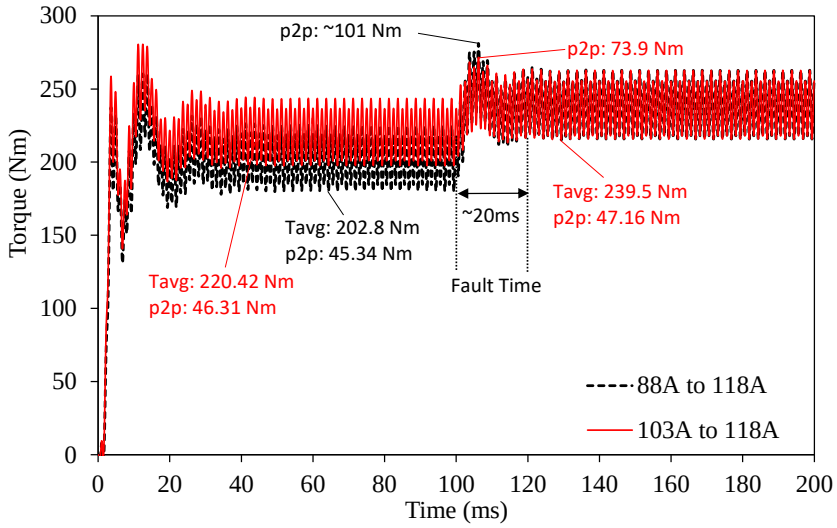

Figure 14. Torque pulsations for maximum inverter current

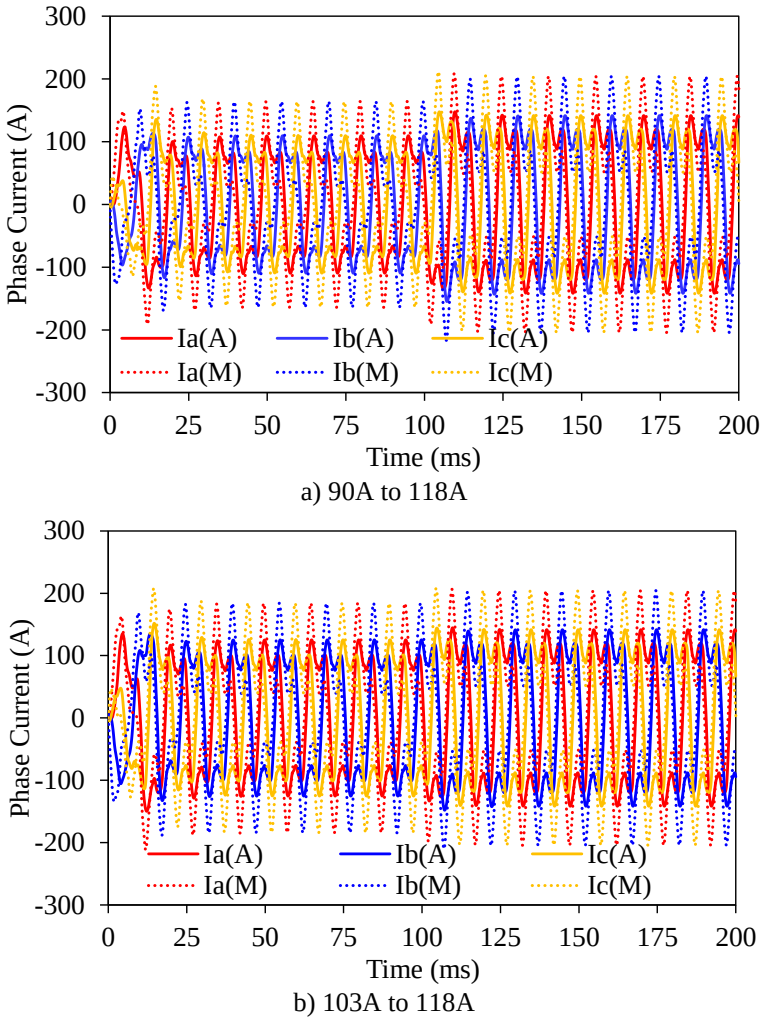

Figure 15. Current pulsations for maximum inverter current

4.2 Operation Region B

For the operation region 'B', the imposed speed is selected as 3krpm, and the maximum inverter current is taken as 118A. Since the inverters do not feed the windings with identical current amplitudes and angles, this operation region is the most critical operating region. Because of the coupling effect of the main and auxiliary windings (see Figure 16), a certain amount of voltage is induced in the auxiliary windings.

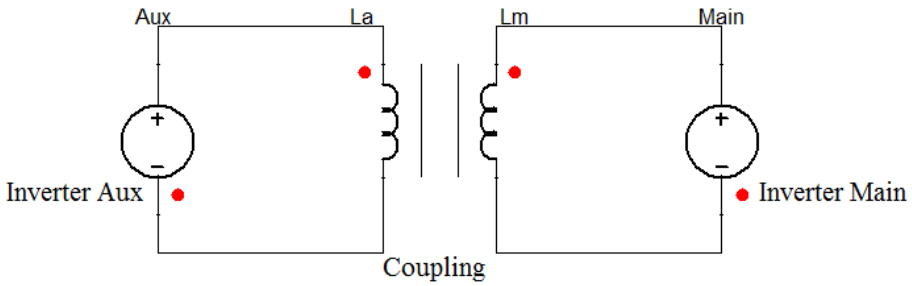

Figure 16. Schematic representation of coupling between the main and aux windings

In addition, if the amount of the induced voltage is higher than that of the inverter's voltage, the direction of the power is changed. Which means that if the current of the inverter is lower than that of the aux winding due to the coupling effect, inner circuit and circulating currents cause the inverter to failure. Therefore, an additional control algorithm is required in order to protect the

inverter from the induced voltage due to the coupling between the auxiliary and main windings. The torque and current pulsations that occurred during the operating mode change are shown in Figure 17 and Figure 18.

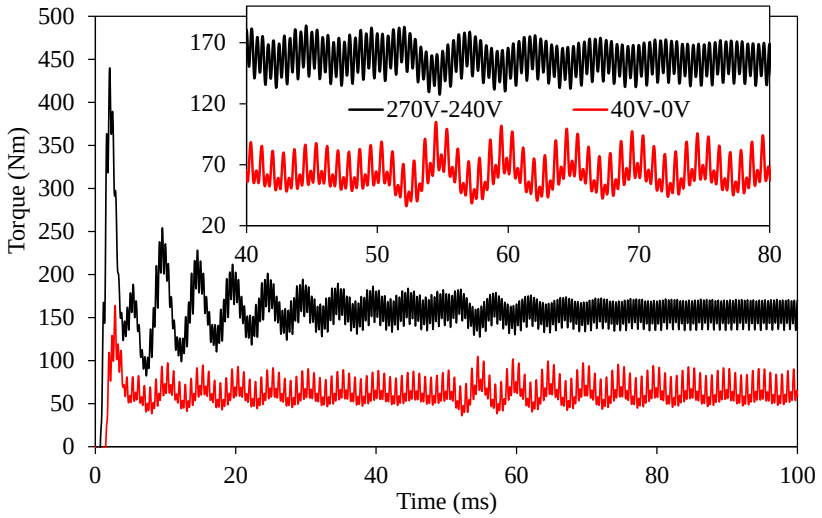

Figure 17. DWIPM machine electromagnetic torque and its transient response during the different mode changing operation

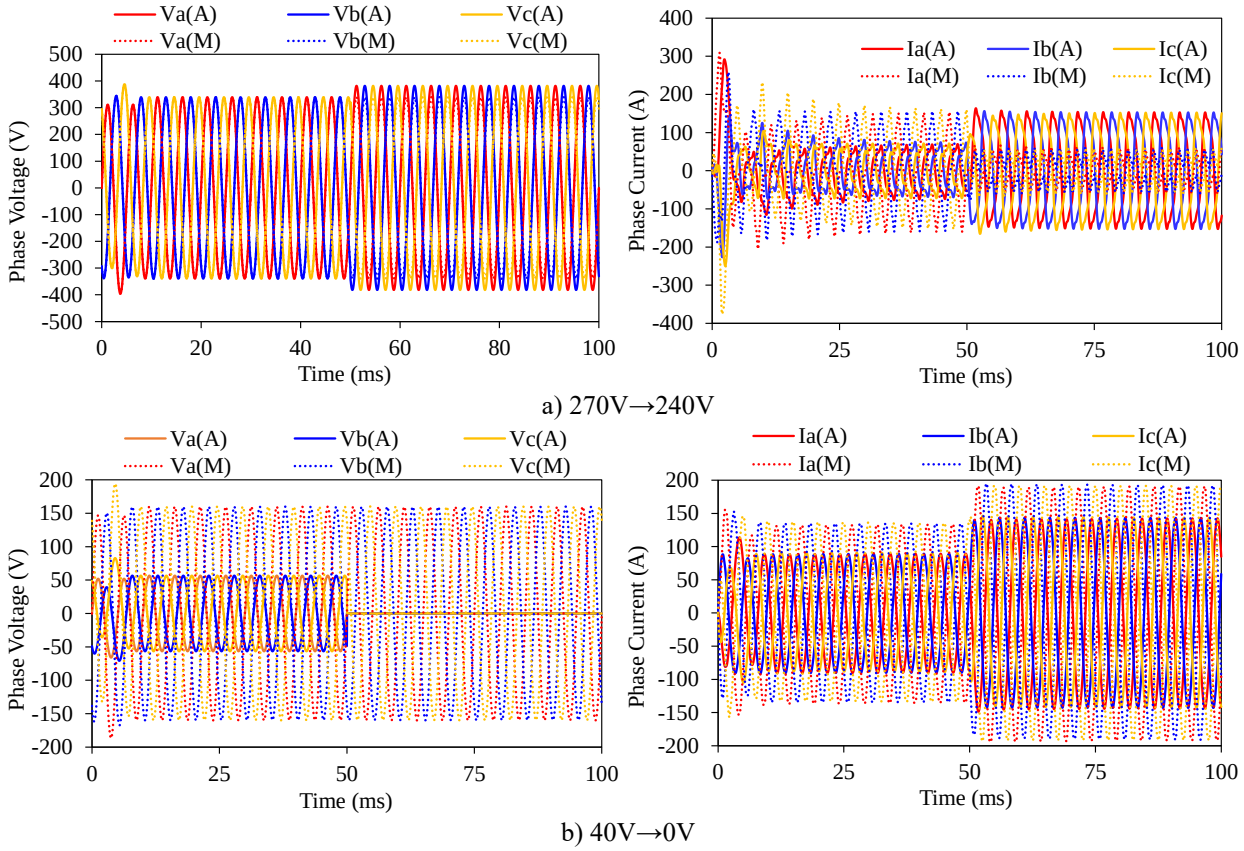

Figure 18. Current pulsations for maximum inverter current

As can be observed, in the operating region 'B', the amount of the current should be reduced in order to waken the flux. Therefore, while the main windings are fed with the maximum inverter voltage, the voltage of the auxiliary windings is reduced from 270V to 240V and 40V to 0V. As seen in the figures, the pulsations are not very high. On the other hand, as explained before, even if the

voltage of the auxiliary is reduced to 0V from 40V (inverter of the auxiliary winding should be open circuit for 0V), because of the coupling effect of the main windings, the current level of the auxiliary winding is increased. Therefore, it can be concluded that the inverter voltage of the auxiliary winding is already lower than the induced voltage of the auxiliary windings. Therefore, since the direction of the power is turned from the motor to the generator, the current coming from the inverter is decreased the amplitude. However, once the auxiliary inverter is open-circuited, the induced voltage of the auxiliary windings is increased (Figure 18(b)). Therefore, in order to avoid possible failures, an additional control algorithm should be added to the control scheme of the inverters for the operating region 'B'.

5. DISCUSSION ON FINDINGS AND CONCLUSION

In this study, a comprehensive investigation of the steady-state performance, flux-weakening characteristics, and transient response of an IPM machine with dual three–phase windings supplied by two parallel inverters have been presented. This dual winding strategy gives IPM machines an extra degree of control by allowing them to adjust the amount of series turns each phase and provides redundancy. It has been revealed that the reconfiguration of the IPM machine's windings with dual windings and excitation with dual inverters significantly improves the flux-weakening capability and makes it possible to minimize the transient torque and current during operation mode change. Thanks to the proposed dual winding topology, the followings have been achieved;

- Significantly improved torque/speed and power/speed characteristics;
- Significantly increased efficiency, particularly in cruise mode;
- Reduced transient response and its effects thanks to the current regulation by relatively small steps;
- Very smooth operating mode changes: it is possible to reduce the torque pulsations ~5 times via gradually incensement of current;

Moreover, it has been revealed that the circulating currents due to the coupling effect between the dual windings should be considered with care to avoid failures.

A synopsis of the future work includes demagnetization analyses and an investigation into the influence of the number of phases on the performance characteristics and transient response.

6. CONFLICT OF INTEREST

Author approves that to the best of his knowledge, there is not any conflict of interest or common interest with an institution/organization or a person that may affect the review process of the paper.

7. AUTHOR CONTRIBUTION

Tayfun GUNDOGDU has the full responsibility of the paper about determining the concept of the research, data collection, data analysis and interpretation of the results, preparation of the manuscript and critical analysis of the intellectual content with the final approval.

8. REFERENCES

Barcaro M., Bianchi N., Magnussen F., Analysis and Tests of a Dual Three-Phase 12-Slot 10-Pole Permanent-Magnet Motor. IEEE Transactions on Industry Applications 46(6), 2355-2362, 2010.

Copt F., Koechli C., Perriard Y., Minimizing the Circulating Currents of a Slotless BLDC Motor Through Winding Reconfiguration. IEEE Energy Conversion Congress and Exposition (ECCE), Montreal, QC, Canada, 20-24 September 2015, pp. 6497-6502.

Daniels B., Gurung J., Huisman H., Lomonova E. A., Feasibility Study of Multi-Phase Machine Winding Reconfiguration for Fully Electric Vehicles, International Conference on Ecological Vehicles and Renewable Energies (EVER), Monte-Carlo, Monaco, 02-10 May 2019, pp: 1-6.

Dubey G. K., Power Semiconductor Controlled Drives. Englewood Cliffs, NJ: Prentice-Hall, 07632, 1989.

Fuchs E. F., Schraud J., Fuchs F. S., Analysis of Critical-Speed Increase of Induction Machines via Winding Reconfiguration with Solid-State Switches. IEEE Transactions on Energy Conversion, 23(3), 774-780, 2008.

Fukuda K., Akatsu K., 5-Phase Double Winding PMSM With Integrated SiC Inverter for in-Wheel Motor, International Conference on Electrical Machines and Systems (ICEMS), Harbin, China, 11-14 August 2019, pp: 1-5.

Gundogdu T., Design and Analysis of Double Fed Interior Permanent Magnet Machines for Traction Applications, IEEE IAS Global Conference on Emerging Technologies (GlobConET), Arad, Romania, 20-22 May 2022, pp: 1036-1042.

Gündoğdu T., Improving the Flux-Weakening Capability of Interior Permanent Magnet Machines by Number of Turns Changing Methodology. Turkish Journal of Science and Technology 17(2), 375-394, 2022.

Hijikata H., Akatsu K., Design Technique and Online Winding Reconfigurations Method of MATRIX Motor, International Power Electronics and Motion Control Conference, Harbin, China, 02-05 June 2012, pp: 713-718.

Im S. H., Park G. M., Gu B. G., Novel Winding Changeover Method for a High Efficiency AC Motor Drive, IEEE Energy Conversion Congress and Exposition (ECCE), Baltimore, MD, USA, 29 Sept. – 03 Oct. 2019, pp: 2347-2352.

Kume T., Iwakane T., Sawa T. Y., Nagai I., A Wide Constant Power Range Vector-Controlled AC Motor Drive Using Winding Changeover Technique. IEEE Transactions on Industry Applications 27(5), 934-939, 1991.

Kume T., Swamy M., A Quick Transition Electronic Winding Changeover Technique for Extended Speed Ranges, IEEE Power Electronics Specialists Conference, Aachen, Germany, 20-25 June 2004, pp: 3384-3389.

Lin M., Li D., Zhao Y., Ren X., Qu R., Improvement of Starting Performance for Line-Start Permanent Magnet Motors by Winding Reconfiguration. IEEE Transactions on Industry Applications 56(3), 2441-2450, 2020.

Maemura A., Morimoto S., Yamada K., Sawa T., Kume T. J., Swamy M. M., A Novel Method for Extending Stroke Length in Moving Magnet Type Linear Motor Drive System by Employing Winding Changeover Technique. IEEJ International Power Electronics Conference, Niigata, Japan, 2005.

Noguchi S., Dohmeki H., Improvement of Torque Ripple Characteristics of Double Winding PMSM with Using Twin Inverters, IEEE International Magnetics Conference (INTERMAG), Singapore, 23-27 April 2018, pp: 1-5.

Sadeghi S., Guo L., Toliyat H. A., Parsa L., Wide Operational Speed Range of Five-Phase Permanent Magnet Machines by Using Different Stator Winding Configurations. IEEE Transactions on Industrial Electronics 59(6), 2621-2631, 2012.

Schraud J., Fuchs E. F., Fuchs H. A., Experimental Verification of Critical-Speed Increase of Single-Phase Induction Machines via Winding Reconfiguration with Solid-State Switches. IEEE Transactions on Energy Conversion 23(2), 460-465, 2008.

Sin S., Ayub M., Kwon B. I., Operation Method of Non-Salient Permanent Magnet Synchronous Machine for Extended Speed Range. IEEE Access 8, 105922-105935, 2020.

Swamy M. M., Kume T. A., Morimoto S., Extended High-Speed Operation Via Electronic Winding-Change Method for AC Motors. IEEE Transactions on Industry Applications 42(3), 742-752, 2006.

Takatsuka Y., Hara H., Yamada K., Maemura A., Kume T., A Wide Speed Range High Efficiency EV Drive System Using Winding Changeover Technique and SiC Devices, International Power Electronics Conference, Hiroshima, Japan, 18-21 May 2014, pp: 1898-1903.

Tang L., Burress T., Pries J. A Reconfigurable-Winding System for Electric Vehicle Drive Applications, IEEE Transportation Electrification Conference and Expo (ITEC), Chicago, IL, USA, 22-24 June 2017, pp: 656-661.

JOURNAL of
MATERIALS and MECHATRONICS:A

e-ISSN 2717-8811
JournalMM, 2022, 3(2), 275-289
https://doi.org/10.55546/jmm.1196409

Araştırma Makalesi / Research Article

Real-Time Application of Traffic Sign Recognition Algorithm with Deep Learning

Faruk Emre AYSAL[1]*, Kasım YILDIRIM[2], Enes CENGİZ[3]

[1] Afyon Kocatepe Üniversitesi, Teknoloji Fakültesi, Mekatronik Mühendisliği Bölümü, Afyonkarahisar, Türkiye,
ORCID ID: https://orcid.org/0000-0002-9514-1425, faysal@aku.edu.tr
[2] Afyon Kocatepe Üniversitesi Teknoloji Fakültesi, Mekatronik Mühendisliği Bölümü, Afyonkarahisar, Türkiye,
ORCID ID: https://orcid.org/0000-0002-5393-3889, kasimm.yildirimm@outlook.com
[3] Sinop Üniversitesi, Ayancık Meslek Yüksek Okulu, Elektronik ve Otomasyon Bölümü, Sinop, Türkiye,
ORCID ID: https://orcid.org/0000-0003-1127-2194, ecengiz@sinop.edu.tr

Geliş/ Received: 29.10.2022; **Kabul / Accepted:** 30.11.2022

ABSTRACT: Autonomous vehicles are one of the increasingly widespread application areas in automotive technology. These vehicles show significant potential in improving transportation systems, with their ability to communicate, coordinate and drive autonomously. These vehicles, which move from source to destination without human intervention, appear to be a solution to various problems caused by people in traffic, such as accidents and traffic jams. Traffic accidents and traffic jams are largely due to driver faults and non-compliance with traffic rules. For this reason, it is predicted that integrating artificial intelligence (AI)-based systems into autonomous vehicles will be a solution to such situations, which are seen as a problem in social life. Looking at the literature, VGGNet, ResNet50, MobileNetV2, NASNetMobile, Feed Forward Neural Networks, Recurrent Neural Networks, Long-Short Term Memory, and Gate Recurrent Units It is seen that deep learning models such as these are widely used in traffic sign classification studies. Unlike previous studies, in this study, a deep learning application was made for the detection of traffic signs and markers using an open-source data set and models of YOLOv5 versions. The original data set was prepared and used in the study. Labeling of this data set in accordance with different AI models has been completed. In the developed CNN models, the training process of the data set containing 15 different traffic sign classes was carried out. The results of these models were systematically compared, and optimum performance values were obtained from the models with hyper parameter changes. Real-time application was made using the YOLOv5s model. As a result, a success rate of 98-99% was achieved.

Keywords: Deep Learning, Autonomous Vehicle, Real-Time, YOLOv5.

*Sorumlu yazar / Corresponding author: faysal@aku.edu.tr

Bu makaleye atıf yapmak için /To cite this article

Aysal, F. E., Yıldırım, K., Cengiz, E. (2022). Real-Time Application of Traffic Sign Recognition Algorithm with Deep Learning. Journal of Materials and Mechatronics: A (JournalMM), 3(2), 275-289.

1. INTRODUCTION

The growth in total number of vehicles in the world has increased exponentially over the last ten years. Population growth in the world causes increased traffic density, increasingly congested roads, transportation problems, air pollution, accidents with injury or loss of life (Jain et al., 2018). These events are undesirable but important consequences of modern transportation systems (Satria and Castro, 2016). The approach of existing rules and regulations to prevent traffic accidents is often not effective enough. Raising awareness, strict enforcement of traffic rules, and scientific engineering measures are seen as the needs of the society to prevent this public health problem (Gopalakrishnan, 2012). These reasons necessitate the optimization of the traffic network to meet the transportation needs of the city (Dorokhin et al., 2020).

The adoption of autonomous vehicle technology is known to have many benefits compared to conventional vehicles, such as higher reliability, better traffic flow, and reduction in traffic congestion (Fagnant et al., 2015). AI, the basis of autonomous vehicle technology, is a general term that can interact with the environment, aims to simulate human intelligence, and implies the use of a computer to model intelligent behavior with minimal human intervention (Glikson and Woolley, 2020). In other words, it is defined as the ability of a system to correctly interpret external data, learn from such data, and use these learnings to achieve specific goals and tasks through flexible adaptation (Kaplan and Haenlein, 2019). Due to the exponential increase in popularity and use of AI-based techniques in various applications over the past few years, there has been a thriving increase in the use of autonomous vehicles around the world (Miglani and Kumar, 2019). Thanks to this increase, it is expected that traditional vehicles will be replaced by smart vehicles that can decide on their own and perform driving tasks in the near future. (Kulkarni et al., 2018). These vehicles, which move to a specific destination without human intervention, emerge as solutions to various problems such as accidents and traffic jams (Sarkar et al., 2018; Rajabli et al., 2020). Deep learning-based detection of traffic signs, which have an important place in the regulation of traffic flow, plays a key role in the decision mechanism of autonomous cars. Therefore, it is predicted that integrating deep learning-based systems into autonomous vehicles will be a solution to the problems seen in social life. In the studies to be carried out for this purpose, image processing-based leather learning applications come to the fore. Image processing is a method of performing some operations on an image to obtain an enhanced image or extract useful information from it. It is a type of signal processing where the input is an image, and the output can be an image or features associated with that image (Kour et al., 2012; Wiley and Lucas, 2018; Bayram, 2020). In the field of image processing, feature and feature determination operations play a very important role. Before the features are obtained, binarization, thresholding, resizing, normalization, etc. are performed on the sampled image. Various image preprocessing techniques are performed. Then, feature extraction techniques are applied to obtain features that will be useful in classification and recognition of images. (Kumar and Bhatia, 2014). Autonomous decision support systems that provide enhanced image recognition performance can be developed by using the data obtained by image processing techniques as training data in various deep learning algorithms (Guo et al., 2016; Zhou et al., 2019; Khan et al., 2018; Hasan et al., 2020; Shrestha et al., 2019; Sampedro et al., 2017; Zhao et al., 2019; Huval et al., 2015; Kulkarni et al., 2018; Miglani et al., 2019; Eraqi et al., 2017).

Lim et al. proposed a method that uses real-time traffic sign detection based on GPGPU (General-Purpose Graphics Processing Unit) and performs zone detection and recognition using a

hierarchical model. This method produces stable results in low-illumination environments. It performed both detection and hierarchical recognition in real-time, and the proposed method reached an F1 score of 0.97 in the aggregated data set. (Lim et al., 2017). Çetin and Ortataş have created different datasets of six signs related to traffic signs and markers used in Turkey. Trained the model with the Haarcascade machine learning algorithm and tested the training data by simulating the behavior of the autonomous vehicle on the track. (Cetin and Ortatas, 2021). Palandz and Bayrakçı trained using the data set consisting of 4000 traffic signposts, ResNet50, MobileNetV2, and NASNetMobile models. They achieved an accuracy of 97.62% in the ResNet50 model, 97.8% in the MobileNetV2 model, and 98.56% in the NASNetMobile model. (Palandiz and Bayrakçı, 2021). Swaminathan et al. performed image recognition application for the detection of traffic signs using Convolutional Neural Network (CNN). They tried to design a system that could respond in real-time with an Arduino-controlled autonomous car. To examine the performance of this road sign recognition system, they conducted various experiments using the Belgian Traffic Signs dataset and achieved 83.7% accuracy with this approach (Swaminathan et al., 2019).

In this study, the accuracy and execution time performances of different deep learning models in real-time were systematically compared on autonomous vehicles. The original data set of various traffic signs prepared by us was included in the study and examined more comprehensively. The data was systematically learned in current deep learning models such as YOLOv4, YOLOv4-tiny, YOLOv5s, YOLOv5m, YOLOv5x, Faster R-CNN, Mask R-CNN. In the classification process, it was seen that the YOLOv5x model performed better than other models.

The rest of the work is organized as follows. In Chapter 2, the material and method part is given. In this section, general information about the dataset and models used is given. As a result of the different model trainings carried out in Chapter 3, the confusion matrix was examined, and the model efficiencies were compared. 4. Finally, the conclusion section is concluded by reporting the results of the most efficient model and talking about the general outlines of the study.

2. MATERIALS AND METHODS

The flow chart of the work carried out is presented in Figure 1. In the first stage, there is the process of preparing the data set containing the traffic signs, which will constitute an important part of the learning stage for different classes (Stop, Green Light, Park, etc.). The next step is to perform different label operations for the data set containing 26 different classes, for the deep learning models (YOLOv5s, YOLOv5m, YOLOv5x) to be used. The labeling process distinguishes itself in the form of rectangles, polygons, points, lines, etc. The reason for this distinction is that the desired output form from deep learning models is not the same. The training outputs may differ with applications such as masking, segmentation, and detection. For this reason, it is important to carry out labeling processes in accordance with the deep learning models that are desired to be used. The learning phase begins with the introduction of the data set, which has been labeled and made ready for the learning phase, to different deep learning models. Then there is a systematic comparison of the learning performances of the models. Among the models that are systematically compared, the best model is determined according to the output data. TensorRT technology is used to make this model compatible with the hardware. As a result of this process, it is aimed to test the model suitable for the hardware in real-time in the field and to report the results.

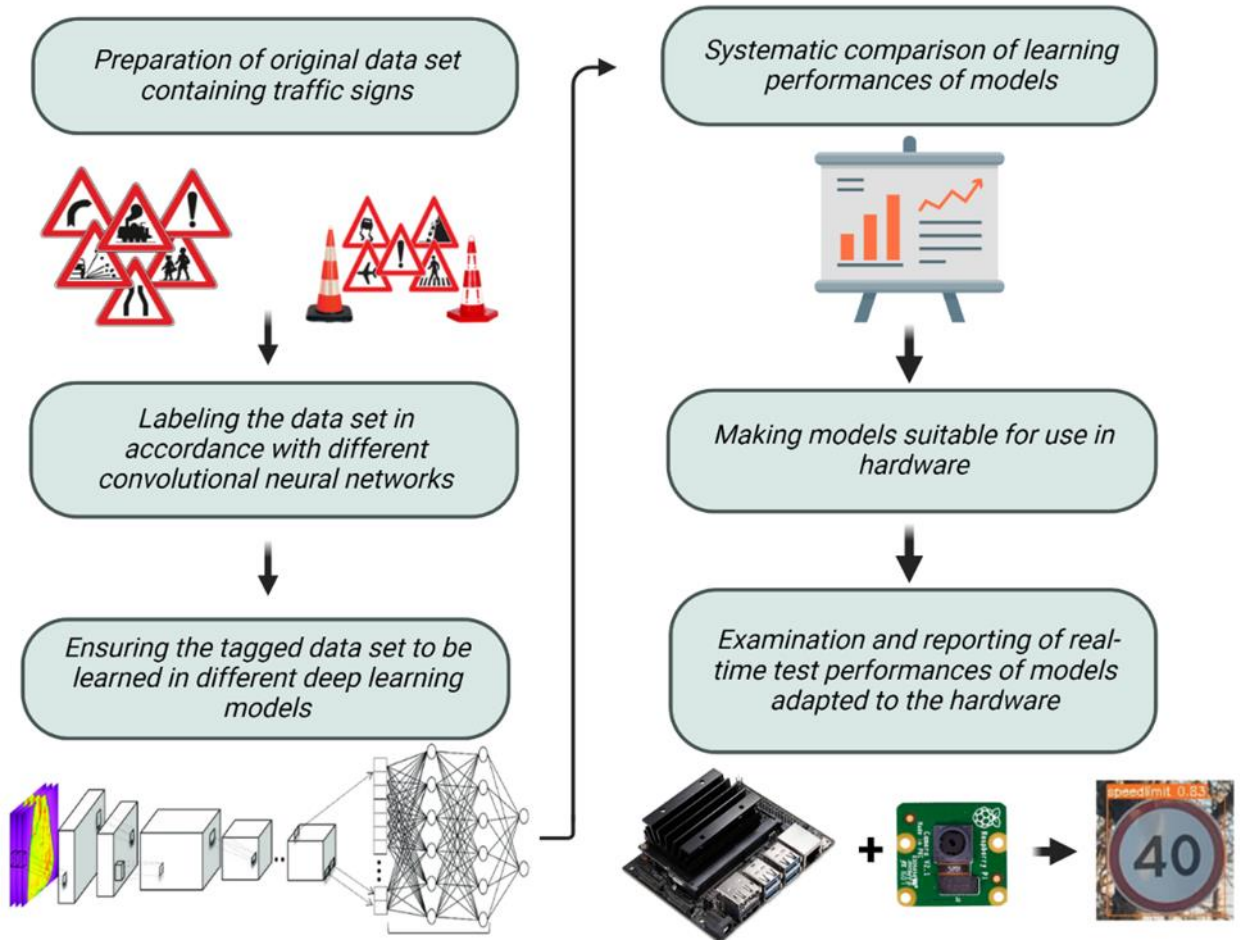

Figure 1. 1 Deep learning process for traffic sign classification

In this study, the traffic sign images were taken in Afyonkarahisar province, and a data set containing 1249 traffic sign images in total was used. Video recording was taken in Afyonkarahisar province by using the camera placed on a standard road vehicle. A total of 1249 traffic sign images were obtained from this video recording and a data set was created. For the preprocessing, the outlier images and tags in the data set were separated, and then the labeling process was carried out on the "makesensei.ai" site. More than 5000+ labeling processes (Figure 9 in Appendix) were performed for 26 different classes in 1249 images. 80% of this images data (1000 pieces of data) was used for model training (Figure 10 in Appendix), and the remaining 20% (249 pieces of data) was used in the testing phase. The distribution of the data set by classes is shown in Table 1

Figure 2 shows an example CNN architecture. Convolutional neural networks are formed by the combination of certain layers. The CNN algorithm consists of layers such as pooling, convolution, full connection, and activation. The convolution layer is the main building block of the neural network architecture. It is responsible for detecting the features of the picture. This layer applies some filter operations to the image to extract the features found in the image. In this way, a new image is obtained by extracting essential features from the image. The activation layer is the layer where the activation function is applied. Activation functions determine how neuron outputs must undergo a change. There are various functions that can be used in the activation layer. Some of these are step, sigmoid, tanh, ReLU, softmax, softplus, swish, and hyperbolic functions.

The pooling layer is generally preferred to reduce the size of the images. The size reduction process causes some information to be lost and, therefore to a decrease in performance. However, it prevents the model from memorizing and reduces the computational load. There are multiple

processes in the pooling layer. These are Minimum pooling, maximum pooling, and average pooling. Among these methods, it is observed that the maximum pooling process is preferred more frequently. Full link layers are usually found at the end of the convolutional neural network architecture and are used to optimize results such as class prediction. In this layer, each neuron is connected to the next neuron.

Table 1. Distribution of data set by classes

"Traffic Sign"	"Train + Test Data"
No Park Stopping	64
50 Km/h	51
30 Km/h	37
70 Km/h	26
Stop Give Way	57
Main Road	45
Stop	60
Red Light	55
Green Light	43
Park	48
80 Km/h	30
60 Km/h	35
Pedestrian Crossing	52
Station	57
40 Km/h	45
No Entry	54
Uneven Road	53
Risk of Ice	34
Bend to Right	44
School Crossing	48
Caution	59
No Turn Right	38
No Turn Left	36
Side Road	44
Level Crossing with Gate	37
Bend to Left	27

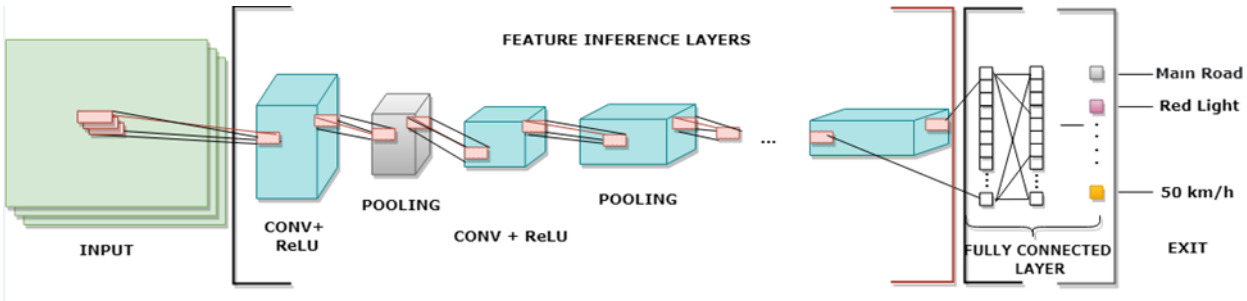

Figure 2. CNN Architecture

One of the important factors affecting the processing performance of convolutional neural network layers is hyper parameters. These parameters are; data size, batch size, dropout, epoch, learning coefficient, etc. It is aimed controlling the sufficient and insufficient learning status of the model by changing these parameters.

The reason for using the YOLO algorithm is that while the YOLO algorithm operates with the one stage method, the other discussed algorithms operate with the Two Stage Method. For example, unlike the prediction filter applied by the R-CNN algorithm to the image data, the YOLO algorithm tries to predict all objects by passing the picture through the neural network at once. In other words, it treats the detection process as a single regression problem. The most prominent feature that distinguishes the YOLOv5 model, which was chosen in line with these features, from different deep learning models is PyTorch-based development and GPU (Graphics Processor Unit) support. Since the separation of CUDA cores is more problematic and inefficient by image processing libraries such as OpenCV, it has been selected with YOLOv5 to ensure that it works optimally on the mission computer, for example, NVIDIA Jetson Nano. The human eye can see an average of 18-25 FPS (Narang et al. 2015). For this reason, it is aimed to improve the situations where the human eye is inadequate by choosing better hardware (Jetson Nano / 28 FPS) than the performance of the human eye.

Figure 3 shows the comparison of different YOLO models according to GPU speeds and IoU (intersection over union) metrics (Web Site 1). The IoU measures the intersection between 2 predictive values. It is used to measure how much the position of the predicted object coincides with the target position. When the graph in Figure 4 is examined according to these metrics, the GPU and IoU performances of the YOLOv5s, YOLOv5m, YOLOv5x models used for this study are seen. According to these results, it is seen that the YOLOv5m model gives better results than other models.

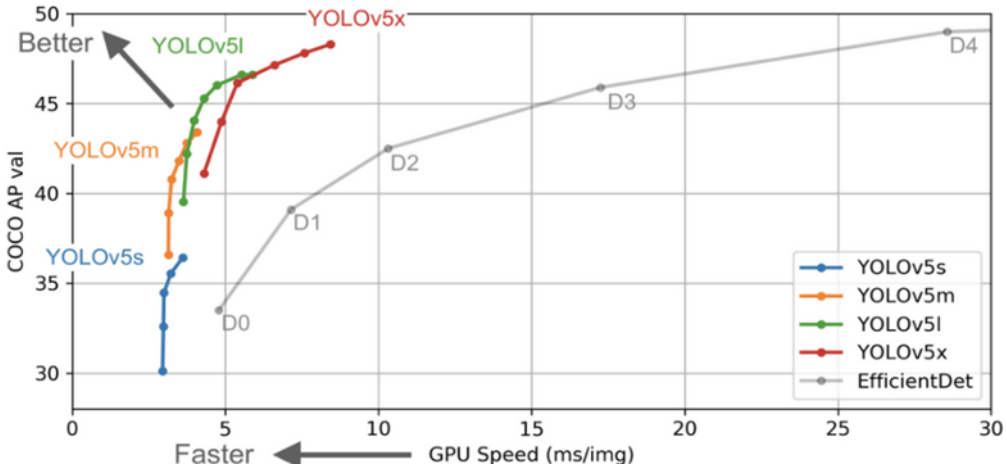

Figure 3. YOLO model comparisons according to GPU Performances and IoU averages (Web Site 1)

Deep learning models that provide learning produced outputs (F1 score, confusion matrix, accuracy value, etc.). According to these results, calculations are made on learning metrics, especially the confusion matrix and F1 score. Values are ranked according to their height status, and their comparisons are evaluated.

The model weight file is formed as a result of the learning. The weight file contains the architecture of the model, the learning weights, etc. contains information. TensorRT technology aims to improve the model weight file by NVIDIA company with five optimization items such as calibration, layers and tensor fusion, automatic core tuning, dynamic tensor memory, and multi-stream execution (parallel processing). The model weight file, which has evolved into a simpler and more efficient state for the hardware as a result of the optimization, is used for real-time tests. FPS results of the real-time tests are shown in Figure 11 in Appendix.

For real-time studies, operations are carried out on Jetson Nano hardware with TensorRT transformation of the model file. With the execution of the "Engine" extension TensorRT file, the model learning metrics are successful is expected to start the target recognition process. The tests are reported considering the high FPS value, which is one of the important criteria in the real-time test phase, and the extent to which the model has achieved the target during this period. LOGITECH C920 HD Pro is used as camera hardware in real-time studies. The camera used provides a 30 FPS video recording feature with clear and detailed 1080p image clarity. The camera's 78° field of view and HD auto light correction were key factors in real-time testing.

3. RESULTS AND DISCUSSION

When the output data of the YOLOv5m model, which provides learning, are examined, it is seen that a success rate of 99.07% is achieved in the confusion matrix for 150 epochs and 16 batch sizes. When Figure 4 is examined, it is calculated that the f1 score value of the training is 0.97, taking into account the precision and recall values. The training results are presented graphically in Figure 4.

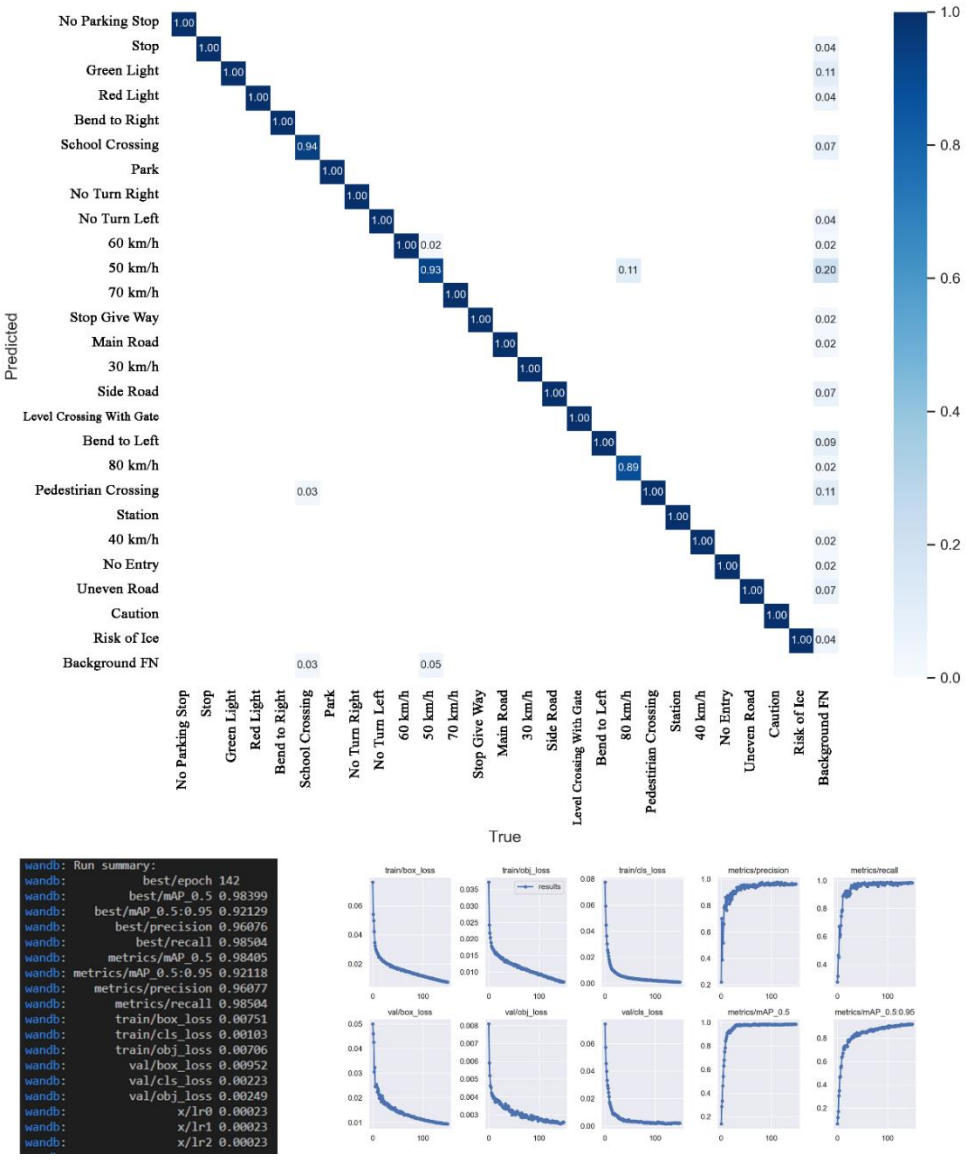

Figure 4. Confusion matrix, model results, and graphs for 150 epochs of the YOLOv5m model

Compared to the YOLOv5m model, the YOLOv5s model, which has a less complex structure, shows success of 98.65% when the confusion matrix is analyzed as a result of the learning performed for 150 epochs and 16 batch "size" values. It is calculated that the training f1 score value is 0.95 as a result of calculating precision and recall values when examined in figure 5. Graphs related to the learning parameters of the training are shown in Figure 5.

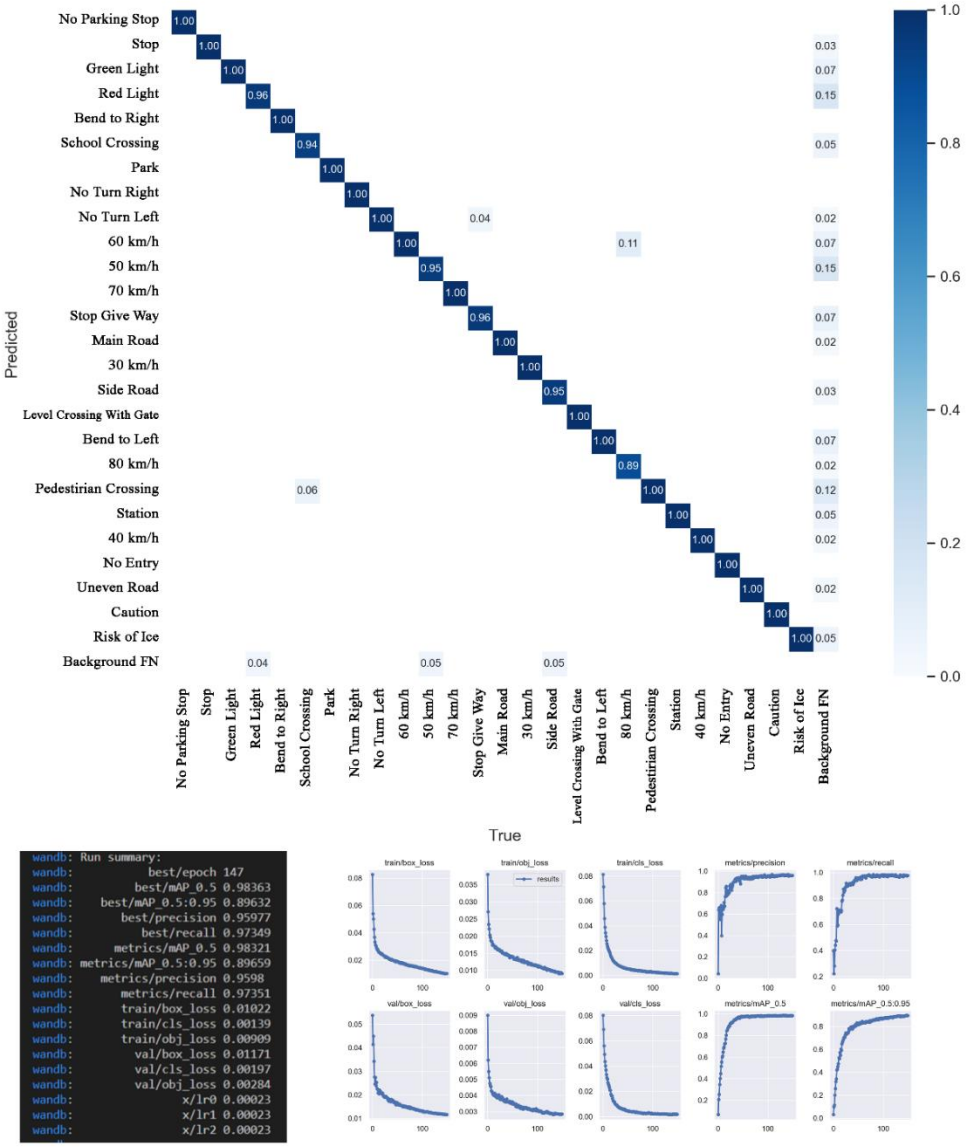

Figure 5. Confusion matrix, model results, and graphs for 150 epochs of the YOLOv5s model

In the YOLOv5x model, which has a more complex structure than the other YOLO models used, a success rate of 98.61% was achieved when the confusion matrix formed as a result of the training for 150 epochs and 16 batch sizes was examined. When Figure 6 is examined, it is calculated that the training f1 score value is 0.97 as a result of processing with precision and recall values. Graphics showing the training status of the train are shown in Figure 6.

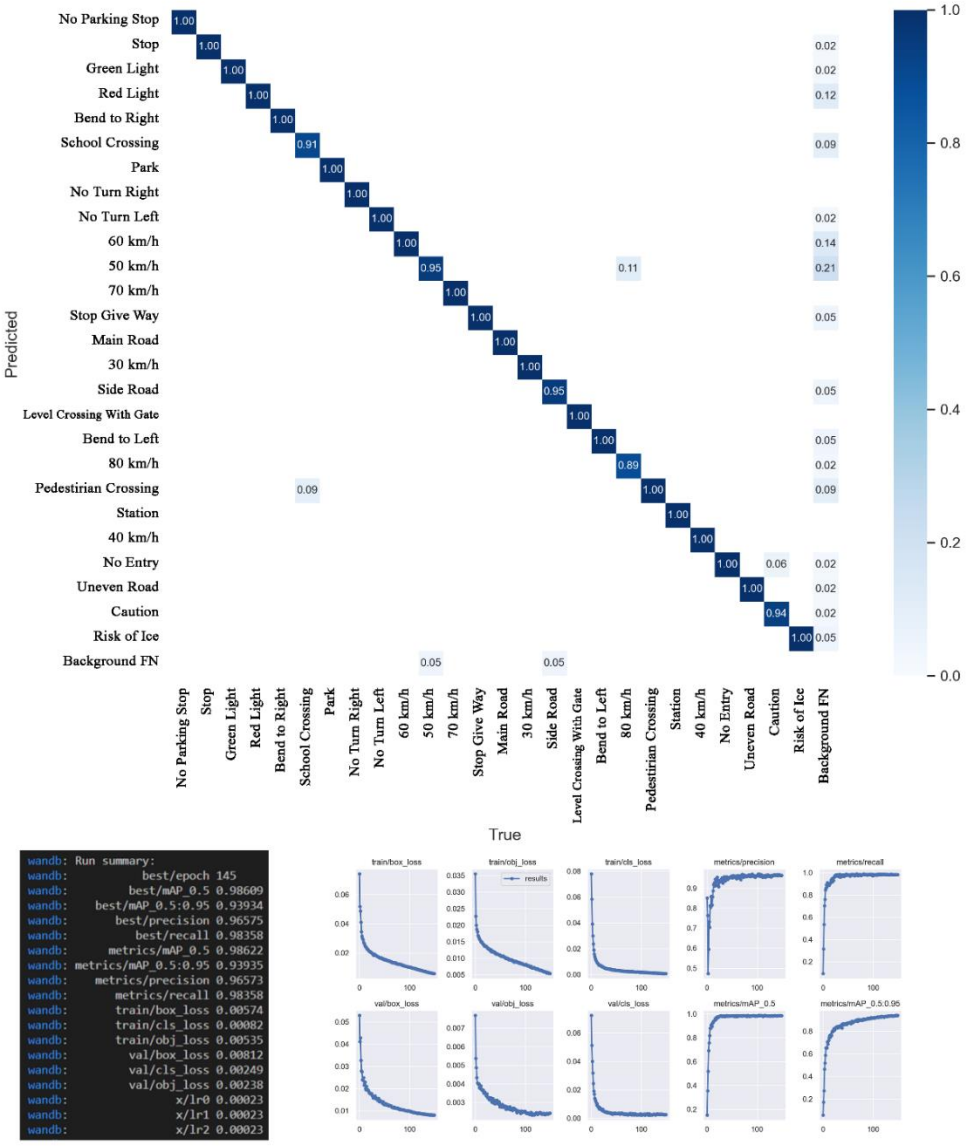

Figure 6. Confusion matrix, model results, and graphs for 150 epochs of the YOLOv5x model

In line with all these results, it has been determined that the YOLOv5m model is the model that gives the most optimum results when the test results and detection times are examined. Experimental studies were carried out in Microsoft Visual Studio Code environment on Intel (R) Core (TM) i7-10700 CPU 2.90GHz, 128 GB RAM, NVIDIA GeForce RTX 3080 Graphics card.

Examining the training results on the YOLOv5s, YOLOv5m, and YOLOv5x models, it was seen that the f1 score and confusion matrix results of the YOLOv5m model were higher than the others. When the YOLOv5s model results are compared with the YOLOv5m model, it is seen that the f1 score of the YOLOv5s model is lower by 0.02. However, YOLOv5s was preferred as the learning model in the real-time study. Considering the weight file size, training and detection time, and FPS (Frame Per Second) of the YOLOv5s model, it is seen that it has high-performance results compared to the YOLOv5m model. Although the learning results of the YOLOv5m model are higher, it has been decided that the YOLOv5s model is more suitable for real-time work. The YOLOv5s model has been tested in real-time on Jetson Nano and Raspberry Pi4B models. When tests were made for different image size values, it was seen that the best FPS values with acceptable accuracy were provided for 320x320 image size on both cards. As a result, for 320x320 image size, a maximum

of 8.2 FPS was obtained when using Jetson Nano and TensorRT conversion, and a maximum of 28.1 FPS after TensorRT conversion. As a result of the studies on Raspberry Pi4B 4GB and Raspberry Pi4B 8GB models, it has been seen that the 4GB model gives 0.5 FPS, and the 8GB model gives a maximum of 2.1 FPS for 320 image size. When the real-time test phases were completed, processing on the Jetson Nano mission computer was determined to be suitable in terms of model efficiency, detection time, and accuracy. The steps of the implementation and decision process are shown in the flow chart in Figure 7.

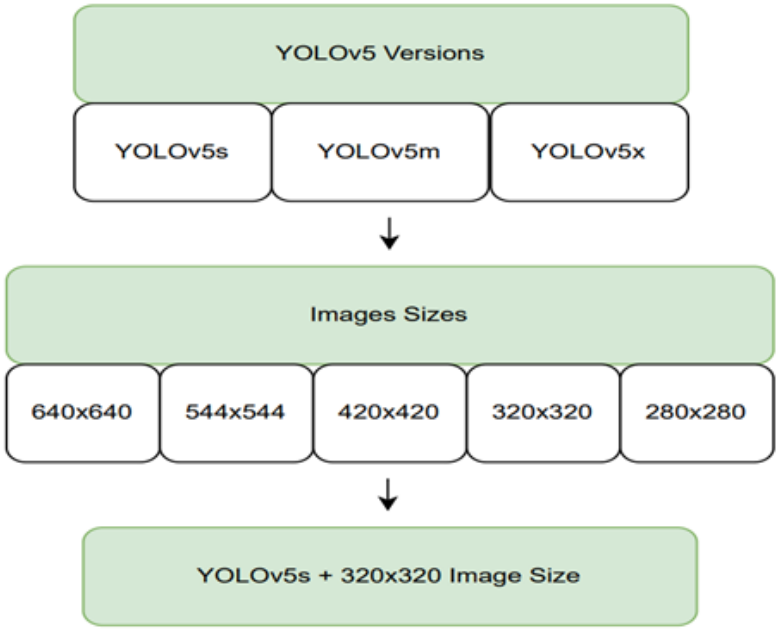

Figure 7. Models and Tested image size values

In Table 2, a comparison of the prominent studies on the classification of traffic markers with deep learning algorithms and the presented study is given. As can be seen from the table, using different CNN models, Lim et al. obtained an F1 score of 0.97. Çetin et al. developed models with a sensitivity of 0.97, and Paladiz et al. developed a sensitivity of 0.83. However, in the presented study, a sensitivity of 0.98 was achieved by using the YOLOv5s model, unlike the previous studies.

Table 2. Comparison of existing studies and presented study

	YOLOv5s Model	YOLOv5m Model	YOLOv5x Model	F1 Score	Accuracy	Raspberry Pİ4B FPS	Jetson Nano FPS
Lim et al.	×	×	×	0.97	×	×	×
Çetin et al.	×	×	×	×	0.97	×	×
Palandız et al.	×	×	×	×	0.83	×	×
This paper	✓	✓	✓	0.97 (YOLOv5m) 0.95 (YOLOv5s)	0.99 (YOLOv5m) 0.98 (YOLOv5s)	1.5 2.1	23.3 28.2

The outputs showing the training status of the model as a result of the determination made on the test class in the training dataset are presented in Figure 8. The “Stop” class of the model is 98%, the “Stop Parking Forbidden” class is 99%, the “Sharp Corner to the Left” class is 98%, the “Rough Road” class is 98%, the “Give Way” class is 98%, the “No Entry” class is 98%, It is seen that it detects the "Stop" class with an accuracy of 99%, the "Hidden Icing" class with an accuracy of 98%,

the "Pedestrian Crossing" class with 98%, and the "Controlled Railway" class with an accuracy of 98%. One of the important criteria not included in other studies is the Frame Per Second (FPS) value. When the model obtained as a result of the training is used with Raspberry Pi4B, it reaches 2.1 FPS, while 28.2 FPS values can be reached with Jetson Nano.

Figure 8. Test results showing the learning status of the model

4. CONCLUSION

In this study, using different YOLOv5 deep learning models, a data set containing 26 different traffic sign images were trained. There are 1249 image data in total in the prepared data set *(Repistority: https://drive.google.com/file/d/1oHkNKT9KZrLrtGcCj7pnjbTd5NkJJXzJ/view?usp=sharing*). 80% of this data (1000 pieces of data) was used for model training, and the remaining 20% (249 pieces of data) was used in the testing phase. The best results were obtained in the YOLOv5m model in computer studies. Accordingly, the f1 score of the developed model is 97%. However, when real-time testing was performed using YOLOv5m, 1.5 and 23.3 FPS values were obtained on Raspberry PI4B and Jetson Nano, respectively. On the other hand, the f1 score of the YOLOv5s model was calculated as 95%. However, when real-time testing was performed with YOLOv5s, 2.1 and 28.2 FPS values were captured on Raspberry PI4B and Jetson Nano, respectively. For this reason, although the f1 score of the YOLOv5m model is higher, it is more appropriate to prefer the YOLOv5s model

in real-time study. It is thought that these success rates obtained with computer technologies will help the traffic movements of autonomous vehicles in detecting traffic sign images with the help of deep learning models.

In addition to this study, adding new images with different backgrounds and angles to the classes in the dataset will help to increase the training and detection rate. Testing the models in real-time on different hardware will be more efficient in terms of the applicability of the study and testing the model efficiency.

5. CONFLICT OF INTEREST

Author approves that to the best of his knowledge, there is not any conflict of interest or common interest with an institution/organization or a person that may affect the review process of the paper.

6. AUTHOR CONTRIBUTION

Faruk Emre Aysal and Enes Cengiz determining the concept and design process of the research and research management, Kasim Yildirim data collection and analysis Faruk Emre Aysal and Kasim Yildirim data analysis and interpretation of results.

7. REFERENCES

Bayram F., Derin öğrenme tabanlı otomatik plaka tanıma. Politeknik Dergisi 23(4), 955-960, 2020.

Çetin E., Ortataş F., Elektrikli ve Otonom Araçlarda Makine Öğrenmesi Kullanarak Trafik Levhaları Tanıma ve Simülasyon Uygulaması. El-Cezeri 8(3), 1081-1092, 2021.

Dorokhin S., Artemov A., Likhachev D., Novikov, A., Starkov E., Traffic simulation: an analytical review. IOP Conference Series: Materials Science and Engineering, 918, 2020.

Eraqi H. M., Moustafa M. N., Honer J., End-to-End Deep Learning for Steering Autonomous Vehicles Considering Temporal Dependencies. 31st Conference on Neural Information Processing Systems (NIPS 2017), Long Beach, CA, USA., 2017.

Fagnant D. J., Kockelman K., Preparing a nation for autonomous vehicles: opportunities, barriers and policy recommendations. Transportation Research Part A: Policy and Practice 77, 167-181, 2015.

Glikson E., Woolley A. W., Human Trust in Artificial Intelligence: Review of Empirical Research. Academy of Management Annals 14(2), 627-660, 2020.

Gopalakrishnan S., A Public Health Perspective of Road Traffic Accidents. Journal of Family Medicine Primary Care 1(2), 144-150, 2012.

Guo Y., Liu Y., Oerlemans A., Lao S., Wu S., Lew M., Deep learning for visual understanding: A review. Neurocomputing 187, 27-48. 2016.

Haenlein M., Kaplan A., A Brief History of Artificial Intelligence: On the Past, Present, and Future of Artificial Intelligence. California Management Review 61(4), 5-14, 2019.

Hasan R. I., Yusuf S. M., Alzubaidi L., Review of the State of the Art of Deep Learning for Plant Diseases: A Broad Analysis and Discussion, Plants 9(10), 1302, 2020.

Huval B., Wang T., Tandon S., Kiske J., Song W., Pazhayampallil J., Ng A. Y., An Empirical Evaluation of Deep Learning on Highway Driving. Computer Science, 2015.

Jain N. K., Saini R. K., Mittal P., A Review on Traffic Monitoring System Techniques, Soft Computing: Theories and Applications, 569-577, 2018.

Kour A., Yadav V. K., Maheshwari V., Prashar D., A Review on Image Processing. International Journal of Electronics Communication and Computer Engineering 4(1), 270-275, 2013.

Kulkarni R., Dhavalikar S., Bangar S., Traffic Light Detection and Recognition for Self Driving Cars Using Deep Learning, Fourth International Conference on Computing Communication Control and Automation (ICCUBEA), Pune/India, August 16-18, 2018.

Kumar G., Bhatia P. K., A Detailed Review of Feature Extraction in Image Processing Systems, Fourth International Conference on Advanced Computing & Communication Technologies, Rohtak/India, February 8-9, 2014, pp: 5-12.

Lim K., Hong Y., Choi Y., Byun H., Real-time traffic sign recognition based on a general purpose GPU and deep-learning. PLOS ONE, 2017.

Miglani A., Kumar N., Deep learning models for traffic flow prediction in autonomous vehicles: A review, solutions, and challenges. Vehicular Communications 20, 100184, 2019.

Narang P; Agarwal A, Sanu A. S., Detecting subtle intraocular movements: Enhanced frames per second recording (slow motion) using smartphones. Journal of Cataract & Refractive Surgery 41(6), 1321-1323, 2015.

Palandız T., Bayrakçı H. C., Yapay Zekâ Kullanılarak Trafik İşaret Levhalarının Sınıflandırılması: Denizli İl Merkezi İçin Örnek Bir Uygulama. International Journal of 3D Printing Technologies and Digital Industry 5(3), 645-653, 2021.

Sampedro C., Ramos A. R., Campoy P., A Review of Deep Learning Methods and Applications for Unmanned Aerial Vehicles, Journal of Sensors, 2017.

Sarkar S. B., Mohan B. C., Review on Autonomous Vehicle Challenges. First International Conference on Artificial Intelligence and Cognitive Computing, 593-603, 2018.

Satria R., Castro M., GIS Tools for Analyzing Accidents and Road Design: A Review. Transportation Research Procedia 18, 242-247, 2016.

Shrestha A., Mahmood A., Review of Deep Learning Algorithms and Architectures, IEEE Access 7, 53040-53065, 2019.

Swaminathan V., Arora S., Bansal R., Rajalakshmi R., Autonomous Driving System with Road Sign Recognition using Convolutional Neural Networks, International Conference on Computational Intelligence in Data Science (ICCIDS), Chennai/India, February 21-23, 2019.

Web Site 1: "YOLOv5 New Version- Improvements and Evaluation", Access date: 20/05/2022, https://blog.roboflow.com/YOLOv5-improvements-and-evaluation/

Wiley V., Lucas T., Computer Vision and Image Processing: A Paper Review. International Journal of Artificial Intelegence Research 2(1), 28-36, 2018.

Zhou L., Zhang C., Liu F., Qiu Z., He Y., Application of Deep Learning in Food: A Review, Comprehensive Reviews in Food Science and Food Safety18(6), 1793-1811, 2019.

Appendix

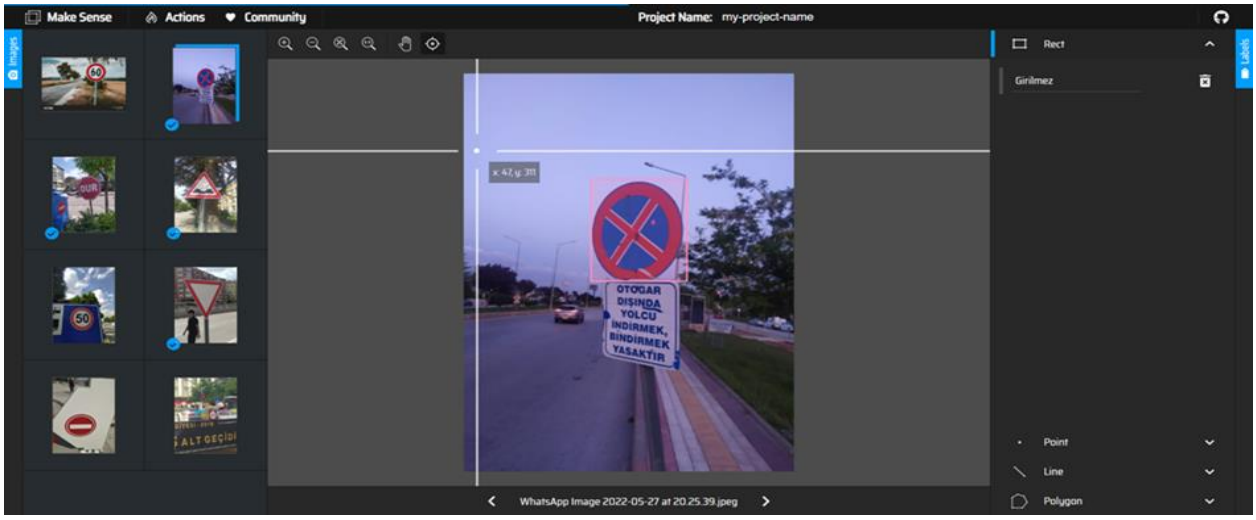

Figure 9. Labelling example

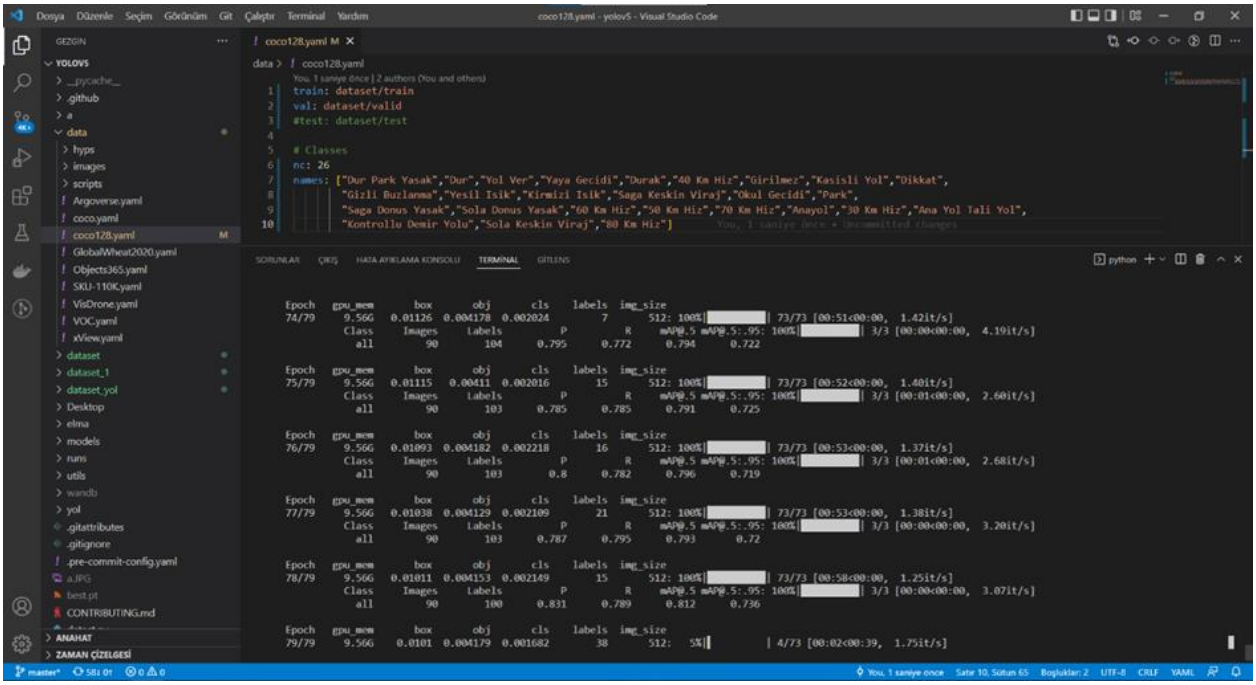

Figure 10. YOLOv5 model training screenshot

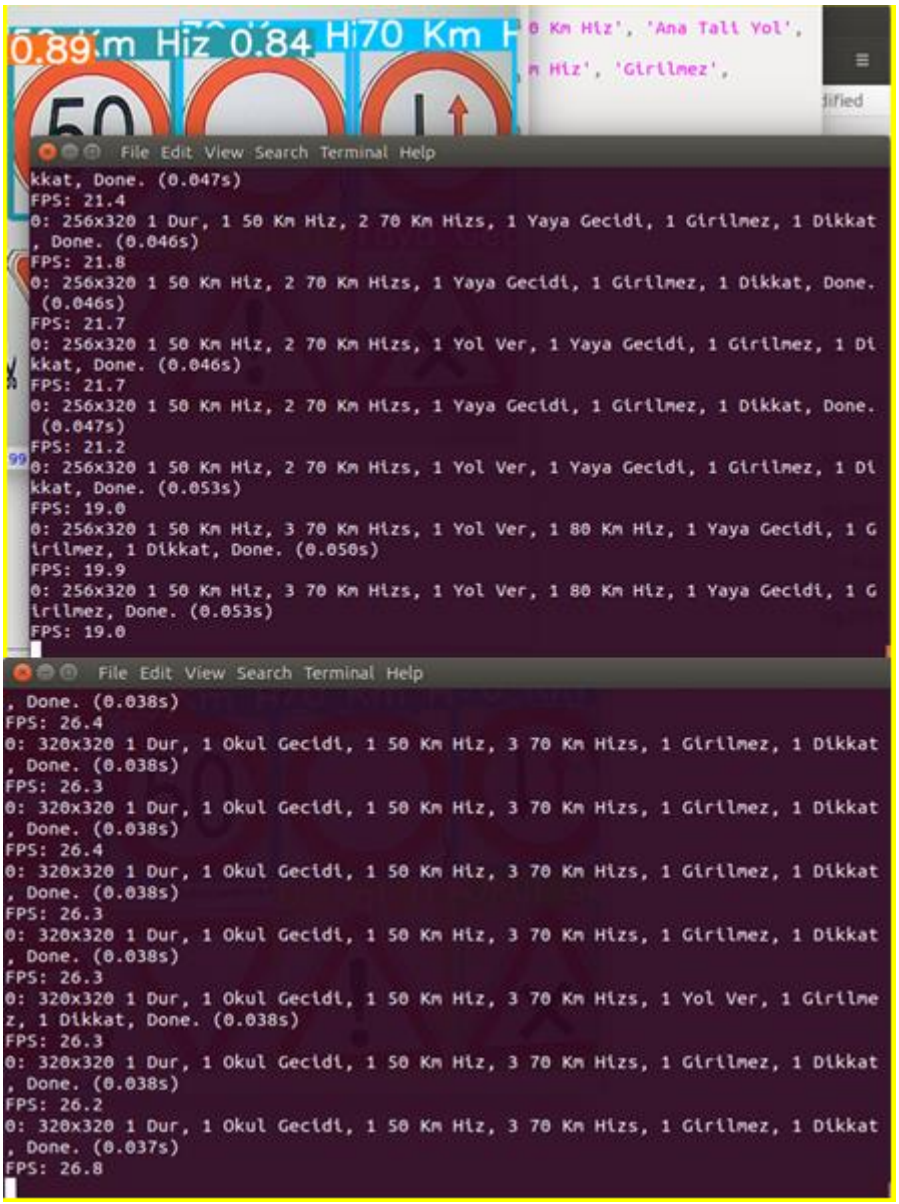

Figure 11. YOLOv5s real-time FPS tests

JOURNAL of
MATERIALS and MECHATRONICS:A

e-ISSN 2717-8811
JournalMM, 2022,3(2), 290-299
https://doi.org/10.55546/jmm.1182481

Araştırma Makalesi / Research Article

Improvement of Machining Vibrational Stabilization for a CNC Lathe in Turning of AISI 420 Stainless Steel by MQL and Cryogenic Methods

Fatih PEHLİVAN [1]*

[1] Karabuk University, Faculty of Engineering, Department of Mechanical Engineering, Karabuk, Türkiye,
ORCID ID: https://orcid.org/0000-0003-2675-6124, fatihpehlivan@karabuk.edu.tr

Geliş/ Received: 30.09.2022; **Kabul / Accepted:** 03.12.2022

ABSTRACT: It is common to find annealed and tempered stainless steels on the market for raw materials. The choice of proper heat treatment settings is one of the most influential aspects in determining the corrosion resistance of annealed materials. The degradation of materials as a result of wear and corrosion is a problem that leads to very considerable economic losses nowadays. By applying lubrication and cooling to the material's surface during operation, the destructive effects of wear and corrosion on the material may be reduced. This study investigates the influence that different machining and lubrication/cooling environments have on vibrational stabilization-based acceleration as well as power consumption during the turning of AISI 420 stainless steel under dry, minimum quantity lubrication (MQL), and cryogenic settings. In all of the turning trials, the cutting speed and the depth of cut were maintained at the same levels. When the data were analyzed, a change from the dry environment to the MQL condition resulted in a drop of 7.04% and 5.2% in power consumption and acceleration, respectively, while a change from the MQL test settings to cryogenic cooling conditions resulted in a decrease of 2.02% and 14.3% in power consumption and acceleration, respectively.

Keywords: AISI 420 stainless steel, Vibration, Power consumption, Minimum quantity lubrication (MQL), Cryogenic cooling, Turning

*Sorumlu yazar / Corresponding author: fatihpehlivan@karabuk.edu.tr

Bu makaleye atıf yapmak için /To cite this article

Pehlivan, F., (2022). Improvement of Machining Vibrational Stabilization for a CNC Lathe in Turning of AISI 420 Stainless Steel by MQL and Cryogenic Methods. Journal of Materials and Mechatronics: A (JournalMM), 3(2), 290-299.

1. INTRODUCTION

Surface treatments using different machining methods are directly or indirectly affected by machining parameters (Danish et al., 2021). Machining parameters that are not chosen well to cause economic losses such as breakage, rapid wear, and burning of cutting tools, as well as economic losses such as deterioration of the workpiece or low surface quality (Sharif et al., 2017). Machining has an important place among other manufacturing methods. In all manufacturing methods, besides the size and geometric tolerances of the product, a satisfactory surface roughness quality is also of great importance (Zhou et al., 2021). The surface structure of the machine parts is directly affected by the change of the workpiece, the tool, the machining conditions or any of the workbench, that is, the machining regime (Iyappan and Ghosh, 2018). The functioning of the manufactured parts as required, their mechanical life and resistance to external influences depend on the surface quality as well as other factors (Sarıkaya et al., 2021). Therefore, there is a need to determine or estimate how roughness occurs with numerical values. It is possible to use the contact vibration (chatter vibration) between the tool and the workpiece in the estimation of the actual value of the roughness, which affects the function and cost of the part (Türkeş and Neşeli, 2014; Takahashi et al., 2021). Because of this importance of surface quality, manufacturer's attention has been focused on reducing the surface roughness of machined parts (Gupta et al., 2020). Chattering or machine tool vibrations, damage to the structure of the work material, tool wear or irregularities of chip formation contribute to surface deterioration during machining (Turkes et al., 2011). Estimating the surface roughness and evaluating the compatibility of machining parameters such as feed or cutting speed increases the product quality and sheds light on obtaining the desired surface roughness (Dubey et al., 2021). Mechanical vibrations should be well known in order to understand chatter vibrations in machine tools. The periodic movement of an object around its equilibrium position is called mechanical vibration (Pecat and Brinksmeier, 2014). In general, vibration is an unwanted and unnecessary energy state. It is a fact that it makes noise, breaks parts and transmits unwanted forces, especially in machine tools (Szaksz and Stepan, 2021). For these reasons, vibration reduction is necessary. In vibration problems, it is necessary to solve the equation of motion. The system is first simplified in terms of mass, spring and damping elements that express its existence, elasticity and friction (Mojahed et al., 2018). The equation of motion is expressed in terms of displacement as a function of time or to give the distance of the mass from the equilibrium position at any moment of motion (Chen et al., 2022). The natural frequency, which is the most important property of the systems, is obtained from the equation of motion. The main source of error in each machining operation is the relative dynamic movement between the tool and the workpiece (Wang et al., 2022). The relative motion between the tool and the workpiece is a natural frequency system and due to the unstable behavior, that occurs with large amplitude relative displacements, it can greatly damage the machined end surface and the cutting tool. If this movement develops beyond the acceptable limits, this phenomenon is called chatter, and the resulting chatter leads to poor surface results, poor dimensional accuracy, increased tool wear, frequent tool breakage and indirectly shortened machine life (Ni et al., 2020).

In dry conditions, researchers have proposed many ways for machining difficult-to-cut materials, including the use of surface texture on cutting inserts (Rao et al., 2021), coated tools (Erden et al., 2021), as well as the use of self-lubricating tools (Akhtar, 2021). All of these approaches, when compared to traditional machining, have shown a decrease in machining forces and friction coefficient. Tool wear and machined surface quality, on the other hand, continue to be a problem. The use of cutting fluids for the machining of difficult-to-cut materials is thus advised. Cutting fluids, on the other hand, provide a variety of health risks to operators as well as significant environmental

consequences (Bertolini et al., 2021). The literature investigates alternative sustainable settings such as compressed air, cryogenic, and minimum quantity lubrication (MQL), among others, except for the assessment of vibrational stabilization. The effect of cutting parameters on natural frequency and surface roughness in turning aluminum alloy AA2024 was investigated by Rogov and Siamak (Rogov and Siamak, 2013) using a TiC-coated carbide insert and two different cutting tools made of AISI 5140 and the predicted optimal cutting parameters were obtained by Taguchi. Kusuma et al. (Kusuma et al., 2014) aimed to investigate the effects of cutting parameters such as depth of cut, feed rate, and spindle speed on tool vibration and surface quality by using microelectromechanical systems (MEMS) accelerometer on a high precision CNC milling machine. The results showed that in the milling machine, the depth of cut was more effective on surface roughness and vibration was more influenced by spindle speed. Zagórski and Kulisz (Zagórski and Kulisz, 2019) aimed to demonstrate the work on vibration and acceleration estimation in milling through artificial neural networks. It was also seen that the extent to which cutting speed, feed rate, and depth of cut affected the acceleration values ax, ay, and az during the milling process performed on the AZ91D magnesium alloy with a PCD cutting tool in this study. Ma et al. (Ma et al., 2020) aimed to demonstrate that vibration control is an important issue during both end-milling and micro-end-milling of complex surfaces to improve machining quality and extend tool life. The results showed that spindle speed had the greatest effect on cutting vibration when compared with the axial depth of cut and feed rate. They also revealed that among axial, feed, and transverse acceleration during micro end milling of the straight groove, the largest acceleration is the transverse acceleration, and the smallest acceleration is the axial acceleration. The machining of AISI 304 steel under minimum quantity cooling lubrication (MQCL) and flood-cutting conditions were experimentally examined by Liu et al. (Liu et al., 2021) to evaluate both tool vibration using the response surface methodology and surface roughness characteristics using the power spectral density. They found that both feed rate and MQCL conditions significantly affected not only surface roughness but also radial and axial vibration. Emami and Karimipour (Emami and Karimipour, 2021) analyzed the influence of cooling and lubrication on the dynamic stability of the turning process both theoretically and experimentally. It was obtained from the results that wet cooling and MQL during the machining process could change the chatter stability limit to a remarkable range. In addition, it was seen that the chatter stability in wet machining was higher than MQL machining in the spindle speed from 550 rpm to 1668 rpm but at spindle speeds above 1668 rpm, the stability in the MQL machining was higher than the stability in wet machining.

Numerous machining experiments using dry, MQL, and cryogenic cooling conditions and outputs of surface roughness, cutting forces, tool wear, etc. can be found in the literature. In addition, there are machining research on vibrational stabilization in dry circumstances exclusively. However, there are no or limited studies on vibrational stabilization with MQL or cryogenic cooling conditions. As the novelty, this study emphasized the effect of machining and lubrication/cooling environments on vibrational stabilization-based acceleration as well as power consumption in the turning of AISI 420 stainless steel on dry, MQL, and cryogenic conditions to fill this gap in the literature.

2. MATERIALS AND METHODS

For the purpose of carrying out the turning tests on the AISI 420 stainless steel, a Taksan TTC-550 CNC lathe was used. As can be seen in Figure 1, the length of the bar is 250 mm, and it has an outer diameter of 50 mm. The chemical composition is 0.15%~C, 1.0%~Si, 1.0%~Mn, 13%~Cr, 0.04%~P, 0.03%~S and the balance is Fe. After heat treatment, the material hardness and tensile

strength increased to 50 HRC, 1570 MPa, respectively. CNMG 120404 ML cutting inserts produced by Korloy was used in the study. In addition, the cutting speed was kept constant at 180 m/min. throughout all of the tests, and the depth of cut was maintained at 0.5 mm. The feed rate was varied between 0.1, 0.15, and 0.2 mm/rev. depending on whether the environment was dry, MQL, or cryogenic. Experiments which are repeated 2 times were carried out in a variety of environments, including dry, MQL, and cryogenic settings. The Werte StN 15 MQL system, which was built by the Werte Mist Company, was deployed for MQL testing. The biodegradable vegetable-based essential oil WerteLubri was used as the cutting fluid, and it was applied with a nozzle having a diameter of 2 mm, which was positioned at a fixed distance of 45 mm from the cutting zone and at 45°. The flow rate was 100 mm/h, and the pressure was 5 bar (Çamlı et al., 2022). The YDS-10 liquid nitrogen tank that was manufactured by Low-Temp Company was utilized in the research involving cryogenic cooling (Figure 1). The cutting region was sprayed with liquid nitrogen (LN2) having the flow rate of 0.71 cm^3/s using a vacuum hose that had been custom-made for the purpose, with a nozzle that had a diameter of 3 mm and a pressure of 0.5 bar throughout (Korkmaz et al., 2022). Cryogenic machining requires the use of a nozzle that is positioned at a constant distance of 45 mm at 45°, just as the MQL nozzle. The experimental setup is shown in Figure 1, which may be found here.

The sample measurement length used for this evaluation was 5 mm. Before beginning each measurement, the validation block was navigated to in order to calibrate the instrument. Measurements of acceleration based on vibration were carried out with the help of the PCE-VD 3-Axis Vibration Datalogger that measures 3-axis shock/vibration via a built-in accelerometer sensor. The power consumption (total consumption over the turning process) measurements have been performed by KAEL Network Analyzer (Turkey) which is logged to CNC system by parallel connection. The values have been directly read from the analyzer.

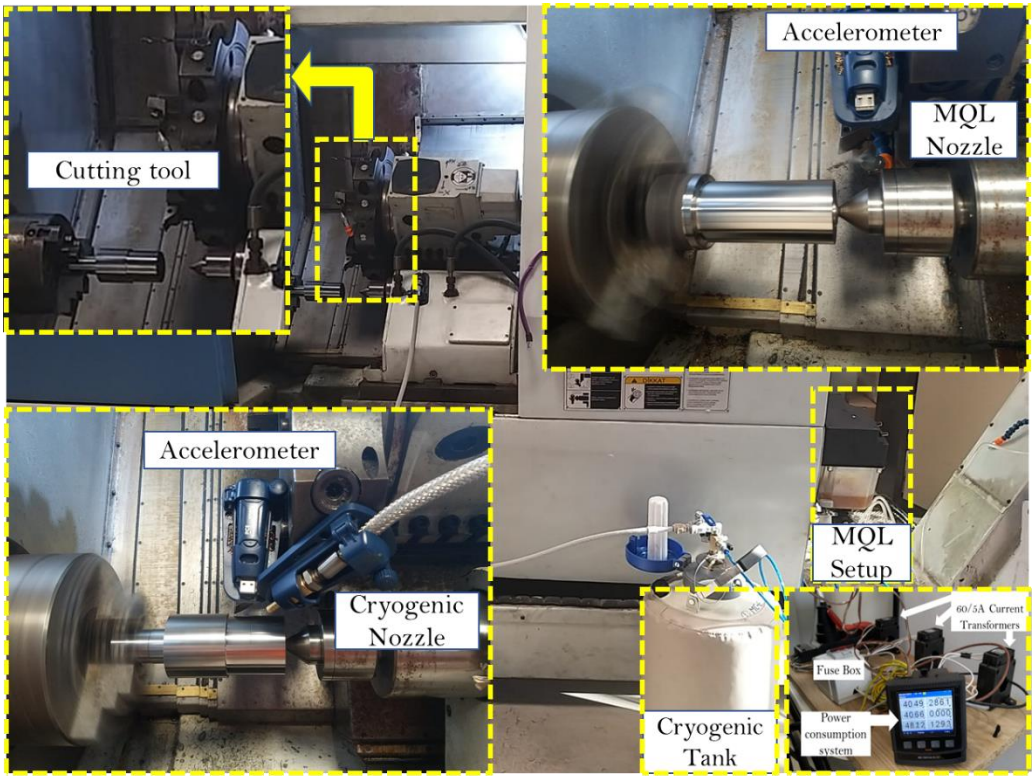

Figure 1. Experimental setup

3. RESULTS AND DISCUSSION

3.1 Evaluation of Acceleration (Vibrational Stabilization) Results

During the turning of AISI 420 stainless steel, the radial acceleration values a_z were observed. The observation results are depicted in Figure 2, regarding feed rates (f = 0.1 mm/rev, f = 0.15 mm/rev, f = 0.2 mm/rev), and cutting environments (dry, MQL and cryogenic). The maximum and minimum values of radial vibration acceleration were obtained using experimental results and then its root mean square (RMS) values were calculated. As shown in Figure 2, the radial vibrations gradually increased with an increase the feed rate from 0.1 mm/rev to 0.2 mm/rev at all cutting environments because vibration values increase as the feed rate increases.

The vibration values in the machining process can be divided into several different steps. As shown in Figure 2, it was seen that the fastest cutting speed in the dry testing condition resulted in the largest acceleration, which was 1.601 m/s^2 at its peak value. The largest acceleration values at low and medium feed rates were observed to be 1.110 m/s^2 and 1.490 m/s^2, respectively. An increase in feed rate from 0.1 to 0.15 mm/rev resulted in an increase in acceleration of about 34%. As the feed rate goes from 0.15 to 0.2 mm/rev, there was a corresponding increase in the acceleration about 7.4%. The acceleration for the cryogenic test condition came out to be 0.864 m/s^2 as the experiment was run with a low feed rate. In the cryogenic tests, the acceleration was found as 1.180 m/s^2 at medium feed rate, while the acceleration value was obtained as 1.280 m/s^2 at high feed rate. In the cryogenic test, whereas the feed rate is increased from 0.1 to 0.15 mm/rev or from 0.15 to 0.2 mm/rev, respectively, the measured acceleration values were increased by 36.6% and 8.5%, respectively. While the dry experiments were changed with the experiments conducted in a cryogenic state, the acceleration value for the low feed rate dropped by 20.2%. When the dry environment was changed with the MQL condition, there was a 5.2% drop at the low feed rate. During the parameters for the MQL test were moved to the cryogenic one with the low feed rate value, average acceleration values dropped by 14.3%. These values for decrease come in at 15.2% for medium feed rates and 18.1% for high feed rates, respectively.

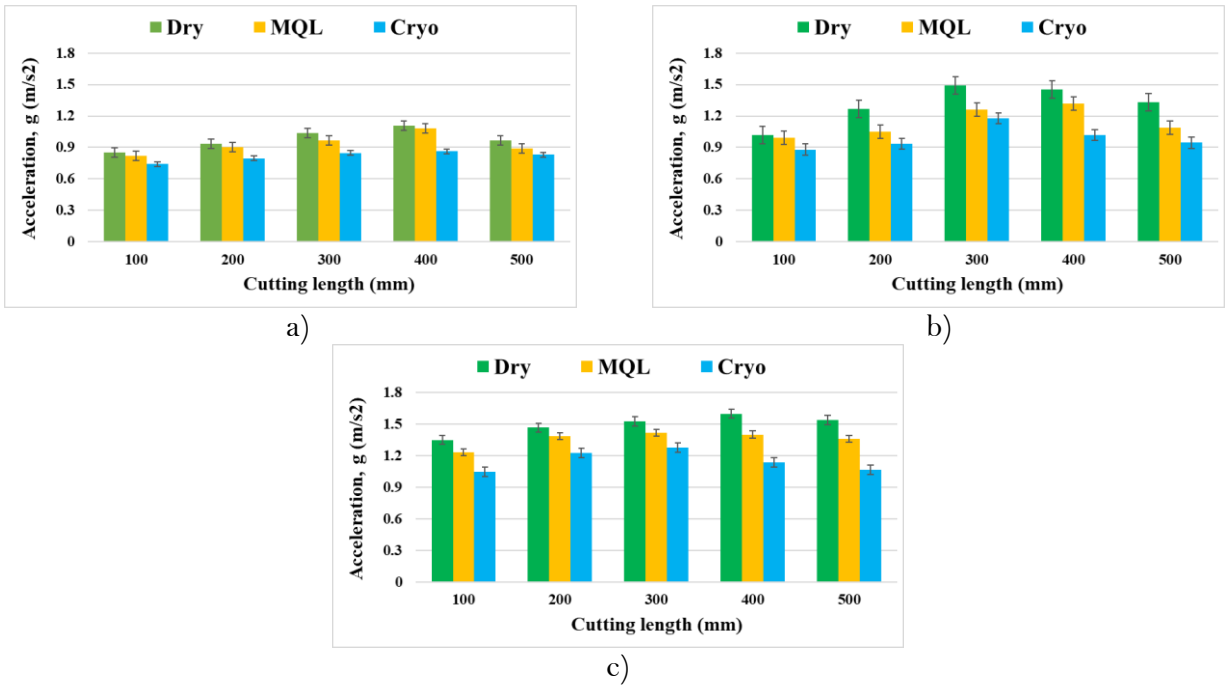

Figure 2. Vibrational evaluation based on acceleration for the different cutting environments, a) f=0.1 mm/rev, b) f=0.15 mm/rev, c) f=0.2 mm/rev

Due to the large contact area between the workpiece and the tool, material accumulation occurs in the same area, and this limits the heat dissipation. As the friction between the workpiece and the tool increased, the chips constantly sticking to the tool edge developed more accumulated edges. Because of this, the temperature has risen sharply. It also increased the cutting resistance, and so tool vibration increased significantly (Liu et al., 2021).

As seen in Figure 2, according to the test results, the vibration values under the cryogenic conditions were lower than the vibration values under both dry cutting and MQL technology. This difference was due to the effect of the cryogenic cooling in tool-workpiece interaction very high temperature occurs. The effect of heat dissipation was supplied at a low temperature, and this also reduced the cutting resistance of the removed material. When the vibration values in the machining performed under dry cutting and cryogenic cooling technology are compared, it was seen that the vibration values in the machining performed under cryogenic cooling technology were less than the under the effect of dry cutting as shown in Figure 2. This can be attributed to the fact that cryogenic machining conditions resulted in a better surface finish for the finished part. This is because cryogenic machining conditions resulted in better chip breakability and less accumulation of chips near the cutting zone. As a result, frictional contact between the chips and the finished workpiece was avoided (Jerold and Kumar, 2012). Moreover, MQL is also better than dry condition due to lubricant effect. It was delivered to the cutting zone to provide adequate lubrication and so it formed an interface with the help of oil droplets between the tool and the workpiece. As a result, vibration was reduced due to the reduction of friction force. The reason why this was so similar to the machining under MQL. Because it provided an extra interface between the tool and the workpiece, reducing the friction force in the region and allowing the heat dissipation. However, the interface formed for the reduction of the friction force did not reduce the friction force that much since it was not composed of oil as in the machining under MQL. Therefore, although it was understood that the vibration values in the machining performed under the MQL technology created more vibration than the cryogenic cooling technology, it had been observed that they finally created less vibration than dry cutting (Krolczyk et al., 2019).

3.2 Power Consumption

The use of electrical power in the machining process may be broken down into a few distinct steps. As shown in Figure 3, it was discovered that the highest feed in the dry testing condition resulted in the largest power consumption, which was 2928 W at its peak value. In terms of the amount of electricity that is used, the low and medium feed rates utilize 2556 W and 2664 W, respectively. The increase in feed rate from 0.1 to 0.15 mm/rev resulted in an increase in power consumption that was 5%. As the feed rate value goes from 0.15 to 0.2 mm/rev, there is a corresponding increase of 9.4% in the power consumption value. The power consumption number for the cryogenic test condition came out to be 2328 W when the experiment was run with a low feed rate. In the cryogenic tests, cutting at a medium feed rate required 2544 W of power, while cutting at a high feed rate used 2664 W of power. When the feed rate in cryogenic testing is increased from 0.1 to 0.15 mm/rev or from 0.15 to 0.2 mm/rev, respectively, there is a 9.3% and 4.7% increase in the amount of power that is consumed. When the dry experiments were switched out for those conducted in a cryogenic state, the value for the low feed rate dropped by 8.9%. When the dry environment was switched out for the MQL condition, there was a 7.04% drop at the low feed rate. When the parameters for the MQL test were moved to the cryogenic one with the low feed rate value, the overall power consumption dropped by 2.02%. These values for decrease come in at 1.38% for medium feed rates and 4.38% for high feed rates, respectively. It is understood from the values that the cryogenic machining required

considerably less power than dry environment. As claimed by Khanna et al. (Khanna et al., 2020), this is due to the cryogen ability to rapidly remove the heat created during dry machining.

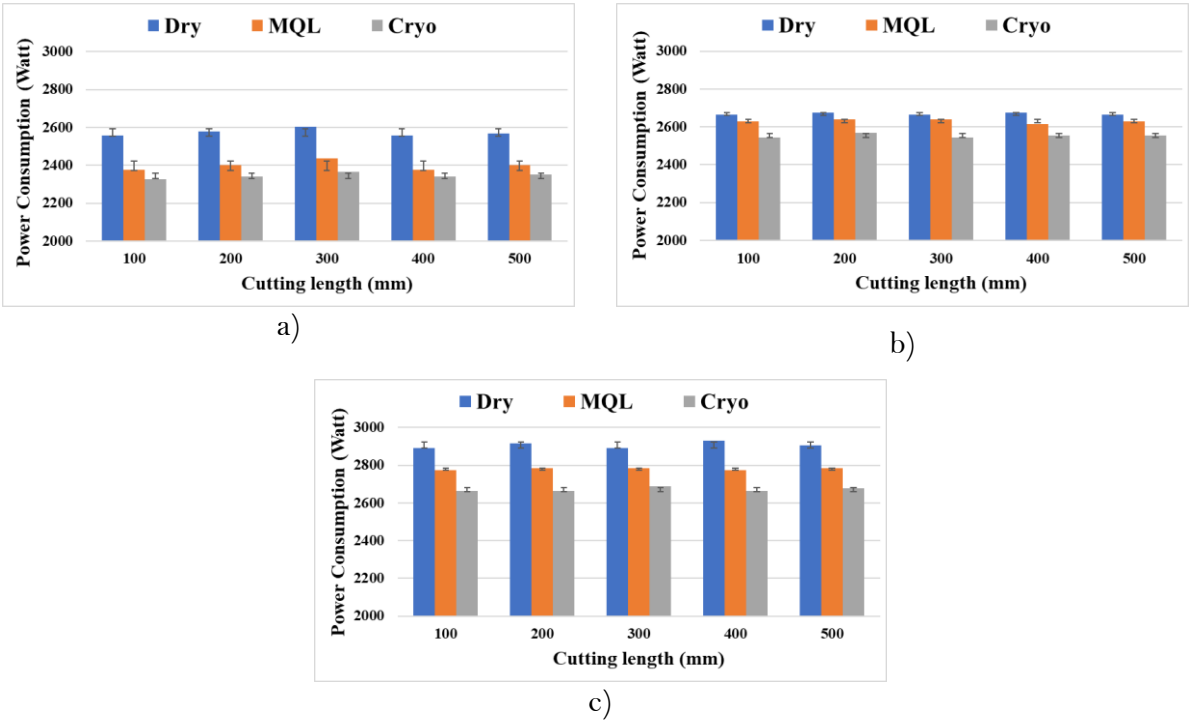

Figure 3. Power consumption based on the different cutting environments, a) f=0.1 mm/rev, b) f=0.15 mm/rev, c) f=0.2 mm/rev

The production of a lubricant-film between two moving surfaces, a reduction in the friction coefficient, and the prevention of wear on the moving surfaces are the goals of lubrication (Korkmaz et al., 2022). Lubricity is intended to make movement simpler by doing these things. The majority of coolants work to minimize friction, while cryogenic cooling works to lower the high temperature in the cutting zone. Together, these effects lessen the amount of power that must be used to machine a given material. This will not only cut down on the amount of energy that is consumed, but it will also lower the amount of heat that is produced (Gupta et al., 2019). When there is less heat produced, there is an increase in the tool life, and the surface integrity of the material being worked on is maintained (Hong and Ding, 2001).

4. CONCLUSION

This experimental investigation was carried out to investigate the machinability of AISI 420 stainless steel in order to determine the impact that employing dry, MQL, and cryogenic cooling had on the machining outputs, namely acceleration based on vibrational stabilization, as well as power consumption. The following are some of the conclusions that may be drawn from this study:

- The increase in feed rate from 0.1 to 0.15 mm/rev led to a rise in the measured acceleration was equal to 34% more. When the value of the feed rate is increased from 0.15 to 0.2 mm/rev, there is a corresponding rise in the value of the power consumption that is 7.4% higher.
- When the dry environment was switched out for the MQL condition, there was a 5.2% drop in acceleration. On the other hand, when the MQL test settings were transferred to cryogenic cooling conditions, there was a 14.3% decrease in acceleration.

- The increase in feed rate from 0.1 to 0.15 mm/rev led to a rise in the amount of consumed power was equal to 5% more. When the value of the feed rate is increased from 0.15 to 0.2 mm/rev, there was a corresponding rise in the value of acceleration that is 9.4% higher.
- When the dry environment was switched out for the MQL condition, there was a 7.04% drop in power consumption. On the other hand, when the MQL test settings were transferred to cryogenic cooling conditions, there was a 2.02% decrease in power consumption.
- It is anticipated that this study will be useful to research and development centers in the machining industries regarding stainless steels. In particular, it is anticipated that this study will be useful to research and development centers that are focused on improving cooling technologies in the machining of stainless-steel components.

5. ACKNOWLEDGEMENTS

This study was supported by Karabuk University Scientific Research Coordinatorship with Project number of KBÜBAP-22-ABP-010.

6. CONFLICT OF INTEREST

Authors approve that to the best of their knowledge, there is not any conflict of interest or common interest with an institution/organization or a person that may affect the review process of the paper.

7. AUTHOR CONTRIBUTION

Fatih PEHLİVAN contributed determining the concept of the research and research management, design process of the research and research management, data analysis and interpretation of the results, critical analysis of the intellectual content, preparation of the manuscript, and final approval and full responsibility.

8. REFERENCES

Akhtar S. S., A critical review on self-lubricating ceramic-composite cutting tools, Ceramics International 47(15), 20745-20767, 2021. doi:10.1016/j.ceramint.2021.04.094.

Bertolini R., Ghiotti A., Bruschi S., Graphene nanoplatelets as additives to MQL for improving tool life in machining Inconel 718 alloy. Wear 476, 203656, 2021. doi:10.1016/j.wear.2021.203656.

Çamlı K.Y., Demirsöz R., Boy M., Korkmaz M. E., Yaşar N., Giasin K., Pimenov D.Y., Performance of MQL and Nano-MQL Lubrication in Machining ER7 Steel for Train Wheel Applications. Lubricants 10(4), 48, 2022. doi:10.3390/lubricants10040048.

Chen Y., Zhang Y.,Tian X., Guo X., Li X., Zhang X., A numerical framework for hydroelastic analysis of a flexible floating structure under unsteady external excitations: Motion and internal force/moment. Ocean Engineering 253, 111288, 2022. doi:10.1016/j.oceaneng.2022.111288.

Danish M., Gupta M. K., Rubaiee S., Ahmed A., Korkmaz M. E., Influence of hybrid Cryo-MQL lubri-cooling strategy on the machining and tribological characteristics of Inconel 718. Tribology International 163, 107178, 2021. doi:10.1016/j.triboint.2021.107178.

Dubey V., Sharma A. K., Vats P., Pimenov D. Y., Giasin K., Chuchala D., Study of a Multicriterion Decision-Making Approach to the MQL Turning of AISI 304 Steel Using Hybrid Nanocutting Fluid. Materials 14(23), 7207, 2021. doi:10.3390/ma14237207.

Emami M., Karimipour A., Theoretical and experimental study of the chatter vibration in wet and MQL machining conditions in turning process. Precision Engineering 72, 41-58, 2021. doi:10.1016/j.precisioneng.2021.04.006.

Erden M. A., Yaşar N., Korkmaz M. E., Ayvacı B., Ross N. S., Mia M., Investigation of microstructure, mechanical and machinability properties of Mo-added steel produced by powder metallurgy method. The International Journal of Advanced Manufacturing Technology 114, 2811-2827, 2021. doi: 10.1007/s00170-021-07052-z.

Gupta M. K., Song Q., Liu Z., Pruncu C. I., Mia M., Singh G., Lozano J. A., Carou D., Khan A. M., Jamil M., Pimenov D. Y., Machining characteristics based life cycle assessment in eco-benign turning of pure titanium alloy. Journal of Cleaner Production 251, 119598, 2019. doi:10.1016/J.JCLEPRO.2019.119598.

Gupta M. K., Mia M., Pruncu C. I., Khan A. M., Rahman M. A., Jamil M., Sharma V. S., Modeling and performance evaluation of Al2O3, MoS2 and graphite nanoparticle-assisted MQL in turning titanium alloy: an intelligent approach. Journal of the Brazilian Society of Mechanical Sciences and Engineering 42(4), 207, 2020. doi:10.1007/s40430-020-2256-z.

Hong S. Y., Ding Y., Micro-temperature manipulation in cryogenic machining of low carbon steel. Journal of Materials Processing Technology 116(1), 22-30, 2001. doi:10.1016/S0924-0136(01)00836-6.

Iyappan S. K., Ghosh A., Anti-friction and wetting behavior of a new polymer composite coating towards aluminium and dry machining of AA2024 alloy by coated end mills. Journal of Materials Processing Technology 252, 280-293, 2018. doi:10.1016/j.jmatprotec.2017.09.033.

Jerold B.D., Kumar M.P., Machining of AISI 316 stainless steel under carbon-di-oxide cooling. Materials and Manufacturing Processes 27(10), 1059-1065, 2012. doi:10.1080/10426914.2011.654153.

Khanna N., Suri N. M., Shah P., Hegab H., Mia M., Cryogenic turning of in-house cast magnesium based MMCs: A comprehensive investigation. Journal of Materials Research and Technology 9(4), 7628-7643, 2020. doi:10.1016/j.jmrt.2020.05.023.

Korkmaz M. E., Gupta M. K., Demirsöz R., Boy M., Yaşar N., Günay M., Ross N. S., On tribological characteristics of TiC rollers machined under hybrid lubrication/cooling conditions. Tribology International 174, 107745. 2022. doi:10.1016/j.triboint.2022.107745.

Korkmaz M. E., Gupta M. K., Demirsöz R., Understanding the lubrication regime phenomenon and its influence on tribological characteristics of additively manufactured 316 Steel under novel lubrication environment. Tribology International 173, 107686, 2022. doi:10.1016/j.triboint.2022.107686.

Krolczyk G. M., Maruda R. W., Krolczyk J. B., Wojciechowski S., Mia M., Nieslony P., Budzik G., Ecological trends in machining as a key factor in sustainable production – A review. Journal of Cleaner Production 218, 601-615, 2019. doi:10.1016/j.jclepro.2019.02.017.

Kusuma N., Agrawal M., Shashikumar P. V., Investigation on the influence of cutting parameters on Machine tool Vibration & Surface finish using MEMS Accelerometer in high precision CNC milling machine', in 5th International & 26th All India Manufacturing Technology, Design and Research Conference (AIMTDR 2014), Assam/India, December 12-14, 2014, pp: 1-6.

Liu N., Liu B., Jiang H., Wu S., Yang C., Chen Y., Study on vibration and surface roughness in MQCL turning of stainless steel. Journal of Manufacturing Processes 65, 343-353, 2021. doi:10.1016/j.jmapro.2021.03.041.

Ma L., Howard I., Pang M., Wang Z., Su J., Experimental investigation of cutting vibration during micro-end-milling of the straight groove. Micromachines 11(5), 494, 2020. doi:10.3390/MI11050494.

Mojahed A., Moore K., Bergman L. A., Vakakis A. F., Strong geometric softening–hardening nonlinearities in an oscillator composed of linear stiffness and damping elements. International Journal of Non-Linear Mechanics 107, 94-111, 2018. doi:10.1016/j.ijnonlinmec.2018.09.004.

Ni C., Zhu L., Zheng Z., Zhang J., Yang Y., Yang J., Bai Y., Weng C., Lu W. F., Wang H., Effect of material anisotropy on ultra-precision machining of Ti-6Al-4V alloy fabricated by selective laser melting. Journal of Alloys and Compounds 848, 156457, 2020. doi:10.1016/j.jallcom.2020.156457.

Pecat O., Brinksmeier, E., Low damage drilling of CFRP/titanium compound materials for fastening. Procedia CIRP 13, 1-7, 2014. doi:10.1016/j.procir.2014.04.001.

Rao C. M., Sachin B., Rao S. S., Herbert M. A., Minimum Quantity Lubrication through the micro-hole textured PCD and PCBN inserts in the machining of the Ti–6Al–4V alloy. Tribology International 153, 106619, 2021. doi:10.1016/j.triboint.2020.106619.

Rogov V. A., Siamak G., Optimization of surface roughness and vibration in turning of Aluminum Alloy AA2024 using Taguchi technique. International Journal of Mechanical, Aerospace, Industrial, Mechatronic and Manufacturing Engineering 7(11), 2330-2339, 2013.

Sarıkaya M. et al., A state-of-the-art review on tool wear and surface integrity characteristics in machining of superalloys. CIRP Journal of Manufacturing Science and Technology 35, 624-658, 2021. doi:10.1016/j.cirpj.2021.08.005.

Sharif M. N., Pervaiz S., Deiab I., Potential of alternative lubrication strategies for metal cutting processes: a review, International Journal of Advanced Manufacturing Technology. The International Journal of Advanced Manufacturing Technology 89, 2447-2479, 2017. doi:10.1007/s00170-016-9298-5.

Szaksz B., Stepan G., Stability charts of a delayed model of vehicle towing. IFAC-PapersOnLine 54(18), 64-69, 2021. doi:10.1016/j.ifacol.2021.11.117.

Takahashi W., Nakanomiya T., Suzuki N., Shamoto E., Influence of flank texture patterns on the suppression of chatter vibration and flank adhesion in turning operations. Precision Engineering 68, 262-272, 2021. doi:10.1016/j.precisioneng.2020.12.007.

Turkes E., Orak S., Neseli S., Yaldiz S., Linear analysis of chatter vibration and stability for orthogonal cutting in turning. International Journal of Refractory Metals and Hard Materials 29(2), 163-169, 2011. doi:10.1016/j.ijrmhm.2010.10.002.

Türkeş E., Neşeli S., A simple approach to analyze process damping in chatter vibration. International Journal of Advanced Manufacturing Technology 70, 775-786, 2014. doi:10.1007/s00170-013-5307-0.

Wang D., Penter L., Hänel A., Ihlenfeldt S., Wiercigroch M., Stability enhancement and chatter suppression in continuous radial immersion milling. International Journal of Mechanical Sciences 235, 107711, 2022. doi:10.1016/j.ijmecsci.2022.107711.

Zagórski I., Kulisz, M., Effect of technological parameters on vibration acceleration in milling and vibration prediction with artificial neural networks. MATEC Web of Conferences 252, 03015, 2019. doi:10.1051/matecconf/201925203015.

Zhou C., Guo K., Sun J., Sound singularity analysis for milling tool condition monitoring towards sustainable manufacturing. Mechanical Systems and Signal Processing 157, 107738, 2021. doi:10.1016/j.ymssp.2021.107738.

JOURNAL of
MATERIALS and MECHATRONICS:A

e-ISSN 2717-8811
JournalMM, 2022, 3(2), 300-313
https://doi.org/10.55546/jmm.1193510

Araştırma Makalesi / Research Article

A Battery Management System Design Including a SOC Estimation Approach for Lead-Acid Batteries

Emre AKARSLAN[1]*, Said Mahmut ÇINAR[2]

[1] Afyon Kocatepe Üniversitesi, Mühendislik Fakültesi, Elektrik Mühendisliği Bölümü, Afyonkarahisar, Türkiye, ORCID ID: https://orcid.org/0000-0002-5918-7266, akarslan@aku.edu.tr
[2] Afyon Kocatepe Üniversitesi, Mühendislik Fakültesi, Elektrik Mühendisliği Bölümü, Afyonkarahisar, Türkiye, ORCID ID: https://orcid.org/0000-0002-6810-1575, smcinar@aku.edu.tr

Geliş/ Received: 24.10.2022; **Kabul / Accepted:** 08.12.2022

ABSTRACT: Storage is one of the most important issues of the last decades. In particular, storage systems are needed in order to benefit more effectively from renewable energy systems where production cannot be controlled. One of the most important problems in storage is that as the amount of energy desired to be stored increases, the need for space also increases. Therefore, it is of great importance to manage energy effectively in such systems. In this study, a battery management system (BMS) that can be used for lead acid batteries has been designed. This BMS has a measurement and control system based on STM 32 microcontroller and is controlled via an interface prepared in the MATLAB Simulink environment and the test data is imported into the MATLAB Workspace environment. The designed system can also perform battery charge-discharge experiments in accordance with the battery characteristics. Charge-discharge experiments were carried out using the designed system, and a model was developed to determine the state of charge (SOC) of the battery using the data collected during these experiments. With the model developed based on Elman Neural Networks, the SOC of battery could be estimated at an error level of less than 1%.

Keywords: Battery Management System (BMS), State of Charge (SOC), Elman Neural Network.

*Sorumlu yazar / Corresponding author: akarslan@aku.edu.tr

Bu makaleye atıf yapmak için /To cite this article

Akarslan, E., Çınar, S. M., (2022). A Battery Management System Design Including a SOC Estimation Approach for Lead-Acid Batteries. Journal of Materials and Mechatronics: A (JournalMM), 3(2), 300-313.

1. INTRODUCTION

The depletion of fossil fuel resources, the energy crisis and global warming have motivated the development of clean energy for electricity generation and smart grids (Hossain Lipu et al., 2021; Ansari et al., 2022). In addition, renewable energy sources come to the fore in this period due to their sustainability and the realization of consumption at the point of production. Among these renewable resources, solar and wind are the most scalable methods of producing clean energy (Zhao et al., 2020). Since the availability of solar and wind energy depends on weather conditions, it becomes difficult to manage the grid, so it becomes essential to develop strategies to ensure uninterrupted supply and develop energy storage systems (Tawalbeh et al., 2022). Lead acid batteries are frequently used in various areas, such as renewable energy systems, uninterruptible power systems, etc., since they are inexpensive, safe, and require less maintenance (Somasundaram et al., 2022). As with all battery types, these batteries should be observed and kept under control when used together. For this purpose, battery management systems (BMS) are used. The BMS is like a brain that monitors and controls parameters such as the cell's current, voltage, and temperatures to prevent damage and deterioration of cells and to extend the cell's life span by keeping it within safe operating ranges (Ren et al., 2019). Batteries are used in many areas, such as portable electronic devices, electric vehicles, smart grids, and battery management systems are needed for safe and effective use. A BMS can undertake a wide variety of tasks such as input/output current and voltage monitoring, charge-discharge control, inter-cell charge balancing, prediction of battery health, prediction of battery charge status, battery protection, and fault diagnosis (Cui et al., 2022; Corkhuff et al., 2018). One of the main tasks of the BMS is to accurately determine the state of charge (SOC) of the battery. The battery's SOC reflects its remaining power. In this context, accurate SOC estimation can improve battery efficiency, extend service life, and ensure battery reliability and safety (Wu et al., 2022; Lv et al., 2021). There are many studies in this field in the literature.

Ren et al. (2019) design a BMS to monitor and control the battery's temperature, SOC and state of health (SOH), thereby increasing the efficiency of rechargeable batteries. In the study, lithium-ion batteries were used for storage, and an active balancing system was preferred. In the study, the battery's remaining capacity was estimated based on each cell terminal voltage measurement. In the balancing process, the output voltage ripples are taken under control by taking into account the SOC estimates. Experimental results show that output voltage ripples can be minimized with more accurate SOC estimations (Ren et al., 2019). Okay et al. (2022) develop a prototype BMS for a grid-connected residential-photovoltaic (PV) system with lithium-ion batteries. It provides safe operation conditions by monitoring and controlling the battery parameters during the charge/discharge process. Furthermore, the BMS manages the energy flow between the PV system, battery, grid, and load (Okay et al., 2021). Liu and Yu (2022) use the square root unscented Kalman filter (SR-UKF) method for SOC estimation on lithium cobalt oxide batteries. They also construct a MATLAB/Simulink model for evaluating experimental results with less than 25 mV error. The experimental results show that more successful results were obtained with the SR_UKF model than with the traditional Kalman filter model (Liu and Yu, 2022). Jin et al. (2021) develop a second-order RC equivalent circuit model for lithium-ion batteries which considers the influence of discharge rate. An extended Kalman filter (EKF) model is employed for SOC estimation. Experiments show that under the condition of intermittent pulse discharge with gradually decreasing amplitude, the precision of estimating SOC can be significantly improved using the proposed approach (Jin et al., 2021). Cui et al. (2022)

construct the Thevenin equivalent circuit model of lithium-ion batteries. The extended Kalman filter approach is used for SOC estimation, and it is shown that this approach eliminates the Gaussian error. A test system is constructed in MATLAB/Simulink environment, and the performance tests are shown that a better performance is achieved than the traditional one (Cui et al., 2022). Singh et al. (2020) propose a model for SOC estimation. The model is utilized from the coulomb counting method, open circuit voltages, and ANFIS, and the effect of the temperature is also considered. The superiority of the proposed method has been demonstrated by experiments carried out under the same load conditions in a laboratory environment (Singh et al., 2020). Kuchly et al. (2021) propose using neural networks in the SOC estimation of a lithium-ion battery. Unlike the existing literature, the past-past current integral is used as input instead of instantaneous information in the proposed method. The results of the presented study revealed the success of artificial neural networks in SOC prediction (Kuchly et al., 2021).

In this study, Lead-acid batteries are selected since these kinds of batteries are preferred in uninterrupted power supplies and renewable energy systems. Serial-connected three 12 V 7 Ah Valve Regulated Lead Acid (VRLA) batteries are used in the experiments. A BMS based on STM32 microcontroller is designed. It is aimed to design a battery management system based on STM microcontroller. The designed BMS can carry out charge-discharge experiments according to battery characteristics and observe parameters such as current, voltage, and temperature during the experiments. Furthermore, passive balancing can be done with the designed system to ensure battery safety. In this scope, several experiments are performed, and parameters are collected. In the second part of the study, the Elman Neural Network based model is constructed for battery SOC estimation in a computer environment using collected data via an embedded system. The experimental results revealed the success of the proposed model.

2. THE EXPERIMENTAL SETUP

The experiment platform consists of a microcontroller development board, personal computer (PC), control board, test batteries, balancing resistors, discharge resistors, and power supply (Figure 1). At the center of the experimental platform is an STM32 Discovery F4 development board. The development board is connected to the PC via two USB ports that perform debugging and data transfer functions. On the control card, some relays controlled balancing resistors and charge-discharge phases, and current, voltage, and temperature sensors conditioning circuits are taken part. In addition, there are suitable terminals for power supply, batteries, temperature sensors, balancing resistors and discharge resistors, power supply connections, and connectors where the cables connecting to the development board are attached. The tested batteries consist of three cells, and the cell temperatures are sensed by the LM35 device attached to the bodies of the batteries. The firmware and user interface are graphically designed in the MATLAB Simulink environment. These components of the experimental setup are detailed below.

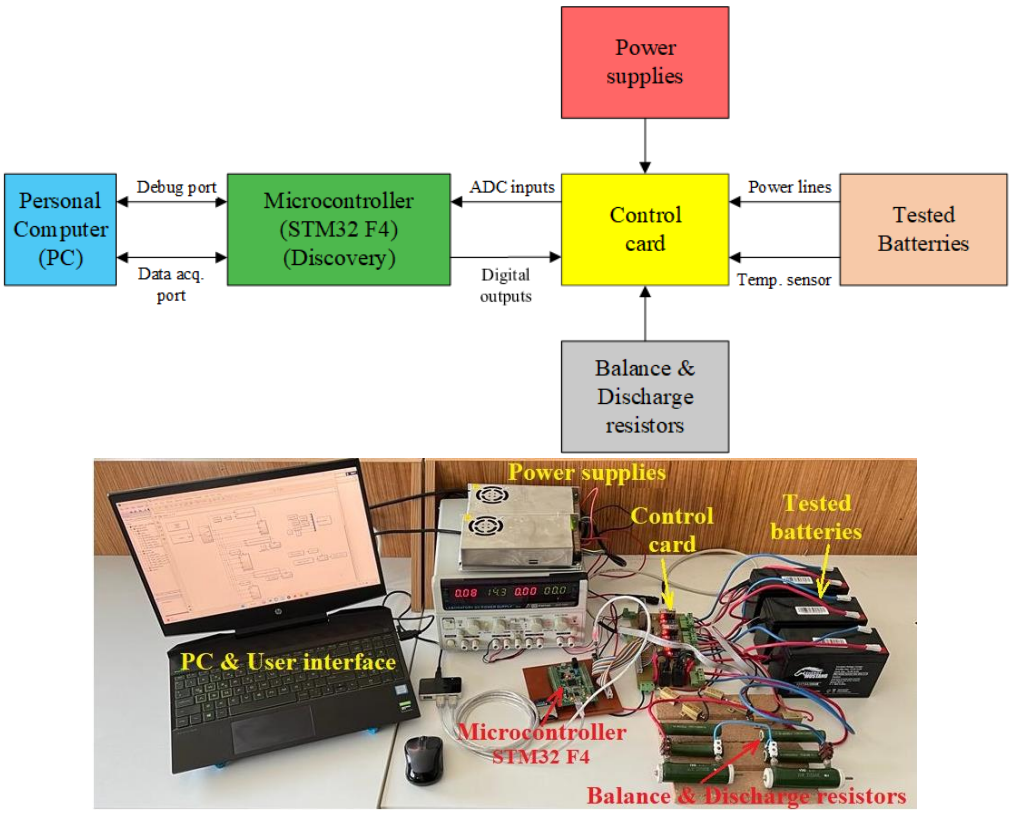

Figure 1. Block diagram of experimental setup

1. Development card and designed expansion shield:

STM32 Discovery-F4 development board has a microcontroller based on ARM Cortex M4 series STM32F407VGT6. The development board also has an ST-LINK/V2-A debugging unit that can be used for programming and debugging the microcontroller. The development board is attached in an expansion shield designed for this study (Figure 2). This shield has two connectors for digital and analog signals, one serial communication ports terminal, and an SD card module. In addition, low-pass filters were added to analog input ports.

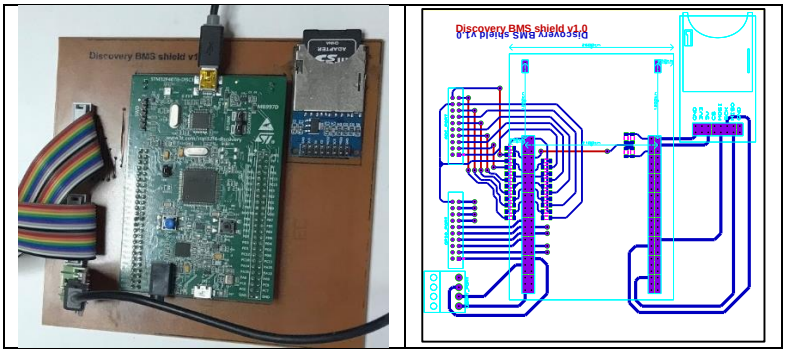

Figure 2. Designed expension shield for STM32 Discovery-F4

2. The control and measurement card:

The control card is sized to fulfill the power control and measurement tasks of three battery cells. The connections between the power control and measurement card and the expansion card are designed to provide electrical isolation. For this purpose, ACS712 series hall-effect based current sensors are used for current measurements, while ACPL series optical insulation-based voltage sensors are used for voltage measurements. In industrial/real applications, although an insulation

standard is not observed as much as in the measuring circuits used in this study, it has been tried to establish a high insulation standard in this presented R&D study. In addition, relays are used to initiate the charge or discharge phases and to activate and deactivate passive balancing resistors. Thus, any high voltage transitions from the power stage that may disrupt the micro-controller inputs or outputs can be prevented. A view of the power control and measurement board of the designed BMS is presented in Figure 3.

3. Firmware software:

The microcontroller's firmware was designed model-based, and for this, MATLAB Code generation, Simulink plugins, IAR Embedded Workbench development, and STM32CubeMx configuration software were used. This firmware performs many functions, such as managing the sampling times of analog signals from current, voltage, and temperature sensors, controlling balancing resistors, starting and stopping the charge and discharge phases, and data transfer via the user interface.

In the firmware design, the microcontroller is firstly configured on STM32CubeMx software (Figure 4). The general purpose input-output (GPIO) pins, an analog-digital converter (ADC), timers, and universal synchronous-asynchronous receive transmit (USART) peripheral modules are configured with the software, and a configuration file (*.ioc) is created. The configuration determines many design parameters, such as ADC channel sampling times, interrupt timing, direct memory access (DMA) dimension, USART baud rate, and DMA receive-transmit buffer dimension.

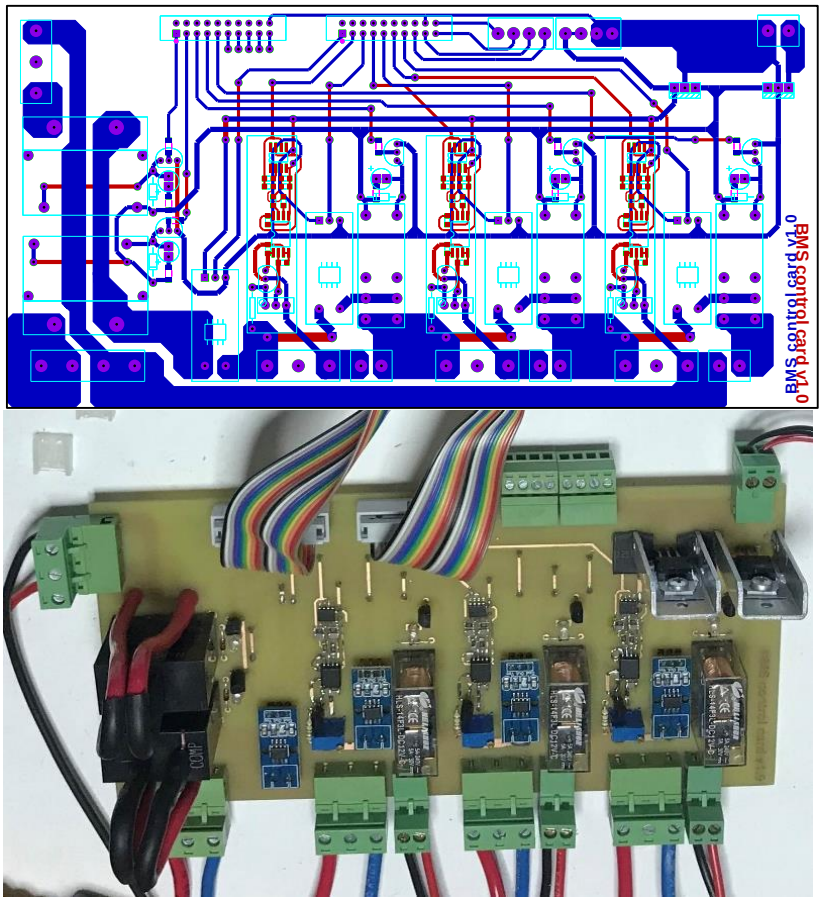

Figure 3. Designed control card

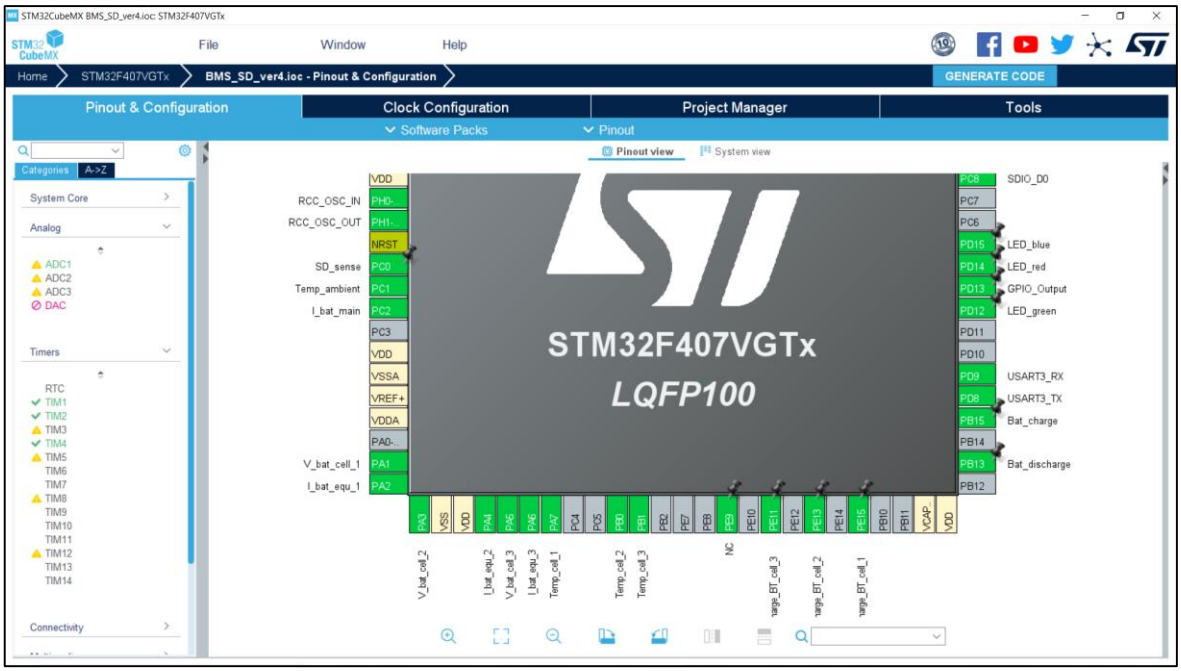

Figure 4. The microcontroller configuration software

After producing the configuration file, ADC sampling, ADC processing, USART sending and receiving, and battery equalizing tasks are programmed as model based in MATLAB/Simulink environment (Figure 5). In the study, the ADC sampling time is set to 4 milliseconds (ms), and ADC results are buffered with the DMA unit. After the buffer is full (total 128x11 words) root mean square (RMS) value of each channel is computed and sent via the USART. The data-packed, which includes the GPIO output logic levels produced by the BMS algorithm operated in the user interface and sent over the serial port at 500 ms intervals, are met with the USART data receive interrupt and buffered with DMA. Finally, the outputs are driven according to receiving data via USART.

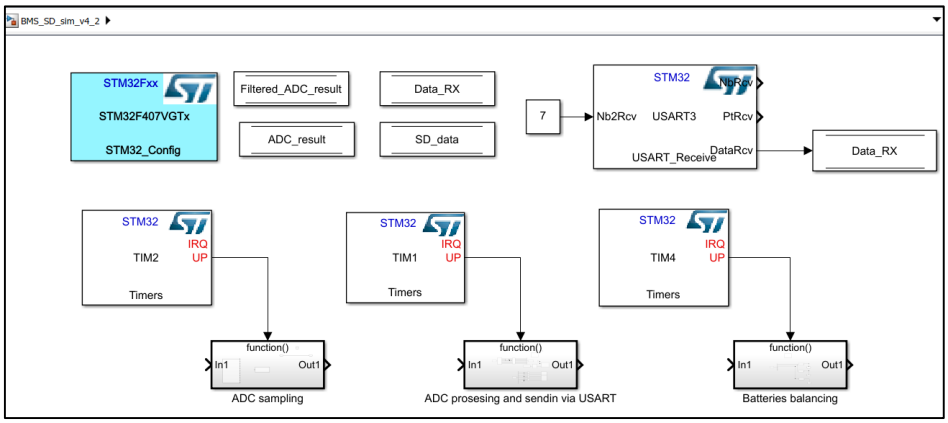

Figure 5. The model-based firmware design

The model prepared in the MATLAB/Simulink environment is built with the Code Generation tool, and C codes compatible with the IAR compiler are created (Figure 6). This way, C codes are produced effortlessly, and prototyping times can be considerably shortened. The generated code can be embedded in the microcontroller via the ST-LINK debug port, and debugging can be performed on the IAR-embedded workbench.

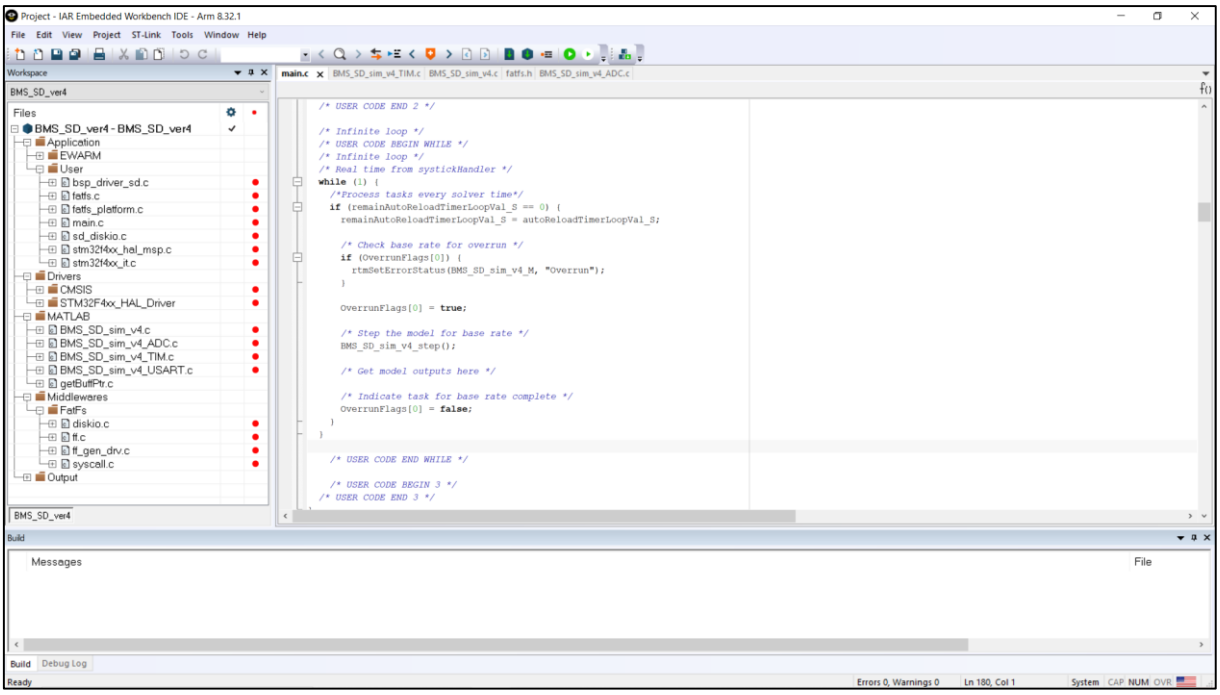

Figure 6. IAR integrated development environment.

4. User interface:

The main function of the user interface (Figure 7) is to display and store the test results. In this application, however, the initiation of the charge and discharge phases and the operation of the BMS passive balancing algorithm are also performed in the user interface. It is considered that these algorithms will be embedded in the firmware in the future. The Cortex M4 series microcontroller used in the study has 1MB flash program memory and 192+4KB RAM memory capacity, which can operate up to 168 MHz. Therefore, when the BMS algorithm running on the interface is embedded in the microcontroller, the algorithm can be run in real-time without any problems.

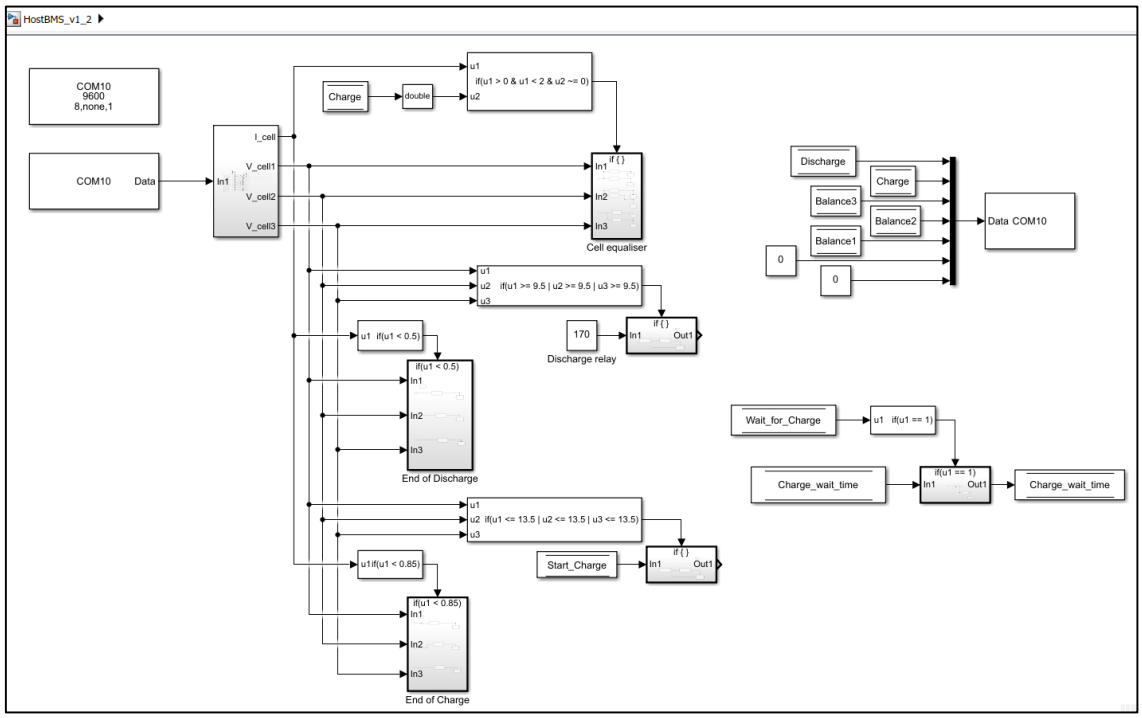

Figure 7. User interface for BMS

3. ELMAN NEURAL NETWORKS

In this study, Elman Neural Network is used for SOC estimation of Lead Acid Batteries. Elman neural network is a dynamic recurrent network proposed by J. L. Elman for solving a signal processing problem (Akarslan, 2022; Elman, 1990). Unlike other types of neural networks, it has a load-bearing layer and therefore provides a better prediction performance (Zhao et al., 2020). The input layer node acts as a signal transmission, while the output layer node works as a linear weight function. A linear or non-linear transfer function can be used in the hidden layer node. The previous value of the hidden layer can be hidden by the additional context layer, called one-step time delays (Zhang et al., 2019). In training, the context layer receives the feedback signal from the hidden layer and puts the previous output of the hidden layer into its input via the memory link. The basic schematic view of ENN is presented in Figure 8. In this study, battery voltage, temperature, and main branch current values are used as inputs for Elman Neural Network, and the network's output is the battery state of charge (SOC).

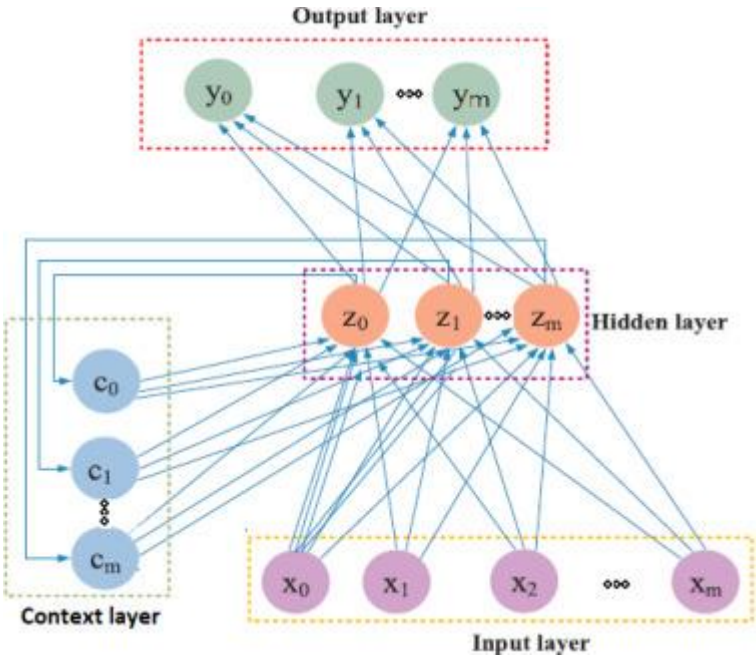

Figure 8. The principle schema of the Elman neural network (Li et al., 2018)

4. EXPERIMENTAL RESULTS

In this study serial connected three 12 V 7 Ah VRLA battery system is used for experiments, and a BMS system is designed. The designed BMS has some abilities, such as performing charge-discharge experiments, collecting current, voltage, and temperature data, providing passive balancing, etc. In this scope, the abilities of the designed BMS are tested. By using designed system, the data set containing 11 time series related to the current, voltage, temperature and ambient temperature of the battery cells is transferred to the MATLAB Workspace screen (Figure 9).

This figure also shows a time graph of the battery voltage in the charge-discharge cycle of the battery. While the battery is being discharged in the first part of the graph (in this part, a linear decrease in voltage is observed since the battery is discharged under constant load in this part), it is charged in the second part. In the charging part, after a sudden increase in voltage is observed with the start of charging, it is observed that the voltage increases almost linearly. In the last part of the

graph, fluctuations in voltage can be seen. This section shows that the passive balancing system is activated.

Figure 10 illustrates the variation of main branch current with time. In the discharge phase, it is seen that the current that can be drawn from the battery decreases over time, while the current drawn by the battery in the charging phase remains constant for a long time. This is provided by the BMS (in accordance with the battery characteristic). It was stated in the battery endurance that it would be appropriate for the battery to draw a maximum current of 2.1 A during charging, and this was also provided by BMS. Figure 5 illustrates the temperature variations in different experiments.

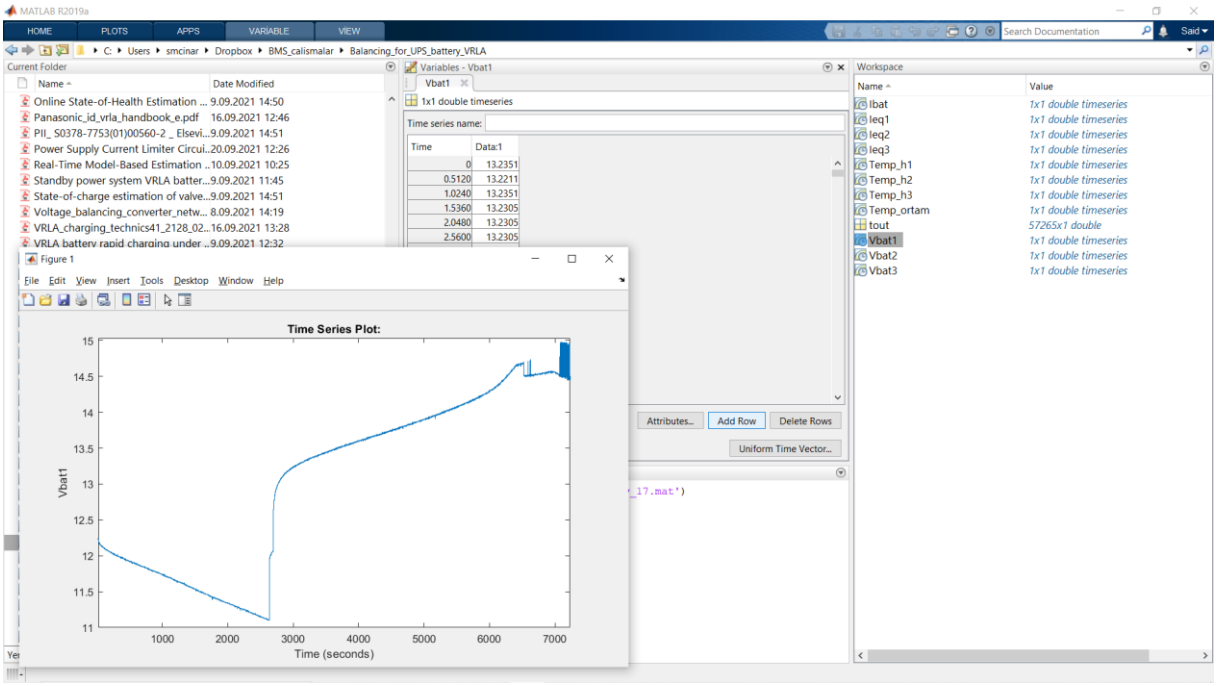

Figure 9. A view of the MATLAB workspace screen with experimental data

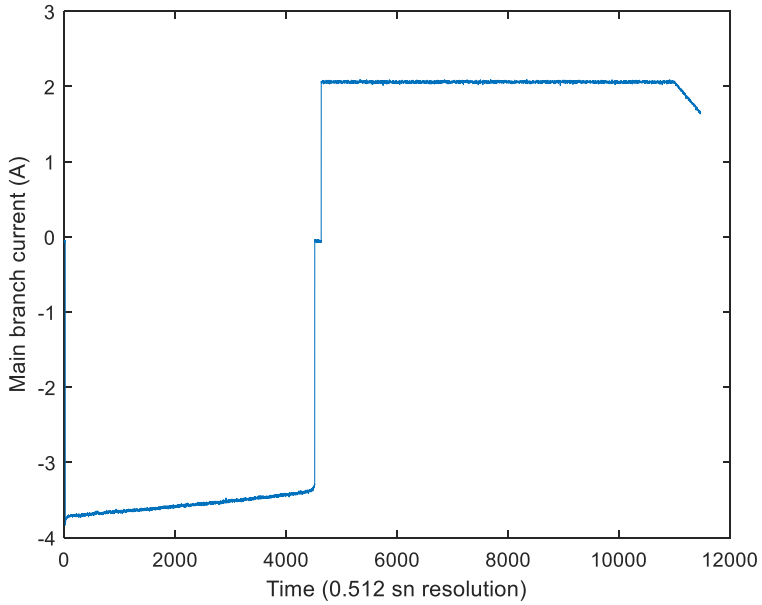

Figure 10. Time graph of main branch current in a discharge-charge cycle

In the study, two charge-discharge cycle experiments were carried out every day, and the graphs in the same color in this figure show the experiments performed on the same day. In the experiments carried out, there is no mechanism to keep the temperature constant, and it is seen that the temperature increases over time (Figure 11). This effect of temperature was also taken into account when evaluating the results. The results mentioned so far show that the state of charge of the battery is related to the current, voltage and temperature values of the battery. For this reason, an Elman neural network model was developed to predict the state of charge of the battery using the three mentioned parameters as inputs.

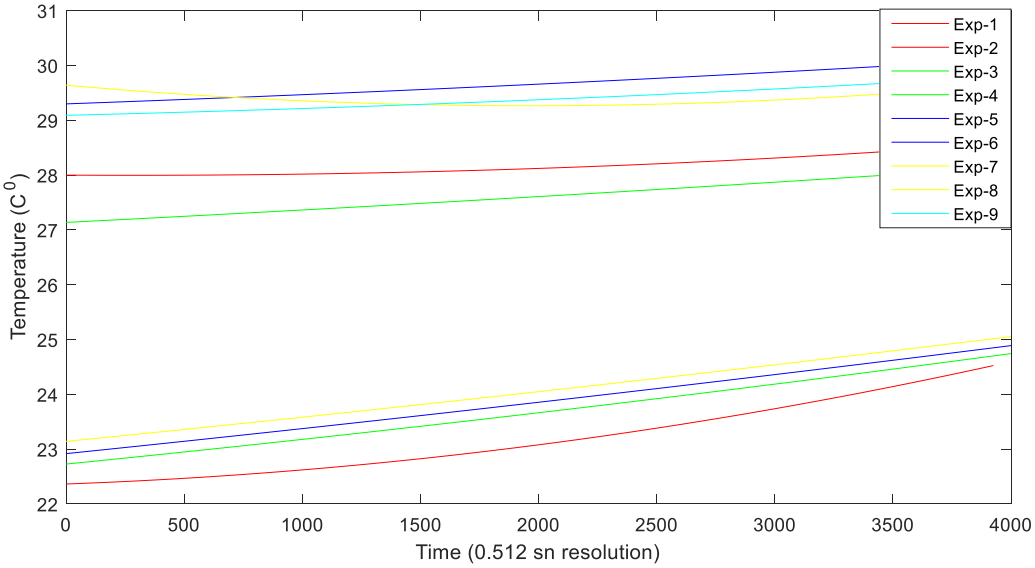

Figure 11. Temperature values observed in the discharge phase of a battery in different experiments

In this context, the data of 12 experiments out of the data of 18 experiments were used in training, and data from 6 experiments were used in the testing phase. Since three battery cells of the same model were used in the experimental setup, the SOC value is estimated for any battery cell at any time, regardless of which battery cell it belongs to, using the specified parameters. However, in order to compare their performance, the performance of the model created in the case of only charging, only discharging, and using all values without knowing which phase they belong to, as mentioned above, is examined. In the created Elman Neural Network, after various trials, it was decided to have two hidden layers and six and eight neurons in these layers, respectively. While tansig and logsig activation functions are used in the hidden layer, the linear activation function is used in the output layer. The variation graph of error in the training phase for the Elman Neural Network is illustrated in Figure 12. In Table 1, the performance values for the estimations in the case of only the charge phase data, only the discharge phase data, and all data are presented.

Table 1. Performance results on SOC estimation

	RMSE	RMSE(%)	MBE	r	r2
Discharge	0.2885	0.61	-0.003	0.9993	0.9986
Charge	0.2879	0.47	-0.0019	0.9995	0.999
Both (C/D)	0.2983	0.53	0.002	0.9996	0.9992

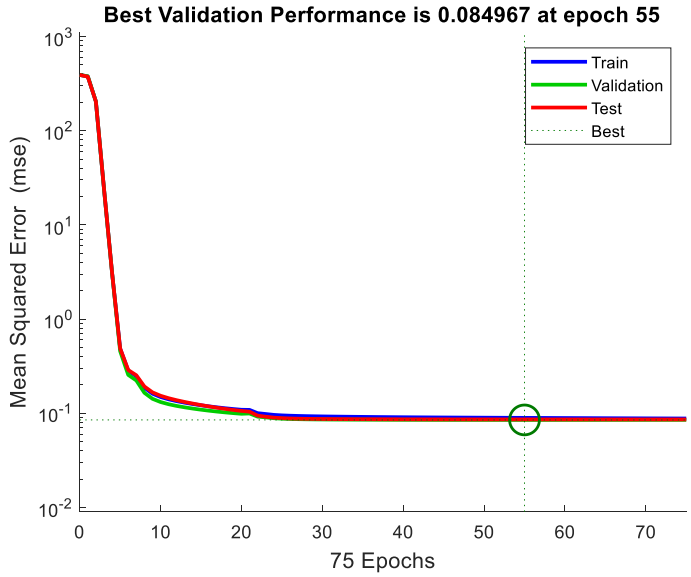

Figure 12. Variation graph of error in training phase for Elman Neural Network

The Root Mean Square Error (RMSE), Mean Bias Error (MBE), correlation coefficient (r), and specificity coefficient (r2) parameters are used as performance criteria. When Table 1 is examined, it is seen that the RMSE value in the SOC estimation is 0.2983 when all data are used. In order to see what this value is compared to the size of the data in the data set, the percentile RMSE value was also calculated and the error was determined to be 0.53%. It shows that quite successful predictions were made. The MBE value was determined as 0.002, which indicates that these estimates are quite balanced. It is seen that the correlation and specificity coefficients are at the level of 0.99. The closeness of these values to 1 reveals the success of the estimation. Figure 13 shows the correlation graph between the actual and predicted values for all data. As seen from the figure, the data were collected on the diagonal axis, indicating the prediction's success.

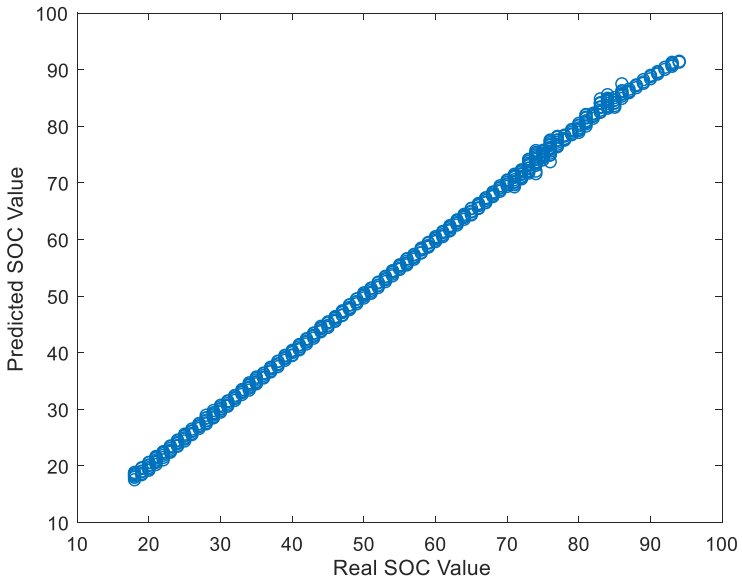

Figure 13. Correlation graph of actual values and predicted values

In order to compare the results obtained from the study with the existing studies, the results obtained from various methods used in the literature are presented in Table 2. When Table 2 is examined, it is seen that very successful estimations are made with the approach used in the study.

Table 2. SOC estimation error comparison

Method	Battery Type	RMSE (%)
Linear Matrix İnequalities (Shen and Rahn, 2013)	Lead- Acid	4.93
Switched Model (Shen and Rahn, 2013)	Lead- Acid	0.35
Dynamic data-driven (Li et al., 2016)	Lead- Acid	2.08
Extended Kalman Filter (Wang et al., 2017)	Li-ion	1.33
Elman Neural Network (This study)	Lead- Acid	0.2983

5. CONCLUSION

In this study, it was aimed and realized to design an STM-based battery management system. The developed BMS has features such as carrying out charge-discharge experiments, controlling the charge-discharging process in accordance with the battery characteristics, observing and recording parameters such as current, voltage, and temperature during the experiments, and protecting the system in case the measured parameters go out of the determined limits. In addition, the designed BMS is capable of passive balancing. The designed BMS was tested on a system with three lead acid batteries connected in series. In the first part of the study, the ability of the BMS to fulfill the desired features was tested and it was observed that the desired features were provided. The designed system can be controlled via a computer, or the system can operate independently of the computer. In the second step, an Elman Neural Networks-based prediction model was created that can predict the battery state of charge at any time by determining the parameters related to the state of charge of the battery. The current, voltage, and temperature data of the batteries are selected as features and used as inputs of the algorithm. The test results show that the state of charge of the battery can be predicted with errors less than 1%. In the presented study, the SOC prediction process is executed on computer using data from the embedded system. It is planned as a future study to carry out the whole process in the embedded system, including the SOC estimation.

6. ACKNOWLEDGEMENTS

This study was supported by Afyon Kocatepe University Scientific Research Projects Coordination Unit with Project number of 18. KARIYER.193.

7. CONFLICT OF INTEREST

Authors approve that to the best of their knowledge, there is not any conflict of interest or common interest with an institution/organization or a person that may affect the review process of the paper.

8. AUTHOR CONTRIBUTION

Emre AKARSLAN; determining the concept and design process of the research, data analysis, writing, experimental studies, and interpretation of results. Said Mahmut ÇINAR; determining the

concept and design process of the research, experimental studies, data collection and analysis, and interpretation of results.

9. REFERENCES

Akarslan E., Learning Vector Quantization based predictor model selection for hourly load demand forecasting, Applied Soft Computing 117, 108421, 2022. https://doi.org/10.1016/J.ASOC.2022.108421.

Ansari S., Ayob A., Hossain Lipu M. S., Hussain A., Md Saad M. H., Remaining useful life prediction for lithium-ion battery storage system: A comprehensive review of methods, key factors, issues and future outlook. Energy Reports 8, 12153-12185, 2022. https://doi.org/10.1016/j.egyr.2022.09.043

Carkhuff B. G., Demirev P. A., Srinivasan R., Impedance-Based Battery Management System for Safety Monitoring of Lithium-Ion Batteries. IEEE Trans Ind Electron 65, 6497-6504, 2018. https://doi.org/10.1109/TIE.2017.2786199.

Cui Y., Lin K., Zhu J., Chen Y., Quantum-inspired degradation modeling and reliability evaluation of battery management system for electric vehicles. Journal of Energy Storage 52, 104840, 2022. https://doi.org/10.1016/J.EST.2022.104840.

Cui Z., Hu W., Zhang G., Zhang Z., Chen Z., An extended Kalman filter based SOC estimation method for Li-ion battery. Energy Reports 8(5), 81-87, 2022. https://doi.org/10.1016/J.EGYR.2022.02.116.

Elman J. L., Finding structure in time. Cognitive Science 14(2), 179-211, 1990. https://doi.org/10.1016/0364-0213(90)90002-E.

Hossain Lipu M. S., Hannan M. A., Karim T. F., Hussain A., Saad M. H. M., Ayob A., Miah M. S., Indra Mahlia T. M., Intelligent algorithms and control strategies for battery management system in electric vehicles: Progress, challenges and future outlook. Journal of Cleaner Production 292, 126044, 2021. https://doi.org/ 10.1016/j.jclepro.2021.126044.

Jin Y., Zhao W., Li Z., Liu B., Wang K., SOC estimation of lithium-ion battery considering the influence of discharge rate. Energy Reports 7(7), 1436-1446, 2021. https://doi.org/10.1016/J.EGYR.2021.09.099.

Kuchly J., Goussian A., Merveillaut M., Baghdadi I., Franger S., Nelson-Gruel D., Nouillant C., Chamaillard Y., Li-ion battery SOC estimation method using a Neural Network trained with data generated by a P2D model, IFAC-PapersOnLine 54(10), 336-343, 2021. https://doi.org/10.1016/J.IFACOL.2021.10.185.

Li Y., Chattopadhyay P., Xiong S., Ray A., Rahn C.D., Dynamic data-driven and model-based recursive analysis for estimation of battery state-of-charge. Applied Energy 184, 266-275, 2016. http://dx.doi.org/10.1016/j.apenergy.2016.10.025

Li X., Zhang L., Wang Z., Dong P., Remaining useful life prediction for lithium-ion batteries based on a hybrid model combining the long short-term memory and Elman neural networks. Journal of Energy Storage 21, 510-518, 2018. https://doi.org/10.1016/j.est.2018.12.011.

Liu Q., Yu Q., The lithium battery SOC estimation on square root unscented Kalman filter, Energy Reports 8(7), 286–294, 2022. https://doi.org/10.1016/J.EGYR.2022.05.079.

Lv J., Wang X., Wang G., Song Y., Research on Control Strategy of Isolated DC Microgrid Based on SOC of Energy Storage System. Electronics 10(7), 834, 2021. https://doi.org/10.3390/ELECTRONICS10070834.

Okay K., Eray S., Eray A., Development of prototype battery management system for PV system. Renew Energy 181,1294-1304, 2022. https://doi.org/10.1016/J.RENENE.2021.09.118.

Ren H., Zhao Y., Chen S., Wang T., Design and implementation of a battery management system with active charge balance based on the SOC and SOH online estimation. Energy 166, 908-917, 2019. https://doi.org/10.1016/J.ENERGY.2018.10.133.

Shen Z, Rahn C. Model-based state-of-charge estimation for a valve-regulated lead-acid battery using matrix inequalities. Journal of Dynamic Systems, Measurement, and Control 135(4), 041015, 2018. https://doi.org/10.1115/1.4023766

Singh K. V., Bansal H. O., Singh D., Hardware-in-the-loop Implementation of ANFIS based Adaptive SoC Estimation of Lithium-ion Battery for Hybrid Vehicle Applications, Journal of Energy Storage 27, 101124, 2020. https://doi.org/10.1016/J.EST.2019.101124.

Somasundaram P., Jegadheesan C., Pal Singh A., Vivekanandhan C., Suganth S., Vikaash R., Shankarguru E., Effect of ambient pressure on charging and discharging characteristics of lead acid battery. Materials Today Proceedings 64(1), 888-894 2022. https://doi.org/10.1016/J.MATPR.2022.05.401.

Tawalbeh M., Murtaza S. Z. M., Al-Othman A., Alami A. H., Singh K., Olabi A. G., Ammonia: A versatile candidate for the use in energy storage systems. Renewable Energy 194, 955-977, 2022. https://doi.org/10.1016/j.renene.2022.06.015

Wang S., Fernandez C., Shang L., Li Z., Li J., Online state of charge estimation for the aerial lithium-ion battery packs based on the improved extended Kalman filter method. Journal of Energy Storage, 9, 69-83, 2017. http://dx.doi.org/10.1016/j.est.2016.09.008

Wu Y., Zhao H., Wang Y., Li R., Zhou Y., Research on life cycle SOC estimation method of lithium-ion battery oriented to decoupling temperature. Energy Reports 8, 4182-4195, 2022. https://doi.org/10.1016/J.EGYR.2022.03.036.

Zhang Y., Yang G., Ma S., Non-intrusive load monitoring based on convolutional neural network with differential input. Procedia CIRP, 83, 670-674, 2019. https://doi.org/10.1016/j.procir.2019.04.110.

Zhao X., Xuan D., Zhao K., Li Z., Elman neural network using ant colony optimization algorithm for estimating of state of charge of lithium-ion battery. Journal of Energy Storage 32, 101789, 2020. https://doi.org/10.1016/j.est.2020.101789.